
Quantum Memory and Teleportation Using Macroscopic Gas Samples

Jacob F. Sherson

Danish National Research Foundation
Center for Quantum Optics - QUANTOP
Department of Physics and Astronomy
University of Aarhus, Denmark

PhD thesis
September 2006

This thesis is submitted to the Faculty of Science at the University of Aarhus, Denmark, in order to fulfil the requirements for obtaining the PhD degree in Physics. The experimental part of the studies have been carried out under the supervision of Prof. Eugene Polzik in the Quantum Optics Laboratory at the Department of Physics and Astronomy, Aarhus University from August 2002 to January 2003, and at the Quantum Optics Laboratory, Niels Bohr Institute, Copenhagen University from February 2003 to August 2006. Throughout the duration of the studies theoretical work has been conducted in Aarhus under the supervision of Prof. Klaus Mølmer.

Contents

List of Publications	vii
Preface	ix
1 Introduction	1
2 Atom-Light Interaction	9
2.1 Atomic Spin Operators	10
2.2 Polarization States of Light	12
2.3 Off-Resonant Coupling	13
2.3.1 Two Level Interaction	14
2.3.2 Full Multi-level Coupling	17
2.4 Propagation Equations	19
2.5 The Rotating Frame	20
2.6 Two Oppositely Oriented Spin Samples	21
2.7 Introducing Canonical Operators	22
2.8 Canonical Description of the Single Cell Interaction	24
3 Entanglement Modeling - Experimental Approach	27
3.1 The Coherent Spin State	29
3.2 Entanglement Generation and Verification	29
3.3 Theoretical Entanglement Modeling	31
3.4 Entanglement Model with Decoherence	33
4 Gaussian Entanglement	35
4.1 General Theory of Covariance Matrices	36
4.2 Entanglement Based on the QND Interaction	40
4.3 Entanglement Based on the Single Cell Interaction with Rotations	41
4.4 Solving the Dynamics Continuously in Time	44
4.4.1 Investigating the Role of the Rotation Frequency	44
4.4.2 Arbitrary Rotation Frequency with Noise	48

4.4.3	The Strongly Rotated Regime	49
5	Experimental Methods	53
5.1	Atomic System	53
5.2	Lasers and Light Characterization	55
5.2.1	Pump Lasers	55
5.2.2	Probe Laser	58
5.2.3	Detection of Polarization States	60
5.3	Magnetic Fields	63
5.3.1	Characterizing the Spin State with the Magneto-Optical Resonance Method	64
5.3.2	Manipulating the Spin State	66
5.4	Decoherence	68
5.5	Experimental Cycle	71
5.6	Projection Noise Level	72
5.6.1	Measuring the Macroscopic Spin	72
5.6.2	Predicting the Projection Noise Level	74
5.6.3	Experimental Investigation	75
5.6.4	Thermal Spin Noise	76
5.6.5	Concluding Remarks on the Projection Noise Level	77
6	Entanglement Results	79
6.1	Conditional Entanglement	79
6.2	Unconditional Entanglement	82
6.3	Concluding Remarks on the Entanglement Experiments	83
7	Quantum Memory Results	85
7.1	Direct Mapping Protocol	86
7.1.1	Mapping with Decoherence	86
7.2	Fidelity	87
7.2.1	The Best Classical Fidelity	88
7.3	The Input State	89
7.3.1	Modulation of Stokes Operators	90
7.4	Experimental Results	92
7.4.1	Mean Values	93
7.4.2	Variances	94
7.4.3	Varying the Feedback Gain	95
7.4.4	Memory Life Time	96
7.4.5	Why Not Unity Gain	96
7.4.6	Concluding Remarks	97
8	Light Atom Teleportation	103
8.1	Light Atom Teleportation with the Faraday Interaction	105
8.2	Experimental Verification	107
8.2.1	Verifying the Mean Values	108

8.2.2	Reconstructing the Atomic Variances	108
8.2.3	Calculating the Fidelity of Teleportation	109
8.3	Experimental Considerations	111
9	Quantum Memory Retrieval	117
9.1	Two-pass Dynamics	119
9.1.1	Constant Interaction Strength	121
9.1.2	Time-dependent Interaction Strength	123
9.2	Four-pass Protocol	125
9.2.1	Four-pass Mapping	125
9.2.2	Four-pass Retrieval	126
9.2.3	Avoiding the Divergence with a Cut-off	126
9.3	Qubit Fidelities	128
9.3.1	Simple "Decay" Model for the 4pass Fidelity	129
9.3.2	General Fidelity Calculation	130
10	Polarization Squeezing by Faraday Rotation	135
10.1	CW Squeezing	136
10.2	Pulsed Squeezing	138
11	Summary and Outlook	141
11.1	Summary	141
11.2	Outlook	142
11.2.1	Atom-atom Teleportation	142
11.2.2	Interfacing with Non-classical Light States	145
A	Effect of Atomic Motion	147
A.1	Modeling Atomic Motion	147
A.2	Atomic Motion as a Source of Decoherence	149
B	Covariance Matrix Update with Decoherence	151
C	High Order Stark Shift	155
D	Important Abbreviations	159
	Bibliography	161

List of Publications

- [I] E. S. Polzik, B. Julsgaard, J. Sherson, and J. L. Sørensen, *Entanglement and quantum teleportation with multi-atom ensembles*, Phil. Trans. Roy. Soc. A **361**, 1391 (2003).
- [II] B. Julsgaard, J. Sherson, J. L. Sørensen, and E. S. Polzik, *Characterizing the spin state of an atomic ensemble using the magneto-optical resonance method*, J. Opt. B: Quantum Semiclass. Opt. **6**, 5 (2004).
- [III] B. Julsgaard, J. Sherson, J. I. Cirac, J. Fiurášek, and E. S. Polzik, *Experimental demonstration of quantum memory for light*, Nature **432**, 482 (2004).
- [IV] J. Sherson and K. Mølmer *Entanglement of large atomic samples: a Gaussian state analysis*, Phys. Rev. A **71**, 033813 (2005)
- [V] J. Sherson, B. Julsgaard, and E. S. Polzik *Distant Entanglement of Macroscopic Gas Samples*, in Decoherence, Entanglement and Information Protection in Complex Quantum Systems, pp. 353-372, eds. W. M. Akulin, A. Sarfati, G. Kurizki, and S. Pellegrin (Springer, Dordrecht, 2005)
- [VI] J. F. Sherson, A. S. Sørensen, J. Fiurášek, K. Mølmer, and E. S. Polzik *Light Qubit Storage and Retrieval using Macroscopic Atomic Ensembles*, Phys. Rev. A **74**, 011802(R)(2006)
- [VII] J. Fiurášek, J. Sherson, T. Opatrny, and E. S. Polzik *Single-passage read-out of atomic quantum memory*, Phys. Rev. A **73**, 022331 (2005)
- [VIII] K. Hammerer, J. Sherson, B. Julsgaard, J.I. Cirac, and E.S. Polzik *Deterministic quantum interface between light and atomic ensembles*, book chapter To appear in *Quantum information with continuous variables of atoms and light*, eds. N.Cerf, G.Leuchs, and E.S. Polzik.
- [IX] J. Sherson, B. Julsgaard, and E. S. Polzik *Deterministic atom-light quantum interface*, quant-ph/0601186, To appear in Advances in Atomic, Molecular, and Optical Physics, Vol 54(2006).

- [X] J. F. Sherson, H. Krauter, R. K. Olsson, B. Julsgaard, K. Hammerer, J. I. Cirac, and E. S. Polzik *Quantum teleportation light and matter*, quant-ph/0605095 (2006), accepted for Nature
- [XI] J. F. Sherson and K. Mølmer *Polarization squeezing by optical Faraday rotation*, quant-ph/0606076, (2006) accepted for publication in Phys. Rev. Lett.

Preface

During my four year PhD studies I have had the pleasure and the responsibility of having two highly competent supervisors. I have been involved in the experiment using room temperature atomic ensembles under the supervision of Prof. Eugene Polzik at the Niels Bohr institute in Copenhagen. At the same time I have done theoretical work on understanding the process of entanglement generation and the implementation of new quantum information protocols under the supervision of Prof. Klaus Mølmer at the University of Aarhus.

Both of them have been enormous sources of inspiration - always having an ingenious solution ready for short term and well as long term projects. During the first two and a half years I also had the pleasure of working with Brian Julsgaard, who taught me all about the daily routines in the lab and always took the time to answer my questions. I also had the fortune of a brief but educational period of overlap with Jens Lykke Sørensen in the lab.

Recently, first the Masters student Rasmus K. Olsson and then also the PhD student Hanna Krauter have made an enthusiastic and competent contributions to the experiment. We have had a wonderful collaboration and they have both contributed to a great atmosphere in the lab in their own way.

I would also like to thank the entire gang at QUANTOP for excellent company and scientific discussions and especially Jörg Helge Müller for always taking the time to discuss technical problems.

Also, I would like to acknowledge the Danish National Research Foundation for providing financial support for the Center for Quantum Optics (QUANTOP) and through it for my PhD studies.

Last but not least I would like to thank my wife for her constant support and understanding, and my family and friends for always being there on the rare occasions when I had time.

During the time of my PhD the focus of this experiment has shifted from a fundamental investigation of the Faraday interaction towards application of this interaction in a quantum information context. The main part of the former

was performed by the PhD student responsible for setting up the experiment - Brian Julsgaard - and is described in detail in his PhD thesis [1]. For simplicity mathematical and experimental details from this work are therefore only included to the extent that it is relevant for the understanding of the quantum information experiments, which form the main topic of this thesis. If possible, details derived primarily by Brian Julsgaard are placed in appendices.

September 2006, Jacob F. Sherson

CHAPTER 1

Introduction

The field of quantum information, although being quite young, has its foundations from the early days of quantum mechanics. In 1935 Einstein, Podolsky and Rosen (EPR) put forth what they believed was a proof that quantum mechanics was an incomplete theory [2]. Their argument, which was based on the basic assumption that two systems cannot influence each other when they are not interacting (locality), briefly told goes as follows. Let two particles characterized by position operators \hat{x}_1 and \hat{x}_2 and momentum operators \hat{p}_1 and \hat{p}_2 , respectively, interact for some time such that $\hat{p}_1 + \hat{p}_2 = 0$ and $\hat{x}_1 - \hat{x}_2 = x_o$ and then separate the two systems in space. A measurement of \hat{x}_1 yielding x means that the position of the second particle is $x - x_o$, which is an eigenstate of the position operator. If on the other hand we had chosen to measure \hat{p}_1 and got p the momentum of the second particle would be given by $-p$, this time an eigenvalue of the momentum operator. Based on the assumption that a measurement of the first particle cannot change the state of the second particle, the authors conclude that the second particle is in an eigenstate of both position and momentum simultaneously. This gives a contradiction because position and momentum do not commute and therefore according to the Heisenberg uncertainty principle cannot be known simultaneously. From this so-called EPR-paradox, the authors conclude that quantum mechanics is incomplete and that the universe is described by a more fundamental, so far undiscovered, theory (hidden variables theory). In the same year Schrödinger published a response in three parts [3] where he claims that instead of giving up quantum mechanics one should give up the assumption of locality: the two particles can indeed influence each other non-locally because their combined state is described by a *single* wave function. He

introduced the word *Verschränkung* or *entanglement* to describe the non-local correlations between the two systems.

Entanglement comes in two distinct forms. The form of entanglement introduced by EPR deals with the combined state of two systems each described by position and momentum variables that form a continuous spectrum of eigenvalues. Another type of entanglement occurs in systems with a discrete spectrum. A famous example is the spin singlet state formed by two spin 1/2 particles, $\psi = |\uparrow\downarrow\rangle - |\downarrow\uparrow\rangle$. If one of the two spins is measured to be in the spin-up state the other one is certain to be in the spin-down state. It turns out that an equivalent formulation of the EPR-paradox can be done in terms of this discrete entanglement.

The paradox remained an unresolved curiosity until John Bell in 1964 derived correlation inequalities [4] that must be satisfied within all hidden variable theories but can be violated in quantum mechanics. In the 70'ies and the 80'ies entanglement was primarily used as a means of testing these inequalities. All experiments such as e.g. [5, 6, 7, 8] gave strong support for the quantum mechanical foundations.¹

In later years, however, entanglement has instead come to be viewed as a potentially revolutionizing resource in future technological applications. This shift was driven by the realization primarily in the early 90'ies that entanglement could be used as a resource in protocols that could improve existing classical information processing, but also in purely quantum mechanical protocols with no classical analogue.

In 1984 Bennett and Brassard proposed a *quantum cryptographic* scheme for the transmission of encrypted messages [10], where the security was guaranteed by the fact that unknown quantum states cannot be cloned [11] and the implicit use of entanglement [12], and in 1991 a protocol based directly on the distribution of entanglement was proposed [13]. The absolute security constitutes a fundamental improvement compared to conventional classical encryption schemes such as e.g. RSA [14], where no formal proof of security exists but breaching it requires such enormous computational power that it is considered practically secure. As we shall see shortly, scientific and technological advances in the field of quantum information processing could offer unprecedented computational power and hence endanger the security of classical encryption schemes.

A year later a *quantum dense coding* protocol showing that 2 bits of information could be sent with a single spin 1/2 particle by the use of entanglement [15]. This and a similar protocol for continuous variables [16] offer the possibility of increasing the capacity of the existing classical communication channels.

Furthermore, in a 1993 complete departure from the paradigm of classical communication it was shown [17] that an unknown quantum state can be transferred from one location to another without physically having to cross the inter-

¹Note however, that to date all of the experiments showing violations have suffered from loopholes allowing for a local-realistic explanation such as low detection efficiency or time-like interval between the detection events. Recently an experimentally feasible setup for a loop-hole free Bell test was proposed [9], so a final confirmation may come in the near future.

mediate distance. This process, known as *quantum teleportation* requires distributed entanglement as a fundamental resource. From these proposals the field of *quantum communication* emerged.

In a parallel development it was shown that the fact that quantum states can exist simultaneously in a superposition of several eigenstates can be employed to speed up certain computational task dramatically. Most notably, Peter Shor [18] showed that the problem of factorizing the product of two primes, upon which much of present day data encryption is based (RSA) [14], could be performed with a number of operations scaling polynomially with the number of bits required to represent the product instead of exponentially by taking advantage of the quantum parallelism arising when several particles existing in superpositions are entangled. It was also shown that using such a *quantum computer* a specified element in an unsorted list containing N elements could be found in $\sim \sqrt{N}$ trials instead of the $\sim N/2$ trial required by a classical computer. These and similar algorithms spurred an intense interest in the development of a quantum computer, where logical operations are performed on a number of two level systems (qubits), each existing in a superposition of the two levels $|0\rangle$ and $|1\rangle$

Following the proposed technological applications for entanglement the experimental effort being put into producing such states was dramatically increased. Entanglement occurs everywhere in nature: in a spin singlet of helium the two electrons are entangled and every time a system interacts with the surroundings it becomes entangled with these. The hard part is to create entanglement in protected and controllable surroundings. There are roughly speaking two different methods for generating entanglement. One can let a system emit or decay into other particles, which because of energy and momentum conservation will be entangled. Alternatively one can let two systems interact for a controlled amount of time and subsequently move them apart.

In the 90'ies the field was dominated by entangled states of light produced in the former way via parametric down conversion in non-linear crystals. Here entanglement between two [19, 20] and subsequently three [21], four [22], and five photons [23] was achieved. The method relies on coincidence detections, which means that the entanglement cannot be created on demand and the resources and time required increases rapidly with the number of photons. In a parallel development the continuous variable quadratures \hat{x} and \hat{p} (analogues of amplitude and phase) of two beams were entangled [24]. This type of entanglement is exactly the type discussed in the original EPR paper.

Although many quantum information protocols can be implemented using light states only, an atomic implementation would be highly desirable because of the potential for extremely long storage times. At the end of the 90'ies and onwards more and more experimental verifications of atomic entanglement appeared. These mostly utilize the second approach to entanglement generation - letting two systems interact. In ion traps two [25] and subsequently four ions [26] were entangled. The ions are separated by a few μm and hence cannot be addressed individually but they interact through the Coulomb interaction and form collective motional degrees of freedom. Using the excited states of these as

intermediate states the ions can be entangled. In parallel experiments first two thermal Rydberg atoms [27] and then two atoms and a photon were entangled. This was done by sending a sufficiently weak thermal beam of Rydberg excited atoms across an initially empty high Q microwave cavity, which was exactly resonant with the microwave transition between two Rydberg states. When the first atom crossed the cavity the ensuing Rabi oscillations were timed such that with 50% likelihood the atom would emit a photon into the otherwise empty cavity. At the passage of the second atom, which was initialized in the ground state, the Rabi oscillation was controlled such that if a photon was present in the cavity it would be absorbed with unity probability. This procedure leaves the two atoms in a near maximally entangled state separated by a few cm.

Having demonstrated entangled states the next main challenge is to create entanglement between two atomic systems in separate environments. This will enable the implementation of distant quantum information processing such as quantum cryptography and quantum networks based on quantum teleportation.

A natural first step is to entangle the atomic state with a light state. This has been achieved for a single ion [28] and for a single neutral atom [29] via pulsed excitation and subsequent spontaneous emission of a single photon into either one of two well defined polarization modes corresponding to decay into two different ground states. The collection efficiency is extremely low so, as in the case of photon pair production via spontaneous optical parametric down conversion, the presence of the entanglement is inferred only after a photon has been detected. In order to transfer this into entanglement between two atomic particles strong coupling between the second particle and the photon has to be achieved. At a single particle level this can only be achieved using ultra high-finesse cavities. As discussed above this has been achieved in the microwave region. The coupling between the atoms and the cavity is controlled by the atomic dipole moment, which for Rydberg states is huge compared to that of atoms in the ground state. To achieve that same coupling with ground state atoms and an optical transition, the field in the cavity has to be increased correspondingly. This is done by increasing the finesse of the cavity, which quickly becomes extremely challenging experimentally. Despite this, very encouraging results have recently also been achieved in the optical domain [30, 31]. Here single photons have been generated deterministically from a single atom in a cavity. Unlike in [28, 29] the process is unitary and hence reversible, which is essential for the realization of a distributed quantum network [32].

The substantial technical difficulties involved in achieving the control and strong coupling at the level of single atoms and single photons motivated a search for alternative routes to achieve atomic entanglement. One of the most successful involves the use of atomic ensembles consisting of macroscopic numbers of particles. The dipole moment of collective variables describing these is dramatically increased compared to a single atom and hence strong coupling with light can be achieved without the use of cavities.

Initial approaches focused predominantly on atom-light coupling via resonant absorption. In [33] it was proposed to create an entangled atomic ensemble by

the complete absorption of entangled light. The initial light and the final atomic entanglement came in the form of "squeezed states". In these weak two particle correlations in a macroscopic ensemble of light or atoms are arranged such that the fluctuations in one of the collective properties (x or p) are reduced at the expense of increased fluctuations in the other. Following this proposal the first macroscopic (10^9 atoms) entangled state was generated [34]. The entanglement, however, existed in the excited states and hence the life time and the degree of entanglement were fundamentally limited by spontaneous emission.

To circumvent this, it was proposed [35, 36] to use an off-resonant interaction to perform a Quantum-Non-Demolition (QND) measurement of certain collective atomic ground state properties, which would project the atomic state into an entangled state. Using ground state properties increases the life time drastically and furthermore makes the atoms indistinguishable over radio- or microwave length scales (corresponding to the frequency separations in the ground state). This significantly simplifies the coupling of light to the atomic sample. Another nice feature of this approach is that the technical implementation is relatively simple because it merely requires coherent light (output of a reasonably quiet laser). In this way spin squeezing [37] and entanglement of the form discussed by EPR between two atomic samples was achieved. The latter experiment forms the basis of all results in this thesis and will be discussed in detail in the following chapters.

In a parallel effort the ideas of resonant transfer were further developed. Using the process of electromagnetically-induced transparency (EIT) [38, 39] in macroscopic atomic ensembles light was slowed [40] and in subsequent experiments stopped and retrieved [41, 42]. The transfer was completely classical - no entanglement was employed or induced - but recently quantum correlations have been verified [43, 44, 45, 46, 47, 48, 49, 50]. In Sec. 7.4.6 these results are compared to ours in some detail.

The reason that both approaches yield coherent dynamics that is not washed out completely by noise from spontaneous emission is actually highly non-trivial. As will be discussed in Sec. 2.3.1 this is not the case for a single particle. When generalizing to an ensemble of atoms, however, the interaction is *coherently enhanced* [51, 36] in one atomic mode (the one dealing with all atoms symmetrically and causing coherent forward scattering) whereas spontaneous emission is distributed isotropically over all modes. This means that the relative importance of spontaneous emission decreases with increasing number of atoms.

In summary, the field of quantum information is based on three fundamental pillars:

- **Entanglement:** two systems can be connected non-locally to give correlated results of measurements
- **Superposition:** quantum mechanical states can exist in multiple eigenstates simultaneously (quantum parallelism).
- **No-cloning theorem:** using only the linearity of quantum mechanics it

was proven in 1982 [11] that an unknown quantum state cannot be copied or cloned.

The fundamental challenge in the field of quantum communication is to establish a quantum network between distant sites linked by an entanglement connection. With this established the two remaining pillars enable distributed quantum computing [52], secret exchange of classical information [13], and faithful transfer of quantum states through the process of quantum teleportation [17, 53] can be achieved. Practically, the difficulty in establishing an entanglement link increases exponentially with the distance because of inevitable signal loss. To circumvent this, the use of quantum repeaters [54, 55, 51, 56] was proposed (see Sec. 7.4.6). In a quantum repeater station A entanglement is established between a system at location B and a system at A and between another system at A and a system located at C . Through entanglement swapping [17, 57, 58, 59] and subsequent purification [60, 61] high quality entanglement between positions B and C can be achieved, thereby doubling the entanglement distance. If this is used successively, entanglement over arbitrary distances can be realized. Since, however, the purification schemes are probabilistic it is essential to have a quantum memory at each station to store the successfully generated entangled states. Otherwise all purification schemes would have to succeed simultaneously and the time required would scale exponentially with distance.

During the time of my Ph.D. studies we have demonstrated several important elements of a working quantum network. First of all by modifying the experimental setup of the initial entanglement experiment [62] we have demonstrated the first entanglement between two atomic objects in separate environments (see chapter 6). Using such entanglement as a resource we have furthermore performed the first mapping of an unknown quantum state into an atomic memory with a quality exceeding the best classical strategy (see chapter 7). Finally we have demonstrated the applicability of such quantum networks by performing the first quantum teleportation between a light state and an atomic state (see chapter 8).

Outline of the Thesis

- Chapter 2 Quantum mechanical description of the macroscopic atomic ensemble and light system and the interaction between the two. Canonical variables for the atomic and light systems will be defined, which will form the basis for all subsequent chapter.
- Chapter 3 Here the entanglement is defined and the basic entanglement experiment is introduced. An experimental criterion for the verification of entanglement is also introduced and simple theoretical predictions for the entanglement are derived.
- Chapter 4 In this chapter atomic and light decoherence is discussed in detail based on the Gaussian covariance matrix formalism. Results valid

for high degrees of decoherence and for light loss between the two samples are derived.

- Chapter 5 In this chapter various experimental details are discussed such as the atomic environment and the specific laser systems used. The main sources of decoherence are also discussed. Finally, the experimental demonstration of projection noise limited performance as well as a comparison with the theoretical predictions are treated.
- Chapter 6 Here the first of the three main experiments of this thesis - the entanglement generation - is discussed. It is divided into two parts. The first, describes the generation of entanglement similar to that of [62] but here the two samples are in separate environments. This represents the first demonstration of "distant" entanglement between two atomic systems. The second part is centered on the experimental generation of an unconditionally entangled state created by feeding back the measurement result onto the spin system. In this way an atomic state is created that is entangled without requiring any knowledge of prior measurement results.
- Chapter 7 Here we report on the first experimental demonstration of storage of an unknown quantum state with a quality exceeding the classical bound. The so-called direct mapping protocol involves a single Faraday interaction followed by a feedback to the atoms. The stored state was measured to have a life time of 5ms.
- Chapter 8 In this chapter the last of the main experiments of this thesis is described. Using light-atom entanglement generated by the Faraday interaction between an auxiliary light pulse and a single atomic sample, an unknown light state was teleported onto the atomic state.
- Chapter 9 In this chapter we derive an experimentally feasible protocol for the retrieval of a state from a quantum memory. Because of the long (1ms) optical pulses conventional retrieval protocols are inapplicable. The best protocol presented in this chapter involves four simultaneous passages of the light through the atomic sample and can approach perfect storage or retrieval by merely increasing the interaction strength sufficiently.
- Chapter 10 In this chapter we present a proposal for the generation of squeezed light based on the simultaneous passage dynamics discussed in the previous chapter. It only works in the case of two simultaneous passages. The dynamics is derived both in the pulsed and in the cw regime and atomic decoherence and reflection losses of light are included.
- Chapter 11 In this chapter we summarize the main results in this thesis and give an outlook where we discuss the possibilities of implementing atom-atom teleportation and interfacing with non-classical light sources.

- Appendix A Effects arising from atomic motion in and out of the probing beam are discussed in the appendix. We show that with such an asymmetric coupling to the atoms the a new set of collective variables can be formed with a correspondingly modified projection noise level. We also show that atomic motion acts as an effective source of decoherence between two probe pulses.
- Appendix B Here we discuss the inclusion of decoherence into the covariance matrix formalism presented in chapter 4. We show that - because for a spin system higher than $1/2$ the thermal noise is no longer identical to the coherent state noise - errors accumulate when applying the covariance matrix update equation iteratively for such systems.
- Appendix C In this appendix we derive the Stark shift between the different magnetic sublevels and discuss the implications on the experiments.
- Appendix D In this appendix we explain some of the abbreviations commonly used in this thesis.

CHAPTER 2

Atom-Light Interaction

All experiments presented in this thesis will revolve around sending a narrowband laser source through glass cells containing a macroscopic number ($\sim 10^{12}$) of cesium atoms.

In this section we introduce the quantum variables for light and atoms and describe the off-resonant dipole atom-light interaction utilizing the ground state $6S_{1/2}$ to the excited state $6P_{3/2}$ transition in cesium. We use collective spin operators for atoms and Stokes operators for light as a convenient way to describe the interaction. The interaction has been investigated semi classically in [63] and the quantum mechanical interaction Hamiltonian was derived for a spin 1/2 system in [36]. The interaction Hamiltonian for the realistic $F = 4$ system taking the complete level structure into account was derived in [1]. Here we will first discuss the effect of the interaction classically and then illustrate the quantum mechanical derivation for the spin 1/2 system. Finally we will present the result of the general effective Hamiltonian which describes the dynamics of the ground state spin and the light. For simplicity the Hamiltonian is specific to the cesium ground state, although, the same procedure can be applied for any other atom with a ground state containing multiple Zeeman sublevels. With this as a starting point we derive equations of motion for the light operators and the atomic operators describing a single atomic ensemble. In this way we show that the spin component along the direction of light propagation is mapped onto the light without being perturbed by the light. Such a Quantum-Non-Demolition (QND) measurement will thus increase our knowledge of that particular spin component, which amounts to squeezing (decreasing the width of) the corresponding probability distribution of that variable.

For technical reasons we then introduce a constant magnetic field along the direction of the mean spin. This complicates the equations of motion significantly because the spin components transverse to the applied magnetic field start to mix through Larmor precession. The simple QND interaction is regained by the introduction of two oppositely oriented ensembles. In this setting entanglement between the two ensembles can be realized by sending a single pulse of light through the atoms instead of the two pulses required in the absence of the magnetic bias field. An even more important advantage is brought about by the possibility of performing measurements at a rather high Zeeman frequency, thus achieving quantum limits of sensitivity with macroscopic numbers of atoms via spectral filtering of classical noise.

In the final parts of this chapter we will rescale the atomic and light variables to obtain a common mathematical framework for the description of the two systems. These *canonical* operators will form the basis of all further discussions of the interaction in the remaining part of the thesis.

2.1 Atomic Spin Operators

The ground states of cesium are characterized by its outermost electron which is in the $6S_{1/2}$ state, i.e. the orbital angular momentum \mathbf{L} is zero. The electron spin \mathbf{S} and consequently the total electronic angular momentum \mathbf{J} has quantum number $S = J = 1/2$. The nuclear spin \mathbf{I} of cesium-133 has $I = 7/2$, and the coupling between the nucleus and the electron gives rise to the total angular momentum $\mathbf{F} = \mathbf{I} + \mathbf{J}$ with quantum numbers $F = 3$ and $F = 4$.

It is indeed the total angular momentum \mathbf{F} which is of interest in this work since F and the magnetic quantum numbers m_F define the energy levels of the ground states in the limit of low magnetic field applicable here. Furthermore, we restrict ourselves to one hyperfine level, $F = 4$, which is possible experimentally since the hyperfine splitting $\nu_{\text{hfs}} = 9.1926\text{GHz}$ is large compared to typical resolutions of our laser systems. We choose to denote the total angular momentum of a *single atom* by \mathbf{j} and for a collection of atoms (in the $F = 4$ state) we refer to the *collective* total angular momentum as \mathbf{J} , i.e.

$$\mathbf{J} = \sum_{i=1}^N \mathbf{j}^{(i)}, \quad (2.1)$$

where N is the number of atoms in the $F = 4$ state and $\mathbf{j}^{(i)}$ is the total angular momentum of the i 'th atom. The reason for using \mathbf{J} and not \mathbf{F} is conventional.

In our experiments the number of atoms N is of order 10^{12} and hence the eigenvalues lie extremely close compared to the length of the vector. We therefore call \hat{J}_y and \hat{J}_z continuous variable operators. Experimentally will always aim at having all atoms polarized along one direction which we denote as the x -axis. With the x -axis as quantization axis we have $m_F = 4$ for all atoms to a high degree of accuracy, and the collective spin \hat{J}_x is really a macroscopic entity. As we

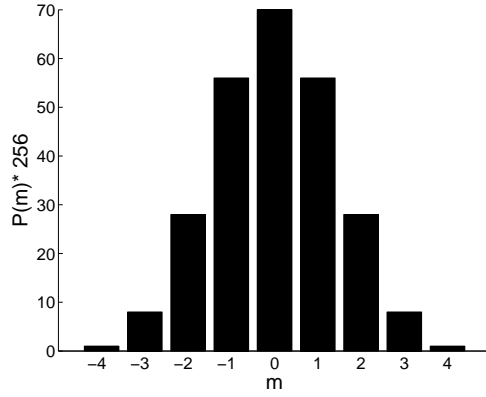


Figure 2.1: \hat{j}_y and \hat{j}_z probability distribution for a single atom in the $|F = 4, m = 4\rangle$ state along x .

shall see in the chapters to come, this state called the coherent spin state (CSS) is extremely important for our experiments. (See chapter 5 for experimental details concerning the atomic state preparation.) With this experimental choice, we may treat the x -component of the collective spin as a c -number, i.e. we replace the operator \hat{J}_x by the number J_x . The transverse spin components \hat{J}_y and \hat{J}_z maintain their quantum nature. They typically have zero or a small mean value. Via the commutation relation the Heisenberg uncertainty relation sets a lower bound for the quantum fluctuations (with $\hbar = 1$)

$$[\hat{J}_y, \hat{J}_z] = iJ_x \quad (2.2)$$

$$\Rightarrow \text{Var}(\hat{J}_y) \cdot \text{Var}(\hat{J}_z) \geq \frac{J_x^2}{4}. \quad (2.3)$$

Here $\text{Var}(\hat{J}_q) = \langle \hat{J}_q^2 \rangle - \langle \hat{J}_q \rangle^2$ represents the variance in the usual sense, i.e. the square of the width of the probability distribution for the operator \hat{J}_q . In this thesis we will refer to this as the variance and the noise of the variable interchangeably.

We wish to determine the statistics of the state consisting of N_{at} atoms all in the $m_F = 4$ state (CSS). To do this, we find the probability distribution of a single atom along the y - and z -directions. This can be done by applying a 90° rotation matrix to the state $|\psi\rangle = |F = 4, m = 4\rangle$ giving $|\psi\rangle \rightarrow \sum_m |F = 4, m'\rangle d_{m',4}^{(4)}$. This gives the probabilities $P(m) = (1, 8, 28, 56, 70, 56, 28, 8, 1)/256$ for measuring $m = (-4, -3, -2, -1, 0, 1, 2, 3, 4)$. This distribution is illustrated in Fig. 2.1. Given the probability distribution we can easily calculate the first and second

moments for a single atom

$$\langle \hat{j}_q \rangle = \sum_{m=-4}^4 P(m)m = 0, \quad \langle \hat{j}_q^2 \rangle = \sum_{m=-4}^4 P(m)m^2 = 2 \quad (2.4)$$

Alternatively we could have used $\langle \hat{j}^2 \rangle = \langle \hat{j}_x^2 + \hat{j}_y^2 + \hat{j}_z^2 \rangle = F(F+1)$ and $\langle \hat{j}_x^2 \rangle = F^2$ to see that $\langle \hat{j}_y^2 \rangle = \langle \hat{j}_z^2 = \frac{F}{2} \rangle$. The central limit theorem then tells us that \hat{J}_y and \hat{J}_z will be distributed according to a Gaussian with mean $N_{\text{at}} \langle \hat{j}_q \rangle = 0$ and variance $N_{\text{at}} \langle \hat{j}_q^2 \rangle = 2N_{\text{at}} = J_x/2$. Comparing this to Eq. (2.3) we see that the CSS is a minimum uncertainty state. In our experiments we will typically have 10^{12} atoms giving a quantum uncertainty of the angle of the collective spin direction of order 10^{-6} .

With a 3D representation of the spin states on a sphere, The CSS will be characterized by an uncertainty disk of width $\sim \sqrt{J_x}$ within which the direction of the spin vector is not defined. Because of the non-commutativity of \hat{J}_y and \hat{J}_z it is impossible to localize the spin state to a single point on the sphere. Any localization in one direction will invariably be followed by a delocalization in the other.

2.2 Polarization States of Light

All our experiments involve narrow-band light interacting with atomic spin states, and it turns out that the polarization states of the light form a convenient language to describe the degrees of freedom of the light.

Consider a pulse of light, or a collection of photons, propagating in the z -direction. The polarization state is well described by the Stokes operators

$$\begin{aligned} \hat{S}_x &= \frac{1}{2} (\hat{n}_{\text{ph}}(x) - \hat{n}_{\text{ph}}(y)) = \frac{1}{2} (\hat{a}_x^\dagger \hat{a}_x - \hat{a}_y^\dagger \hat{a}_y), \\ \hat{S}_y &= \frac{1}{2} (\hat{n}_{\text{ph}}(+45^\circ) - \hat{n}_{\text{ph}}(-45^\circ)) = \frac{1}{2} (\hat{a}_x^\dagger \hat{a}_y + \hat{a}_y^\dagger \hat{a}_x), \\ \hat{S}_z &= \frac{1}{2} (\hat{n}_{\text{ph}}(\sigma_+) - \hat{n}_{\text{ph}}(\sigma_-)) = \frac{1}{2i} (\hat{a}_x^\dagger \hat{a}_y - \hat{a}_y^\dagger \hat{a}_x), \end{aligned} \quad (2.5)$$

where $\hat{n}_{\text{ph}}(x)$ is the number of photons in the pulse with x -polarization, and so on. In the last equality we used

$$\begin{aligned} \hat{a}_+ &= \frac{\hat{a}_x + i\hat{a}_y}{\sqrt{2}}, & \hat{a}_- &= \frac{\hat{a}_x - i\hat{a}_y}{\sqrt{2}}, \\ \hat{a}_{45} &= \frac{\hat{a}_x + \hat{a}_y}{\sqrt{2}}, & \hat{a}_{-45} &= \frac{\hat{a}_x - \hat{a}_y}{\sqrt{2}}. \end{aligned} \quad (2.6)$$

The Stokes operators are dimensionless as written here, they count photons. At our convenience we later break these up into temporal or spatial slices.

A crucial assumption in all our experiments is that light consists of a strong component linearly polarized along the x -direction and a much weaker component polarized in the y -plane. This means that we can treat the x -mode operators \hat{a}_x , \hat{a}_x^\dagger , and hence $\hat{S}_x \rightarrow S_x$ as a c -number. Note, the similarity to the approximation of a well polarized sample of spins in the previous section. Specifically we find (with $\hat{a}_x^\dagger = \hat{a}_x = A_x$ being real) that

$$\hat{S}_y = A_x \cdot (\hat{a}_y + \hat{a}_y^\dagger)/2, \quad \hat{S}_z = A_x \cdot (\hat{a}_y - \hat{a}_y^\dagger)/2i. \quad (2.7)$$

Thus, in our approximation the quantum properties of \hat{S}_y and \hat{S}_z are solely encoded in the y -polarized part of the light.

It can be shown that the Stokes vector satisfies angular momentum commutation relations

$$[\hat{S}_y, \hat{S}_z] = iS_x \quad (2.8)$$

$$\Rightarrow \text{Var}(\hat{S}_y) \cdot \text{Var}(\hat{S}_z) \geq \frac{S_x^2}{4} \quad (\text{pulse of light}). \quad (2.9)$$

As in the atomic case we can easily calculate the variance of the coherent state of light in which all photons are polarized along x . For a single photon we get $\langle \hat{s}_q \rangle = 0$ and $\langle \hat{s}_q^2 \rangle = 1/4$, which means that the variance for N_{ph} photons is $\langle \hat{S}_q \rangle = \frac{N_{\text{ph}}}{4} = \frac{S_x}{2}$. Comparing this to Eq. (2.9) we again see that the coherent state is a minimum uncertainty state.

In general we will use a formalism which allows for variations of the instantaneous Stokes operators across the pulse. In the following we will restate some of the important results concerning the correlation properties of the Stokes operators from the appendices of [1]. Taking the spatial Fourier transform of the light field described by the operators $[\hat{a}(k), \hat{a}^\dagger(k')] = \delta(k - k')$ we get a description in terms of $[\hat{a}(z, t), \hat{a}^\dagger(z', t)] = \delta(z - z')$. Analogously to Eq. (2.5) this gives rise to the Stokes operators $\hat{S}_i(z, t)$ which have dimension 1/length and can be interpreted in terms of the number of photons per unit length in appropriate bases. They obey the commutation relation $[\hat{S}_y(z, t), \hat{S}_z(z', t)] = i\hat{S}_x(z, t)\delta(z - z')$ and in the coherent state $\langle \hat{S}_i(z, t)\hat{S}_i(z', t) \rangle = \frac{S_x}{2}\delta(z - z')$, where $i = y, z$. For propagation in free space the time and space arguments are trivially connected through $\hat{S}_i(z, t) = \hat{S}_i(0, t - z/c)$ and we therefore define $\hat{S}_i^{\text{in}}(t) = c \cdot \hat{S}_i(z = 0, t)$ and $\hat{S}_i^{\text{out}}(t) = c \cdot \hat{S}_i(z = L, t)$, where L is the length of the sample. These operators are connected to the number of photons per unit time in different bases and have the same commutation and correlation functions as $\hat{S}_i(z, t)$ with t substituted for z .

2.3 Off-Resonant Coupling

In our experiments linearly polarized light propagates along the z -direction through an atomic sample polarized transversely to the direction of propagation. The

question is now how the properties of the spin affect the light. The full Hamiltonian for the realistic multi-level interaction has been derived elsewhere [1, 64, 65], so here we will merely give a semi-classical picture of the interaction followed by a derivation of the equations of motion for a two level atom to illustrate the general procedure.

Classically when off-resonant light propagates through a polarizable medium, it experiences a phase shift because of the index of refraction of the dispersive medium. Now, from Eq. (2.6) we see that light linearly polarized along e.g. the x -axis can be decomposed into equal parts of σ_+ and σ_- polarized light. With the z -axis as quantization axis this light will drive $\Delta m = 1$ and $\Delta m = -1$ transitions respectively. For a dispersive interaction with a two level system (see Fig. 2.2) this means that the σ_+ component will acquire a phase shift $\delta_+ = \delta_0 N_-$ proportional to the population in $m = -1/2$, N_- and correspondingly the σ_- component acquires a phase $\delta_- = \delta_0 N_+$. Rearranging Eq. (2.6) we can now determine the effect of this phase shift on the linear polarization

$$\begin{aligned} a_x &= \frac{a_- - a_+}{\sqrt{2}} = \frac{1}{\sqrt{2}} \frac{e^{i\delta_0 N_+} + e^{i\delta_0 N_-}}{\sqrt{2}} = e^{i\delta_0(N_+ + N_-)/2} \cos(\delta_0(N_- - N_+)) \\ a_y &= i \frac{a_- + a_+}{\sqrt{2}} = \frac{1}{\sqrt{2}} \frac{e^{i\delta_0 N_+} - e^{i\delta_0 N_-}}{\sqrt{2}} = e^{i\delta_0(N_+ + N_-)/2} \sin(\delta_0(N_- - N_+)) , \end{aligned} \quad (2.10)$$

where initially we took $a_x = 1$, $a_y = 0$, $a_+ = -1/\sqrt{2}$, and $a_- = 1/\sqrt{2}$. We see that the effect of the dispersive medium is to rotate the light polarization by an angle proportional to the population difference in the two ground state level, which apart from a factor $1/2$ is exactly \hat{J}_z . This effect is known as the Faraday rotation. Since the interaction is dispersive n_+ at n_- are both conserved individually and therefore by angular momentum conservation so is the spin projection in the z -direction. This means that sending linearly polarized light through through an atomic sample and subsequently measuring the polarization rotation a measurement of \hat{J}_z can be implemented that does not change the value of value of \hat{J}_z . This is the essence of a QND measurement and is the main ingredient in experimental generation of atomic entanglement. To determine the effect of the interaction on the light a quantum mechanical treatment is necessary.

2.3.1 Two Level Interaction

Next we will illustrate quantum mechanical treatment by solving the dynamics for a two level model [36] (see Fig. 2.2). A σ_+ and a σ_- polarized field component interacts off resonantly with the $m = -1/2$ to $m' = 1/2$ and the $m = 1/2$ to $m' = -1/2$ atomic transitions respectively. In terms of the light operators \hat{a}_\pm and the atomic operators $\hat{\sigma}_{ij} = |i\rangle \langle j|$ the Hamiltonian for the interaction is given

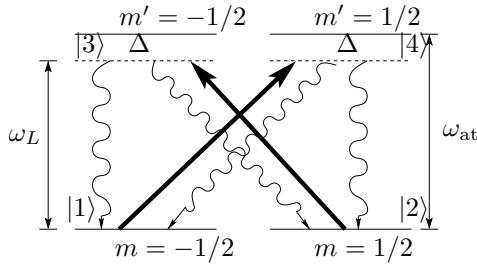


Figure 2.2: Two-level atom illustration of the off-resonant Faraday interaction.

by

$$\begin{aligned} \hat{H} = & \hbar\omega_L \hat{a}_+^\dagger \hat{a}_+ + \hbar\omega_{\text{at}} \hat{\sigma}_{44} + \hbar g \left(\hat{\sigma}_{41} \hat{a}_+ e^{-i\omega_L t} + \hat{a}_+^\dagger e^{i\omega_L t} \hat{\sigma}_{14} \right) \\ & \hbar\omega_L \hat{a}_-^\dagger \hat{a}_- + \hbar\omega_{\text{at}} \hat{\sigma}_{33} + \hbar g \left(\hat{\sigma}_{32} \hat{a}_- e^{-i\omega_L t} + \hat{a}_-^\dagger e^{i\omega_L t} \hat{\sigma}_{23} \right) , \end{aligned} \quad (2.11)$$

where each line represents a single two level atom interacting with a single light field [39, 66]. We have $g = -d\sqrt{\frac{\omega_L}{2\hbar\epsilon V}}$, where d is the dipole matrix element $\langle i | er | j \rangle$, ω_L is the laser frequency, and V is the quantization volume. The light-atom interaction is here treated in a one dimensional theory. (For a discussion of some effects of the three dimensional nature of the interaction see [67, 68]) We wish to determine the atomic ground state populations $\hat{\sigma}_{11}$ and $\hat{\sigma}_{22}$ and the ground state coherence $\hat{\sigma}_{12}$

$$\begin{aligned} \frac{d\hat{\sigma}_{11}}{dt} &= -i \left(\hat{a}_+^\dagger e^{i\omega_L t} \hat{\sigma}_{14} - \hat{\sigma}_{41} \hat{a}_+ e^{-i\omega_L t} \right) \\ \frac{d\hat{\sigma}_{22}}{dt} &= -i \left(\hat{a}_-^\dagger e^{i\omega_L t} \hat{\sigma}_{23} - \hat{\sigma}_{32} \hat{a}_- e^{-i\omega_L t} \right) \\ \frac{d\hat{\sigma}_{12}}{dt} &= -i \left(\hat{a}_-^\dagger e^{i\omega_L t} \hat{\sigma}_{13} - \hat{\sigma}_{42} \hat{a}_+ e^{-i\omega_L t} \right) . \end{aligned} \quad (2.12)$$

To do this we define slowly varying operators and adiabatically eliminate [39] the coherences between the ground and excited levels. We will illustrate the procedure with one of them and state the results for the rest. From the Heisenberg equation, the equations of motion can be derived

$$\frac{d\hat{\sigma}_{14}}{dt} = \frac{1}{i\hbar} [\hat{\sigma}_{14}, \bar{H}] = -i \left(\omega_{\text{at}} \hat{\sigma}_{14} + g \hat{a}_+ e^{-i\omega_L t} (\hat{\sigma}_{11} - \hat{\sigma}_{44}) \right) . \quad (2.13)$$

Defining the slowly rotating operator $\tilde{\sigma}_{14} = \hat{\sigma}_{14} e^{i\omega_L t}$ and the detuning $\Delta = \omega_{\text{at}} - \omega_L$ we get the new differential equation

$$\frac{d\tilde{\sigma}_{14}}{dt} = -i \left(\Delta \tilde{\sigma}_{14} + g \hat{a}_+ (\hat{\sigma}_{11} - \hat{\sigma}_{44}) \right) \approx -i \left(\Delta \tilde{\sigma}_{14} + g \hat{a}_+ \hat{\sigma}_{11} \right) , \quad (2.14)$$

where the latter expression is valid because the detuning is very large and hence the excited state population small. Since the detuning is large the dynamics of

$\tilde{\sigma}_{14}$ is much faster than the evolution of the ground state population. This means that $\tilde{\sigma}_{14}$ quickly reaches a steady state whenever $\hat{\sigma}_{11}$ is changed. Because of this *adiabatic following* we can always use the steady state solution of Eq. (2.14) obtained by setting the derivative to zero. In this way we obtain

$$\begin{aligned}\tilde{\sigma}_{14} &= -\frac{g\hat{a}_+\hat{\sigma}_{11}}{\Delta}, & \tilde{\sigma}_{24} &= -\frac{g\hat{a}_+\hat{\sigma}_{12}}{\Delta}, \\ \tilde{\sigma}_{13} &= -\frac{g\hat{a}_-\hat{\sigma}_{12}}{\Delta}, & \tilde{\sigma}_{23} &= -\frac{g\hat{a}_-\hat{\sigma}_{22}}{\Delta}.\end{aligned}\quad (2.15)$$

Using the definition of the slowly rotating variables, these solutions can be used to solve for the ground state operators Eq. (2.12). The diagonal variables $\hat{\sigma}_{11}$ and $\hat{\sigma}_{22}$ turn out to be zero so all the dynamics is contained in the ground state coherence

$$\frac{d\hat{\sigma}_{12}}{dt} = \frac{ig^2}{\Delta}(\hat{a}_-\hat{a}_- - \hat{a}_+\hat{a}_+)\hat{\sigma}_{12}. \quad (2.16)$$

Note that this dynamics is reproduced by the effective Hamiltonian

$$\begin{aligned}\hat{H}_{\text{eff}} &= -\frac{\hbar g^2}{\Delta}(\hat{\sigma}_{11}\hat{a}_+\hat{a}_+ + \hat{\sigma}_{22}\hat{a}_-\hat{a}_-) \\ &= \frac{\hbar g^2}{2\Delta}([\hat{\sigma}_{22} - \hat{\sigma}_{11}] \cdot [\hat{a}_+\hat{a}_+ - \hat{a}_-\hat{a}_-] - [\hat{a}_+\hat{a}_+ + \hat{a}_-\hat{a}_-] \cdot [\hat{\sigma}_{11} + \hat{\sigma}_{22}]) \\ &= \frac{2\hbar g^2}{\Delta} \left(\hat{J}_z \hat{S}_z - \frac{1}{2} \mathbf{1} \cdot N_{\text{ph}} \right) \rightarrow \frac{2\hbar g^2}{\Delta} \left(\hat{J}_z \hat{S}_z - \frac{1}{2} N_{\text{at}} N_{\text{ph}} \right),\end{aligned}\quad (2.17)$$

where in the last equation we gave the generalization to a spin sample containing multiple atoms. We used the spin definitions for a single and N_{at} atoms $\hat{j}_z = \frac{1}{2}[\hat{\sigma}_{22} - \hat{\sigma}_{11}]$ and $\hat{J}_z = N_{\text{at}}\frac{1}{2}[\hat{\sigma}_{22} - \hat{\sigma}_{11}]$, the Stokes definition in Eq. (2.5), and the number of photons $N_{\text{ph}} = \hat{a}_+\hat{a}_+ + \hat{a}_-\hat{a}_-$.

The last term in the Hamiltonian is merely an overall Stark shift of the energy levels and can safely be neglected. The remaining part rotates the atomic spin vector around the z -axis by an angle determined by \hat{S}_z and simultaneously the Stokes vector is rotated by an angle determined by \hat{J}_z . This means that, as in the classical case treated above, information about \hat{J}_z is transferred to the light but we see that through the quantum mechanical back-action a similar process occurs in the atomic state.

We will discuss the equations of motion in a lot more detail later in this chapter but at this point we would like to comment on the importance of spontaneous emission. All coherences involving the excited state will decohere because of spontaneous emission. This can be added phenomenologically by including a term $-\gamma\hat{\sigma}_{ij}$ in the differential equations for $\hat{\sigma}_{ij}$ involving the excited states. ¹

¹To preserve the correct statistical properties we should really also add a Langevin noise term [39] but we will ignore those for now, focusing on the decrease in the signal caused by spontaneous emission. We will treat dissipation more properly in chapters 4 and 10 and appendix B.

Incorporating this in the calculations above we obtain

$$\frac{d\hat{\sigma}_{12}}{dt} = \frac{ig^2}{\Delta}(\hat{a}_-^\dagger \hat{a}_- - \hat{a}_+^\dagger \hat{a}_+) \hat{\sigma}_{12} - \frac{g^2}{\Delta} \frac{\gamma}{\Delta} (\hat{a}_-^\dagger \hat{a}_- + \hat{a}_+^\dagger \hat{a}_+) \hat{\sigma}_{12} \quad (2.18)$$

The first part is the one giving the coherent evolution and the second part describes the effect of spontaneous emission. Here we clearly see the difference in the scaling of the two with detuning. As expected the dispersive part falls off as $1/\Delta$, whereas the part coming from absorption effects falls off as $1/\Delta^2$. The extra factor γ/Δ in front of the spontaneous emission term will be very small because of the large detuning but this does not mean that it is negligible for a single atom. This is because the damping term involves the sum of the number of photons in the two circular polarization, whereas the signal term is proportional to the difference. Since in the experiments these photon numbers are almost identical (by having a clean linear polarization), we see that for a single atom spontaneous emission will dominate completely if the total number of photons is large.

For an ensemble of atoms we will be interested in the dynamics of the operator $\hat{J}_y = N_{\text{at}} \frac{1}{2i} [\hat{\sigma}_{12} - \hat{\sigma}_{21}]$. Solving Eq. (2.18) and inserting into the definition of \hat{J}_y we obtain

$$\hat{J}_y(t) = \left(\hat{J}_y(0) + a \hat{S}_z J_x \right) e^{-\eta t/2}, \quad (2.19)$$

where for we also used $J_x = N_{\text{at}} \frac{1}{2} [\hat{\sigma}_{12} + \hat{\sigma}_{21}]$ and for compactness and consistency with coming results define $a = \frac{2g^2}{\Delta}$ and $\eta = \frac{2g^2\gamma\phi}{\Delta^2}$, where ϕ is the photon flux per unit time. In Sec. 2.7 we will show that the size of the desired interaction relative to the effect of spontaneous emission can be written as $\alpha = \frac{N_{\text{at}}g^2}{2\gamma}$, which is called the optical depth of the sample (typically ~ 30 in our experimental settings). We see that whereas at a single atom level spontaneous emission entirely dominated the coherent processes for a large number of photons, this is not the case for an ensemble of atoms. The remarkable property is called *collective enhancement* [51] and is crucial for achieving a strong coupling between that atomic and light systems. Another way to understand this process is that the coherent interaction occurs only between a single well defined atomic mode (symmetrized over all atoms) and a single light mode. Spontaneous emission, on the other hand, is distributed uniformly over all modes. This means that for a large number of atoms the effect of spontaneous emission on the mode of interest becomes negligible.

2.3.2 Full Multi-level Coupling

We now consider the case of a propagating beam of light coupled off-resonantly to the $6S_{1/2, F=4} \rightarrow 6P_{3/2, F'=3,4,5}$ transitions in cesium (see Fig. 5.1). Neglecting absorption effects and adiabatically eliminating the optically excited states an effective Hamiltonian describing the light interacting with only ground state degrees of freedom is obtained [1, 64, 65]².

²[1] contains a factor of two error which has been corrected in Eq. (2.20).

$$\begin{aligned} \hat{H}_{\text{int}}^{\text{eff}} = & -\frac{\hbar c \gamma}{8A\Delta} \frac{\lambda^2}{2\pi} \int_0^L \left(a_0 \cdot \hat{\phi}(z, t) + a_1 \cdot \hat{S}_z(z, t) \hat{j}_z(z, t) \right. \\ & \left. + a_2 \left[\hat{\phi}(z, t) \hat{j}_z^2(z, t) - \hat{S}_-(z, t) \hat{j}_+^2(z, t) - \hat{S}_+(z, t) \hat{j}_-^2(z, t) \right] \right) \rho A dz. \end{aligned} \quad (2.20)$$

Again we have assumed a one-dimensional theory for the light which is sufficient for a beam cross section A that is much larger than the squared wavelength λ^2 . The small letter spin operators $\hat{j}(z, t)$ are dimensionless and refer to single atoms at position z at time t . The integration then runs over the entire sample of length L with atomic density ρ . The factor γ in front of Eq. (2.20) is the natural FWHM line width of the optical transition $6S_{1/2} \rightarrow 6P_{3/2}$ and Δ is the detuning from the $F = 4$ to $F' = 5$ transition with red being positive.

As for the operators, $\hat{\phi}(z, t)$ is the photon flux per unit length, $\hat{S}_+ = \hat{S}_x + i\hat{S}_y = -\hat{a}_+^\dagger \hat{a}_-$ and $\hat{S}_- = \hat{S}_x - i\hat{S}_y = -\hat{a}_-^\dagger \hat{a}_+$ are raising and lowering operators converting σ_+ -photons into σ_- -photons or vice versa, and $\hat{j}_\pm = \hat{j}_x \pm i\hat{j}_y$ are the usual raising and lowering operators for the spin.

The parameters a_0 , a_1 , and a_2 for the $F = 4$ ground state in cesium are given by

$$\begin{aligned} a_0 &= \frac{1}{4} \left(\frac{1}{1 - \Delta_{35}/\Delta} + \frac{7}{1 - \Delta_{45}/\Delta} + 8 \right) \rightarrow 4, & (F = 4) \\ a_1 &= \frac{1}{120} \left(-\frac{35}{1 - \Delta_{35}/\Delta} - \frac{21}{1 - \Delta_{45}/\Delta} + 176 \right) \rightarrow 1, \\ a_2 &= \frac{1}{240} \left(\frac{5}{1 - \Delta_{35}/\Delta} - \frac{21}{1 - \Delta_{45}/\Delta} + 16 \right) \rightarrow 0, \end{aligned} \quad (2.21)$$

where the limit for very large values of the detuning is also given. The detunings $\Delta_{35}/2\pi = 452.2$ MHz and $\Delta_{45}/2\pi = 251.0$ MHz are given by the splitting in the excited state. Let us comment on the different terms in the Hamiltonian (2.20). The first term containing a_0 just gives a Stark shift to all atoms independent of the internal state but proportional to the photon density $\hat{\phi}(z, t)$. The second term containing a_1 rotates the Stokes vector \mathbf{S} and the spin vector \mathbf{J} around the z -axis, known as Faraday rotation - we look more closely into this below. The last terms proportional to a_2 are higher order couplings between the light and the atoms and since a_2 is small for a sufficiently large detuning these can normally be neglected.

All these terms conserve individually the z -projection of the total angular momentum of light and atoms, e.g. the $\hat{S}_- \hat{j}_+^2$ term can change a σ_+ photon into a σ_- photon (changing the light angular momentum along z by $-2\hbar$) while the atoms receive $2\hbar$ mediated by the atomic raising operator \hat{j}_+^2 . The total angular momentum must have its z -projection invariant since the physical system is axially symmetric around the direction of light propagation (the z -axis).

The term proportional to a_1 is of main relevance. This term represents the QND interaction, which will form the basis of all our experiments. The higher

order terms proportional to a_2 create some minor problems which can be minimized with large detuning. For a detailed treatment of the higher order (atomic alignment) effects we refer to [1, 64]. The zero order term proportional to a_0 produces an overall phase shift and can be omitted.

2.4 Propagation Equations

The Hamiltonian (2.20) is a very convenient starting point for many calculations and we now show the procedure to derive equations of motion. For the spin operators we need the Heisenberg evolution $\partial\hat{j}_i/\partial t = \frac{1}{i\hbar} [\hat{j}_i, \hat{H}]$ and for the Stokes operators the Maxwell-Bloch equations $(\partial/\partial t + c \cdot \partial/\partial z)\hat{S}_i(z, t) = \frac{1}{i\hbar} [\hat{S}_i(z, t), \hat{H}_{\text{int}}]$ (see [1]), where the z -differentiation comes from the commutator of $\hat{S}_i(z, t)$ with the pure light part of the Hamiltonian. For the latter we neglect retardation effects, i.e. we do not calculate dynamics on the time scale L/c of propagation of the light across the sample. This is equivalent to setting the speed of light to infinity and hence leaving out the $\partial/\partial t$ term. If we consider only the term proportional to a_1 and neglect the rest we find

$$\begin{aligned}\frac{\partial\hat{j}_x(z, t)}{\partial t} &= +\frac{c\gamma}{8A\Delta} \frac{\lambda^2}{2\pi} a_1 \hat{S}_z(z, t) j_y(z, t), \\ \frac{\partial\hat{j}_y(z, t)}{\partial t} &= -\frac{c\gamma}{8A\Delta} \frac{\lambda^2}{2\pi} a_1 \hat{S}_z(z, t) j_x(z, t), \\ \frac{\partial\hat{j}_z(z, t)}{\partial t} &= 0.\end{aligned}\tag{2.22}$$

and

$$\begin{aligned}\frac{\partial}{\partial z} \hat{S}_x(z, t) &= +\frac{\gamma\rho}{8\Delta} \frac{\lambda^2}{2\pi} a_1 \hat{S}_y(z, t) \hat{j}_z(z, t), \\ \frac{\partial}{\partial z} \hat{S}_y(z, t) &= -\frac{\gamma\rho}{8\Delta} \frac{\lambda^2}{2\pi} a_1 \hat{S}_x(z, t) \hat{j}_z(z, t), \\ \frac{\partial}{\partial z} \hat{S}_z(z, t) &= 0.\end{aligned}\tag{2.23}$$

We observe that $\hat{j}_z(z, t)$ and $\hat{S}_z(z, t)$ are individually conserved during the interaction which is also apparent from the Hamiltonian (2.20) since these operators commute with the a_1 -term. The effect of the interaction is that the spin rotates around the z -axis with an amount proportional to \hat{S}_z , and the Stokes vector rotates around the z -axis proportionally to \hat{j}_z .

Below we assume that these rotations are small and that the dominant classical (mean) polarization vector of light and the orientation vector of the collective atomic spin stay oriented along the x -direction after the interaction. This turns out to be a very good approximation for experimentally attainable values of the interaction strength. Under this assumption the first line of the systems (2.22)

and (2.23), respectively, can be omitted. Furthermore, given the QND structure of the remaining equations, we can sum over the individual atomic spins and obtain the same equation for the collective spin variables (2.1). In our continuous notation we have $\hat{J}_i(t) = \int_0^L \hat{j}_i(z, t) \rho A dz$. As for the light operators we concentrate on the in- and out-going parts only. Hence we define $\hat{S}_i^{\text{in}}(t) = c\hat{S}_i(z=0, t)$ and $\hat{S}_i^{\text{out}}(t) = c\hat{S}_i(z=L, t)$. The multiplication by the speed of light c turns the normalization into photons per unit time instead of per unit length. With the assumption of small rotation angles, integrating equations (2.22) and (2.23) over space from $z=0$ to $z=L$ leads to the following very important equations:

$$\hat{S}_y^{\text{out}}(t) = \hat{S}_y^{\text{in}}(t) + aS_x \hat{J}_z(t), \quad (2.24a)$$

$$\hat{S}_z^{\text{out}}(t) = \hat{S}_z^{\text{in}}(t), \quad (2.24b)$$

$$\frac{d}{dt} \hat{J}_y(t) = aJ_x \hat{S}_z^{\text{in}}(t), \quad (2.24c)$$

$$\frac{d}{dt} \hat{J}_z(t) = 0, \quad (2.24d)$$

where $a = -\frac{\gamma}{8A\Delta} \frac{\lambda^2}{2\pi} a_1$. In and out refer to light before and after passing the atomic sample, respectively.

We note from equations (2.24a) and (2.24d) that in the case of a large interaction strength (i.e. if $aS_x \hat{J}_z$ dominates \hat{S}_y^{in}) a measurement on \hat{S}_y^{out} amounts to a QND measurement of \hat{J}_z . Using off-resonant light for QND measurements of spins has also been discussed in [35, 69]. Equation (2.24c) implies that a part of the state of light is also mapped onto the atoms - we denote this as back action. This opens up the possibility of using this sort of system for quantum memory which will be the topic of Sec. 7.

2.5 The Rotating Frame

In the experiment a constant and homogeneous magnetic field is added in the x -direction. We discuss the experimental reason for this below. For our modeling, the magnetic field adds a term $H_B = \Omega_L \hat{J}_x$ to the Hamiltonian, where $\Omega_L = g_F \mu_B B / \hbar$. For the ground state of cesium we have $g_F(F=4) \approx 0.2504$ and $g_F(F=3) \approx -0.2512$. This makes the transverse spin components precess at the Larmor frequency Ω_L depending on the strength of the field. Introducing the rotating frame coordinates:

$$\begin{pmatrix} \hat{J}'_y \\ \hat{J}'_z \end{pmatrix} = \begin{pmatrix} \cos(\Omega_L t) & \sin(\Omega_L t) \\ -\sin(\Omega_L t) & \cos(\Omega_L t) \end{pmatrix} \begin{pmatrix} \hat{J}_y \\ \hat{J}_z \end{pmatrix} \quad (2.25)$$

we can easily show that equations (2.24a)-(2.24d) transform into:

$$\hat{S}_y^{\text{out}}(t) = \hat{S}_y^{\text{in}}(t) + aS_x \left(\hat{J}'_y(t) \sin(\Omega_L t) + \hat{J}'_z(t) \cos(\Omega_L t) \right), \quad (2.26a)$$

$$\hat{S}_z^{\text{out}}(t) = \hat{S}_z^{\text{in}}(t), \quad (2.26b)$$

$$\frac{d}{dt} \hat{J}'_y(t) = aJ_x \hat{S}_z^{\text{in}}(t) \cos(\Omega_L t), \quad (2.26c)$$

$$\frac{d}{dt} \hat{J}'_z(t) = aJ_x \hat{S}_z^{\text{in}}(t) \sin(\Omega_L t). \quad (2.26d)$$

Thus, the atomic imprint on the light is encoded at the Ω_L -sideband instead of at the carrier frequency. The primary motivation for adding the magnetic field is the fact that lasers are generally much more quiet at high sideband frequencies than at the carrier frequency. A measurement without a magnetic field is a DC measurement for which the technical noise easily dominates the subtle quantum signal. Also, as the measurement time is longer than $1/\Omega_L$, Eq. (2.26a) enables us to access both J'_y and J'_z at the same time. We are of course not allowed to perform non-destructive measurements on these two operators simultaneously since they are non-commuting. This is precisely reflected in the fact that neither \hat{J}'_y nor \hat{J}'_z are constant in equations (2.26c) and (2.26d). This makes the dynamics quite complex: the light is being fed into both atomic quadratures

$$\begin{aligned} \hat{J}'_y(t) &= \hat{J}'_y(0) + \int_0^t aJ_x \hat{S}_z^{\text{in}}(t') \cos(\Omega_L t') dt', \\ \hat{J}'_z(t) &= \hat{J}'_z(0) + \int_0^t aJ_x \hat{S}_z^{\text{in}}(t') \sin(\Omega_L t') dt', \end{aligned} \quad (2.27)$$

while at the same time the atomic state is being transferred back onto the light, thus transferring a part of \hat{S}_z^{in} for all earlier times onto $\hat{S}_y^{\text{out}}(t)$. This is generally an unwanted source of noise, which we usually call the back action noise of light. Later in this chapter we shall see that equations (2.26) can be solved and written in a much more transparent form, which as described in Chapter 8 will enable the implementation of quantum teleportation using this interaction. For now, however, we will start by showing that the simple QND-type interaction can be regained by adding another atomic sample.

2.6 Two Oppositely Oriented Spin Samples

Inspired by the above we now assume that we have two atomic samples with oriented spins such that $J_{x1} = -J_{x2} \equiv J_x$. In this setting the equations of

motion (2.26a)-(2.26d) translate into:

$$\hat{S}_y^{\text{out}}(t) = \hat{S}_y^{\text{in}}(t) + aS_x \left([\hat{J}'_{y1}(t) + \hat{J}'_{y2}(t)] \sin(\Omega_L t) + [\hat{J}'_{z1}(t) + \hat{J}'_{z2}(t)] \cos(\Omega_L t) \right), \quad (2.28a)$$

$$\frac{d}{dt}(\hat{J}'_{y1}(t) + \hat{J}'_{y2}(t)) = a(J_{x1} + J_{x2})\hat{S}_z^{\text{in}}(t) \cos(\Omega_L t) = 0, \quad (2.28b)$$

$$\frac{d}{dt}(\hat{J}'_{z1}(t) + \hat{J}'_{z2}(t)) = a(J_{x1} + J_{x2})\hat{S}_z^{\text{in}}(t) \sin(\Omega_L t) = 0. \quad (2.28c)$$

The fact that the sums $\hat{J}'_{y1}(t) + \hat{J}'_{y2}(t)$ and $\hat{J}'_{z1}(t) + \hat{J}'_{z2}(t)$ have zero time derivative relies on the assumption of opposite spins of equal magnitude. The constancy of these terms together with Eq. (2.28a) allows us to perform QND measurements on the two sums. We note that each of the sums can be accessed by considering the two operators

$$\int_0^T \hat{S}_y^{\text{out}} \cos(\Omega_L t) dt = \int_0^T \hat{S}_y^{\text{in}} \cos(\Omega_L t) dt + \frac{aS_x T}{2} (\hat{J}'_{z1}(t) + \hat{J}'_{z2}(t)), \quad (2.29a)$$

$$\int_0^T \hat{S}_y^{\text{out}} \sin(\Omega_L t) dt = \int_0^T \hat{S}_y^{\text{in}} \sin(\Omega_L t) dt + \frac{aS_x T}{2} (\hat{J}'_{y1}(t) + \hat{J}'_{y2}(t)). \quad (2.29b)$$

We have used the fact that $\int_0^T \cos^2(\Omega_L t) dt \approx \int_0^T \sin^2(\Omega_L t) dt \approx T/2$ and that $\int_0^T \cos(\Omega_L t) \sin(\Omega_L t) dt \approx 0$. As will be discussed in Sec. 5.2.3 each of the operators on the left hand side can be measured simultaneously by making an \hat{S}_y -measurement and multiplying the instantaneous photo-current by $\cos(\Omega_L t)$ or $\sin(\Omega_L t)$ followed by integration over the duration T . The possibility to gain information about $\hat{J}'_{y1}(t) + \hat{J}'_{y2}(t)$ and $\hat{J}'_{z1}(t) + \hat{J}'_{z2}(t)$ enables us to generate entangled states, the topic of chapters 3 and 6. At the same time we must lose information about some other physical variable. This is indeed true, the conjugate variables to these sums are $\hat{J}'_{z2}(t) - \hat{J}'_{z1}(t)$ and $\hat{J}'_{y1}(t) - \hat{J}'_{y2}(t)$, respectively. These have the time evolution

$$\frac{d}{dt}(\hat{J}'_{y1}(t) - \hat{J}'_{y2}(t)) = 2aJ_x \hat{S}_z^{\text{in}}(t) \cos(\Omega_L t), \quad (2.30a)$$

$$\frac{d}{dt}(\hat{J}'_{z1}(t) - \hat{J}'_{z2}(t)) = 2aJ_x \hat{S}_z^{\text{in}}(t) \sin(\Omega_L t). \quad (2.30b)$$

We see how noise from the input \hat{S}_z -variable is piling up in the difference components while we are allowed to learn about the sum components via \hat{S}_y measurements.

2.7 Introducing Canonical Operators

Sections 2.1 and 2.2 show that there is a striking similarity in the basic structure of the light and atomic systems. They both obey angular momentum commutation relations and are both prepared such that one of the components is effectively

nothing but a classical number. This means that both systems are effectively two dimensional systems with extremely close-lying eigenvalues. Implementing the Holstein-Primakoff approximation [70] by rescaling the two remaining quantum variables of each system with the classical third component, both systems can be mapped into canonical harmonic oscillator variables. In simple terms this approximation merely state that if the uncertainty disk associated with the spin system is sufficiently small compared the length of the spin vector space in the vicinity of the uncertainty disc is essentially flat and we can transform from a three dimensional theory to a two dimensional one. For a single atomic sample without a magnetic field we define:

$$\begin{aligned}\hat{X}_{\text{ass}} &= \frac{\hat{J}_y}{\sqrt{J_x}}, & \hat{P}_{\text{ass}} &= \frac{\hat{J}_z}{\sqrt{J_x}}, \\ \hat{x}_{\text{as}} &= \frac{1}{\sqrt{S_x T}} \int_0^T \hat{S}_y(t) dt, & \hat{p}_{\text{as}} &= \frac{1}{\sqrt{S_x T}} \int_0^T \hat{S}_z(t) dt.\end{aligned}\quad (2.31)$$

For two samples we get two sets of canonical variables by defining the atomic operators:

$$\hat{X}_{\text{ac}} = \frac{\hat{J}'_{y1} - \hat{J}'_{y2}}{\sqrt{2J_x}}, \quad (2.32a)$$

$$\hat{P}_{\text{ac}} = \frac{\hat{J}'_{z1} + \hat{J}'_{z2}}{\sqrt{2J_x}}, \quad (2.32b)$$

$$\hat{X}_{\text{as}} = -\frac{\hat{J}'_{z1} - \hat{J}'_{z2}}{\sqrt{2J_x}}, \quad (2.32c)$$

$$\hat{P}_{\text{as}} = \frac{\hat{J}'_{y1} + \hat{J}'_{y2}}{\sqrt{2J_x}}, \quad (2.32d)$$

where the meaning of s and c will become clear below. Note, that in this thesis we will adopt the convention of capitalizing the non-local atomic operators in order to distinguish them from the single cell atomic operators. Similarly we define the light operators:

$$\hat{x}_c = \sqrt{\frac{2}{S_x T}} \int_0^T \hat{S}_y(t) \cos(\Omega_L t) dt, \quad (2.33a)$$

$$\hat{p}_c = \sqrt{\frac{2}{S_x T}} \int_0^T \hat{S}_z(t) \cos(\Omega_L t) dt, \quad (2.33b)$$

$$\hat{x}_s = \sqrt{\frac{2}{S_x T}} \int_0^T \hat{S}_y(t) \sin(\Omega_L t) dt, \quad (2.33c)$$

$$\hat{p}_s = \sqrt{\frac{2}{S_x T}} \int_0^T \hat{S}_z(t) \sin(\Omega_L t) dt. \quad (2.33d)$$

when referring to both \hat{x}_c and \hat{x}_s we will simply write \hat{x}_L for convenience. Each pair of \hat{x}, \hat{p} operators now satisfy a commutation relation, $[\hat{x}_q, \hat{p}_q] = i$. Equations (2.24a-2.24d) and (2.28a-2.28c) now translate into

$$\hat{x}_i^{\text{out}} = \hat{x}_i^{\text{in}} + \kappa \hat{P}_{ai}^{\text{in}}, \quad (2.34a)$$

$$\hat{p}_i^{\text{out}} = \hat{p}_i^{\text{in}}, \quad (2.34b)$$

$$\hat{X}_{ai}^{\text{out}} = \hat{X}_{ai}^{\text{in}} + \kappa \hat{p}_i^{\text{in}}, \quad (2.34c)$$

$$\hat{P}_{ai}^{\text{out}} = \hat{P}_{ai}^{\text{in}}, \quad (2.34d)$$

where we recall that $i = c, s, ss$ refer to the definitions above. Note, that in the case of two samples the two sets of interacting light and atomic operators are decoupled. The parameter describing the strength of light/matter-interactions is given by $\kappa = a\sqrt{J_x S_x T}$. The limit of strong coupling between the two systems is reached around $\kappa \approx 1$. This set of equations represents the starting point for numerous applications, which will be presented in the chapters to come. While most applications presented in this thesis are realized for the two-cell setup it should be clear that an implementation for a single sample without a bias magnetic field is also possible.

Now that the light and atomic systems are treated symmetrically we can return to the determination of the ratio of the coherent part of Eq. (2.19) and the spontaneous emission part. Transforming the equation to the canonical formalism we obtain

$$\hat{x}_a^{\text{out}} = (\hat{x}_a^{\text{in}} + \kappa \hat{p}_L^{\text{in}}) e^{-\eta t/2}. \quad (2.35)$$

We are typically interested in the variance of such an expression

$$\text{Var}(\hat{x}_a^{\text{out}}) = (\text{Var}(\hat{x}_a^{\text{in}}) + \kappa \text{Var}(\hat{p}_L^{\text{in}})) e^{-\eta t}. \quad (2.36)$$

κ^2 is therefore a measure of the coherent part of the interaction, which is then reduced by a factor $1 - \eta t$ (for small values of ηt). We therefore want

$$\frac{\kappa^2}{\eta t} = \frac{\left(a\sqrt{N_{\text{at}}N_{\text{ph}}/4}\right)}{a\gamma N_{\text{ph}}/\Delta} = \frac{N_{\text{at}}g^2}{2\gamma} \quad (2.37)$$

to be much larger than one. Note that in this calculation we reverted to the notation of Sec. 2.3.1.

2.8 Canonical Description of the Single Cell Interaction

With the canonical formalism established we will also treat the complicated case of a single sample in the presence of a magnetic field. We introduce time dependent canonical light operators $(\hat{x}_L(t), \hat{p}_L(t)) = (\hat{S}_y(t), \hat{S}_z(t))/\sqrt{S_x}$ with dimension $1/\sqrt{\text{time}}$ and commutation relation $[\hat{x}_L(t), \hat{p}_L(t')] = i\delta(t-t')$ and the dimensionless atomic operators $\hat{x}_a(t) = \hat{J}_y(t)/\sqrt{J_x}$ and $\hat{p}_a = \hat{J}_z/\sqrt{J_x}$ with $[\hat{x}_a, \hat{p}_a] = i$. In

terms of these variables Eq. (2.26) turn into:

$$\hat{x}_L^{\text{out}}(t) = \hat{x}_L^{\text{in}}(t) + \frac{\kappa}{\sqrt{T}} (\hat{x}_a(t) \sin(\Omega_L t) + \hat{p}_a(t) \cos(\Omega_L t)), \quad (2.38a)$$

$$\hat{p}_L^{\text{out}}(t) = \hat{p}_L^{\text{in}}(t), \quad (2.38b)$$

$$\frac{d}{dt} \hat{x}_a(t) = \frac{\kappa}{\sqrt{T}} \hat{p}_L(t) \cos(\Omega_L t), \quad (2.38c)$$

$$\frac{d}{dt} \hat{p}_a(t) = \frac{\kappa}{\sqrt{T}} \hat{p}_L(t) \sin(\Omega_L t). \quad (2.38d)$$

(Remember that in this thesis lowercase atomic operators will always refer to single cell operators.) The atomic solutions are easily found:

$$\begin{aligned} \hat{x}_a(t) &= \hat{x}_a^{\text{in}} + \frac{\kappa}{\sqrt{T}} \int_0^t \hat{p}_L(t') \cos(\Omega_L t') dt', \\ \hat{p}_a(t) &= \hat{p}_a^{\text{in}} + \frac{\kappa}{\sqrt{T}} \int_0^t \hat{p}_L(t') \sin(\Omega_L t') dt', \end{aligned} \quad (2.39)$$

where $\hat{x}_a^{\text{in}} = \hat{x}_a(0)$ and $\hat{p}_a^{\text{in}} = \hat{p}_a(0)$. These are then inserted into Eq. (2.38a):

$$\begin{aligned} \hat{x}_s^{\text{out}} &= \sqrt{\frac{2}{T}} \int_0^T \hat{x}_L^{\text{out}}(t) \sin(\Omega_L t) dt \\ &= \hat{x}_s^{\text{in}} + \frac{\kappa}{\sqrt{2}} \hat{x}_a^{\text{in}} + \frac{\kappa^2}{T} \sqrt{\frac{2}{T}} \int_0^T dt \int_0^t dt' \hat{p}_L^{\text{in}}(t') \cos(\Omega_L t') \sin^2(\Omega_L t) \\ &= \hat{x}_s^{\text{in}} + \frac{\kappa}{\sqrt{2}} \hat{x}_a^{\text{in}} + \frac{\kappa^2}{T} \sqrt{\frac{2}{T}} \int_0^T dt' \hat{p}_L^{\text{in}}(t') \cos(\Omega_L t') \frac{T-t'}{2}, \end{aligned} \quad (2.40)$$

where the last equality is obtained by interchanging the order of integration and performing the inner one. The \hat{p}_a part of Eq. (2.38a) does not contribute because the product $\cos(\Omega_L t) \cdot \sin(\Omega_L t)$ averages out. We see clearly that the light is mapped back onto itself in what we previously called the back action noise of light. Also, we note that the temporal mode function for this term ($f(t') = (T-t')/(T\sqrt{2T})$) is different from the mode function of the usual top-hat mode of e.g. \hat{x}_s ($f(t) = \sqrt{2/T}$). This means that modes other than the symmetric one are admixed into the light. Projecting the noise term onto the symmetric mode it can be shown that the rest can be attributed to an admixture of the orthogonal mode:

$$\hat{p}_{s,1}^{\text{in}} = \sqrt{3} \left(\frac{2}{T} \right)^{3/2} \int_0^T dt \left(\frac{T}{2} - t \right) \sin(\Omega_L t) \hat{p}_L^{\text{in}}(t), \quad (2.41)$$

and equivalently for $\hat{p}_{c,1}^{\text{in}}$. With this expansion the light after the interaction can be written as:

$$\begin{aligned}\hat{x}_c^{\text{out}} &= \hat{x}_c^{\text{in}} + \frac{\kappa}{\sqrt{2}}\hat{p}_a^{\text{in}} \pm \left(\frac{\kappa}{2}\right)^2 \hat{p}_s^{\text{in}} \pm \frac{1}{\sqrt{3}} \left(\frac{\kappa}{2}\right)^2 \hat{p}_{s,1}^{\text{in}}, & \hat{x}_a^{\text{out}} &= \hat{x}_a^{\text{in}} + \frac{\kappa}{\sqrt{2}}\hat{p}_c^{\text{in}} \\ \hat{x}_s^{\text{out}} &= \hat{x}_s^{\text{in}} \pm \frac{\kappa}{\sqrt{2}}\hat{x}_a^{\text{in}} \pm \left(\frac{\kappa}{2}\right)^2 \hat{p}_c^{\text{in}} \pm \frac{1}{\sqrt{3}} \left(\frac{\kappa}{2}\right)^2 \hat{p}_{c,1}^{\text{in}}, & \hat{p}_a^{\text{out}} &= \hat{p}_a^{\text{in}} \pm \frac{\kappa}{\sqrt{2}}\hat{p}_s^{\text{in}}.\end{aligned}\tag{2.42}$$

The lower sign in the equations above apply to the interaction of light with a sample with opposite orientation of the mean spin such as the second atomic sample introduced in Sec. 2.6. For such a sample we define $\hat{x}_a = -\hat{J}_{y,2}/\sqrt{|J_x|}$ and $\hat{p}_a = \hat{J}_{z,2}/\sqrt{|J_x|}$. The equations of motion for such a sample are simply given by Eq. (2.26) with the substitution $J_x \rightarrow -J_x$. When the definitions of the atomic canonical variables are inserted into these the canonical equations of motion for such a sample are given by equations (2.38) with an effective Larmor precession $\Omega_L \rightarrow -\Omega_L$. (Note that the physical Larmor precession in the sample is unchanged.) Inserting these equations of motion into the definitions of $\hat{x}_{c,s}$ (with the physical Ω_L retained) Eq. (2.42) with the lower sign can be derived. Combining now the effect of the sequential interaction with the two atomic samples we easily regain equations (2.34).

This formalism is extremely useful compared to equations (2.26a) and (2.27) since the effect of different combinations of interactions and manipulations is easily calculated. This is illustrated in chapter 8, where a single cell teleportation scheme is presented that outperforms the one based on the QND interaction. The advantage is perhaps even more apparent in chapter 11 where we describe the hunt for new useful quantum information protocols.

CHAPTER 3

Entanglement Modeling - Experimental Approach

As we saw in the introduction entanglement appears when two systems are interconnected in such a way that a local description of each system separately is insufficient. More formally we say that two systems A and B are entangled if the density matrix ρ_{AB} for the combined Hilbert space $H = H_A \otimes H_B$ cannot be decomposed into products of density matrices from each Hilbert space:

$$\rho_{AB} \neq \sum_i p_i \rho_A \otimes \rho_B . \quad (3.1)$$

For pure states the degree of entanglement is given [71]:

$$E(\rho_{AB}) = S(\rho_A) = S(\rho_B) , \quad (3.2)$$

where e.g. ρ_A is the full density matrix traced over B and $S(\rho) = -Tr(\rho \log_2 \rho)$ is the von Neumann entropy. This entanglement measure has the following properties [72]: 1) it vanishes for separable states, 2) it is unchanged under local unitary operations and 3) it cannot be increased using local operations and classical communication (LOCC).

As an illustration take a singlet state $\psi = \frac{1}{\sqrt{2}}(|10\rangle - |01\rangle)$. Using the basis $(|11\rangle, |00\rangle, |10\rangle, |01\rangle)$ we get:

$$\rho_{AB} = \begin{pmatrix} 0 & 0 & 0 & 0 \\ 0 & 0 & 0 & 0 \\ 0 & 0 & 1 & -1 \\ 0 & 0 & -1 & 0 \end{pmatrix} \Rightarrow \rho_B = \frac{1}{2}\mathbf{I}_2 \Rightarrow \rho \log_2 \rho = -\frac{1}{2}\mathbf{I}_2 , \quad (3.3)$$

where \mathbf{I}_2 is the 2x2 identity matrix. From this we easily see that $E(\rho_{AB}) = 1$. This fundamental unit of entanglement is sometimes referred to as an ebit.

For mixed states it is impossible to formulate a unique entanglement measure because the decomposition into pure states is not unique. Some useful measures are the distillable entanglement [71] quantifying the amount of pure state entanglement that can be extracted from the state, the entanglement of formation [71, 73], which quantifies the minimum pure state entangled resources to create the state, and the logarithmic negativity [74, 75], which is simple to compute but does not as the others reduce the von Neumann entropy for pure states.

Another method is to formulate criteria to distinguish between entangled and separable states. A simple necessary and sufficient criterion was developed very early for 2×2 and 2×3 dimensional systems [76], but as the dimension increases such criteria cease to be sufficient. In this thesis we will primarily be concerned with infinite dimensional Gaussian harmonic oscillator states. Since such states are uniquely defined by their first and second moments analytical results can again be derived in this regime. In 2000 two different necessary and sufficient criteria for continuous variable systems were developed. One [77] is based on an extension of the low dimensional criterion, whereas the other one [78] is based on variances of canonical variables. We will use the latter, which adapted to our system states that in order to be entangled the atomic states have to fulfill:

$$\text{Var}(\hat{P}_{ac}) + \text{Var}(\hat{P}_{as}) = \text{Var}\left(\frac{\hat{p}_{a1} + \hat{p}_{a2}}{\sqrt{2}}\right) + \text{Var}\left(\frac{\hat{x}_{a1} - \hat{x}_{a2}}{\sqrt{2}}\right) < 1, \quad (3.4)$$

where the non-local variables are defined in Eq. (2.32). Demonstration of entanglement is thus reduced to the fulfillment of this criterion, and we will in this thesis quantify the degree of entanglement by the amount with which the separability criterion is violated. The state for which the criterion is maximally violated (no uncertainty) is exactly the state introduced in the introduction by EPR. We know from Sec. 2.1 that the coherent spin state is a minimum uncertainty state. This state corresponds to a vacuum state of the canonical operators. Hence, the fluctuations in such states, which are also called projection noise, form an extremely important benchmark in experiments with atomic ensembles. If we can reliably initialize our atomic system exactly at this boundary between quantum and classical correlations it follows that we only need to acquire a little extra information about the state of the atomic state to break the entanglement bound and project the state into a so-called two-mode squeezed or Einstein-Podolsky-Rosen entangled state. It follows from equations (2.34a) and (2.34d) that the Faraday interaction followed by a measurement of \hat{x}_L of a light pulse transmitted through two atomic ensembles should do exactly this. In this chapter we will introduce the experimental measurement cycle and derive simple expressions for the effect on the atomic state and the expected degree of entanglement.

3.1 The Coherent Spin State

To create entangled or squeezed states one has to generate states which exhibit less fluctuations than all equivalent classical states. The boundary occurs at the *coherent spin state* (CSS) in which all spins are independent realizations of a single spin oriented along a specific direction. The characteristics of this state were introduced in Sec. 2.1 and will be discussed in more detail in Sec. 5.6. For now we only need to quantify the role of the coherent spin state as a boundary between classical and purely quantum mechanical states. In analogy with Eq. (2.3) a Heisenberg uncertainty relation can be formed using the canonical atomic operators:

$$\text{Var}(\hat{X}_{ai})\text{Var}(\hat{P}_{ai}) \geq \frac{|\langle [\hat{X}_{ai}, \hat{P}_{ai}] \rangle|^2}{4} = \frac{1}{4}. \quad (3.5)$$

It can easily be shown that ground state of a harmonic oscillator (here the coherent spin state) is a minimum uncertainty state. Inserting this into the entanglement condition Eq. (3.4) we see that it is indeed the classical state with the least possible noise. For a state to be squeezed, it has to have less noise in one of the quadratures. Since the Heisenberg uncertainty relation still has to be fulfilled it follows that the other quadrature has to exhibit excessive fluctuations, it is anti-squeezed. We see that in order to *entangle* two samples we have to *squeeze* the non-local operators specified in the entanglement criterion. We will use these two notations interchangeably.

3.2 Entanglement Generation and Verification

We now turn to the actual understanding of entanglement generation and verification. We concentrate here on generation of an entangled state conditioned on the result of a measurement. Generation of an unconditional entangled state with the help of feedback is described in the Sec. 6.2. For generation of conditional entanglement we perform the following steps: First the atoms are prepared in coherent states with oppositely oriented mean spin corresponding to the creation of vacuum states of the two modes $(\hat{X}_{ac}, \hat{P}_{ac})$ and $(\hat{X}_{as}, \hat{P}_{as})$. Next, a pulse of light called the *entangling pulse* is sent through the atoms and we measure the two operators \hat{x}_c^{out} and \hat{x}_s^{out} (defined in Eq. (2.33)) with outcomes A_1 and B_1 , respectively. These results bear information about the atomic operators \hat{P}_{ac} and \hat{P}_{as} and hence we reduce the variances $\text{Var}(\hat{P}_{ac})$ and $\text{Var}(\hat{P}_{as})$. To prove that we have an entangled state we must confirm that the variances of \hat{P}_{ac} and \hat{P}_{as} fulfill the criterion (3.4). That is, we need to know the mean values of \hat{P}_{ac} and \hat{P}_{as} with a total precision better than unity. To demonstrate that, we send a second *verifying pulse* through the atomic samples again measuring \hat{x}_c^{out} and \hat{x}_s^{out} with outcomes A_2 and B_2 . Now it is a matter of comparing A_1 with A_2 and B_1 with B_2 . If the results are sufficiently close the state created by the first pulse was entangled.

Let us be more quantitative. The interaction (2.34a) mapping the atomic operators \hat{P}_{ai} to field operators \hat{x}_i is very useful for large κ , and useless if $\kappa \ll 1$. We will describe in detail the role of κ for all values. To this end we first describe the natural way to determine κ experimentally. If we repeatedly perform the first two steps of the measurement cycle, i.e. prepare coherent states of the atomic spins, send in the first measurement pulse, and record outcomes A_1 and B_1 , we may deduce the statistical properties of the measurements. Theoretically we expect from (2.34a)

$$\langle A_1 \rangle = \langle B_1 \rangle = 0 \quad \text{and} \quad \text{Var}(A_1) = \text{Var}(B_1) = \frac{1}{2} + \frac{\kappa^2}{2}. \quad (3.6)$$

The first term in the variances is the shot noise (SN) of light. This can be measured in the absence of the interaction where $\kappa = 0$. The quantum nature of the shot noise level is confirmed by checking the linear scaling with the photon number of the pulse. The second term arises from the projection noise (PN) of atoms. Hence, we may calibrate κ^2 to be the ratio $\kappa^2 = \text{PN}/\text{SN}$ of atomic projection noise to shot noise of light. Theoretically $\kappa^2 = aJ_x S_x T$ has a linear scaling with the macroscopic spin J_x . This scaling is confirmed experimentally in Sec. 5.6.

Next we describe how to deduce the statistical properties of the state created by the *entangling pulse*. Based on the measurement results A_1 and B_1 of this pulse we must predict the mean value of the second measurement outcome. If $\kappa \rightarrow \infty$ we ought to trust the first measurement completely since the initial noise of \hat{x}_i^{in} is negligible giving the estimates for the second pulse result $\langle A_2 \rangle_{\text{est}} = A_1$ and $\langle B_2 \rangle_{\text{est}} = B_1$. On the other hand, if $\kappa = 0$ there is no atomic contribution to the light, so the second pulse result is entirely uncorrelated with the first pulse results, $\langle A_2 \rangle_{\text{est}} = \langle B_2 \rangle_{\text{est}} = 0$. It is natural to take in general $\langle A_2 \rangle_{\text{est}} = \alpha A_1$ and $\langle B_2 \rangle_{\text{est}} = \alpha B_1$. We need not know a theoretical value for α . The actual value can be deduced from the data. If we repeat the measurement cycle N times with outcomes $A_1^{(i)}$, $B_1^{(i)}$, $A_2^{(i)}$, and $B_2^{(i)}$, the correct α is found by minimizing the conditional variance

$$\begin{aligned} \text{Var}(A_2|A_1) + \text{Var}(B_2|B_1) = \\ \min_{\alpha} \frac{1}{N-1} \sum_i^N \left((A_2^{(i)} - \alpha A_1^{(i)})^2 + (B_2^{(i)} - \alpha B_1^{(i)})^2 \right). \end{aligned} \quad (3.7)$$

In order to deduce whether we fulfill the entanglement criterion (3.4) we compare the above to our expectation from (2.34a). For the verifying pulse we get

$$\begin{aligned} \left\langle (\hat{x}_i^{\text{out}} - \langle \hat{x}_i^{\text{out}} \rangle)^2 \right\rangle &= \left\langle \left(\hat{x}_i^{\text{in},2\text{nd}} + \kappa \left[\hat{P}_{ai}^{\text{ent}} - \langle \hat{P}_{ai}^{\text{ent}} \rangle \right] \right)^2 \right\rangle \\ &= \frac{1}{2} + \kappa^2 \text{Var}(\hat{P}_{ai}^{\text{ent}}), \end{aligned} \quad (3.8)$$

where $\hat{x}_i^{\text{in},2\text{nd}}$ refers to the incoming light of the *verifying pulse* which has zero mean. $\hat{P}_{ai}^{\text{ent}}$ refers to the atomic state after the passage of the entangling pulse.

We see that the practical entanglement criterion becomes

$$\begin{aligned} \text{Var}(A_2|A_1) + \text{Var}(B_2|B_1) &= 1 + \kappa^2 \left(\text{Var}(\hat{P}_{ac}^{\text{ent}}) + \text{Var}(\hat{P}_{as}^{\text{ent}}) \right) \\ &< 1 + \kappa^2 = \text{Var}(A_1) + \text{Var}(B_1). \end{aligned} \quad (3.9)$$

Simply stated, we must predict the outcomes A_2 and B_2 with a precision better than the statistical spreading of the outcomes A_1 and B_1 with the additional constraint that A_1 and B_1 are outcomes of quantum noise limited measurements.

3.3 Theoretical Entanglement Modeling

We described above the experimental procedure for generating and verifying the entangled states. Here we present a simple way to derive what we expect for the mean values (i.e. the α -parameter) and for the variances $\text{Var}(\hat{P}_{ai}^{\text{ent}})$.

We calculate directly the expected conditional variance of A_2 based on A_1 :

$$\begin{aligned} &\left\langle (\hat{x}_c^{\text{out},2\text{nd}} - \alpha \hat{x}_c^{\text{out},1\text{st}})^2 \right\rangle \\ &= \left\langle \left(\hat{x}_c^{\text{in},2\text{nd}} - \alpha \hat{x}_c^{\text{in},1\text{st}} + \kappa \left[\hat{P}_{ac}^{\text{ent}} - \alpha \hat{P}_{ac}^{\text{in}} \right] \right)^2 \right\rangle \\ &= \frac{1}{2} (1 + \alpha^2 + \kappa^2 (1 - \alpha)^2). \end{aligned} \quad (3.10)$$

In the second step we assume that a perfect QND measurement without any decoherence is performed, i.e. $\hat{P}_{ac}^{\text{ent}} = \hat{P}_{ac}^{\text{in}}$. By taking the derivative with respect to α we obtain the theoretical minimum

$$\begin{aligned} \text{Var}(A_2|A_1) + \text{Var}(B_2|B_1) &= 1 + \frac{\kappa^2}{1 + \kappa^2} \\ \Rightarrow \text{Var}(\hat{P}_{ac}^{\text{ent}}) + \text{Var}(\hat{P}_{as}^{\text{ent}}) &= \frac{1}{1 + \kappa^2} \end{aligned} \quad (3.11)$$

obtained with the α -parameter

$$\alpha = \frac{\kappa^2}{1 + \kappa^2}. \quad (3.12)$$

It is interesting that, in principle, any value of κ leads to the creation of entanglement. The reason for this is our prior knowledge of the input state. The atoms are in a coherent state which is as well defined in terms of variances as is possible for separable states. We need only an ‘‘infinitesimal’’ extra knowledge about the spin state to go into the entangled regime.

Alternatively we can derive the same result by examining the marginal probability distributions of the quantum variables. When initiated in the coherent state all variables will have a Gaussian probability distribution:

$$P_{\hat{q}}(q) = \frac{1}{\sqrt{2\pi\sigma^2}} e^{-q^2/2\sigma^2}. \quad (3.13)$$

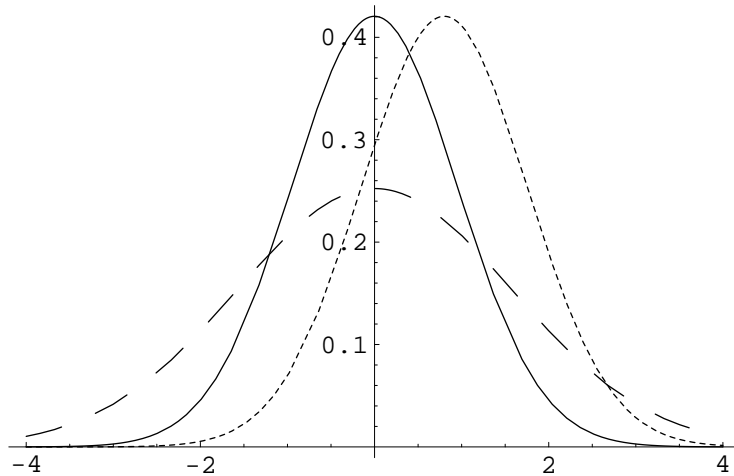


Figure 3.1: Illustration of the second probability distribution in an entanglement experiment. Based on the result of the measurement on the entangling pulse the expected distribution for the verifying pulse will be a displaced Gaussian (dotted). The width of this distribution is more narrow than the distribution from the first (or second) pulse alone (dashed). With a quantum feedback the atomic distribution can be shifted to have zero mean value. This gives an unconditionally entangled state and a second pulse distribution with zero mean and reduced width (solid).

As before we denote the results of the first and the second measurements by A_1 and A_2 respectively. Then the probability distribution of A_2 conditioned on A_1 is given by:

$$\begin{aligned}
 P(A_2|A_1) &= \frac{P(A_2 \cap P(A_1))}{P(A_1)} \\
 &= \frac{\int_{-\infty}^{\infty} dP_a P_{\hat{P}_a}(P_a) P_{\hat{x}_L^{\text{in},1\text{st}}}(A_1 - \kappa P_a) P_{\hat{x}_L^{\text{in},2\text{nd}}}(A_2 - \kappa P_a)}{\int_{-\infty}^{\infty} dP_a P_{\hat{P}_a}(P_a) P_{\hat{x}_L^{\text{in},1\text{st}}}(A_1 - \kappa P_a)}. \quad (3.14)
 \end{aligned}$$

This gives a Gaussian displaced by exactly A_1 times the α parameter of Eq. (3.12) and a variance given by the first equation of (3.11). An example of such a displaced distribution is shown in Fig. 3.1 (dotted). Also shown is $P(A_2)$ (dashed), which corresponds to neglecting the knowledge gained from the first pulse. Finally we show the result of shifting the atomic state by $A_1\alpha$ between the pulses (solid). This illustrates the different methods of obtaining an entangled state. Either we run the sequence N times and based on the method sketched in Sec. 3.2 find the optimal α . With this we can find the width of the shifted distribution. This represents a conditionally entangled state, because the entanglement property only appears when the knowledge of the first pulse result is applied.

A second approach to entanglement generation is in each cycle to actively shift

the atomic distribution to zero mean value via a quantum feedback based on the first measurement result. This creates an unconditionally entangled state where the entanglement is present directly from the second pulse measurement results. The experimental realization of both methods will be discussed in chapter 6.

It is also interesting to see what happens to the conjugate variables \hat{X}_{ai} in the entangling process. This is governed by Eq. (2.34c). We do not perform measurements of the light operator \hat{p}_i^{in} so all we know is that both \hat{X}_{ai}^{in} and \hat{p}_i^{in} are in the vacuum state. Hence $\text{Var}(\hat{X}_{ai}^{\text{ent}}) = (1 + \kappa^2)/2$ and we preserve the minimum uncertainty relation $\text{Var}(\hat{X}_{ai}^{\text{ent}})\text{Var}(\hat{P}_{ai}^{\text{ent}}) = 1/4$.

3.4 Entanglement Model with Decoherence

Practically our spin states decohere between the light pulses and also in the presence of the light. We model this decoherence naively by attributing the entire effect to the time interval between the two pulses, i.e. we assume that there is no decoherence in the presence of the light but a larger decoherence between the pulses. We may then perform an analysis in complete analogy with the above with the only difference that $\hat{P}_{ac}^{\text{ent}} = \beta\hat{P}_{ac}^{\text{in}} + \sqrt{1 - \beta^2}\hat{V}_p$ where \hat{V}_p is a vacuum operator admixed such that $\beta = 0$ corresponds to a complete decay to the vacuum state and $\beta = 1$ corresponds to no decoherence. Completing the analysis we find the theoretical conditional variances

$$\begin{aligned} \text{Var}(A_2|A_1) + \text{Var}(B_2|B_1) &= 1 + \kappa^2 \frac{1 + (1 - \beta^2)\kappa^2}{1 + \kappa^2} \\ \Rightarrow \text{Var}(\hat{P}_{ac}^{\text{ent}}) + \text{Var}(\hat{P}_{as}^{\text{ent}}) &= \frac{1 + (1 - \beta^2)\kappa^2}{1 + \kappa^2} \end{aligned} \quad (3.15)$$

obtained with α -parameter

$$\alpha = \frac{\beta\kappa^2}{1 + \kappa^2}. \quad (3.16)$$

In the limit $\beta \rightarrow 1$ these results agree with (3.11) and (3.12). For $\beta \rightarrow 0$ we have $\alpha \rightarrow 0$ (outcomes A_1 and B_1 are useless) and the variance approaches that of the vacuum state which is a separable state. In a similar manner, losses of light due to e.g. reflection losses or imperfect detection efficiency can be treated. The only effect turns out to be a redefinition of $\kappa \rightarrow \sqrt{1 - \epsilon}\kappa$ in equations (3.15) and (3.16), where ϵ is the fraction of the light power lost. Note that in the analysis above, the decoherence is assumed to be towards the coherent spin state. To model decoherence towards e.g. a thermal state more sophisticated methods will have to be employed. Also, the inclusion of decoherence is very coarse grained since we assumed all of the decoherence to occur in a single step. In reality the entangling interaction and the atomic decoherence occur continuously in time. Both of these issues will be addressed in the following chapter.

CHAPTER 4

Gaussian Entanglement

In this chapter we wish to supplement and extend the calculations in the previous chapter concerning the evolution of the atomic state. We do this by utilizing explicitly the fact that the states are very well described by Gaussian probability distributions. For such states the powerful formalism of correlation matrices for Gaussian states [72, 79] is applicable. In this framework the effect of a light measurement on the atomic statistics is given explicitly. Here we will introduce the formalism which involves a description in terms of a covariance matrix and a prescription for the update of this matrix incorporating interaction, decoherence, as well as the effect of the light detection. We illustrate the use of the formalism by rederiving all entanglement results from the previous chapter. This is done by treating the interaction as a single process and is therefore only valid in the limit of low decoherence. We will extend the range of validity by splitting the incoming light pulse into small segments and treating the interaction with each sequentially. These results will then be compared to the simple expressions.

We stress that this is not the first time entanglement generation in such systems has been considered. Entanglement utilizing a series of two sequential QND interactions for a single sample without rotations has been studied several years ago [36] and a quantum trajectory approach with simulated state vector dynamics was presented in [80, 81] to provide a microscopic description of the dynamics. Because of the dimensions of the Hilbert spaces involved, however these simulations were restricted to a few tens of atoms. We retain in the following the careful attention of [80, 81] to the quantum mechanical effects of the measurement while combining it with the efficient Gaussian description.

4.1 General Theory of Covariance Matrices

As discussed previously both the atomic and light systems when initialized in coherent states are very accurately described by Gaussian distribution functions. Since the atom-light Hamiltonian is bi-linear in the quadratures the interaction will preserve the Gaussian form as will the effect of homodyne measurements [72, 79]. We will be interested in systems composed of n atomic and m canonical light operators. From these we form the vector:

$$\mathbf{y} = (\hat{O}_{a,1}, \dots, \hat{O}_{a,n}, \hat{O}_{L,1}, \dots, \hat{O}_{L,m}) . \quad (4.1)$$

Within the Gaussian approximation all information about the system is contained in the first two moments of the quantum variables. We are interested in the entanglement properties of the samples which are not changed by local displacement operations so the second moments are of primary interest. These are collected in the $(n+m) \times (n+m)$ covariance matrix defined by

$$\gamma_{ij} = \langle y_i y_j + y_j y_i \rangle - 2 \langle y_i \rangle \langle y_j \rangle , \quad (4.2)$$

which we see is merely a collection of two times the covariance of the corresponding operators.

In the following we will review some basic properties of covariance matrices (see e.g [72, 82, 83] and appendix A of [84]). They can be related to the Wigner function by

$$W(\xi) = \frac{1}{\pi^N \sqrt{\det \gamma}} \exp(\xi \gamma^{-1} \xi^T) , \quad (4.3)$$

where $2N$ is the dimension of the covariance matrix. As an introduction we will state the covariance matrix for a number of simple single mode states ($\mathbf{y} = (x, p)$):

$$\begin{array}{ll} \text{vacuum} & \langle \mathbf{y} \rangle = \begin{pmatrix} 0 \\ 0 \end{pmatrix} & \gamma = \begin{pmatrix} 1 & 0 \\ 0 & 1 \end{pmatrix} \\ \text{coherent state}(\alpha) & \langle \mathbf{y} \rangle = \frac{1}{\sqrt{2}} \begin{pmatrix} \text{Re}(\alpha) \\ \text{Im}(\alpha) \end{pmatrix} & \gamma = \begin{pmatrix} 1 & 0 \\ 0 & 1 \end{pmatrix} \\ \text{squeezed state} & \langle \mathbf{y} \rangle = \begin{pmatrix} 0 \\ 0 \end{pmatrix} & \gamma = \begin{pmatrix} e^r & 0 \\ 0 & e^{-r} \end{pmatrix} \\ \text{thermal state} & \langle \mathbf{y} \rangle = \begin{pmatrix} 0 \\ 0 \end{pmatrix} & \gamma = \begin{pmatrix} n & 0 \\ 0 & n \end{pmatrix} , \end{array} \quad (4.4)$$

where in the last expression $n = \frac{1}{1 - e^{-\hbar\omega/kT}}$ is the mean number of photons in the thermal field. For two systems ($\mathbf{y} = (x_1, p_1, x_2, p_2)$) the covariance matrix for an uncorrelated (separable) state is merely $\gamma = \text{Diag}(\gamma_1, \gamma_2)$, whereas for a two-mode squeezed state with squeezing in $x_1 - x_2$ and $p_1 + p_2$ (corresponding to the state that we ideally create in our entanglement experiments) it is:

$$\gamma = \begin{pmatrix} \cosh(r) & 0 & \sinh(r) & 0 \\ 0 & \cosh(r) & 0 & -\sinh(r) \\ \sinh(r) & 0 & \cosh(r) & 0 \\ 0 & -\sinh(r) & 0 & \cosh(r) \end{pmatrix} , \quad (4.5)$$

where r is the squeezing parameter.

Covariance matrices always obey $\det(\gamma) \geq 1$ and they represent pure states if and only if $\det(\gamma) = 1$. We see that all of the covariance matrices stated above represent pure states except the thermal state. A Heisenberg uncertainty relation can be formulated for covariance matrices:

$$\gamma - i \begin{pmatrix} \sigma & 0 & & \\ 0 & \sigma & & \\ & & \dots & \\ & & & \sigma \end{pmatrix} \geq 0, \quad \sigma = \begin{pmatrix} 0 & 1 \\ -1 & 0 \end{pmatrix}. \quad (4.6)$$

The matrices $\sigma_{ij}(i, j = 1, 2)$ specify the commutation relations between the $x(1)$ and $p(2)$ variables of a single mode. The matrix equation above means that the eigenvalues of the system on the left hand side are always positive for a physically realizable state. Finally we would like to mention one very important property of all Gaussian states. They cannot be distilled by the application of Gaussian operations [79, 85]. This means that two sets of Gaussian entangled states - in contrast to discrete variables - cannot be converted into a single entangled state with a higher degree of entanglement if the Gaussian structure is preserved throughout. This is very unfortunate because it severely hinders the practical feasibility of distributed entanglement over arbitrary distances for a Gaussian approach.

Next we wish to add dynamics to the formalism. The evolution of \mathbf{y} and γ in the Heisenberg picture due to a general unitary interaction is given by:

$$\mathbf{y}^{\text{out}} = S\mathbf{y}^{\text{in}} \quad (4.7a)$$

$$\gamma^{\text{out}} = S \cdot \gamma^{\text{in}} \cdot S^T, \quad (4.7b)$$

where S is the interaction matrix, which can be determined by matching Eq. (4.7a) to the equations of interaction. For the QND Faraday interaction described by Eq. (2.34) we obtain

$$\mathbf{y} = \begin{pmatrix} \hat{X}_a \\ \hat{P}_a \\ \hat{x}_L \\ \hat{p}_L \end{pmatrix}, \quad S = \begin{pmatrix} 1 & 0 & 0 & \kappa \\ 0 & 1 & 0 & 0 \\ 0 & \kappa & 1 & 0 \\ 0 & 0 & 0 & 1 \end{pmatrix}. \quad (4.8)$$

To describe the evolution of the atomic state due to a measurement of light, let the covariance matrix before the homodyne measurement be given by:

$$\gamma = \begin{pmatrix} \gamma_a & \gamma_c \\ \gamma_c^T & \gamma_b \end{pmatrix} \quad (4.9)$$

where γ_a is an $n \times n$ matrix describing the atomic subsystem, and γ_b is an $m \times m$ matrix describing the light system. All atom-light correlations are contained in γ_c . After the detection the atomic part of the correlation matrix is then given by [72, 79]:

$$\gamma_a \rightarrow \gamma_a - \gamma_c(\pi\gamma_b\pi)^{-1}\gamma_c^T \quad (4.10)$$

where π specifies the light quadrature or sum of quadratures being measured. In the case of perfect detection of e.g. only the i 'th light quadrature we get $\pi_{ii} = 1$ and the rest of the entries equal to zero. Please note that Eq. (4.10) expresses nothing but classical update of estimators based on a measurement - similar to Eq. (3.14) - coupled with the Heisenberg uncertainty principle, stating that if we measure an operator, the conjugate operator becomes completely unknown. This wipes out all correlations between the conjugate operator and the remainder of the system. $(\cdot)^-$ denotes the Moore-Penrose pseudo-inverse of a matrix ($XX^-X = X; X^-XX^- = X^-$). In our case we will only need $\text{Diag}(b, 0)^- = \text{Diag}(1/b, 0)$. Note that the evolution of the covariance matrix is deterministic i.e. it does not depend on the, inherently random, detection results.

We see that determining the atomic dynamics is in this formalism reduced to straight forward matrix algebra, which is in sharp contrast to the heuristic optimization approach presented in the previous chapter. We will use Eq. (4.7b) combined with Eq. (4.10) on the Faraday dynamics shortly, but first we will comment on the inclusion of decoherence into this formalism. For this we will assume a pulse duration of T . We saw in Eq. (2.19) that due to the interaction with the light field every atom is excited and decays by spontaneous emission to any of the atomic ground states with a certain rate. We will write this atomic depumping parameter as $\eta_T \equiv \eta T = \Phi T \frac{\sigma_{CS}}{A} \left(\frac{\Gamma}{\Delta}\right)^2$. Φ is the photonic flux, A is the cross section of the atomic sample illuminated by the light, Δ is the detuning from resonance, σ_{CS} is the cross section on resonance for the probed transition, and Γ is the HWHM of the corresponding spontaneous decay rate. η has the physical interpretation that the scattering probability per photon is given by the ratio between the interaction cross section σ_{CS} and the physical cross section of the beam. The entire process is then reduced by the Lorentzian response.

Of course every absorption event also acts as source of decoherence for the light system. In terms of the definitions above the photon absorption probability is $\epsilon = N_{\text{at}} \frac{\sigma_{CS}}{A} \left(\frac{\Gamma}{\Delta}\right)^2$.¹ On resonance the total absorption will be given by the optical density $\alpha = N_{\text{at}} \frac{\sigma_{CS}}{A}$. We will in Sec. 5.6 give explicit expressions for α and η based on the full multi-level interaction.

Taking a fully polarized atomic sample at $t = 0$ this gives the following relation for the coupling parameter, $\kappa_T^2(t = 0) = \eta_T \alpha$. Later in this chapter we will split the pulse into many small segments of duration τ . For the segment at some later time, t , the decay of the mean spin has reduced the coupling constant, $\kappa_\tau^2(t) = \kappa_\tau^2(0)e^{-\eta t}$. Here we implicitly assumed that $\tau \ll t$ such that the mean spin can be considered constant during the passage of the light segment. As will be discussed in Sec. 5.6.2 our experiments using room temperature gas samples are performed at $\alpha \approx 32$ and in an entire pulse the accumulated atomic depumping is typically a few percent. In dense cold atomic samples optical depths surpassing 100 are routinely achieved and in Bose-Einstein condensates it can even approach 1000. This means that the interaction strength κ^2 can

¹In reality the probability of absorption is given by $P(\text{abs}) = 1 - e^{-\epsilon}$, which for $\epsilon \ll 1$ means that $P(\text{abs}) \approx \epsilon$ and similarly for η_τ

either be increased greatly without a corresponding increase in the total atomic depumping or a similar κ^2 can be achieved with a lot lower depumping.

When light absorption and subsequent atomic decoherence is included the interaction between a subset of the atomic operators and a subset of the light operators is governed by (see App. B):

$$\gamma^{\text{out}} = \bar{D}S\gamma^{\text{in}}S\bar{D} + D\gamma_{\text{noise}} \quad (4.11)$$

where D is a diagonal matrix with η and ϵ on the positions of the participating atomic and light operators respectively and $\bar{D} = \sqrt{1 - D}$. γ_{noise} is like D with the replacements $\eta \rightarrow \xi$ and $\epsilon \rightarrow 1$. The factors \bar{D} represent the reduction in the signal that we derived in Sec. 2.3.1, whereas the $D\gamma_{\text{noise}}$ term represents the added noise due to the Langevin terms that have to be added in order to preserve commutation relations. As described in App. B, for a spin 1/2 system the factor $\xi \equiv N_{\text{at}}/\langle J_x(t) \rangle$ starts out as two and increases exponentially because of the decay of the mean spin due to excitation and subsequent decay of atoms. Briefly, the factor of two arises because of two contributions. First of all, the atomic state becomes more noisy because of the loss of correlations between the fraction of atoms being excited and the rest. Secondly, the decohered atoms are transferred into a thermal state. The extension to higher spin systems is also discussed in App. B. Here the variances of the coherent state and the thermal state are no longer identical. When applying Eq. (4.11) once, this merely means that another value of ξ has to be used. When used iteratively, however, this difference leads to errors of the order of $e^{\eta t}$ and it therefore has very limited validity.

As will be discussed in Sec. 5.4 the main source of decoherence in our experiments are light induced collisions, which rapidly affect the transverse spins (and hence the canonical operators) without causing a reduction in the mean spin. This is traditionally called a T_2 process. For such a decoherence towards the CSS a beam splitter addition of atomic noise - such as applied in Sec. 3.4 - is more appropriate (see appendix B). In this case the exponential increase of the noise term and the exponential decrease in the interaction strength are absent and $\xi = 1$ and κ are constant in time. Note also that setting $\eta = \xi = 0$ Eq. (4.11) can be used to model losses of light due to e.g. spurious reflections from glass surfaces in the setup.

In the following sections we will apply Eq. (4.11) for a single pulse to derive simple expressions analogous to the one derived in Sec. 3.4, the validity of which will be limited to $\eta_T \ll 1$. This will be done first using the QND interaction. Since, however it is based on non-local operators it does not take into account properly any light loss between the cells. In our experimental implementation the light experiences significant reflection losses, so this could potentially be an important effect. To get a simple but relatively reliable estimate of the effect, the dynamics will be derived based on the single cell interactions Eq. (2.42). Both of these approaches are, however, only valid for $\eta_T \ll 1$. Therefore the remainder of the chapter will be devoted to extending this range of validity. This will be done by splitting the pulse into many segments and treating the interaction with the atomic sample sequentially in time with Eq. (4.11). Thus, when the dynamics

is solved we can compare to the single pulse solution and hopefully gain some intuition concerning the validity of these.

4.2 Entanglement Based on the QND Interaction

As a demonstration of the power of the approach we will start by deriving Eq. (3.11) based on the two-cell QND interactions given in equations (2.34). For this interaction \mathbf{y} S are given by Eq. (4.8). This system of equations describes both squeezing of a single atomic sample and the generation of entanglement between two samples via squeezing of the non-local \hat{p} operators given in (2.32). Performing the matrix multiplications specified in Eq. (4.7b) and inserting the result into Eq. (4.10) we easily derive the squeezing of one of the non-local atomic variables and the anti-squeezing of the other:

$$\gamma_a = \begin{pmatrix} 1 + \kappa^2 & 0 \\ 0 & 1 \end{pmatrix} - \kappa^2 \begin{pmatrix} 0 & 1 \\ 1 & 0 \end{pmatrix} \begin{pmatrix} \frac{1}{1 + \kappa^2} & 0 \\ 0 & 0 \end{pmatrix} \begin{pmatrix} 0 & 1 \\ 1 & 0 \end{pmatrix} = \begin{pmatrix} 1 + \kappa^2 & 0 \\ 0 & \frac{1}{1 + \kappa^2} \end{pmatrix}. \quad (4.12)$$

This is a very simple derivation but following the same steps much more complicated problems can be solved with equal ease. To illustrate this we now include noise due to spontaneous emission as prescribed in Eq. (4.11). Letting $D = \text{diag}(\eta_T, \eta_T, 2\epsilon, 2\epsilon)$, where ϵ is the light loss from a single cell, and $\gamma_{\text{noise}} = \text{diag}(2, 2, 1, 1)$ we get:

$$\gamma_a = \begin{pmatrix} 1 + \eta_T + (1 - \eta_T)\kappa^2 & 0 \\ 0 & 2\eta_T + \frac{1 - \eta_T}{1 + (1 - 2\epsilon)\kappa^2} \end{pmatrix}. \quad (4.13)$$

The second term in the squeezed quadrature is always smaller than unity for a non-zero interaction strength. The ultimate degree of squeezing will then be determined by the interplay between the beneficial action of the second term and the deleterious effect of the first term. In Fig. 4.1 the squeezed part of Eq. (4.13) is plotted using the transformation $\kappa^2 = \eta_T \alpha$ for the experimentally motivated values $\epsilon = \left(\frac{\Gamma}{\Delta}\right)^2 \alpha = \left(\frac{2.5\text{MHz}}{700\text{MHz}}\right)^2 \alpha$ and $\alpha = 30$. Clearly the degree of squeezing reaches a maximum after which the part growing linearly with η_T will start to dominate. For the chosen parameters ϵ makes a negligible contribution. As mentioned briefly in the preceding section, however, ϵ can also be interpreted as pure light loss through e.g. reflection. In our experiments this is a much more significant effect. Therefore, the squeezing is also shown in Fig. 4.1 for $\epsilon = 0.1$. Thus, with a typical experimental atomic depumping of $\eta_T \sim 0.05$ we expect to achieve approximately 30-40% noise reduction.

As discussed briefly in Sec. 4.1 and in more detail in appendix B atomic decoherence towards the CSS (no decay of the mean spin vector) is treated by setting $\xi = 1$. Doing this, we get $\gamma_{\text{noise}} = \text{diag}(1, 1, 1, 1)$ and the term $2\eta_T$ in the squeezed part of Eq. (4.13) becomes η_T . With the transformation $\eta_T = 1 - \beta^2$ this is identical to Eq. (3.15).

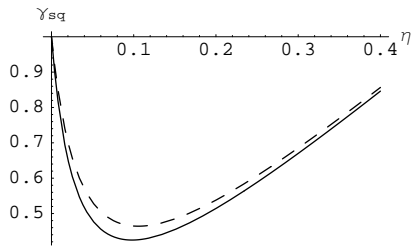


Figure 4.1: The variance of the squeezed quadrature (Eq. (4.13)) calculated via the QND interaction. Solid: $\epsilon = (2.5/700)^2 \alpha$. Dashed: $\epsilon = 0.1$. $\alpha = 30$ for both.

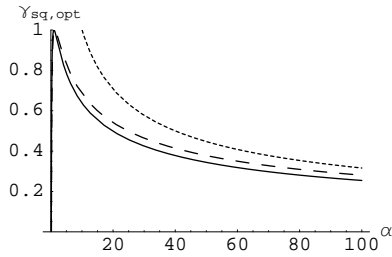


Figure 4.2: Optimal squeezing (Eq. (4.15)) as a function of the optical depth. Solid: $\epsilon = (2.5/700)^2 \alpha$. Dashed: $\epsilon = 0.1$. Dotted: high α limit (Eq. (4.15)) with $\epsilon = 0.1$

With the transformation $\kappa^2 = \eta_T \alpha$, the squeezed quadrature of Eq. (4.13), $\gamma_{a, sq}$, can be optimized with respect to η_T to give:

$$\eta_{\text{opt}} = \frac{\sqrt{\frac{1+\alpha(1-2\epsilon)}{2}} - 1}{\alpha(1-2\epsilon)}. \quad (4.14)$$

Note that this expression is only positive - and thus physically meaningful - for $\alpha > 1/(1-2\epsilon)$ reflecting the fact that for $\alpha < 1/(1-2\epsilon)$ the noise term of $\gamma_{a, sq}$ ($2\eta_T$) will dominate the squeezing part. Inserting Eq. (4.14) into $\gamma_{a, sq}$ gives:

$$\gamma_{a, sq} = \frac{2\sqrt{2(1+\alpha(1-2\epsilon))} - 3}{\alpha(1-2\epsilon)} \rightarrow \frac{2\sqrt{2}}{\sqrt{\alpha(1-2\epsilon)}} \quad \alpha \gg 1. \quad (4.15)$$

This expression is plotted in Fig. 4.2 for the same two values of ϵ as before along with the expression in the limit of high optical densities (Eq. (4.15)).

4.3 Entanglement Based on the Single Cell Interaction with Rotations

Whereas Eq. (4.13) is generally valid for a single sample as long as $\eta_T \ll 1$, for two samples a non-zero ϵ will remove a fraction of the light and thus modify $\kappa \rightarrow \kappa\sqrt{1-\epsilon}$ and $\eta_T \rightarrow (1-\epsilon)\eta_T$ for the interaction with the second sample. This asymmetry is not accounted for in Eq. (4.13), which is therefore only valid in the limit of vanishing ϵ . This deficiency can be remedied by treating the interaction of the light with each atomic sample sequentially. This can be done in the pulsed regime based on the pulsed single cell interactions of Eq. (2.42). We introduce decoherence as a single step after each passage of the pulse through an atomic sample. We know from Eq. (2.34) that the non-local operators $\hat{P}_{ac} = \frac{\hat{p}_{a1} + \hat{p}_{a2}}{\sqrt{2}}$

and $\hat{P}_{as} = \frac{\hat{x}_{a1} - \hat{x}_{a2}}{\sqrt{2}}$ get squeezed. They each form a closed system of interaction with a set of variables $(\hat{x}_c, \hat{p}_s, \hat{p}_{s,1})$ and $(\hat{x}_s, \hat{p}_c, \hat{p}_{c,1})$ respectively. The degree of squeezing will be the same for the two non-local variables and it therefore suffices to investigate one of them. Defining the vector:

$$\mathbf{y} = \begin{pmatrix} \hat{p}_{a1} \\ \hat{p}_{a2} \\ \hat{x}_c \\ \hat{p}_s \\ \hat{p}_{s,1} \end{pmatrix}, \quad (4.16)$$

we get the interaction matrices:

$$S_1 = \begin{pmatrix} 1 & 0 & 0 & \frac{\kappa}{\sqrt{2}} & 0 \\ 0 & 1 & 0 & 0 & 0 \\ \frac{\kappa}{\sqrt{2}} & 0 & 1 & (\frac{\kappa}{2})^2 & \frac{1}{\sqrt{3}}(\frac{\kappa}{2})^2 \\ 0 & 0 & 0 & 1 & 0 \\ 0 & 0 & 0 & 0 & 1 \end{pmatrix}, \quad S_2 = \begin{pmatrix} 1 & 0 & 0 & 0 & 0 \\ 0 & 1 & 0 & -\frac{\kappa}{\sqrt{2}} & 0 \\ 0 & \frac{\kappa}{\sqrt{2}} & 1 & -(\frac{\kappa}{2})^2 & -\frac{1}{\sqrt{3}}(\frac{\kappa}{2})^2 \\ 0 & 0 & 0 & 1 & 0 \\ 0 & 0 & 0 & 0 & 1 \end{pmatrix} \quad (4.17)$$

Setting γ_{in} to be a 5x5 identity matrix and starting without decoherence we calculate:

$$\gamma_{out} = S_2 \cdot S_1 \cdot \gamma_{in} \cdot S_1^T \cdot S_2^T = \begin{pmatrix} \frac{2+\kappa^2}{2} & \frac{-\kappa^2}{2} & \frac{\kappa}{\sqrt{2}} & \frac{\kappa}{\sqrt{2}} & 0 \\ \frac{-\kappa^2}{2} & \frac{2+\kappa^2}{2} & \frac{\kappa}{\sqrt{2}} & \frac{-\kappa}{\sqrt{2}} & 0 \\ \frac{\kappa}{\sqrt{2}} & \frac{\kappa}{\sqrt{2}} & 1+\kappa^2 & 0 & 0 \\ \frac{\kappa}{\sqrt{2}} & \frac{-\kappa}{\sqrt{2}} & 0 & 1 & 0 \\ 0 & 0 & 0 & 0 & 1 \end{pmatrix}. \quad (4.18)$$

We note that after the complete interaction, $\hat{p}_{s,1}$ is uncorrelated with the rest of the system. This expresses the exact cancellation of the back action noise in the two-cell setup. Following the splitting in Eq. (4.9) we can include the effect of a detection of the mode \hat{x}_c as specified in Eq. (4.10). With $\pi = \text{Diag}(1, 0, 0)$ we get $\pi\gamma_b\pi = \text{Diag}(1+\kappa^2, 0, 0)$. Rotating to the sum-difference basis we easily find the familiar result:

$$\gamma_a^{sd} = Rsd^{-1}\gamma_a Rsd = \begin{pmatrix} \frac{1}{1+\kappa^2} & 0 \\ 0 & 1+\kappa^2 \end{pmatrix}, \quad (4.19)$$

where $Rsd = \{\{1, 1\}, \{-1, 1\}\}/\sqrt{2}$. We see that during this process $\hat{P}_{ac} = \frac{\hat{p}_{a1} + \hat{p}_{a2}}{\sqrt{2}}$ gets squeezed and $\hat{X}_{as} = \frac{\hat{p}_{a1} - \hat{p}_{a2}}{\sqrt{2}}$ anti-squeezed. (Note, however, that these are not conjugate variables.)

At this point we introduce decoherence caused by light absorption and spontaneous emission. This is done as a single step after the interaction with each cell and is thus very coarse grained requiring $\eta_T \ll 1$:

$$\gamma_{out} = \bar{D}_2 S_2 [\bar{D}_1 S_1 \gamma_{in} S_1^T \bar{D}_1 + D_1 \gamma_{noise}] S_2^T \bar{D}_2 + D_2 \gamma_{noise}, \quad (4.20)$$

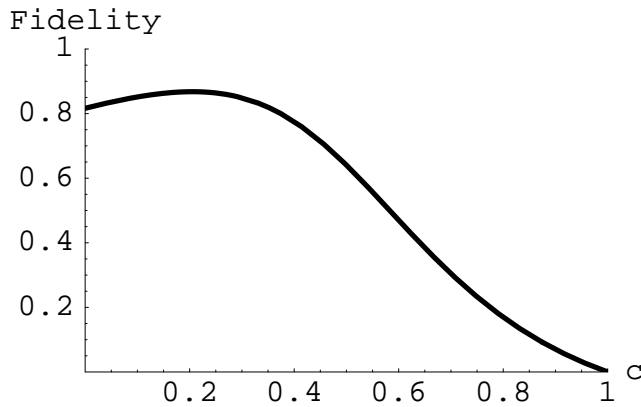


Figure 4.3: Squeezing vs single cell light loss. Solid: full solution to Eq. (4.20). Dashed: QND solution (Eq. (4.22)). Dotted: Eq. (4.21). $\alpha = 30$ and $\eta = 0.05$ for all.

where $D_1 = \text{diag}(\eta_T, 0, \epsilon, \epsilon, \epsilon)$, $D_2 = \text{diag}(0, \eta_T(1 - \epsilon), \epsilon, \epsilon, \epsilon)$, and $\gamma_{\text{noise}} = \text{diag}(2, 2, 1, 1, 1)$, where the factor $(1 - \epsilon)$ in the atomic depumping of the second cell arises because of the light loss in the first interaction. Similarly the interaction strength for the second interaction is modified to $\kappa \rightarrow \sqrt{1 - \epsilon}\kappa$. Performing the matrix multiplication is simple but cumbersome. As in the noise free calculation we find $\pi\gamma_b\pi = \text{Diag}(*, 0, 0)$, where this time the one non-zero entry is a complicated expression of η_T , ϵ , and κ^2 . The unapproximated covariance matrix arising from inserting the full Moore-Penrose expression into Eq. (4.10) has been calculated but it is quite lengthy so instead we derive fairly simple analytical expressions to first order in the noise parameters $\mathbf{n} = (\eta_T, \epsilon)$ and compare it to the full solution numerically. For this purpose we only keep noise terms up to second order in \mathbf{n} in the Moore-Penrose inverse. Next we calculate the atomic covariance matrix in the sum-difference basis and throw away all terms higher than first order in \mathbf{n} . For the squeezed quadrature we obtain:

$$\gamma_{a,sq}^{sd} = \frac{1 + \eta_T + \kappa^2(2\eta_T + \epsilon - 17\epsilon\eta_T) + \kappa^4\frac{\epsilon}{12} + \kappa^6\frac{\epsilon^2}{192}}{1 + \kappa^2(1 - 2\epsilon) + \kappa^4\frac{\epsilon}{12}}. \quad (4.21)$$

Note that the term $17\epsilon\eta_T$ was kept because of the high value of the numerical coefficient.

It would be interesting to compare the solutions in this section with the results obtained using the simple QND interaction, where the two atomic ensembles were considered as a single system. Rewriting the squeezed part of Eq. (4.13) as:

$$\gamma_{a,sq} = \frac{1 + \eta_T + 2\eta_T(1 - 2\epsilon)\kappa^2}{1 + (1 - 2\epsilon)\kappa^2}, \quad (4.22)$$

the similarity with Eq. (4.21) is obvious and for $\epsilon = 0$ they are identical. As can be seen, however, if $\epsilon \neq 0$ they do not even agree in the limit of weak interactions,

where the terms proportional to κ^4 and κ^6 can be neglected. This difference can be attributed to the asymmetric coupling of light to the two ensembles, which arises to do $\epsilon \neq 0$. To illustrate this, equations (4.21) and (4.22) are compared to the full solution of Eq. (4.20) in Fig. 4.3 for different values of ϵ . As can be seen, the simple QND expression somewhat overestimates the degree of squeezing even for low values of ϵ . Thus, it should be used with caution if more than rough estimates are required.

4.4 Solving the Dynamics Continuously in Time

So far, all expressions including the effects of dissipation have been derived assuming the change in the size of the mean spin, J_x , to be negligible, since otherwise as discussed in Sec. 4.1 the factor ξ in the γ_{noise} of Eq. (4.11) along with the interaction strength κ should be considered time dependent. The range of validity can be extended beyond $\eta T \ll 1$ by splitting the incoming pulse into many segments and treating the interaction with the atoms sequentially. For each segment the inclusion of noise is calculated with $\xi(t) = 2e^{\eta t}$ and the decreased interaction strength caused by the decay of the mean spin is modeled by $\kappa^2(t) = \kappa^2(0)e^{-\eta t}$, where t is the time of arrival of the particular light segment. In this way $\gamma(t + \tau)$ can be derived based on $\gamma(t)$. In the continuous limit ($\tau \rightarrow 0$) a differential equation for the covariance matrix can be obtained, which when solved describes the dynamics continuously in time. A large part of the remaining results were derived in [86]. Similar techniques have been applied to the case of squeezed light [87] and magnetometry [88, 89].

In this section, we will introduce this method by applying it to the case of two atomic ensembles with an arbitrary rotation frequency and no decoherence in order to investigate how the transition from the static regime to the highly rotated one occurs. Next decoherence will be added to this, and in the end the method will be applied to the QND and rotated single cell interactions used in Sec. 4.2 and 4.3. For these however one should remember that they are both based on the assumption that the atoms rotate many times during the pulse so the strict continuous limit does not make physical sense in these cases.

4.4.1 Investigating the Role of the Rotation Frequency

So far the results for the entanglement have been derived for a strongly rotated system in the sense that we assume that the atoms rotate many times during a pulse corresponding to $T \gg 1/\Omega_L$. It would be mildly interesting to investigate how the entanglement evolves along the transition from a static regime without rotations to the strongly rotated regime. To do this we define the following set of

canonical observables:

$$\mathbf{y} = \begin{pmatrix} \hat{x}_{a1} \\ \hat{p}_{a1} \\ \hat{x}_{a2} \\ \hat{p}_{a2} \\ \hat{x}_L \\ \hat{p}_L \end{pmatrix} = \begin{pmatrix} J_{y1}/\sqrt{J_x} \\ J_{z1}/\sqrt{J_x} \\ -J_{y2}/\sqrt{J_x} \\ J_{z2}/\sqrt{J_x} \\ S_y/\sqrt{S_x} \\ S_z/\sqrt{S_x} \end{pmatrix}, \quad (4.23)$$

where the Stokes operators are integrated over some time τ . The interacting occurs according to $H_{\tau,i} \propto \kappa p_i p_L$, where $i = 1, 2$ refers to the atomic sample.

To model the continuous interaction between the atoms and the incoming cw-light field we split the light field into independent slices of duration τ . The interaction between the samples and each light segment are then treated one after the other. The continuous interaction and detection of the resulting field then corresponds to taking the $\tau \rightarrow 0$ limit.

The matrices describing the interaction between the light segment and each of the atomic samples from t to $t + \tau$ are given by:

$$S_1 = \begin{pmatrix} 1 & 0 & 0 & 0 & 0 & \kappa_\tau \\ 0 & 1 & 0 & 0 & 0 & 0 \\ 0 & 0 & 1 & 0 & 0 & 0 \\ 0 & 0 & 0 & 1 & 0 & 0 \\ 0 & \kappa_\tau & 0 & 0 & 1 & 0 \\ 0 & 0 & 0 & 0 & 0 & 1 \end{pmatrix} \quad S_2 = \begin{pmatrix} 1 & 0 & 0 & 0 & 0 & 0 \\ 0 & 1 & 0 & 0 & 0 & 0 \\ 0 & 0 & 1 & 0 & 0 & \kappa_\tau \\ 0 & 0 & 0 & 1 & 0 & 0 \\ 0 & 0 & 0 & \kappa_\tau & 1 & 0 \\ 0 & 0 & 0 & 0 & 0 & 1 \end{pmatrix}$$

Taking into account also the Larmor precession during this time and the detection, the correlation matrix will evolve according to:

$$\gamma(t + \tau) = M[R \cdot S_2 \cdot S_1 \cdot \gamma(t) \cdot S_1^T \cdot S_2^T \cdot R^T] \quad (4.24)$$

where R denotes a block diagonal matrix rotating the atomic variables of the samples an angle $\pm\omega\tau$ and leaving the light variables unchanged. $M[\dots]$ denotes the effect of the homodyne detection calculated according to Eq. (4.10) with $\pi = \text{diag}(1, 0)$ corresponding to a perfect homodyne measurement of \hat{x}_L .

When Eq. (4.24) is evaluated for short time segments τ , the change in γ is quadratic in κ_τ . κ_τ^2 is proportional to the photon number in the beam segment, i.e. proportional to τ and rewriting $\kappa_\tau^2 = \tilde{\kappa}^2 \tau$, the differential limit for the atomic correlation matrix can be formed:

$$\frac{d\gamma_a}{dt} = \mathbf{r}\gamma_a + \gamma_a \mathbf{r}^T + \tilde{\kappa}^2 (\tilde{A} - \gamma_a \tilde{B} \gamma_a^T) \quad (4.25)$$

where:

$$\tilde{A} = \begin{pmatrix} 1 & 0 & 1 & 0 \\ 0 & 0 & 0 & 0 \\ 1 & 0 & 1 & 0 \\ 0 & 0 & 0 & 0 \end{pmatrix}, \quad \tilde{B} = \begin{pmatrix} 0 & 0 & 0 & 0 \\ 0 & 1 & 0 & 1 \\ 0 & 0 & 0 & 0 \\ 0 & 1 & 0 & 1 \end{pmatrix}, \quad \mathbf{r} = \omega \begin{pmatrix} 0 & 1 & 0 & 0 \\ -1 & 0 & 0 & 0 \\ 0 & 0 & 0 & -1 \\ 0 & 0 & 1 & 0 \end{pmatrix} \quad (4.26)$$

We note that the evolution of the atomic covariance matrix caused by the measurements given by Eq. (4.10) is deterministic (despite the random outcomes of the detection) and non-linear.

The nonlinear differential Eq. (4.25) can be solved using the Ricatti method as e.g. mentioned in the appendix of [90]. The generic Ricatti equation is:

$$\frac{d\mathbf{V}}{dt} = \mathbf{C} - \mathbf{D}\mathbf{V}(t) - \mathbf{V}(t)\mathbf{A} - \mathbf{V}(t)\mathbf{B}\mathbf{V}(t) \quad (4.27)$$

Using the decomposition $\mathbf{V}(t) = \mathbf{W}(t)\mathbf{U}^{-1}(t)$ it can be shown that the nonlinear differential equation can be replaced by the linear equation:

$$\begin{pmatrix} \frac{d\mathbf{W}(t)}{dt} \\ \frac{d\mathbf{U}(t)}{dt} \end{pmatrix} = \begin{pmatrix} -\mathbf{D} & \mathbf{C} \\ \mathbf{B} & \mathbf{A} \end{pmatrix} \begin{pmatrix} \mathbf{W}(t) \\ \mathbf{U}(t) \end{pmatrix} \quad (4.28)$$

Matching our equation to the generic Ricatti equation and observing that $\gamma_a^T = \gamma_a$ we obtain the linear set of equations

$$\begin{pmatrix} \frac{d\mathbf{W}(t)}{dt} \\ \frac{d\mathbf{U}(t)}{dt} \end{pmatrix} = \begin{pmatrix} \mathbf{r} & \tilde{\kappa}^2 \tilde{\mathbf{A}} \\ \tilde{\kappa}^2 \tilde{\mathbf{B}} & \mathbf{r} \end{pmatrix} \begin{pmatrix} \mathbf{W}(t) \\ \mathbf{U}(t) \end{pmatrix} \quad (4.29)$$

where we have also used that $\mathbf{r} = -\mathbf{r}^T$.

Choosing the \mathbf{W} and \mathbf{U} matrices to start out as 4x4 identity matrices this system of coupled linear differential equations can be solved. Not surprisingly, the result can be simplified greatly by applying a time dependent rotation of $\mp\omega t/2$ to the atomic variables of sample one and two respectively, thus implementing a transformation to a rotating frame. A further simplification can be made by noting that the measured quadratures are really the sum of \hat{p}_a 's (\hat{P}_{ac}) and the difference of \hat{x}_a 'es (\hat{P}_{as}). The transformation to the sum/difference basis is done by $\gamma^{sd} = Rsd^{-1}\gamma Rsd$, where

$$Rsd = \frac{1}{\sqrt{2}} \begin{pmatrix} 1 & 1 & 0 & 0 \\ 0 & 0 & 1 & 1 \\ 1 & -1 & 0 & 0 \\ 0 & 0 & 1 & -1 \end{pmatrix} \quad (4.30)$$

is simply a collection of the new basis vectors (\hat{P}_{as} , \hat{X}_{ac} , \hat{P}_{ac} , \hat{X}_{as}) in terms of the old ones. After the transformation we get:

$$\gamma_a^{sd} = \begin{pmatrix} a_+ & 0 & 0 & 0 \\ 0 & \frac{1}{a_-} & 0 & 0 \\ 0 & 0 & \frac{1}{a_+} & 0 \\ 0 & 0 & 0 & a_- \end{pmatrix} \quad (4.31)$$

where $a_{\pm} = 1 + \tilde{\kappa}^2 t \pm \frac{\tilde{\kappa}^2}{\omega} \sin(\omega t)$. Defining the total accumulated interaction at time t as $\kappa_t^2 \equiv \tilde{\kappa}^2 t$ and the total rotated angle $\theta \equiv \omega t$ we get the main result of

this section:

$$a_{\pm} = 1 + \kappa_t^2 \pm \frac{\kappa_t^2}{\theta} \sin(\theta) \rightarrow \begin{cases} 1 + \kappa_t^2 \pm \kappa_t^2 & \theta \rightarrow 0 \\ 1 + \kappa_t^2 & \theta \rightarrow \infty \end{cases} \quad (4.32)$$

We see that as $\theta \rightarrow 0$ we get $1 + 2\kappa_t^2$ and 1 , i.e. the characteristic squeezing and anti-squeezing of the measured and their conjugate variables respectively - and no change in the unobserved ones. For $\theta \rightarrow \infty$, i.e. after many rotations we squeeze the two quadratures symmetrically and anti-squeeze their conjugate variables by the factor $1 + \kappa_t^2$. Note that the reduced squeezing by a factor of two in the rotated case comes from the fact that the measurement strength is harmonically varied between the two quadratures (\hat{P}_{ac}) and (\hat{P}_{as}) which amounts to half the total interaction strength being spent measuring each quadrature. The result without rotations matches a very early prediction in [36] and the strongly rotated result has been derived a number of times by now.

As an quantification alternative to the degree of violation of the entanglement criterion (3.4) we calculate the Gaussian Entanglement of Formation(GEoF) of [91]. This measure agrees with the Von Neuman entropy for pure states and it can easily be calculated from the covariance matrix. It is given by:

$$GEoF(\Delta) = c_+(\Delta) \log_2[c_+(\Delta)] - c_-(\Delta) \log_2[c_-(\Delta)] \quad (4.33)$$

where $c_{\pm}(\Delta) = (\Delta^{-1/2} \pm \Delta^{1/2})^2/4$ and

$$\Delta^2 = \text{Var}(\hat{x}_{a1} - \hat{x}_{a2})\text{Var}(\hat{p}_{a1} + \hat{p}_{a2}) = \gamma_{a,22}^{sd} \gamma_{a,33}^{sd} . \quad (4.34)$$

Note that the small Δ approximation:

$$GEoF(\Delta) \approx \log_2\left(\frac{1}{\Delta}\right) + \frac{1}{\ln 2} - 2 \quad (4.35)$$

shows an error of 10^{-5} at $\Delta = 1/100$, 0.001 at $\Delta = 1/10$, and only 1% at $\Delta = 1/5$ so it is widely applicable. From equations (4.31) and (4.32) Δ^2 can be shown to be

$$\Delta^2 = \frac{1}{(1 + \kappa_t^2)^2 - \frac{\kappa_t^4}{\theta^2} \sin^2(\theta)} \quad (4.36)$$

which tells us that the entanglement will scale as $\log_2(\kappa_t^2) = 2 \log_2(\kappa_t)$ with rotation and with $\log_2(\kappa_t)$ without rotations. The factor of two is exactly what one should expect since rotations enable us to squeeze both quadratures compared to squeezing only one of them. This effect was also observed in [80].

In Fig. 4.4 we show the entanglement plotted as a function of κ_t and θ . As can be seen, the transition from the static to the rotated regime occurs before one full revolution is reached. That is, given a total interaction time, t , there is no real gain in choosing the frequency larger than $\omega_{\text{crit}} = 1/t$. This arises from the fact that we measure $\hat{P}_{ac} \cos(\theta) + \hat{P}_{as} \sin(\theta)$ and this operator commutes with the operators measured at all previous times (other values of θ). It is therefore

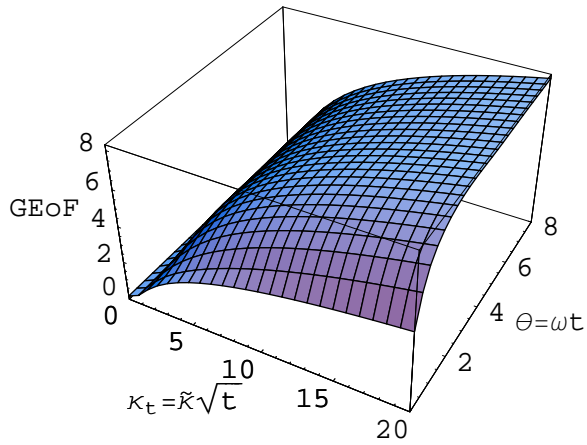


Figure 4.4: 3D plot of GEOF as a function of the accumulated interaction strength κ_t and the rotated angle θ . The plot clearly shows that the transition from the static to the rotated regime has occurred already before one full revolution of the atomic spins has taken place. In both the static and the rotated regions we clearly see the logarithmic behavior of the GEOF as a function of κ_t .

the accumulated measurement on each quadrature that counts and this will not benefit from many rotations compared to a single rotation at a slower rotation frequency. In our experiments $\nu_L \approx 320\text{kHz}$ and $T_{\text{probe}} \approx 1\text{ms}$ so the spins will rotate several hundreds of times in one pulse and the results are thus firmly obtained in the ω independent regime.

We also note that the level of entanglement in Fig. 4.4 is of the order of unity, so there is roughly the same amount of entanglement in the macroscopic samples as in a single spin singlet.

4.4.2 Arbitrary Rotation Frequency with Noise

We would now like to determine the effect of noise from spontaneous emission on the results of the preceding section. Again this is done as prescribed by Eq. (4.20) with $D_1 = \text{diag}(\eta_1, \eta_1, 0, 0, \epsilon, \epsilon)$, $\bar{D}_1 = \sqrt{1 - D_1}$ and $\gamma_{\text{noise},1} = \text{diag}(\xi, \xi, 0, 0, 1, 1)$ for the interaction with the first sample and similarly $D_2 = \text{diag}(0, 0, \eta_2, \eta_2, \epsilon, \epsilon)$, $\gamma_{\text{noise},2} = \text{diag}(0, 0, \xi, \xi, 1, 1)$ for the second. Because of the decay of the mean spin both the noise terms and the interaction strength become time-dependent - $\xi(t) = 2e^{\eta t}$ and $\tilde{\kappa}^2(t) = \tilde{\kappa}^2(0)e^{-\eta t}$ - which complicates the solution of the dynamics immensely.

The differential equation for the correlation matrix in the sum/difference basis with dissipation included is:

$$\frac{d\gamma_a^{sd}}{dt} = (\tilde{\mathbf{r}} - \eta/2\mathbf{I}_4)\gamma^{sd} + \gamma^{sd}(\tilde{\mathbf{r}} - \eta/2\mathbf{I}_4)^T + \tilde{A} - (1 - \epsilon)\tilde{\kappa}^2\gamma^{sd}\tilde{B}(\gamma^{sd})^T, \quad (4.37)$$

where

$$\tilde{A} = \begin{pmatrix} \tilde{\kappa}^2(1 + \sqrt{1 - \epsilon}) & 0 & 0 & 0 \\ 0 & \tilde{\kappa}^2(1 - \sqrt{1 - \epsilon}) & 0 & 0 \\ 0 & 0 & 0 & 0 \\ 0 & 0 & 0 & 0 \end{pmatrix} + \eta\xi(t)\mathbf{I}_4 \quad (4.38)$$

$$\tilde{B} = \begin{pmatrix} 0 & 0 & 0 & 0 \\ 0 & 0 & 0 & 0 \\ 0 & 0 & 1 + \sqrt{1 - \epsilon} - \epsilon/2 & -\epsilon/2 \\ 0 & 0 & -\epsilon/2 & 1 - \sqrt{1 - \epsilon} - \epsilon/2 \end{pmatrix}, \quad (4.39)$$

where terms $\epsilon\eta$ have been neglected compared to η and $\tilde{\mathbf{r}} = \omega \cdot [\text{anti} - \text{diag}(-1, -1, 1, 1)]$, starting from the lower left corner.

Without rotations the Ricatti Eq. (4.37) can be solved exactly. To lowest order in ϵ the two components involved in the measurement give:

$$\gamma_{11}^{sd} = \text{Var}(\hat{x}_{a1} + \hat{x}_{a2}) = e^{-\eta t} [e^{2\eta t} + 2\alpha\eta t] \quad (4.40)$$

$$\begin{aligned} \gamma_{33}^{sd} &= \text{Var}(\hat{p}_{a1} + \hat{p}_{a2}) \\ &= e^{\eta t} \frac{\delta + 1 + e^{-2\eta t\delta}(\delta - 1)}{\delta + 1 + \alpha(2 - 3\epsilon) + e^{-2\eta t\delta}(\delta - 1 - \alpha(2 - 3\epsilon))} \end{aligned} \quad (4.41)$$

where $\delta = \sqrt{1 + \alpha(4 - 3\epsilon)}$. The two remaining components increase exponentially, $\gamma_{22}^{sd} = e^{\eta t} + \frac{\epsilon}{2}\tilde{\kappa}^2 t e^{-\eta t}$ and $\gamma_{44}^{sd} = e^{\eta t}$. For γ_{33}^{sd} the further approximation $\alpha\epsilon e^{\eta t\delta} \ll 16\delta$ was made. In Fig. 4.5 the absolute difference between Eq. (4.41) and the full result is plotted as a function of ηt for $\alpha = 100$ and for $\alpha = 1000$ ($\epsilon = (2.5/700)^2\alpha$ for both). As can be seen, the error starts to increase exponentially at a critical value. Since the covariance matrix is calculated by sequentially treating the interaction with very short pulse segments the dynamics includes correctly the effect of the decaying mean spin and the full result is valid beyond the $\eta t \ll 1$ approximation which has so far been limiting.

The same analysis can be performed for decoherence towards the CSS. For this κ is independent of time and $\xi = 1$. Letting for simplicity $\epsilon = 0$ we get the squeezed quadrature:

$$\gamma_{33}^{sd} = \frac{\delta + 1 + e^{-\eta t\delta}(\delta - 1)}{\delta + 1 + \alpha + e^{-\eta t\delta}(\delta - 1 - \alpha)}, \quad (4.42)$$

where we note the similarity to Eq. (4.41) except for the factor $e^{\eta t}$.

4.4.3 The Strongly Rotated Regime

In Sec. 4.2 the entanglement for two strongly rotated atomic samples was calculated based on the QND interaction (2.34) and noise decoherence was included through a single step for the entire pulse. Thus, the solution was only valid in

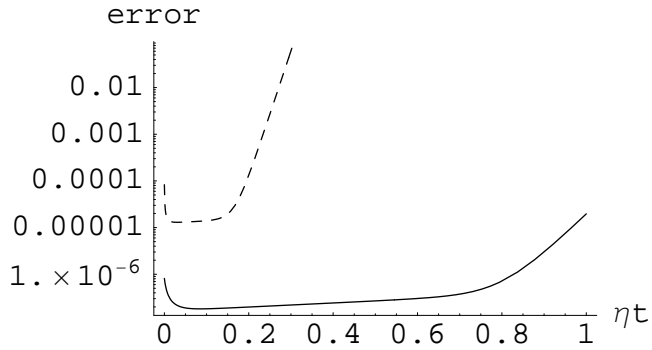


Figure 4.5: The absolute error between γ_{33}^{sd} from the full solution to the differential equation (4.37) without rotations and the approximation, Eq. (4.41) vs. η . Dashed: $\alpha = 1000$. Solid: $\alpha = 100$. $\epsilon = 1.3 \cdot 10^{-5}\alpha$.

the $\eta t \ll 1$ regime. Following the methods of the previous sections a differential equation for the time evolution can instead be derived:

$$\frac{d\gamma_a}{dt} = -\eta\gamma + \begin{pmatrix} \kappa^2 + \eta\xi & 0 \\ 0 & \eta\xi \end{pmatrix} - \kappa^2(1-2\epsilon)\gamma_a \begin{pmatrix} 0 & 0 \\ 0 & 1 \end{pmatrix} \gamma_a \quad (4.43)$$

When this is inserted into the Ricatti equation with exponentially decreasing κ^2 and $\xi(t) = 2e^{\eta t}$ we can derive the unapproximated solution:

$$\gamma_a = \begin{pmatrix} e^{\eta t} + \kappa^2 t e^{-\eta t} & 0 \\ 0 & e^{\eta t} \frac{\delta' + 1 + e^{-2\delta' \eta t} (\delta' - 1)}{\delta' + 1 + \alpha(1-2\epsilon) + e^{-2\delta' \eta t} (\delta' - 1 - \alpha(1-2\epsilon))} \end{pmatrix} \quad (4.44)$$

where $\delta' = \sqrt{1 + 2\alpha(1-2\epsilon)}$. Letting $\epsilon \rightarrow \epsilon/2$ this expression is identical to the one derived in [87] for spin squeezing in a single sample without a bias magnetic field. In the limit of small ηt the anti-squeezed component reduces to the one in Eq. (4.13), whereas the squeezed component reduces to:

$$\gamma_{a,sq} \approx \frac{1 - \eta t \delta' + 2\eta t}{1 + (1-2\epsilon)\kappa^2 - \eta t \delta' + \eta t}. \quad (4.45)$$

Here the additional constraint $2\eta t \delta' \ll 1$ was also applied. We see that this resembles but is not identical to the single shot result in Eq. (4.13). In Fig. 4.6 the full solution and the first and third order expansions in ηt are compared to the single shot result for $\alpha = 20$. As expected the first order expansion shows large deviations after $\eta \sim 0.01$ corresponding to the point at which the constraint $2\eta t \delta' \ll 1$ fails. The second order expansion lies close to the single shot expression so we have to go to third order to get an improved results. This shows that the single shot expression is quite useful, however, as can be seen it should not be trusted beyond $\eta \sim 0.05$.

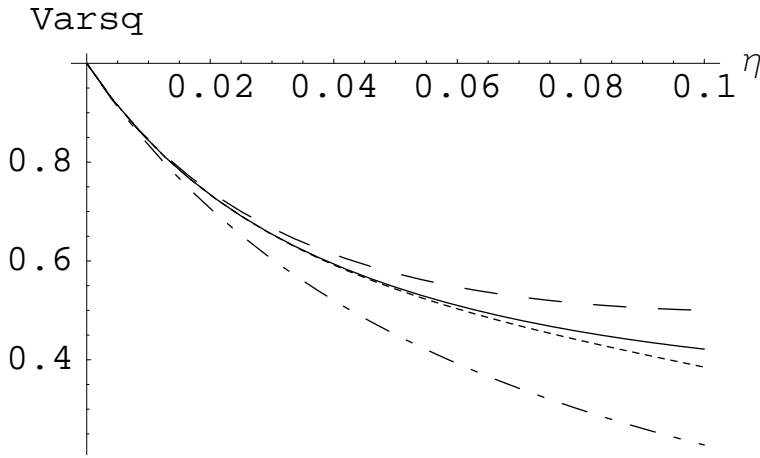


Figure 4.6: Comparing the squeezing predicted by the full solution (solid) and first (dash-dotted) and third order (dashed) approximations hereof with the prediction of the simple single pulse theory (dashed). $\alpha = 20$, $\epsilon = 0$

As in the previous section we also solve Eq. (4.43) for a T_2 process. In this case we get the squeezed component:

$$\gamma_{a,22} = \frac{\tilde{\delta} + 1 + e^{-\tilde{\delta}\eta t}(\tilde{\delta} - 1)}{\tilde{\delta} + 1 + \alpha(1 - 2\epsilon) + e^{-\tilde{\delta}\eta t}(\tilde{\delta} - 1 - \alpha(1 - 2\epsilon))} \quad (4.46)$$

where this time $\tilde{\delta} = \sqrt{1 + 4\alpha(1 - 2\epsilon)}$.

As discussed in Sec. 4.3 loss of light in the first sample, represented by ϵ creates asymmetries between the two samples, which cannot be incorporated into the QND formalism. We therefore formulate the differential equation based on the single cell interactions which in Sec. 4.3 were used for the entire pulse as a whole. In the sum/difference basis, where $y_1 = \hat{X}_{as}$ and $y_2 = \hat{P}_{ac}$, we obtain a differential equation very similar to Eq. (4.43):

$$\frac{d\gamma_a}{dt} = -\eta\gamma_a + \frac{\epsilon\kappa^2}{4} \begin{pmatrix} 1 & 1 \\ 1 & 1 \end{pmatrix} + \begin{pmatrix} \kappa^2(1 - \epsilon) + \eta\xi & 0 \\ 0 & \eta\xi \end{pmatrix} - \kappa^2(1 - \epsilon)^2\gamma_a \begin{pmatrix} 0 & 0 \\ 0 & 1 \end{pmatrix} \gamma_a. \quad (4.47)$$

The primary difference is the presence of the matrix proportional to $\epsilon\kappa^2/4$, which introduces off-diagonal elements because of the non-symmetric coupling between the two samples. This matrix makes the system extremely difficult to solve analytically since e.g. the squeezing part now contains a sum of an $e^{\eta t}$ term and an $e^{-\eta t}$ term. Thus, the coefficients in the differential equation can no longer be made time independent via a suitable transformation of the variables. Instead, in Fig. 4.7 the maximal deviation of the numerical solution of Eq. (4.47) compared to the solution of the differential equation based on the QND interaction, Eq.

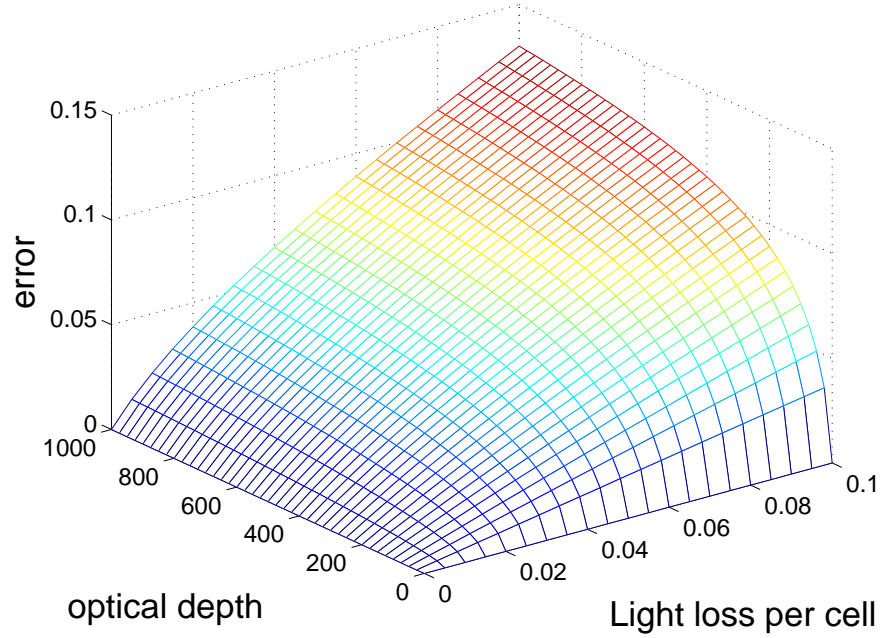


Figure 4.7: Error when using the two-cell QND interaction instead of the single cell interactions maximized of η ranging from zero to one.

(4.44) over the range $0 \leq \eta t \leq 1$ is plotted as a function of α and ϵ . As in the single shot case (see e.g. Fig. 4.3) the QND solution systematically overestimates the degree of squeezing. The figure can be interpreted in two ways. If the dominant source of light loss is absorption $\epsilon = (\Gamma/\Delta)^2\alpha$ and the figure shows what happens as the detuning is changed. Alternatively, if reflection losses dominate the figure shows how much worse it is to have half of the losses between the cells compared to having all of the reflection losses after the cell. As can be seen the reduction in the degree of squeezing can be significant even for moderate losses between the samples. Note also that it is the absolute error being plotted. The relative error is much more dramatic. For instance, at $\alpha = 300$ and $\epsilon = 0.1$ the QND expression predicts a minimal variance of 0.10, whereas the expression obtained from the single cell interactions predicts 0.20.

CHAPTER 5

Experimental Methods

In this chapter we describe the typical setup for our experiments. It is centered around two glass cells filled with cesium vapor at room temperature placed in two separate magnetically insulating shields with a bias magnetic field inside. Atoms in the cells are optically pumped, and we discuss technical details concerning the pumping lasers and the probe laser used for the interaction with the atoms. Applying an RF magnetic field with the frequency equal to the Larmor frequency of the bias field, the spin state can be manipulated. We discuss how this can be used to investigate the degree of optical pumping and the different sources of decoherence. Finally we describe the experimental determination of the projection noise level.

5.1 Atomic System

In our experiments the atomic system consists of about $\sim 10^{12}$ ^{133}Cs atoms at approximately room temperature. ^{133}Cs has a nuclear spin of $I = 7/2$ which together with the single unpaired electron gives a hyperfine split ground state with total angular momentum $F = 3$ and $F = 4$. The relevant level scheme can be seen in Fig. 5.1. This element is interesting partly because the ground state transition is used to define the unit of time and partly because of the availability of lasers at the appropriate wavelengths.

During the past years we have used several different designs for the glass cells containing the atomic vapor. In Fig. 5.2 the type used for the generation of unconditional entanglement (Sec. 6.2) and the quantum mapping experiment

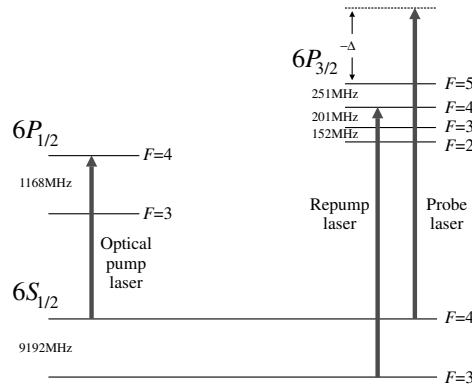


Figure 5.1: The relevant level structure of ^{133}Cs along with the frequencies of the three lasers used in our experiments.

(chapter 7) is shown on the left and the new design used for the teleportation experiment (chapter 8) on the right. The former is non-cubic with a total inside volume of $18 \pm 1 \text{ cm}^3$ and has an effective cross sectional area of $A_{\text{eff}} = 6.0 \text{ cm}^2$. The windows are not optically flat, which is why a new generation had to be manufactured for the teleportation experiment, where an interferometer was required. The new cells are cubic with an inner volume of $(2.2 \text{ cm})^3 \approx 10.6 \text{ cm}^3$. Both generations have a "finger" attached. Inside this, there is a reservoir of solid cesium, which acts as a source for the cesium vapor in the main part of the cell. The two sections are divided by a small opening with a typical size smaller than a millimeter. The temperature of the finger determines the vapor pressure in the cell and thereby the size of the macroscopic spin J_x (proportional to the number of atoms) with which we interact. To change the vapor pressure by about a factor of three merely requires a temperature change from e.g. 20°C to 30°C . The temperature is controlled via a well distributed airflow. This method is chosen because metal heating/cooling elements cause severe problems since the atoms are disturbed by random magnetic fields created by thermal currents even if aluminum is used (see [1]).

In our experiments, the quantum signal is encoded in the magnetic sublevels of a ground state hyperfine level. Thus, the atomic sample has to be highly shielded from the environment, since even small magnetic gradients across the cell volume will cause the individual atoms to dephase and thereby the quantum signal to be lost. Different measures are taken to protect the quantum state of the atomic system (see Fig. 5.2). First, the outer shielding is achieved by placing the atomic sample inside cylinders made of magnetically shielding material (dubbed μ -metal because of its high magnetic susceptibility). In fact, the shielding mount consist of multiple consecutive layers of μ -metal and iron in order to optimize the shielding. In this way external field can be damped by approximately a factor 100.

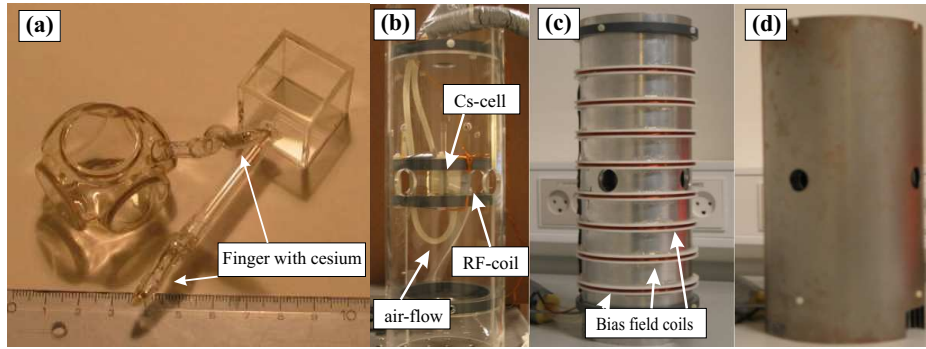


Figure 5.2: a) Two generations of the glass cells containing the cesium vapor. To each, a stem is attached containing a reservoir of condensed cesium. b) The inner cylinder containing the vapor cell and the RF-coils used for state manipulation (see Sec. 5.3). c) The aluminum cylinder onto which bias field coils and magnetic field gradient compensation coils are wound. d) The outer shielding consisting of μ -metal.

Just inside the magnetic shielding we have an aluminum cylinder upon which multiple Helmholtz and anti-Helmholtz coils are attached. In this way a bias magnetic field is created along the desired direction of the macroscopic spin (in our case the x-direction) and magnetic field gradients are actively canceled.

The last layer of protection consists of a paraffin coating on the inside of the vapor cells. This acts as a buffer and strongly suppresses depolarization as well as dephasing when atoms hit the walls. Despite the fact that the atoms move at a velocity $v_{rms,3D} = \sqrt{3k_B T / m_{Cs}} \approx 235 \text{ m/s}$ and thus collide with the walls once every $100 \mu\text{s}$, we have measured mean spin life times $\sim 300 \text{ ms}$, spin coherence times $\sim 40 \text{ ms}$, and spin polarizations exceeding 99% by the methods described in Sec. 5.3.1. Further information on paraffin coated cells can be found in [92, 93, 94].

5.2 Lasers and Light Characterization

5.2.1 Pump Lasers

In the experiments we wish to optically pump all atoms into the $m_F = 4$ magnetic sublevel of the $F = 4$ $6S_{1/2}$ ground state. We do this primarily by sending a σ^+ polarized laser resonant with the 894 nm $6S_{1/2}$ $F = 4 \rightarrow 6P_{1/2}$ $F' = 4$ transition (D1-line) through the atoms. We call this laser the *optical pump laser* (see Fig. 5.1). With the chosen polarization it will drive $\Delta m = +1$ transitions. Subsequently the atoms will spontaneously decay to the ground state through $\Delta m = -1, 0, +1$ transitions. On average this will pump the atoms in the ground state towards the extreme $m_F = 4$ state, which is a dark state since there is no $F = 5$ hyperfine level in the $6P_{1/2}$ manifold. During the pumping process,

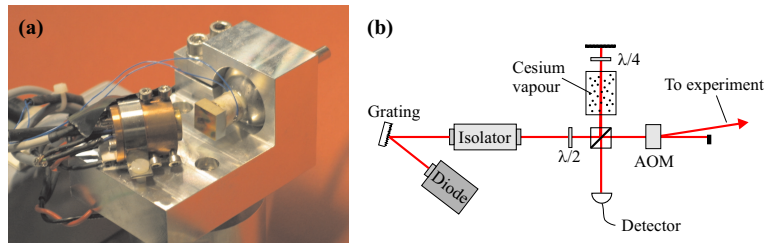


Figure 5.3: a) The home built laser setup for the pumping diodes. b) A schematic showing how a part of the pump beams is split off for the saturated absorption lock. The remaining light is passed through an AOM and the first order spot is used for the experiment. Thus controlling the AOM, the pump beams can be turned on and off.

however, some of the atoms decay into the $F = 3$ ground state. Therefore we introduce the *repumping laser*, which is also σ^+ polarized and resonant with the 852nm $6S_{1/2} F = 3 \rightarrow 6P_{3/2} F' = 4$ transition (D2-line)(see Fig. 5.1). In this way atoms are pumped back into $F=4$ and very high degrees of optical pumping into the desired state can be achieved. In addition, controlling the power in the repumping laser we can to some extent control the number of atoms in the $F = 4$ ground state and hence the number of atoms participating in the interaction with the probe light. This is a valuable tool when investigating the scaling of our quantum signals with the number of atoms.

As shown in Fig. 5.3 both pumping lasers are home built based on diffraction grating stabilization in the Littrow configuration such that the first order diffraction is reflected directly back into the laser diode. The diffraction grating has 1800 lines per millimeter. The bare laser diode is anti-reflex coated and can be purchased from Eagleyard Photonics GmbH in Germany. The output power of each laser is in the vicinity of 30mW.

We wish to lock both lasers to an atomic resonance. At room temperature, however, the atomic motion causes significant Doppler broadening, which means that each line is transformed into a Gaussian profile with a width (see e.g. [66]):

$$\delta\nu_{D,HWHM} = \frac{\nu_0}{c} \left(\frac{2k_B T}{m_{Cs} \ln 2} \right)^{1/2} \approx 188\text{MHz} , \quad (5.1)$$

where $c/\nu_0 = \lambda = 852\text{nm}$ and we let $T = 295\text{K}$. This is of course much too wide for a useful lock. The problem can be overcome via the method of saturated absorption spectroscopy [95, 96, 97]. As sketched in Fig. 5.3 a small part of the beam is split off and sent through a cesium vapor cell. After the passage, the beam is attenuated and reflected off a mirror and passes through the cesium sample again. The transmitted power is then detected. If the laser frequency is within the Doppler profile certain velocity classes of the atoms will be resonant with the light. In the second passage the Doppler shift has reversed sign and hence the light will be resonant with the classes of atoms moving with the opposite velocity. This means that the weak beam will be absorbed. If however, the light

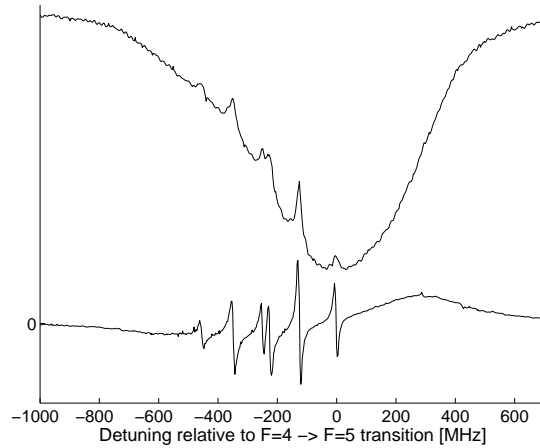


Figure 5.4: Cesium saturated absorption spectroscopy. The detuning is defined relative to the $F = 4 \rightarrow F' = 5$ transition blue detuning being positive. Below the error signal generated via the Pound Drever Hall technique. All six expected peaks are visible.

is tuned exactly to an atomic resonance the same velocity class of atoms (zero velocity) will be resonant for both passages. The result is a strong reduction in the absorption of the weak beam caused by the atomic saturation induced by the strong beam (see Fig. 5.4). In addition, peaks (called cross-over resonances) will appear exactly halfway between two resonances because atoms with a certain velocity will be resonant with one transition for the first passage and with the other for the second. In total, for e.g. the 852nm D2 line there will be six resonances within the Doppler profile both starting from the $F = 3$ and the $F = 4$ ground states. In this way structure with a resolution approaching the natural line width $\Gamma_{\text{FWHM}} = 5.22\text{MHz}$ can be observed.

The saturated absorption signal is not, however useful as an error signal for a laser lock since we wish to lock to the center of the peak and an excursion to either side produces the same changes in the signal. Using the Pound-Drever-Hall technique [98, 99] a signal that inverts sign when crossing the resonance can be derived. In this technique the laser frequency ω_c is modulated weakly with some frequency ω to create sidebands at frequencies $\omega_c \pm \omega$ around the carrier frequency ω_c . When the light passes through an absorbing atomic medium and is subsequently detected the photo current will contain a component oscillating with e.g. $\sin(\omega t)$ proportional to the difference in the absorption of the two sidebands and a component oscillating with $\cos(\omega t)$ proportional to the difference between the phase shift of the carrier and average shift of the two sidebands. If ω is small compared to the atomic structure observed the former corresponds to the derivative of the absorption whereas the latter is the second derivative of the dispersion. If the photo current is mixed with a $\sin(\omega t + \phi)$ signal either one

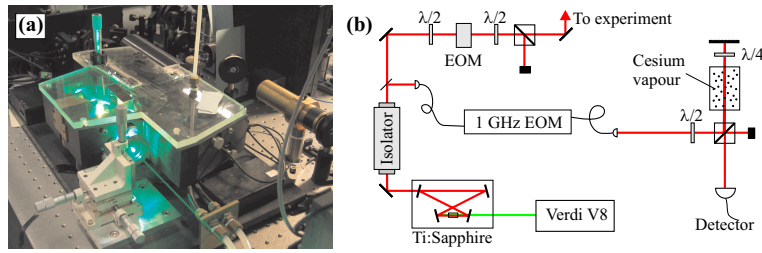


Figure 5.5: a) A picture of the Ti:Sapphire laser used as a quantum probe the the entanglement and quantum mapping experiments. b) A schematic showing how a small fraction of the beam is split off and sent through a fiber coupled EOM. This creates sidebands one of which is then locked to the atomic resonance. Thus, the part of the beam which did not pass through the EOM is detuned compared to the atomic resonance. This light is then shaped temporally by another EOM and is subsequently sent to the main experiment.

can be picked out with an appropriate choice of the phase ϕ . In this way we can generate signals with a sharp zero crossing at the resonance that can be used as error signals in a feedback loop to the laser. Examples of such error signals can be seen in figures 5.4 and 5.6.

The remainder of the pump light is sent through an acousto-optic modulator (AOM). Here a crystal acts as an effective diffraction grating for light via a spatial modulation of the refractive index created by a piezoelectric transducer oscillating at a frequency of 125MHz. A diffracted beam emerges at angles given by $\sin(\theta) = m\lambda/(2\Lambda)$, where Λ is the wavelength of the sound wave and m is the diffraction order. Using e.g. the first order spot, we see that the light beam can be turned on and off by controlling the RF-power to the AOM. Alternatively, the process can be thought of as absorption of a phonon, which shifts the frequency of the light in e.g. the first order beam by 125MHz.

5.2.2 Probe Laser

For the quantum mechanical investigation of the interaction between light and atoms we use a *probing laser*, which is detuned to the blue side (high ν) of the 852nm $6S_{1/2} F = 4 \rightarrow 6P_{3/2} F' = 5$ transition (see Fig. 5.1). In order to minimize absorptive effects the detuning has to be much larger than the Doppler width, however, it also has to be much smaller than the hyperfine splitting of 9GHz in order to solely address atoms in the $F = 4$ hyperfine multiplet. We typically have detunings around 1GHz.

Experiments on unconditional entanglement (Sec. 6.2) and quantum mapping (Sec. 7) were performed using the output of a commercial Microlase MBR-110 Ti:Sapphire laser, which is pumped by the 532 nm output of a solid-state diode pumped, frequency doubled Verdi V-8 laser. The Ti:Sapphire crystal is mounted in a bow tie ring cavity which is machined out of a monolithic block to reduce

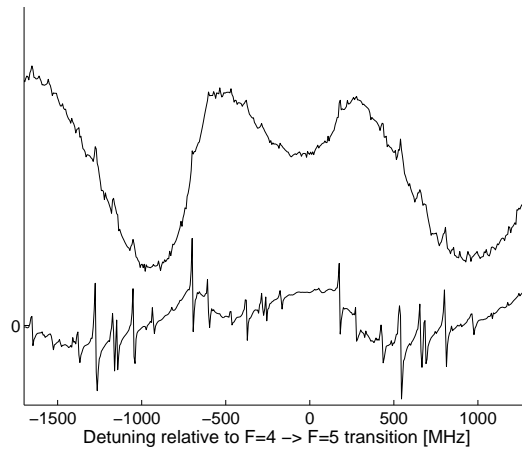


Figure 5.6: Saturated absorption signal of the part of the probe laser modulated to create sidebands (here at 950MHz). To the left, the blue sideband is resonant with the cesium atoms giving a red detuning and vice versa to the right.

the laser line width. It is further reduced down to ca. 100kHz via a lock to an ultra stable external reference cavity. The output of the Ti:Sapphire laser at 852nm is typically about 1W. As illustrated in Fig. 5.5 a fraction of the light is split off and sent through a fiber coupled electro-optic modulator (EOM), which is modulated at a frequency between 700 – 1200MHz. This creates sidebands at this frequency. Sending the light through an absorption saturation spectroscopy setup we can shift the laser frequency to bring either the blue (high ν) or the red (low ν) sideband into resonance with the cesium cell, thereby creating a controllable red or blue detuning respectively in the carrier propagating further down towards the section of the table where the experiments are performed. An absorption signal with 950MHz sidebands along with the derived error signal can be seen in Fig. 5.6. Note that apart from the six peaks for each band there are also additional cross over resonances between the bands. In our experiments we typically lock to one of the resonances on the right to a blue detuned carrier.

The beam is shaped into pulses of a desired temporal intensity profile by sending it through an electro-optic modulator (EOM). In an EOM the difference in the index of refraction of the two optical axes can be controlled by applying a high-voltage across the EOM. Thus, if the optical axes are tilted 45° compared to the incoming linear light polarization, the light polarization is preserved if no voltage is applied and it is rotated 90° if an appropriate voltage is applied. This means that with a polarizing beam splitter after the EOM, the light can be turned on and off via the applied voltage and hence any beam shape can be realized experimentally (see Fig 5.5). The reason for using an EOM rather than an AOM for the shaping of the probe beam is that it was found to be much

less noisy at frequencies around 322 kHz, which is essential for obtaining the necessary quantum noise limited behavior at such frequencies. Both the AOMs and the EOM are turned on and off smoothly in order not to introduce additional Fourier components around 322kHz.

For the light to atom teleportation experiment discussed in chapter 8 a TOPTICA distributed feedback (DFB) diode laser was used as probe laser instead of the Ti:Sapphire. In a DFB diode, the frequency selective element - a Bragg grating - is integrated into the active section of the semiconductor. Thus, single-frequency operation and relatively high coherence (coherence length 70-100 m) are obtained. The locking and pulse shaping for this laser is done exactly as for the Ti:Sapphire laser.

The two lasers have extremely different noise characteristics. Every laser contains a certain amount of amplitude noise. Via the balanced \hat{S}_y detection described in Sec. 5.2.3 such noise is suppressed by more than 20dB. In this way SN-limited detection of the Stokes components is achieved. In Fig. 5.7 the result of the balanced \hat{S}_y detection (SN) is shown for the TOPTICA diode laser along with the corresponding measurement using only a single detector. The latter measurement is sensitive to both the SN and the amplitude noise. Shot noise scales linearly with the light power and amplitude noise scales quadratically. If there was no amplitude noise present, the two curves would be identical. As can be seen, there is an amplitude noise component, which at 5mW amounts to $\sim 20\%$ of the SN level. An equivalent measurement with the Ti:Sapphire laser would show 10dB of amplitude noise. We know that the main source of this noise is amplitude fluctuations in the output of the Verdi pump. Toward the end of 2005 the amplitude noise increased up to 20dB making it extremely difficult to obtain SN-limited performance. This is the main reason for the change to the TOPTICA laser.

On the other hand, in terms of phase or frequency noise the situation is reversed. The Ti:Sapphire has a linewidth ~ 200 kHz, whereas the linewidth of the TOPTICA is ~ 6 MHz. Of course, when observing in a narrow band around 322kHz this makes an enormous difference. This turned out to be one of the large experimental challenges in the teleportation experiment discussed in chapter 8. Here the TOPTICA laser was used and since the experiment required an interferometer, we observed conversion of phase noise to amplitude noise to such an extent that the light was no longer SN limited. As discussed in Sec. 8.3 this problem was overcome partly by making the path length in the two arms of the interferometer equal (*white light position*) and partly by drastically reducing the power in one of the interferometer arms.

5.2.3 Detection of Polarization States

The Stokes parameters are measured with low intrinsic noise photo detectors. We use high quantum efficiency silicon photo diodes from Hamamatsu and home made amplifiers characterized by negligible electronic noise compared to the shot noise of light at optical power higher than 1mW. In Fig. 5.8 a) we depict how the

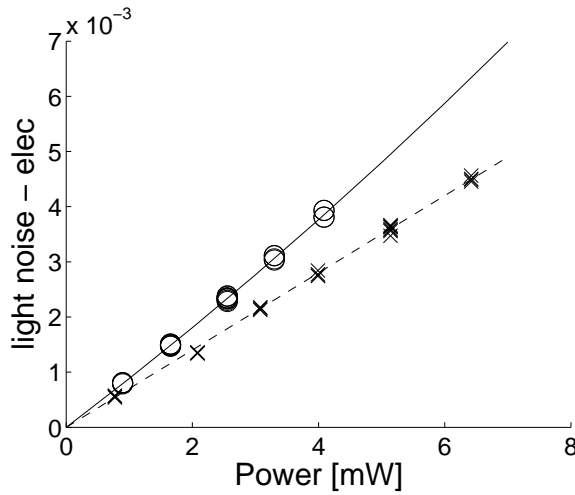


Figure 5.7: Light noise measurements performed on the TOPTICA probe laser at various optical powers.. Crosses: balanced \hat{S}_y detection (SN, see Sec. 5.2.3 for a description of the measurement). Circles: single detector measurement sensitive to SN and amplitude noise in the laser.

\hat{S}_y -component of light is measured. Remembering the definition in Eq. (2.5), we have to measure the light in the $\pm 45^\circ$ basis and then subtract the two resulting photo currents. The splitting into $\pm 45^\circ$ components is done by first rotating the incoming light by 45° with a $\lambda/2$ wave plate and then sending the light onto a polarizing beam splitter. The light at each output is then detected and the resulting photo currents subtracted. To measure \hat{S}_z instead we first interchange \hat{S}_y and \hat{S}_z using an appropriately aligned $\lambda/4$ wave plate and subsequently detect \hat{S}_y as just described.

Note that our method of detecting \hat{S}_y and \hat{S}_z and thereby \hat{x}_L and \hat{p}_L is very closely related to the standard homodyne detection [100] of a weak beam characterized by quadratures x and p (see Fig. 5.8 b)). There the weak signal (\hat{a}) is mixed with a strong classical local oscillator signal at the same frequency ($Ae^{i\phi}$) on a 50:50 beam splitter and the power in each output arm is detected:

$$\begin{aligned}
 i_1 &= \frac{1}{2} \langle (Ae^{i\phi} + \hat{a}) (Ae^{-i\phi} + \hat{a}^\dagger) \rangle = A^2/2 + Ae^{-i\phi} \langle (\hat{a} + \hat{a}^\dagger e^{2i\phi}) \rangle + \langle \hat{a}^\dagger \hat{a} \rangle \\
 i_2 &= \frac{1}{2} \langle (Ae^{i\phi} - \hat{a}) (Ae^{-i\phi} - \hat{a}^\dagger) \rangle = A^2/2 - Ae^{-i\phi} \langle (\hat{a} + \hat{a}^\dagger e^{2i\phi}) \rangle + \langle \hat{a}^\dagger \hat{a} \rangle .
 \end{aligned}
 \tag{5.2}$$

From this we see that taking the difference between the two gives a signal proportional to \hat{x}_L with $\phi = 0$ and \hat{p}_L with $\phi = \pi/2$. The equations also describe our implementation, where the local oscillator is supplied by the strong polarization component in the light beam itself.

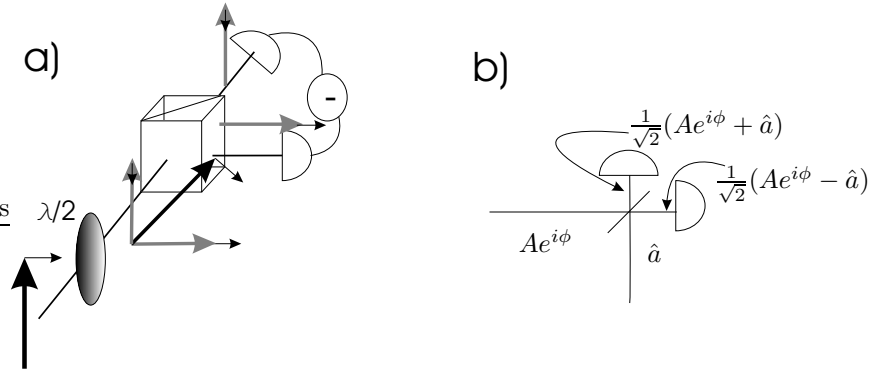


Figure 5.8: **a)** The setup for measuring \hat{S}_y . A pulse containing a strong classical component in the vertical polarization and a weak quantum component in the horizontal polarization is rotated 45° using a $\lambda/2$ waveplate. Then a polarizing beam splitter splits the new horizontal and vertical components, which each are measured. Half of the difference of the two photo currents is \hat{S}_y . Adding a $\lambda/4$ -retardation plate before the $\lambda/2$ waveplate turns this measurement into a measurement of \hat{S}_z component. **b)** The conventional method for detecting the quadratures \hat{x}_L and \hat{p}_L of a weak quantum beam.

By passing the differential photo current $i(t) \equiv i_1(t) - i_2(t)$ from a Stokes measurement through a lock-in amplifier we can detect the sine and cosine components at the Larmor precession frequency Ω_L . Remember, that these together with the rotating frame transverse spin components form the canonical variables of interest (see equations (2.32) and (2.33)). Practically, the current $i(t)$ is split into two parts which are multiplied by $\cos(\Omega_{LO}t)$ and $\sin(\Omega_{LO}t)$ respectively, where Ω_{LO} is a local oscillator frequency supplied by the lock-in amplifier. This creates signals at the frequencies $\Omega_{LO} - \Omega_L$ and $\Omega_{LO} + \Omega_L$. The sum frequency is filtered out and the result is then integrated over the duration of the pulse. If the two frequencies are matched sufficiently well (see Sec. 5.3.2), according to (2.33a-d), with appropriate scaling, this exactly corresponds to measuring the \hat{x}_c and \hat{x}_s components of light. Correspondingly, in an \hat{S}_z -detection we would measure \hat{p}_c and \hat{p}_s . The effective bandwidth of the measurement is first limited by the peaked detectors, which have a response width of $\sim 15\text{kHz}$. In Fig. 5.9 the spectral response of each of the two detectors necessary for an \hat{S}_y detection are shown along with the corresponding electronic noise level. The power is $\sim 1\text{mW}$ on each detector. As discussed at the end of Sec. 5.2.2 it is very important to balance the response of the two detectors in order to suppress amplitude noise. For the balancing it is very important that the spectral response of both detectors is overlapped, since otherwise it is impossible to balance the detectors over the entire measurement bandwidth.

The commercial lock-in amplifier has a 10kHz filter at the output. The ultimate bandwidth of the measurement is set by the integration over the pulse

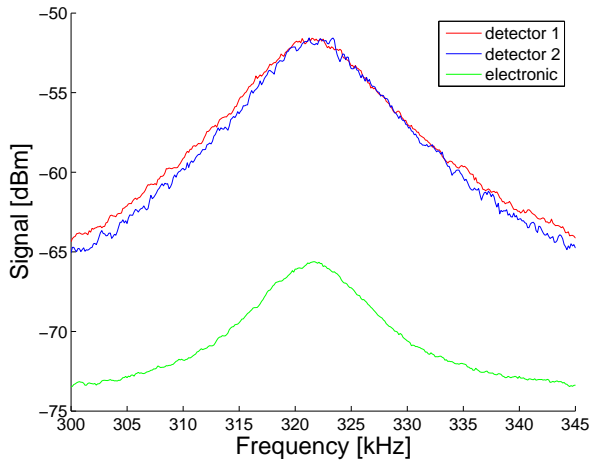


Figure 5.9: The spectral response of the two detectors used in the Stokes detection along with the corresponding electronic noise level. Matching the spectral response of the two is crucial for the suppression of amplitude noise.

duration, which acts as an effective low pass filter of a few hundred Hertz. In the future we may implement probing of the photo-current directly or the output of the lock-in amplifier, which would improve the temporal resolution and hence enable us to measure temporal modes other than the symmetric one (top hat intensity profile in time) such as e.g. the one being imposed onto light in the single cell interaction (Eq. (2.41)).

5.3 Magnetic Fields

As discussed in Sec. 2.5, our experiments are performed in the presence of a homogeneous magnetic field in the direction of the macroscopic mean spin. The interaction of atoms with a magnetic field is governed by the Hamiltonian

$$\hat{H}_{\text{mag}} = g_F \mu_B \mathbf{J} \cdot \mathbf{B} + O(B^2), \quad (5.3)$$

where we remember that that \mathbf{J} is the total angular momentum of the atom including the nuclear spin. For the $F = 4$ ground state of cesium, $g_F \approx 0.2504$. The second term $O(B^2)$ reminds us that the above linear equation is only approximately true. When the magnetic energy becomes comparable to the hyperfine splitting of the ground state the response is non-linear. At the magnetic fields we apply (~ 1 Gauss) this effect is very small but it still turns out to be an excellent tool for probing the population distribution among different m -levels. This will be discussed further in Sec. 5.3.1.

Adding a constant bias magnetic field B_x in the x -direction leads to the

equations of motion (2.26) with Larmor precession at frequency $\Omega_L = g_F \mu_B B_x / \hbar$. It is convenient to remember the expression $g_F \mu_B / \hbar = 350 \text{kHz/Gauss}$. If we furthermore add an RF magnetic field at frequency Ω along the y -direction such that in the absence of light

$$\mathbf{B}_{\text{ext}} = B_x \mathbf{e}_x + (B_c \cos(\Omega t + \phi) + B_s \sin(\Omega t + \phi)) \mathbf{e}_y \quad (5.4)$$

with constants B_c and B_s we may derive for the rotating frame coordinates \hat{J}'_y and \hat{J}'_z of (2.25) that

$$\frac{\partial \hat{J}'_y(t)}{\partial t} = -\omega_s \sin(\Omega_L t) \sin(\Omega t + \phi) J_x, \quad \frac{\partial \hat{J}'_z(t)}{\partial t} = -\omega_c \cos(\Omega_L t) \cos(\Omega t + \phi) J_x, \quad (5.5)$$

with $\omega_{c,s} = g_F \mu_B B_{c,s} / \hbar$. Choosing the phase and the frequency of the RF-drive such that $\phi = 0$ and $\Omega = \Omega_L$ we obtain:

$$J_x(t) = J_x(0), \quad \frac{\partial \hat{J}'_y(t)}{\partial t} = -\frac{\omega_s J_x}{2}, \quad \frac{\partial \hat{J}'_z(t)}{\partial t} = -\frac{\omega_c J_x}{2}. \quad (5.6)$$

These equations are valid for interaction times T such that $\omega_c T, \omega_s T \ll 1 \ll \Omega T$. We see that with pulses of RF-magnetic fields we are able to change the spin components \hat{J}'_y and \hat{J}'_z independently by an amount controlled by the sine and cosine components B_s and B_c . This has several experimental applications, which are discussed below.

5.3.1 Characterizing the Spin State with the Magneto-Optical Resonance Method

Equation (5.6) describes the introduction of a deterministic non-zero mean value in the rotating frame transverse spin components via the application of RF magnetic fields. When such a state is probed by the Faraday interaction (2.28a) the oscillating transverse spin components introduce an oscillating polarization rotation in the optical probe. This effect is called the magneto-optical resonance effect and is used extensively for spin state characterization in our experiment as described in detail in [101]. In order to quantitatively explain the Magneto-Optical Resonance Signal (MORS) as the RF-frequency is scanned across Ω_L , we need to return to the second order term mentioned in Eq. (5.3). The single atom transverse spin components \hat{j}_y and \hat{j}_z can be expressed in terms of coherences $\hat{\sigma}_{m,m\pm 1}$ in the following way:

$$\begin{aligned} \hat{j}_y &= \frac{1}{2} \sum_m \sqrt{F(F+1) - m(m+1)} (\hat{\sigma}_{m+1,m} + \hat{\sigma}_{m,m+1}), \\ \hat{j}_z &= \frac{1}{2i} \sum_m \sqrt{F(F+1) - m(m+1)} (\hat{\sigma}_{m+1,m} - \hat{\sigma}_{m,m+1}). \end{aligned} \quad (5.7)$$

Another way to understand the buildup in the transverse spin components is that a magnetic field transverse to the mean spin simultaneously drives $\Delta = 1$

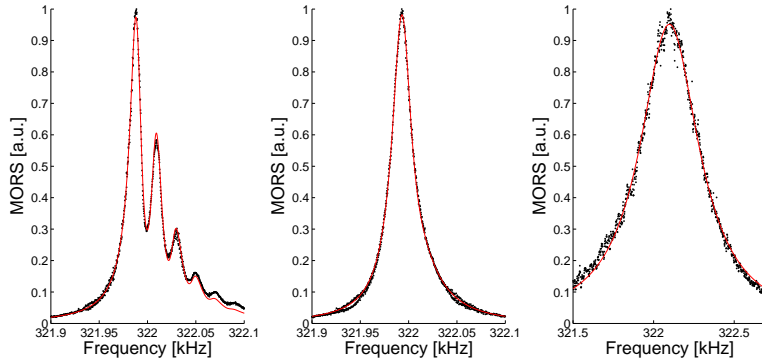


Figure 5.10: MORS in arbitrary units for an atomic samples pumped by the repump only (left), the repump and a very weak ($\sim 25\mu\text{W}$) optical pump (middle), and the repump along with a strong ($\sim 1\text{mW}$) optical pump (right). Since the optical pump is resonant with the atoms it broadens each resonance $\hat{\sigma}_{m,m+1}$. Overlaid is the fit based on a spin temperature model. From this we obtain orientations of 0.819, 0.948, and ~ 0.99 .

and $\Delta = -1$ transitions. This populates the $\hat{\sigma}_{m,m+1}$ coherences, which through Eq. (5.7) creates the buildup in the transverse spin components. In the absence of the second order term in (5.3) the energy separation $\hbar\Omega_L$ between states $|m\rangle$ and $|m+1\rangle$ is the same for all m and all terms $\hat{\sigma}_{m+1,m}$ have the same resonant frequency. The second order term in (5.3), however, makes the frequency of the coherences $\hat{\sigma}_{m+1,m}$ slightly different for different values of m . It can be shown, that the quadratic Zeeman frequency difference ω_{QZ} between $\hat{\sigma}_{m,m+1}$ and $\hat{\sigma}_{m-1,m}$ is $\omega_{\text{QZ}} = 2\Omega_L^2/\omega_{\text{hfs}}$ where $\omega_{\text{hfs}} = 2\pi \cdot 9.1926\text{GHz}$ is the hyperfine splitting of the Cesium ground state. We typically have $\Omega_L = 2\pi \cdot 322\text{kHz}$ and the effect is small ($\sim 23\text{Hz}$) but detectable.

In the special case that the amplitude and frequency of the driving RF-field vary slowly compared to the spin coherence time, the off-diagonal coherences follow the diagonal populations adiabatically and we may write e.g. \hat{J}_y as [101]

$$\hat{J}_y = \text{Re} \left[\text{const} \cdot \sum_{m=-F}^{F-1} \frac{[F(F+1) - m(m+1)] \cdot e^{i\Omega t}}{i(\Omega_{m+1,m} - \Omega) - \Gamma_{m+1,m}/2} [\hat{\sigma}_{m+1,m+1} - \hat{\sigma}_{m,m}] \right] \quad (5.8)$$

where $\Gamma_{m+1,m}$ are the FWHM line widths giving an exponential $e^{-\Gamma t/2}$ decay of each coherence. The Larmor frequency Ω_L has been replaced by the individual coherence evolution frequencies $\Omega_{m+1,m}$. For \hat{J}_z we have to take the imaginary part of the terms in square brackets of Eq. (5.8). We see that two adjacent magnetic sublevels act as a single two level system with the usual Lorentzian response to a driving field. Scanning the RF frequency we get eight Lorentzian peaks ($2F$), the magnitudes of which will depend on the populations of the

magnetic sublevels. We define the MORS as

$$\text{MORS} \propto \langle \hat{J}_y \rangle^2 + \langle \hat{J}_z \rangle^2, \quad (5.9)$$

which we from Eq. (2.28a) see is proportional to the sum of the square of each of the two outputs of the lock-in amplifier. This signal we analyze in a spin temperature model in which the populations can be described by $\hat{\rho}_{m,m} \propto \epsilon^m$. By determining ϵ experimentally we can calculate the orientation of the atomic sample

$$p = \frac{1}{4} \sum_{m=-4}^4 m \hat{\rho}_{m,m} \quad (5.10)$$

Three examples of MORS taken with a very weak probe laser can be seen in Fig. 5.10. In the first, the sample is only pumped by the repumping laser. Since it is not resonant with the $F = 4$ atoms (see Fig. 5.1) it does not decrease the life time of the coherences, which is thus determined primarily by collisions and magnetic dephasing. The decoherence mechanisms will be discussed further in Sec. 5.4. For now it is merely important that under these conditions the individual peaks are well resolved and a reliable fit to the data can be obtained. With this, we get $p = 0.819$. Next, the optical pump is turned on slightly. As can be seen this broadens each peak to such an extent that they are no longer individually resolved. They do, however, cause an asymmetry in the signal that enables a fit. With only a few μW we get $p = 0.948$ - a significant improvement compared to the previous result. The last signal shows the broadening with the optical pump power typically used in the experiments ($\sim 1\text{mW}$). Note, that for this plot the x-axis is rescaled. Using the methods discussed in [101] for strongly broadened signals we can estimate the orientation to be ~ 0.99 . Thus, in our experiments only the outermost coherence ($m_F = 4 \leftrightarrow m_F = 3$) is significantly populated.

A second application of the MORS method is that measuring the widths of the resonances under different experimental conditions allows us to quantify the effect of different decoherence mechanisms as discussed in Sec. 5.4.

5.3.2 Manipulating the Spin State

The MORS is primarily taken with a continuous wave probe. We could however also apply a short RF pulse in the pulsed setup. Choosing $\Omega = \Omega_L$ and an appropriate phase, strength and envelope function of the RF-field we can create and thus manipulate the mean value of either of the spins or any combination of these in the settings under which the actual quantum experiments are performed. Experimentally we design the magnetic pulse as

$$B_i = A_{\text{control},i} A_{\text{RF}} B_y(t), \quad (5.11)$$

where $i = c, s$, B_i was defined in Eq. (5.4), A_{RF} controls the strength of the RF-signal, $B_y(t)$ is the envelope function determining the shape of the magnetic

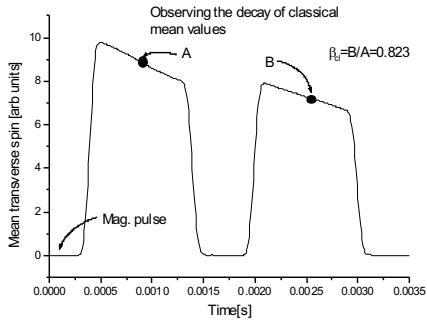


Figure 5.11: Observing the oscillating Faraday rotation of light to probe the evolution of the spin state following the application of a short magnetic RF pulse prior to the first probe. β_{cl} gives a rough estimate of the decoherence between two pulses.

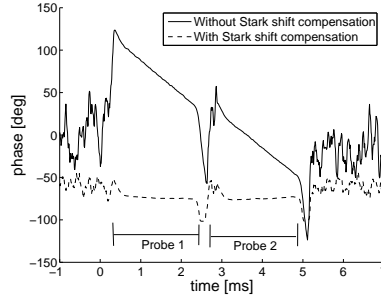


Figure 5.12: Observing the evolution of the phase between the two outputs of the lockin-amplifier for the experiment as in Fig. 5.11. A constant phase correspond to $\Omega_L = \Omega_{LO}$.

pulse, and $A_{\text{control},i}$ are overall weight factors. This has two applications. First, we can actively feed back the result of a quantum probing of the spin state, thus creating a particular desired state. This is the keystone element for the creation of deterministic entanglement, discussed in Sec. 6.2, and for the quantum mapping experiment discussed in Sec. 7.

Secondly, if A_{control} is set to a large DC value it enables us to create a large classical mean value in the transverse spins and observe the evolution of this state. (Note, that the shift is large compared to CSS distribution but still extremely small compared to the macroscopic mean spin.) An example of this is shown in Fig. 5.11. Here, a magnetic pulse is applied prior to the first probe and the decay of the created state is observed during each probe. From this we can extract the characteristic decoherence time T_2 , which as we shall see in Sec. 5.4 can be related directly to the width of the MORS. A rough estimate of the decoherence from one pulse to the next, β , which was discussed in the context of entanglement estimation in Sec. 3.4, can be calculated by taking the ratio of the mean values of each pulse as indicated in Fig. 5.11. It is related to T_2 by $\beta_{cl} \approx 1 - t/T_2$. Note, that we use the subscript "cl" because we only observe the decay of a classical state. As we shall see in Sec. 6.2 the decay of a quantum mechanical state can be faster because of atomic motion. This is also discussed in detail in App. A.2.

In Fig. 5.11 we plotted the modulus of the two outputs of the lockin-amplifier $R(t) \propto \sqrt{\langle \hat{J}_y \rangle^2 + \langle \hat{J}_z \rangle^2}$, which is insensitive to rotations between the two. These can be observed if we instead plot the relative phase between the two outputs of the lockin-amplifier. If Ω_{LO} is not matched precisely to Ω_L the signal will oscillate between \hat{J}_y and \hat{J}_z with frequency $\Omega_L - \Omega_{LO}$ and correspondingly

the relative phase will grow as $(\Omega_L - \Omega_{LO})t$. In this way, changing either the bias magnetic field or the frequency of the local oscillator the two can be matched precisely by making the phase evolution flat in time. This we could also have done observing the MORS and placing the strongest peak at Ω_L . A much more crucial application arises because - as discussed in App. C - terms proportional to a_2 in the effective Hamiltonian (2.20) introduce an intensity dependent Stark shift of the atomic coherences. This means that Ω_L cannot be overlapped with Ω_{LO} both in the presence and in the absence of light. To solve this problem we have an additional Helmholtz coil in the x-direction and send a current through when the light is on in order to compensate for the Stark shift. The adjustment of the necessary current can only be done observing the phase evolution. In Fig. 5.12 we show the phase evolution both with and without the Stark shift compensation in the situation where $\Omega_L = \Omega_{LO}$ in the absence of light. Without the compensation we get a phase evolution of $\sim 90^\circ$, which corresponds to a Stark shift of 125Hz. Since the shift is in opposite directions for the two samples (see Eq. (C.6)) the mismatch between the two is comparable to the bandwidth of our detection, so this is a quite significant effect. With the compensation we can keep the phase constant within 5 degrees giving a maximal frequency mismatch of 7Hz. Note that when the probe pulse is off there is no signal on the lockin-amplifier and the phase is consequently ill defined.

5.4 Decoherence

As mentioned earlier, all atoms are optically pumped into an extreme Zeeman sublevel with the x -axis as quantization axis. A conventional way of categorizing sources of decoherence is according to whether they affect the magnitude of the spin along this axis or merely along transverse directions. The appropriate life times of these are called T_1 and T_2 and defined as:

$$J_x(t) = e^{-t/T_1} J_x(0) \quad \text{and} \quad J_{\text{trans}}(t) = e^{-t/T_2} J_{\text{trans}}(0) \quad (5.12)$$

in the absence of additional interactions. Apart from the effects caused by the probe light the dominant processes are collisions with the walls and other atoms giving $T_1 \approx 300\text{ms}$. The presence of the bias magnetic field is extremely important for the life time because it imposes an energy barrier against spin flipping transitions. Experimentally we have found a dramatic dependence of T_1 and the bias field up to $\sim 0.1\text{Gauss}$ after which it is more or less constant. With our $B = 0.92\text{Gauss}$ we are safely in the constant regime. Even though the probe detunings are quite high in our experiments (700-1200MHz) making the desired refractive Faraday interaction dominant by far, the small probability of absorption still reduces T_1 by about a factor of 2 depending on probe power and detuning. It is, however, still very large compared to typical probe durations (0.5-2 ms).

The lifetime of the transverse spin components, however, turns out to be much more critical for our experiments. As can be seen from Eq. (5.7) the transverse

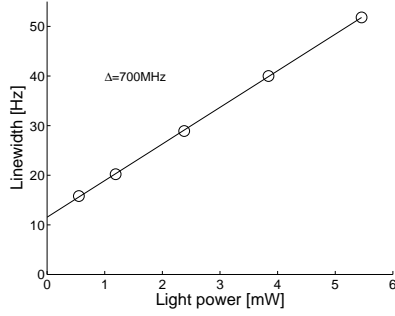


Figure 5.13: Line width of the σ_{34} coherence in the MORS as a function of optical power. In a single trace it is impossible to separate the expected power broadening from absorption from the light induced collisions.

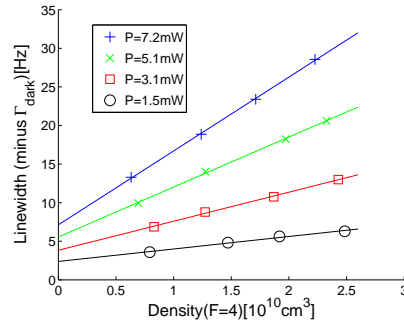


Figure 5.14: Line width of the σ_{34} coherence in the MORS as a function of atomic density for different optical powers. The fact that the slopes are not equal reveals light induced collisions. $\Delta = 1000\text{MHz}$

spin components are determined by coherences between magnetic sublevels in the x -basis. Therefore anything that affects the lifetime of J_x will also affect T_2 . In addition, however, the total transverse spin components are also sensitive to random phase changes in each atom. As discussed in Sec. 5.3 we can use the widths obtained in MORS signals in different experimental settings to quantify and separate the effect of different decoherence mechanisms. The FWHM obtained from such signals are related to T_2 by:

$$\Gamma_{\text{trans}}[\text{Hz}] = \frac{1}{\pi T_2[\text{s}]} \quad (5.13)$$

We can separate the mechanisms into two main categories: some are mediated by the probe light and the rest are independent of the presence of the probe. Starting with the latter, these combine to a decay rate, Γ_{dark} , and consist mainly of phase changing and spin-flip collisions with the walls and other atoms and random phase changes because of atomic motion through inhomogeneous magnetic fields. The effect of these are reduced by the paraffin coating on the inside of the glass cells, the diluteness of the atomic sample, and the application of additional DC-magnetic fields to cancel field gradients. To determine Γ_{dark} we measure the width of the $m_F = 3 \leftrightarrow 4$ coherence for different probe powers and find the residual width in the absence of light. An example of this is shown in Fig. 5.13. As can be seen, we obtain a width of the order of 12 Hz corresponding to a lifetime of the transverse spin of $T_2^{\text{dark}} \approx 27\text{ms}$. At very low densities, Γ_{dark} as low as 5 Hz has been observed. We see that this will limit but not completely destroy correlations between two subsequent pulses in e.g. an entanglement experiment as described in Sec. 3.

Turning to the probe induced decoherence mechanisms, we have already mentioned absorption and subsequent spontaneous emission in the discussion of T_1 .

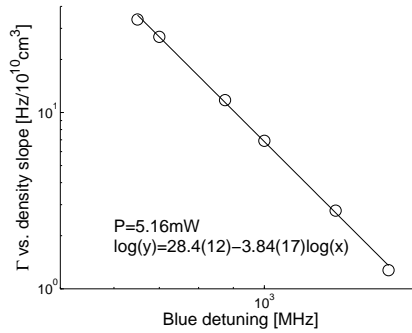


Figure 5.15: Slope from Γ vs. density curves such as in Fig. 5.14 as a function of the the blue detuning at which they are taken. Power fixed at 5.16mW. The linear dependence in a log-log plot reveals a power law behavior.

Adding this effect to the other decoherence mechanism, we would expect a total decoherence rate of the general form:

$$\Gamma_{\text{ideal}} = a + b \cdot \rho + c \cdot P , \quad (5.14)$$

ρ is the atomic density, P is the light power, and a , b , and c are coefficients, which can be determined experimentally. If Γ is plotted vs. ρ we would expect a line with constant slope b and offset determined by the optical power. In Fig. 5.14 we show measurements of the decoherence rate vs. atomic density for different optical powers. The results clearly contradict the simple model of Eq. (5.14), since the slope grows with increasing power. It turns out that the experiments fit a model:

$$\Gamma_{\text{exp}} = a + b \cdot \rho + c \cdot P + d \cdot \rho \cdot P , \quad (5.15)$$

where the size of the expected pure power broadening term, c , agrees with solutions of the Maxwell-Bloch equations for the full multi-level atomic system in the presence of Doppler broadening. The last term could represent light induced collisions, but a clear theoretical understanding of the nature of these is still missing. For the experimentally relevant densities and powers this term contributes around 30 Hz of broadening and is thus the main source of decoherence. We stress that this is a pure T_2 process since we do not observe similar features when investigating the decay of the longitudinal spin. Hence, the atoms practically decay towards the fully polarized state, i.e. the coherent spin state. This was also assumed implicitly in the inclusion of decoherence for the entanglement and quantum mapping protocols in Sec. 3.4, where decoherence was modeled by an admixture of a vacuum state with the same variance as the coherent spin state.

The line width as a function of the density such as Fig. 5.14 has been measured for several different detunings. The result can be seen in Fig. 5.15 in a log-log plot. The linearity means that the light induced collisions obey a power law $\Gamma_{\text{LIC}} \propto \Delta^{-3.84(17)}$. The high exponent is quite unexpected since it suggests an

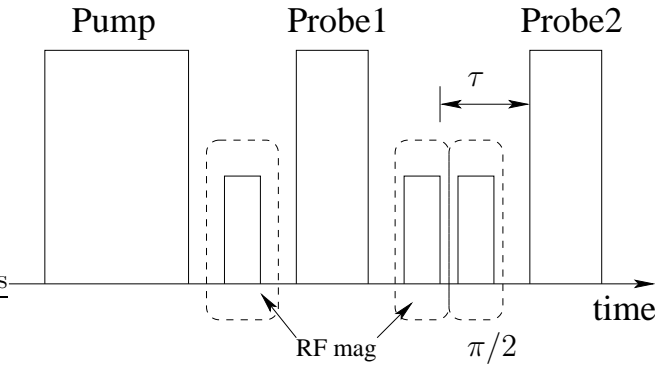


Figure 5.16: Generic experimental cycle. There will always be a pump pulse initializing the spin in the CSS, and two probes. We have the option of applying an RF magnetic pulse before each probe. The first is used for state diagnostics, whereas the second is used for quantum feedback. In the mapping experiment a $\pi/2$ pulse in $\hat{X}_a\hat{P}_a$ -space is used to retrieve information about \hat{X}_a instead of \hat{P}_a . The duration from the end of the feedback pulse till the start of the second probe will constitute the storage time.

exotic interaction type such as collisions between two excited atoms. Work is currently going on to determine the nature more precisely of these interactions. On the other hand the exponent is encouraging since it means that the effect of the light induced collisions should fall off much more rapidly than the desired Faraday interaction. Whether this beneficial scaling can be exploited experimentally is currently under investigation.

5.5 Experimental Cycle

All our experiments are based on a generic probing sequence which is illustrated in Fig. 5.16. The experimental cycle starts with optical pumping, which is supposed to erase any trace of the final state of the previous cycle and prepare the atomic system in the completely uncorrelated coherent spin state. The effect of the optical pumping on existing coherences can be calculated by inserting widths found in MORS such as Fig. 5.10 (right) into Eq. (5.12). During optical pumping we typically have $\Gamma = 500\text{--}1000\text{Hz}$ giving characteristic times of $T_2 \approx 0.3\text{--}0.6\text{ms}$. This means that during a typical optical pumping period of 4ms only a fraction $e^{-4/T_2[\text{ms}]}$ of the state after a previous cycle will be present in the next cycle.

Following the pump pulse we have the possibility of creating a non-zero mean value in either or both of the atomic quadratures by the application of an RF magnetic pulse typically of duration 200 μs . This is primarily used for diagnostics such as e.g. the Stark shift compensation discussed in Sec. 5.3.2 and it is absent for the main experiments of this thesis.

Next a 0.5-2ms *probing pulse* is sent through the atoms. As described in Sec. 5.2.3 $\hat{S}_y(t)$ is measured, processed in the lock-in amplifier, and subsequently

integrated over the duration of the pulse. In the end a single number for each of the cosine and sine quadratures is stored in the computer. After this we have the possibility to do atomic state manipulations, either by shifting the state via another 200 μ s RF pulse or by performing rotations between \hat{x}_a and \hat{p}_a by applying an additional DC bias magnetic field, which will speed up or slow down the Larmor precession. The pulse sequence ends with a second *verifying pulse*, which is identical to the probing pulse. All together, a typical measurement cycle lasts around 10ms.

Thus, the result of a single experimental cycle will be four numbers stored in the computer. To determine the variance of \hat{S}_y we repeat the measurement cycle 10,000 times. We have chosen this number because it reduces the statistical error in the calculated variance to an acceptable level ($\sim 1.4\%$), while still minimizing drifts in the experimental setup.

5.6 Projection Noise Level

Since the Heisenberg uncertainty relation sets the starting point of all our calculations, one of the most important tasks in our experiments is the achievement of quantum noise limited performance. Practically, it is also one of the most difficult tasks. When we detect polarization states of light we observe noise in the signals. After the light has passed the atomic samples, there is a contribution to this noise from the light itself and from the atomic spins. The noise contribution from atoms in the minimum uncertainty state (the coherent spin state) is called projection noise.

We discussed the ratio of the projection noise to the quantum noise of light (shot noise) already in Sec. 3.2. We found that theoretically this ratio should be

$$\kappa^2 = a^2 J_x S_x T. \quad (5.16)$$

The ratio κ^2 came from the canonical interaction equations (2.34a-d) and a was defined immediately below Eq. (2.24d). In the present section we discuss how to determine this projection noise level experimentally and how to predict the noise level from independent measurements.

5.6.1 Measuring the Macroscopic Spin

The ratio of projection noise to shot noise is proportional to the macroscopic spin J_x . This linearity is the fingerprint of quantum noise and is essential to verify experimentally. For this we need a good measure of J_x .

We know that in the by now familiar Faraday interaction the light polarization is rotated by an amount proportional to the atomic spin in the direction of light propagation. Obviously this effect can also be utilized for measuring the macroscopic spin by letting a linearly polarized laser field propagate through the atomic samples along the x -direction. To see what happens in this setting we consider equations (2.22) and (2.23). These equations assume propagation along

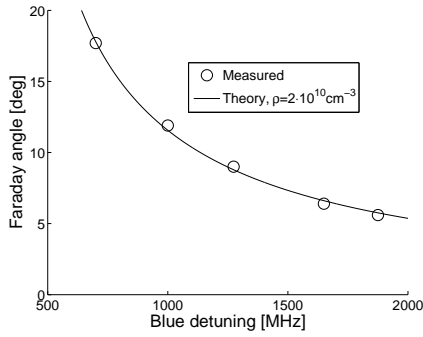


Figure 5.17: Measured Faraday angle vs. detuning

the z -direction so we assume the spin to be polarized along the z -direction in the following. For linearly polarized light we have $\langle \hat{S}_z \rangle = 0$ and the mean values of the transverse spin components \hat{j}_x, \hat{j}_y are unaffected. We know, however, that the noise properties are changed so to avoid this we keep the intensity of the beam extremely small. It can easily be shown that the a_0 and a_2 terms of the Hamiltonian (2.20) play no role in this calculation. We are left with the evolution of \hat{S}_x and \hat{S}_y according to Eq. (2.23) and after integration over the sample we find

$$\begin{aligned} S_x^{\text{out}} &= S_x^{\text{in}} \cos(2\theta_F) - S_y^{\text{in}} \sin(2\theta_F), \\ S_y^{\text{out}} &= S_x^{\text{in}} \sin(2\theta_F) + S_y^{\text{in}} \cos(2\theta_F), \end{aligned} \quad (5.17)$$

where “in” refers to the polarization state before the sample at $z = 0$ and “out” refers to the state after the sample at $z = L$. The angle θ_F is given by (in radians)

$$\theta_F = -\frac{a_1 \gamma \lambda^2 \rho L}{32\pi \Delta} \cdot \langle \hat{j}_z \rangle. \quad (5.18)$$

If a linearly polarized beam of light is rotated by the angle θ , the Stokes vector is rotated by 2θ . Thus, in the above, θ_F is the polarization rotation caused by the spin orientation along the direction of light propagation. We note that the angle θ_F depends on the density ρ of atoms times the length L that the light traverses. We wish to re-express this in terms of the macroscopic spin size $J_z = N_{\text{at}} \langle \hat{j}_z \rangle$ of the entire sample (remember we have the spins polarized along z in this discussion). To this end we note that $N_{\text{at}} = \rho V \equiv \rho A_{\text{cell}} L$ where V is the vapor cell volume and A_{cell} is the area of the vapor cell transverse to the beam direction. This will be an effective area for cells that are not exactly box like. Returning to the usual convention of spin polarization along the x -axis we then rewrite Eq. (5.18) as

$$\theta_F = -\frac{a_1 \gamma \lambda^2 J_x}{32\pi A_{\text{cell}} \Delta}. \quad (5.19)$$

Using $\gamma/2\pi = 5.22\text{MHz}$ and $\lambda = 852.3\text{nm}$ we get:

$$\theta_F[\text{deg}] = -\frac{a_1 N_{\text{at}} \cdot 8.64 \cdot 10^{-8}}{A_{\text{cell}}[\text{cm}^2] \Delta[\text{MHz}]} \quad (5.20)$$

In Fig. 5.17 the dependence of the Faraday angle on the detuning is tested. As can be seen we find very nice agreement with the theoretical prediction.

5.6.2 Predicting the Projection Noise Level

Now, let us return to the predicted ratio of projection to shot noise (5.16). This prediction relies on equations (2.24a-2.24d) which are derived under the assumption that all atoms in the sample interact with the laser beam which has a cross sectional area A . In experiments the laser beam does not intersect all the atoms. In appendix. A we show that the random motion of atoms in and out of the beam modifies the expected variance of the transverse spin components \hat{J}_y and \hat{J}_z by statistical effects from the usual $J_x/2$ to $p^2(1 + \sigma^2)J_x/2$ where $p = A/A_{\text{cell}}$ is the mean time of an atom inside the laser beam and σ^2 is the relative variance of p . We furthermore present a simple model for p and σ and show that the atomic motion acts as an effective source of decoherence between two probe pulses. We incorporate atomic motion into Eq. (5.16) by replacing A with A_{cell} in the factor a and multiplying the whole expression by $1 + \sigma^2$. We then find

$$\begin{aligned} \kappa^2 &= a^2 J_x S_x T \cdot p^2 (1 + \sigma^2) = \left(\frac{\gamma}{8A_{\text{cell}}\Delta} \frac{\lambda^2}{2\pi} a_1 \right)^2 J_x S_x T (1 + \sigma^2) \\ &= \frac{(1 + \sigma^2) \gamma \lambda^3 a_1 P \cdot T \cdot \theta_F}{32\pi^2 A_{\text{cell}} \Delta \hbar c}. \end{aligned} \quad (5.21)$$

In the last step we replaced $S_x = \phi/2 = P/2\hbar\omega = P\lambda/4\pi\hbar c$ where P is the optical power. We also inserted Eq. (5.19) to express κ^2 as a function of θ_F . However, we must remember that the area A_{cell} in (5.19) refers to the transverse area for a beam propagating in the x -direction while the A_{cell} from the relation $p = A/A_{\text{cell}}$ refers to the transverse area for a beam along z . Hence, the last step above is valid for a vapor cell of cubic symmetry only, but it can still be an irregularly shaped cell. In other cases the generalization is straightforward. We have reached an expression for κ^2 in terms of convenient parameters from an experimental point of view. With $\gamma/2\pi = 5.22\text{MHz}$ and $\lambda = 852.3\text{nm}$ we obtain our final theoretical estimate for the projection to shot noise ratio expressed in convenient units:

$$\kappa_{\text{th}}^2 = \frac{56.4 \cdot P[\text{mW}] \cdot T[\text{ms}] \cdot \theta_F[\text{deg}] \cdot a_1(\Delta) \cdot (1 + \sigma^2)}{A_{\text{cell}}[\text{cm}^2] \cdot \Delta[\text{MHz}]}, \quad (5.22)$$

where $a_1(\Delta)$ was defined in Eq. (2.21).

As discussed in chapter 4 a conventional way of writing the interaction strength is in terms of the optical depth on resonance α and the depumping parameter

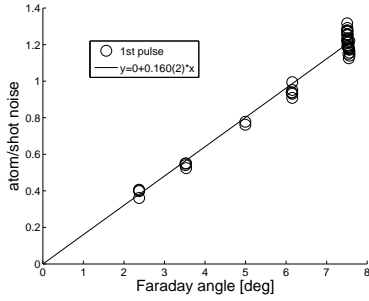


Figure 5.18: Measured atomic noise relative to shot noise of light. The linearity is a clear signature of the projection noise limitation.

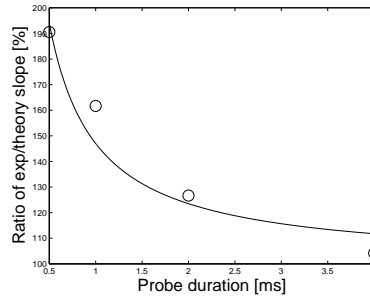


Figure 5.19: Slope of measured κ^2 vs. θ normalized to the experimentally predicted level (without the factor $1 + \sigma^2$) vs. T_{probe} . The fit gives $\kappa_{\text{exp}}^2/\kappa_{\text{th}}^2 = 1 + 0.47(13)/T[\text{ms}]$.

η_T :

$$\kappa^2 = \alpha \cdot \eta_T = \frac{N_{\text{at}}\sigma_{\text{CS}}}{A} \cdot \frac{N_{\text{ph}}\sigma_{\text{CS}}}{A} \frac{\Gamma^2}{\Delta^2}, \quad (5.23)$$

where Γ is the HWHM of the optical transition. Comparing to Eq. (5.21) we calculate the resonant cross-section $\sigma_{\text{CS}} \approx 4.08 \cdot 10^{-14} \text{m}^2 \cdot a_1$, which can be compared to the simple estimate $\sigma_{\text{CS}} = \lambda^2/2\pi \approx 1.16 \cdot 10^{-13} \text{m}^2$. Using Eq. (5.20) and $N_{\text{ph}} = 4.29 \cdot 10^{12} P[\text{mW}]T[\text{ms}]$ we can derive convenient expressions for the optical depth and the depumping parameter:

$$\alpha = 4.72 \cdot 10^{-3} \theta_{\text{F}}[\text{deg}] \Delta[\text{MHz}] \quad (5.24)$$

$$\eta_T = \frac{1.19 \cdot 10^4 a_1 P[\text{mW}]T[\text{ms}]}{A_{\text{cell}}[\text{cm}^2] \Delta[\text{MHz}]^2}. \quad (5.25)$$

Inserting typical values we get an optical depth at room temperature around 32 and η_T ranging from 1.5% to 6%.

5.6.3 Experimental Investigation

Turning to the experimental investigation of the projection noise level, we first have to determine shot noise level of light (SN), i.e. the measured noise of \hat{S}_y in the absence of interaction with the atomic system. From Eq. (2.3) we expect the noise of light in a coherent input state to be equal to $S_x/2$, which means that it scales linearly with the power. In Fig. 5.7 this scaling is verified. Note that electronic noise is subtracted and therefore the curve goes through the origin. In practice, for the light noise measurements the atomic Larmor frequency is shifted outside the measurement bandwidth by applying additional DC magnetic fields along the x-direction.. This additional field is then turned off and we

perform 10,000 measurement cycles with the light-atom interaction within the measurement bandwidth. We reconstruct the atomic variance by:

$$\kappa^2 = \frac{\text{Var}(\text{atom})}{SN} = \frac{\text{Var}(\hat{S}_y, \text{raw}) - SN - \text{Var}(\text{elec})}{SN}, \quad (5.26)$$

where $\text{Var}(\hat{S}_y, \text{raw})$ is the variance calculated from the first pulse of each measurement cycle only and $\text{Var}(\text{elec})$ is the electronic noise. To verify that we are in fact measuring the atomic projection noise we repeat this measurement for a number of different atomic densities. Quantum noise gives a linear scaling, whereas all classical noise sources will produce a quadratic scaling. In Fig. 5.18 the result of such an experiment is shown. The data are clearly linear. With $\Delta/2\pi = 825\text{MHz}$, $T = 2.0\text{ms}$, $P = 5.14\text{mW}$, and $\sigma^2 = 0$ for the moment, we predict a linear slope of 0.168 which is somewhat higher than the measured value of 0.160(2). To compare this to the simple model described in (A.4) we estimate our beam diameter to be 1.2cm which gives $A \approx 1.13\text{cm}$; moreover, $v_0 = 13.7\text{cm/ms}$ (cesium at room temperature) and the cell is cubic with $L = 2.2\text{cm}$. For $T = 2.0\text{ms}$ we get the prediction $\sigma^2 = 0.26$ modifying the expected slope to 0.212. As mentioned in appendix A.1, numerical simulations of atomic motion have shown that the variance estimate (A.4) is almost four times too high. So our best estimate of a theoretical slope is 0.178 which is 10% higher than the measured value.

To test the scaling properties predicted in the atomic motion calculations, we fix the power P , detuning Δ and macroscopic spin size J but vary the probe duration T . The measured noise is plotted in Fig. 5.19 relative to the prediction (5.22) with $\sigma^2 = 0$. We see that as T is increased we do see a lower and lower noise level which corresponds to decreasing σ^2 . The solid line in the figure represents a fit where $\sigma^2 = (0.47 \pm 0.13)/T[\text{ms}]$. This series was taken with the old cells having $A_{\text{cell}} \approx 6.0\text{cm}^2$ and $L = 3.0\text{cm}$ and $A_{\text{beam}} \approx 2.0\text{cm}^2$. For $T = 1\text{ms}$ we get the prediction $\sigma^2 = 0.44$. This is in very good agreement with the measured data, but this agreement must be viewed as fortuitous. We also note the relatively high uncertainty of 0.13. Indeed, this series should mostly be interpreted qualitatively since each individual point is not extracted from an entire line but rather only from a single series of 10,000 measurements. All together, however, we have a qualitative understanding of the physics and a quantitative agreement within $\sim 10\%$.

5.6.4 Thermal Spin Noise

Another issue concerning the projection noise level is the question of thermal spin noise. For the establishment of the correct noise level we must be in the CSS with high precision. For the CSS the spin is completely polarized along the x -direction and $\text{Var}(\hat{j}_y) = \text{Var}(\hat{j}_z) = F/2 = 2$ for the $F = 4$ ground state. As a very different example we may consider a completely unpolarized sample. We then have by symmetry $\text{Var}(\hat{j}_x) = \text{Var}(\hat{j}_y) = \text{Var}(\hat{j}_z) = (\hat{j}_x^2 + \hat{j}_y^2 + \hat{j}_z^2)/3 = F(F + 1)/3 = 20/3$. This is a factor of 10/3 higher than the CSS noise and, even for fairly good polarization, the thermal noise may be significant. As described in Sec.

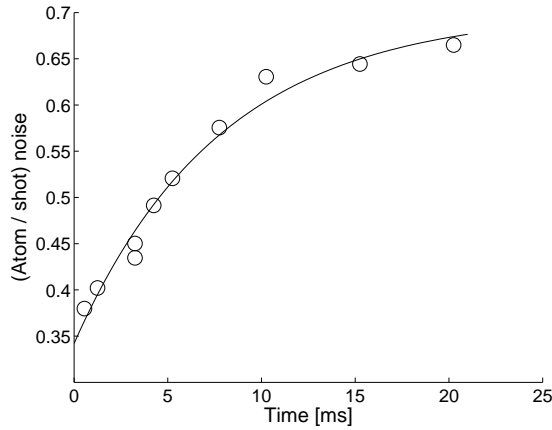


Figure 5.20: Coherent state noise compared to the completely unpolarized spin noise. The data is taken with a vapor cell in which the spin life time is very short. The noise level increases on a time scale of roughly 8ms to the thermal equilibrium level. The increase in noise is consistent with predictions for the coherent and unpolarized spin states.

5.3.1, however, we create spin polarization of 99% for our quantum information experiments. This means that we expect the contribution of thermal noise to be very small compared to the projection noise.

To test our prediction for the thermal noise level, we perform measurements on very poor vapor cells where the macroscopic spin life time is small. We optically pump the sample and wait for some variable delay time before probing the spin noise. For long times the spins reach thermal equilibrium, where the noise of each atom in $F = 4$ contributes $20/3$. The fraction of atoms in $F = 4$ is $9/16$, whereas the remaining $7/16$ are in the $F = 3$ state and do not contribute because of the large detuning. Initially, all atoms are in $F = 4$ in the CSS and they each contribute the value 2 to the noise. Hence the measured noise must be on the form

$$\text{Measured noise} \propto 2 \cdot \exp(-\Gamma t) + \frac{20}{3} \cdot \frac{9}{16} (1 - \exp(-\Gamma t)). \quad (5.27)$$

The predicted ratio of final to initial noise is thus $15/8 \approx 1.88$ which is consistent with the experimentally determined ratio of 2.05 ± 0.09 . To sum up, there is strong evidence that we really do create the CSS with the correct minimum uncertainty noise.

5.6.5 Concluding Remarks on the Projection Noise Level

Let us sum up the discussion of the projection noise level. To reach the quantum noise limited performance one should first observe the atomic noise grow linearly with the macroscopic spin size J_x . An experimental example of this was shown

in Fig. 5.18. The linearity of the noise basically arises from the fact that different atoms yield independent measurements when their spin state is detected. Technical noise sources from e.g. external electromagnetic fields couple to all atoms and the effect on the noise variance would be quadratic.

However, linearity alone is not enough. An ensemble of independent and unpolarized atoms would also show a linear increase in the spin noise with an increase in the number of atoms. Since unpolarized atoms have larger noise variance than the 100% polarized atomic sample, we must know independently that the spin orientation is high. In our experiments the spin samples are polarized better than 99%.

One may argue that the small fraction of atoms that are not in the completely polarized state could, in principle, form exotic-multi particle states with a very high variance of the detected spin noise. The results discussed in Sec. 5.6.4 prove that this is not the case.

Finally, as derived in App. A the atomic motion leads to an increased ratio of atomic to shot noise. Generally a large ratio of atomic projection noise to shot noise is good for the quantum information protocols. However, as discussed in appendix A.2 we do not gain anything by the increase of the atomic noise caused by atomic motion since there is an accompanying increase in the decoherence rate.

CHAPTER 6

Entanglement Results

We now turn to the experimental demonstration of entanglement generation. First the boundary between the classical and the quantum fluctuations has to be established. As discussed in Sec. 5.6 this projection noise level is found by performing several measurements of \hat{x}_L as a function of the macroscopic spin size and verifying a linear increase of the atomic noise of each measurement. This linearity combined with nearly perfect orientation of the sample ensures the correct projection noise level. Once this is established we implement a probing sequence (see Fig. 5.16) in which the initial probing pulse is followed by a second pulse after a short delay (without state manipulation in between). To verify entanglement we need to fulfill the criterion (3.9), in which case our ability to predict the outcome of the second probing of the atomic state conditioned on the result of the first measurement exceeds the classical limit. In a separate experiment we have used the knowledge gained from the first pulse to shift the atomic state towards zero mean value by applying an RF feedback pulse between the two probe pulses. The unconditional entangled state created in this way will be discussed in Sec. 6.2.

6.1 Conditional Entanglement

First, however, we discuss the basic entanglement experiment introduced in chapter 3, where we look for the conditional variance of the two probing results. As described in Sec. 3.2 we find the conditional variances by multiplying the results of the first pulse by some number α and then subtracting the product

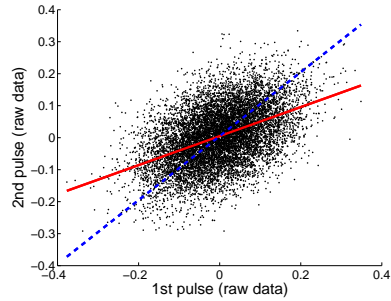


Figure 6.1: Second pulse \hat{S}_y result as a function of the first pulse \hat{S}_y result. In red (solid) is shown the linear fit and in blue (dashed) the unity slope curve which would be optimal for infinite signal to noise ratio.

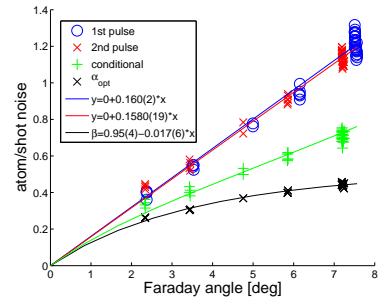


Figure 6.2: Atomic noise in units of shot noise as a function of θ_F for the two probe pulses along with the conditional variance of the two calculated based on the optimal weight factors (x 'es).

from the second pulse result. The correct α is the one minimizing the conditional variance Eq. (3.7) and is essentially the signal to noise ratio of the first measurement. Theoretically it is given by Eq. (3.16), where the effect of a simple beam splitter like decoherence is included. The optimization of the conditional variance is equivalent to performing a linear fit of the second pulse result as a function of the first. The result of such a fit is shown in Fig. 6.1. Clearly the blue dashed curve, which has unity slope, seems like the best fit because it follows the overall distribution of the points nicely. The true results, however, is the solid red curve, which has the slope of 0.45. This clearly illustrates the trade off between accommodating the correlated atomic part and the uncorrelated light part: If we calculate the conditional variance with an $\alpha > 0$ the noise of the light part will be amplified, whereas an $\alpha < 1$ will result in a non-perfect cancellation of the atomic part. Therefore, the signal to noise ratio will determine how close the optimal α lies to either zero or one.

In Fig. 6.2 the first pulse, the second pulse, and the conditional atomic variances are shown as a function of the Faraday angle. All of these are calculated in units of shot noise analogously to Eq. (5.26). The first pulse data is identical to the ones treated in Sec. 5.6.3. Since the measurement is of a QND-type the variance of the first and the second pulses should be identical (neglecting the small effects due to the $\sim 3\%$ decay of the mean spin) and we see that the slopes from the linear fits of each set do indeed overlap nicely within the uncertainty. Based on the decoherence discussions of sections 3.4 and 5.4 we expect the optimal weight factors α used in the calculated of the conditional variance to follow Eq. (3.16) with $\beta = \beta_o + \tilde{\beta}\theta_F$. Fitting to such an expression we obtain $\beta = 0.95(4) - 0.017(6)\theta_F$, which agrees reasonably with independently measured values of β at different densities. Inserting this result into Eq. (3.15) we calculate the expected value for the conditional variance. Considering the fact that it is

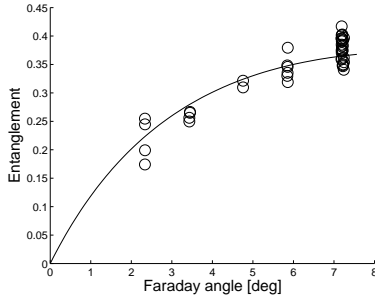


Figure 6.3: The degree of generated entanglement as a function of the atomic density. The data are obtained as one minus the ratio of the conditional variance and the projection noise, both from Fig. 6.2.

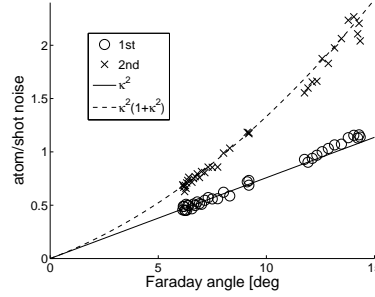


Figure 6.4: Anti-squeezing. Between the probe pulses a $\pi/2$ in the atomic xp -space is performed, thus reading out the state of the anti-squeezed quadratures \hat{X}_{ai} . The curves represent the expected behavior based and an independently measured projection noise level.

based on such a simple theory the agreement with experimental results must be considered very satisfactory. The degree of entanglement defined as the extent with which the entanglement criterion (3.4) is violated is shown in Fig. 6.3. For high densities the noise of the atomic part of the second pulse is reduced by approximately 36% compared to the projection noise if the knowledge from the first pulse is applied.

Since the variables \hat{P}_{ac} and \hat{P}_{as} are squeezed in the entanglement generation process there must also be conjugate variables which are anti-squeezed. As can be seen from Eq. (2.34c), for coherent input states the variances of \hat{X}_{ac} and \hat{X}_{as} are increased by a factor $1 + \kappa^2$, which is exactly the factor by which the conjugate variables are squeezed. To verify the anti-squeezing, we have in a separate experiment introduced a $\pi/2$ rotation in the atomic xp -space between the two pulses. As can be seen from Eq. (2.32) this can be realized experimentally by e.g. performing a π rotation to the transverse spins of second sample. Such a transformation is achieved simply by changing the bias magnetic field and thereby the Larmor precession frequency for an appropriate period of time. Because of this, \hat{X}_{ai} will be mapped onto the second pulse instead of \hat{P}_{ai} . Prior to this measurement we have determined the projection noise level. In Fig. 6.4 the experimental data along with the expected curve are shown. Since this is not a fit the agreement is certainly quite good.

6.2 Unconditional Entanglement

As we have just seen, two subsequent probes of the spin state yield correlated results. The actual results, however, vary from shot to shot, representing random realizations of the probability distribution of the spins (see Fig. 3.1). That is, we create a non-local state with reduced variance but with a non-deterministic mean value. Thus, the entanglement only appears when the knowledge gained in the first pulse is applied. To create a unconditionally entangled state in which no knowledge of prior measurement results is necessary would of course constitute a very important advance. We have realized this experimentally by simply feeding the result of the first measurement pulse back to the atoms using an RF-magnetic pulse as discussed in Sec. 5.3.2. In Sec. 3.3 we showed that the atomic statistics following such a feedback is identical to that of the conditional state except that the mean value of the former is zero in every implementation. This procedure is very closely related to the way in which unconditional spin squeezing is generated in [102] except that there the feedback is applied continuously in time, which is more robust against errors in the feedback strength.

To calibrate the feedback strength we first create a large classical mean value in the transverse spin by applying an RF pulse before the first probe pulse as described in Sec. 5.3.2 and then we apply a similar magnetic pulse between the two probe pulses with the integrated output of the lock-in amplifier as control voltage (multiplied with -1 to get negative feedback). The mean value created by the first pulse and therefore also the strength of the control voltage will be proportional to A_{RF} . With Eq. (5.11) this shows us that the total strength of the second magnetic pulse will be proportional to A_{RF}^2 . With a given initial DC control voltage we can therefore adjust A_{RF} until the second magnetic pulse exactly cancels the first one. The exact setting of A_{RF} will depend on the decay of the classical mean value, β_{cl} .

Next, we repeat the feedback adjustment without a magnetic pulse in the beginning. The control signal will therefore be given by the measured quantum mechanical realizations of \hat{S}_y and \hat{J}_z . In Fig. 6.5 we show the first, second, and conditional variances as a function of the applied A_{RF} . As before we have separated out the atomic noise contribution and normalized to SN. We see a quadratic dependence of the noise of the second pulse on A_{RF} , which arises from the amplification of a stochastic signal with a constant factor proportional to A_{RF} . In the calculation of the variance this factor is squared. We also note, that at a specific RF voltage the second pulse noise coincides with the conditional one. Here, the mean value of the second pulse is no longer a certain fraction of the mean value of the first pulse. This proves that we have created an entangled state with zero mean, that is, unconditional entanglement, since the state has lower variance than the CSS variance indicated by the black line.

To make absolutely sure that this is not an experimental artifact we take a series of data points alternating between having the feedback on and off. This is shown in Fig. 6.6. As can be seen, without the feedback we retrieve the ordinary noise level for the second pulse. Note that Fig. 6.6 cannot prove any

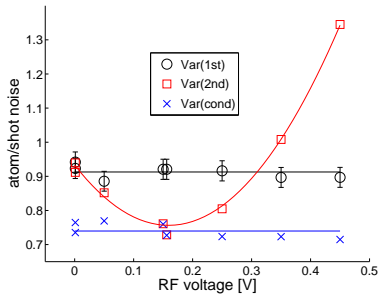


Figure 6.5: Atomic noise normalized to SN vs. feedback voltage. When the second pulse noise matches the conditional noise the mean value of the created state is zero, which implies unconditional entanglement.

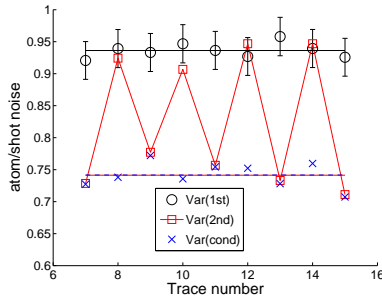


Figure 6.6: Deterministic entanglement generation. For a fixed atomic density negative feedback of the first pulse measurement is alternately turned on and off, thus switching between conditional and unconditional entanglement generation.

entanglement in itself. We need Fig. 6.2 to establish the projection noise limit, which has to be overcome.

Finally, the RF voltage at which we have quantum mechanical feedback, $A_{\text{RF,QM}}$, tells us something about the decay rate of quantum mean values:

$$A_{\text{RF,QM}} = \frac{\kappa^2}{1 + \kappa^2} \beta_{\text{QM}} \frac{A_{\text{RF,cl}}}{\beta_{\text{cl}}} \quad (6.1)$$

where the last factor establishes the voltage necessary to compensate for a mean value created by a pulse with $\kappa^2 \rightarrow \infty$ in the ideal case of no decoherence at all. In our experiment κ^2 is of the order of one and the created mean value compared to the feedback signal (the light) will therefore according to Eq. (3.16) be smaller by a factor $\beta\kappa^2/(1+\kappa^2)$, thus explaining the front factor in Eq. 6.1. Inserting the experimental values of $A_{\text{RF,cl}}$, $A_{\text{RF,QM}}$, and $\beta_{\text{cl}} = 0.78$ we get $\beta_{\text{RF,QM}} = 0.613$. The difference between the decay parameters is caused by the additional effective decoherence caused by the inhomogeneous coupling between the light and atoms when the light beam does not fill the entire cell. This is discussed in greater detail in appendix A.

6.3 Concluding Remarks on the Entanglement Experiments

The entanglement experiments discussed in this chapter represents fundamental improvements in two ways compared to the original entanglement experiment [62]. First, as discussed in Sec. 6.2 the entangled state has been created unconditionally. This means that no knowledge of the results of previous measurements

is required. Secondly and perhaps of more practical importance the entanglement is created between two atomic systems in separate environments 0.5 meters apart - a feat that had so far not been achieved between two atomic systems. This represents a major breakthrough towards the creation of truly distant entanglement, which combined with quantum teleportation will enable quantum communication over long distances. The distance can easily be extended by an order of magnitude or two but at longer distances propagation effects may decrease the coupling efficiency. If the light can be coupled into a fiber with sufficient efficiency between the samples, the distance may be increased but losses of light will fundamentally limit the obtainable degree of entanglement. Very recently entanglement between two atomic samples was also verified in [48, 50]. A detailed comparison between the results obtained in those experiments and ours is presented in Sec. 7.4.6

It proved quite an experimental challenge to create the distant entanglement because of the high demands on the homogeneity of the two atomic environments. In the following we present a short discussion of the main obstacles. Any difference in the Larmor precession frequency would quickly cause the two samples to dephase and thereby all entanglement is lost. The Stark shift compensation methods discussed in Sec. 5.3.2 was essential for the elimination of such effects. Another problem encountered was connected to the method of heating the cells. In the first implementation of the distant entanglement the cells were situated on top of an aluminum block, the temperature of which could be controlled through a flow of water. Instead of getting entanglement for this system the noise grew linearly with time (see [1]). The source turned out to be random thermal currents in the aluminum generating stochastic magnetic fields. Physically this corresponds to a rapid succession of RF pulses such as the ones described in Sec. 5.3, each with a random phase. This induces a random walk process in \hat{J}_y and \hat{J}_z for which the variance grows linearly in time. For this reason the current heating method consisting of an airflow was developed. Finally ground loops through the different wires of the setup turned out to shift the Larmor frequency so these also had to be located and fixed.

CHAPTER 7

Quantum Memory Results

Light inherently represents an ideal medium to transfer quantum information between distant sites. This property, however, also makes it fundamentally unsuited for storage of such information over significant periods of time. Remember that when dealing with quantum information one cannot simply measure the state and store the measurement results because the measurement result does not provide complete information about the state but rather projects the state into an eigenstate of the measurement observable. We will get back to this fundamental limitation on the classical storage of quantum states in Sec. 7.2.1. Because of the potentially long coherence times atomic media are optimal for storage. To implement a faithful storage the memory process will have to utilize some sort of quantum interactions between the input and the storage medium. In this chapter we will discuss the experimental implementation [62] of a quantum memory using a protocol called the "direct mapping protocol". In chapter 8 we describe the implementation of an alternative quantum memory based on a non-local transfer of the light state onto the target atomic state via a process called quantum teleportation [103].

For a complete quantum memory we require 1) that the light state to be stored is supplied by a third party in an unknown state, 2) that this state is mapped onto an atomic state with a fidelity higher than the best classical fidelity, and finally 3) that the stored state can be retrieved from memory. The first two criteria have been met experimentally in [104] and [103], whereas the last one still remains an unsolved experimental challenge for the reasons discussed in the introduction of chapter 9, where recently developed experimentally feasible protocols for retrieval will also be discussed.

7.1 Direct Mapping Protocol

In Eq. (2.34c) one of the light variables is mapped onto one of the atomic variables. This represents a natural starting point for a quantum memory protocol in which the entire light mode described by the two non-commuting variables \hat{x}_L^{in} and \hat{p}_L^{in} is faithfully stored. In the so-called "direct mapping protocol" of [104] the mapping is completed by measuring the remaining light quadrature $\hat{x}_L^{\text{out}} = \hat{x}_L^{\text{in}} + \kappa \hat{P}_a^{\text{in}}$ and feeding the result back into the atomic \hat{X}_a with an electronic gain of g :

$$\hat{X}_a^{\text{out}} = \hat{X}_a^{\text{in}} + \kappa \hat{p}_L^{\text{in}}, \quad (7.1a)$$

$$\hat{P}_a^{\text{out}'} = \hat{P}_a^{\text{out}} - g \hat{x}_L^{\text{out}} = \hat{P}_a^{\text{in}}(1 - \kappa g) - g \hat{x}_L^{\text{in}}. \quad (7.1b)$$

As discussed in Sec. 2.7 this interaction takes place for two decoupled sets of operators simultaneously involving the part of the light oscillating as $\cos(\Omega_L t)$ and $\sin(\Omega_L t)$ respectively. By putting different modulations into the cosine and sine parts of the incoming light we can therefore in principle store two independent light states simultaneously.

If $\kappa = g = 1$ and the initial atomic state is assumed to be a coherent state with zero mean value the mean values of both light variables are stored faithfully in the atoms. Although the initial atomic state has zero mean, it is a quantum mechanically fluctuating state, and any uncanceled atomic part increases the noise of the final state and thus degrades the mapping performance. This will be quantified in Sec. 7.2. Although this protocol works for any state, in the following we discuss storage of coherent states of light, i.e. vacuum states which are displaced by an unknown amount in phase space.

7.1.1 Mapping with Decoherence

Just as in the case of entanglement generation the spin states decohere. Again we can model this by a beam splitter type admixture of vacuum components right after the passage of the first light pulse. We can furthermore model light damping (e.g. reflection losses) in a similar way to obtain:

$$\hat{X}_a^{\text{out}} \rightarrow \beta(\hat{X}_a^{\text{in}} + \kappa \hat{p}_L^{\text{in}}) + \sqrt{1 - \beta^2} V_{XA}, \quad (7.2a)$$

$$\hat{P}_a^{\text{out}} \rightarrow (\beta - g\kappa\sqrt{1 - \epsilon})\hat{P}_a^{\text{in}} - g\sqrt{1 - \epsilon}\hat{x}_L^{\text{in}} + \sqrt{1 - \beta^2} V_{PA} - g\sqrt{\epsilon} V_{XL}, \quad (7.2b)$$

where ϵ is the fraction of the light power lost and V_{ij} are uncorrelated vacuum state operators. We see that \hat{p}_L^{in} and \hat{x}_L^{in} are mapped with gains $g_{BA} = \beta\kappa$ and $g_F = g\sqrt{1 - \epsilon}$ respectively. The variances can easily be calculated to be:

$$\text{Var}(\hat{X}_a^{\text{out}}) = \frac{1}{2} (1 + g_{BA}^2), \quad (7.3a)$$

$$\text{Var}(\hat{P}_a^{\text{out}}) = \frac{1}{2} \left(1 + \frac{g_F^2}{1 - \epsilon} + \frac{g_F^2 g_{BA}^2}{\beta^2} - 2g_F g_{BA} \right). \quad (7.3b)$$

7.2 Fidelity

As mentioned above the input state are displaced vacuum states. These have a Wigner function:

$$P_{\text{dv}}(x, p) = \frac{1}{2\pi\sqrt{\frac{1}{2} \cdot \frac{1}{2}}} \exp\left(-\frac{(x-x_1)^2}{2 \cdot \frac{1}{2}} - \frac{(p-p_1)^2}{2 \cdot \frac{1}{2}}\right), \quad (7.4)$$

where we inserted the coherent state variance $1/2$. By integrating over one of the variables x or p we obtain the probability distribution function of the other. The mean photon number in such a state described by mean values x_1 and p_1 is:

$$\langle \hat{n} \rangle = \frac{1}{2} \langle \hat{x}^2 + \hat{p}^2 - 1 \rangle = \frac{1}{2} (x_1^2 + p_1^2) \quad (\text{coherent states}), \quad (7.5)$$

where for the last equality we used the coherent state variance $\text{Var}(\hat{x}) = \langle \hat{x}^2 \rangle - \langle \hat{x} \rangle^2 = \frac{1}{2}$.

To evaluate the quality of mapping we calculate the fidelity of the output state (characterized by mean values x_2 and p_2 and variances σ_x^2 and σ_p^2) with respect to the input state. This is just the overlap between the two averaged over the input state distribution. We define the overlap (OL) as

$$\begin{aligned} \text{OL} &= \frac{1}{\pi\sigma_x\sigma_p} \int_{-\infty}^{\infty} e^{-(x-x_1)^2 - (x-x_2)^2/2\sigma_x^2} dx \int_{-\infty}^{\infty} e^{-(p-p_1)^2 - (p-p_2)^2/2\sigma_p^2} dp \\ &= \frac{2}{\sqrt{(1+2\sigma_x^2)(1+2\sigma_p^2)}} \exp\left(-\frac{(x_1-x_2)^2}{1+2\sigma_x^2} - \frac{(p_1-p_2)^2}{1+2\sigma_p^2}\right). \end{aligned} \quad (7.6)$$

With this definition the overlap is unity only when $x_1 = x_2$, $p_1 = p_2$, $\sigma_x^2 = \sigma_p^2 = 1/2$. In the experiments there is no significant offset error and the mean values are mapped faithfully between the right variables but with a gain which is not necessarily unity. This means that the input and output mean values are related by $x_1 \equiv x$, $p_1 \equiv p$, $x_2 = g_x x$, $p_2 = g_p p$. The extra noise imposed by the mapping procedure is assumed to be constant and independent of x_1 and p_2 . In this case the overlap function can be written

$$\text{OL}(x, p) = \frac{2}{\sqrt{(1+2\sigma_x^2)(1+2\sigma_p^2)}} \exp\left(-\frac{(1-g_x)^2 x^2}{1+2\sigma_x^2} - \frac{(1-g_p)^2 p^2}{1+2\sigma_p^2}\right) \quad (7.7)$$

The fidelity is now calculated by

$$F = \int_{-\infty}^{\infty} dx \int_{-\infty}^{\infty} dp P(x, p) \text{OL}(x, p) \quad (7.8)$$

where the appropriate input state distribution function must be chosen. We will assume a Gaussian distribution of displaced vacuum states given by

$$P(x, p) = \frac{1}{2\pi n_o} \exp\left(-\frac{x^2 + p^2}{2n_o}\right). \quad (7.9)$$

Using Eq. (7.5) we calculate the mean photon number of the distribution given in Eq. (7.9):

$$\int_{-\infty}^{\infty} dx \int_{-\infty}^{\infty} dp \frac{1}{2}(x^2 + p^2)P(x, p) = n_o. \quad (7.10)$$

It is very important to distinguish between the Eq. (7.4), which gives the probabilities of obtaining certain measurement results given a particular displaced vacuum state, and Eq. (7.9), which gives the probability of selecting a particular displaced vacuum state as the input state for a memory experiment. Correspondingly $\langle \hat{n} \rangle$ is the mean photon number of a particular state, whereas n_o is the mean photon number for a distribution of states.

The integration of Eq. (7.8) can be decomposed into pure x - and p -factors and is easily performed:

$$F(g_x, g_p, \sigma_x^2, \sigma_p^2) = \frac{2}{\sqrt{[2n_o(1 - g_x)^2 + 1 + 2\sigma_x^2] \cdot [2n_o(1 - g_p)^2 + 1 + 2\sigma_p^2]}}. \quad (7.11)$$

The experimental task now only consists of verifying that the mean value of the output state depends linearly on the mean value of the input state and to determine the experimentally obtained variances $\sigma_x^2(g_x)$ and $\sigma_p^2(g_p)$. For unity gain Eq. (7.11) reduces to:

$$F(\sigma_x^2, \sigma_p^2) = \frac{2}{\sqrt{[1 + 2\sigma_x^2] \cdot [1 + 2\sigma_p^2]}}. \quad (7.12)$$

For the storage of an arbitrary coherent light state using the direct mapping protocol without decoherence Eq. (7.1) and $\kappa = g = 1$ we can easily calculate the output state variance, since each canonical operator contributes a variance of $1/2$ (= one vacuum noise unit). One quadrature is mapped perfectly whereas the other contains two units of noise because of the remaining \hat{X}_a^{in} contribution. Inserting this into Eq. (7.12) we see that the optimal storage fidelity is 82%. This can be remedied by initially squeezing the atomic state, in which case 100 % fidelity can be reached in the limit of infinite squeezing.

7.2.1 The Best Classical Fidelity

To verify quantum mapping the experimentally determined fidelities have to exceed the best classical mapping performance. Briefly stated a classical mapping strategy, which recently was proven to be optimal [105], is first to split the light beam in two using a 50:50 beam splitter. Next, \hat{S}_y is measured in one output port and \hat{S}_z in the other. The results are then fed into orthogonal atomic components with a gain of $\sqrt{2}g$ (the $\sqrt{2}$ is to compensate for the reduction in the signal due to the beam splitter) giving:

$$\hat{X}_a^{\text{out}} = \hat{X}_a^{\text{in}} + \sqrt{2}g \frac{\hat{x}_1^{\text{in}} + \hat{x}_1^{\text{vac}}}{\sqrt{2}}, \quad \hat{P}_a^{\text{out}} = \hat{P}_a^{\text{in}} + \sqrt{2}g \frac{\hat{p}_1^{\text{in}} + \hat{p}_1^{\text{vac}}}{\sqrt{2}}. \quad (7.13)$$

This gives the variances $\text{Var}(\hat{X}_a^{\text{out}}) = \text{Var}(\hat{P}_a^{\text{out}}) = \frac{1}{2}(1 + 2g^2)$. When inserted into the expression for the fidelity, Eq. (7.11) we obtain:

$$F^{\text{class}} = \frac{1}{n_o(1-g)^2 + 1 + g^2}. \quad (7.14)$$

Differentiating this we obtain the optimal gain $g_{\text{opt}} = n_o/(1 + n_o)$, which gives the optimal classical fidelity:

$$F_{\text{opt}}^{\text{class}} = \frac{1 + n_o}{1 + 2n_o} \rightarrow \frac{1}{2}, \quad n_o \rightarrow \infty \quad (7.15)$$

for coherent states drawn out of a Gaussian distribution with mean photon number n_o . This means that $F_{\text{opt}}^{\text{class}}$ decreases monotonically from unity for the vacuum state to 1/2 for an arbitrary coherent state. The optimal classical mapping variance is:

$$\text{Var}(\hat{X}_a^{\text{class}}) = \text{Var}(\hat{P}_a^{\text{class}}) = \frac{1}{2} \left(1 + \frac{2n_o^2}{(1 + n_o)^2} \right) \rightarrow \frac{3}{2}, \quad n_o \rightarrow \infty. \quad (7.16)$$

That is, for an infinite input range, i.e. a flat distribution in phase space, and $g = 1$ the light state is mapped with the correct mean values in both quadratures and has three units of vacuum noise instead of the one unit in the initial state. The two additional units come from the vacuum noise introduced in the beam splitter and the initial atomic noise.

7.3 The Input State

The initial states for both the atomic and light systems will be coherent states. The statistical properties of such states have been discussed both theoretically and experimentally in previous chapters but always for vacuum states, i.e. states with zero mean value. For the mapping we wish to create a coherent state of light displaced by an arbitrary amount in $\hat{x}\hat{p}$ -space.

In our experiments we use electro-optical modulation to create weak coherent states with a controllable shift of \hat{S}_y and \hat{S}_z and thereby in \hat{x}_L and \hat{p}_L . We let light propagate in the z -direction and denote the complex field amplitude of the x - and y -polarization as E_x and E_y . (In this section we are only interested in the effect on the mean values of the light quadratures and therefore for now we ignore the quantum properties of the light.) The light passes an EOM with optical axis tilted by an angle θ from the x -axis. In an EOM the difference between the phase shifts experienced by light polarized along each of the two optical axes depends linearly on a voltage applied transversely to the direction of light propagation. The impact on the light is

$$\begin{bmatrix} E'_x \\ E'_y \end{bmatrix} = \begin{bmatrix} c^2 e^{i\delta_1} + s^2 e^{i\delta_2} & cs(e^{i\delta_2} - e^{i\delta_1}) \\ cs(e^{i\delta_2} - e^{i\delta_1}) & s^2 e^{i\delta_1} + c^2 e^{i\delta_2} \end{bmatrix} \begin{bmatrix} E_x \\ E_y \end{bmatrix}, \quad (7.17)$$

where δ_1 and δ_2 are the phase shifts along the optical axes of the EOM and $c = \cos \theta$, $s = \sin \theta$. Analogously to Eq. (2.5) Stokes operators are defined as

$$S_x = \frac{1}{2} (|E_x|^2 - |E_y|^2) \quad (7.18)$$

$$S_y = \frac{1}{2} (E_x^* E_y + E_y^* E_x) \quad (7.19)$$

$$S_z = \frac{1}{2i} (E_x^* E_y - E_y^* E_x) \quad (7.20)$$

Inserting Eq. (7.17) into these, the transformation of the Stokes operators after the EOM can be derived:

$$\begin{aligned} S'_x &= S_x \cdot [1 - \sin^2(2\theta) \cdot (1 - \cos(\delta_2 - \delta_1))] \\ &+ S_y \cdot [-\sin(2\theta) \cos(2\theta) \cdot (1 - \cos(\delta_2 - \delta_1))] \\ &+ S_z \cdot [-\sin(2\theta) \cdot \sin(\delta_2 - \delta_1)] \end{aligned} \quad (7.21)$$

$$\begin{aligned} S'_y &= S_x \cdot [-\sin(2\theta) \cos(2\theta) \cdot (1 - \cos(\delta_2 - \delta_1))] \\ &+ S_y \cdot [1 - \cos^2(2\theta) \cdot (1 - \cos(\delta_2 - \delta_1))] \\ &+ S_z \cdot [-\cos(2\theta) \sin(\delta_2 - \delta_1)] \end{aligned} \quad (7.22)$$

$$\begin{aligned} S'_z &= S_x \cdot [\sin(2\theta) \cdot \sin(\delta_2 - \delta_1)] \\ &+ S_y \cdot [\cos(2\theta) \cdot \sin(\delta_2 - \delta_1)] \\ &+ S_z \cdot [\cos(\delta_2 - \delta_1)] \end{aligned} \quad (7.23)$$

We note that for $\theta = 0$ S_x is conserved, whereas a rotation by an angle δ in $S_y S_z$ -space is implemented.

7.3.1 Modulation of Stokes Operators

Experimentally we modulate the Stokes operators by setting the EOM control voltage to a small RF-modulation around some static DC high-voltage V_{DC} . This gives a phase shift $\delta_2 - \delta_1 \equiv \delta_{\text{DC}} + \delta$ where δ_{DC} is controlled by changing V_{DC} and δ is time-varying with $|\delta| \ll 1$. We also take $\theta \ll 1$ and assume the initial conditions $S_y = S_z = 0$. Then to first order in δ we have

$$\begin{aligned} S'_x &= S_x [1 - 4\theta^2 (1 + \delta \sin \delta_{\text{DC}} - \cos \delta_{\text{DC}})] \\ S'_y &= S_x \cdot (-2\theta) [1 - \cos(\delta_{\text{DC}}) + \sin(\delta_{\text{DC}})\delta] \\ S'_z &= S_x \cdot 2\theta [\sin(\delta_{\text{DC}}) + \cos(\delta_{\text{DC}})\delta] \end{aligned} \quad (7.24)$$

By tuning δ_{DC} we can decide whether the modulation should be in \hat{S}_y or \hat{S}_z and can thus span the entire \hat{S}_y - \hat{S}_z phase space. Our EOM has a half wave voltage of ca. 400V. In the experiment we apply a weak RF-field giving a phase shift

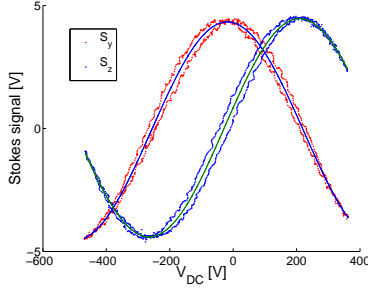


Figure 7.1: Mean values of \hat{S}_y and \hat{S}_z while applying a small RF-voltage matched with the Larmor frequency and a slowly varying offset voltage to the EOM.

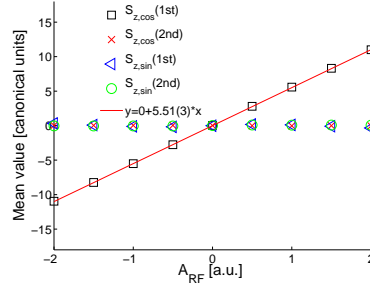


Figure 7.2: Calibration of the input light state modulation as a function of the size of the RF control. Only the first pulse is modulated and $\langle \hat{S}_y \rangle$ is locked to zero.

$\delta = \delta_{\text{RF}} \cos(\Omega t + \phi)$, which gives:

$$\begin{aligned}
 \langle \hat{x}_c \rangle &= \sqrt{\frac{2}{S_x T}} \int_0^T \langle S_y \rangle \cos(\Omega t) dt = -\sqrt{2S_x T} \theta \delta_{\text{RF}} \cos(\phi) \sin \delta_{\text{DC}} , \\
 \langle \hat{x}_s \rangle &= \sqrt{\frac{2}{S_x T}} \int_0^T \langle S_y \rangle \sin(\Omega t) dt = \sqrt{2S_x T} \theta \delta_{\text{RF}} \sin(\phi) \sin \delta_{\text{DC}} , \\
 \langle \hat{p}_c \rangle &= \sqrt{\frac{2}{S_x T}} \int_0^T \langle S_z \rangle \cos(\Omega t) dt = \sqrt{2S_x T} \theta \delta_{\text{RF}} \cos(\phi) \cos \delta_{\text{DC}} , \\
 \langle \hat{p}_s \rangle &= \sqrt{\frac{2}{S_x T}} \int_0^T \langle S_z \rangle \sin(\Omega t) dt = -\sqrt{2S_x T} \theta \delta_{\text{RF}} \sin(\phi) \cos \delta_{\text{DC}} ,
 \end{aligned} \tag{7.25}$$

where we used $\cos(\Omega t + \phi) = \cos(\Omega t) \cos(\phi) - \sin(\Omega t) \sin(\phi)$. We see that the relative size of the modulation in the sine and cosine subsystems is controlled by the phase of the RF-signal, ϕ , the relative size of \hat{S}_y and \hat{S}_z is controlled via the offset voltage, δ_{DC} , and the overall size of the modulation can be controlled via the strength of the RF-signal, δ_{RF} . In Fig. 7.1 we plot $\langle \hat{x}_c \rangle$ and $\langle \hat{p}_c \rangle$ as a function of the DC-voltage applied to the EOM. As expected from Eq. (7.25) we get sinusoidal curves of equal amplitude but shifted by 90° with respect to each other. In the mapping experiment we split off a portion of the light after the EOM and use it to lock either to $\langle \hat{S}_y \rangle = 0$ or $\langle \hat{S}_z \rangle = 0$. For each, we run sets of 10,000 measurement cycles at various values of δ_{RF} . In each cycle δ_{RF} is only non-zero during the first pulse. Analogous to the shot noise calibration prior to the entanglement experiment we calculate the variance of the light state based on the 10,000 repetitions of an identical measurement cycle with the atoms turned off. Varying δ_{RF} we verify that the variance is always equal to the vacuum shot noise level. Thus, we really do create minimum uncertainty displaced vacuum states. To quantify the displacement we calculate the mean value for each set of

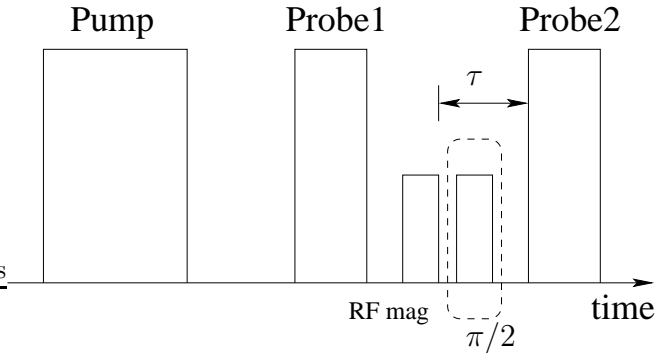


Figure 7.3: A four ms optical pump prepares the atoms in the CSS. After a short delay the first probe pulse is sent through the atoms and subsequently measured. A feedback using an RF magnetic pulse completes the mapping. After a storage time τ the second probe pulse is sent through the atoms to reconstruct the atomic statistics. A series of 10,000 cycles without (with) a $\pi/2$ pulse read out information about $\hat{P}_a(\hat{X}_a)$.

10,000 cycles. The result is transformed into canonical units by:

$$\langle \hat{x}_L \hat{p}_L \text{ units} \rangle = \frac{\langle \text{meas units} \rangle}{\sqrt{2} \sqrt{\text{meas variance}}} \cdot \frac{1}{\sqrt{1-\epsilon}}, \quad (7.26)$$

where the factor $\sqrt{2}$ ensures a vacuum variance of $\frac{1}{2}$ and $\sqrt{1-\epsilon}$ reconstructs the value in the cell instead of at the detector. The results for such a calibration of the input state modulation is shown in Fig. 7.2. Here \hat{S}_y is locked to zero and only the cosine quadrature of the first pulse is modulated. From the linear fit to the mean value as a function of the strength of the applied RF-signal we extract a slope which in the actual mapping experiment will be used to calculate the size of the input modulation. In Sec. 7.4.1 this will be compared to the second pulse mean value to establish the gain. Using Eq. (7.5) we can determine the mean number of photons in the displaced vacuum states of Fig. 7.2 to range from zero to 50 photons.

7.4 Experimental Results

Once the input state has been properly calibrated the atoms are turned back on and we implement an experimental cycle (see Fig. 7.3), which is almost identical to the one used to create unconditional entanglement in Sec. 6.2. After the CSS has been created during the pumping pulse we send a light pulse with a known modulation in either \hat{S}_y or \hat{S}_z through the atomic samples. We then measure \hat{S}_y of the transmitted beam and feed the measurement result back with a certain electronic gain. If properly done, this completes the mapping. At the time of the experiment no experimentally feasible protocol for the retrieval of a stored state existed. The reasons for this and the recent theoretical proposals to circumvent

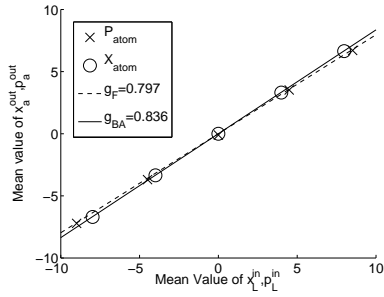


Figure 7.4: Mean value of the read out pulse as a function of the mean values of the input light variables, \hat{X}_L^{in} and \hat{p}_L^{in} , to be stored.

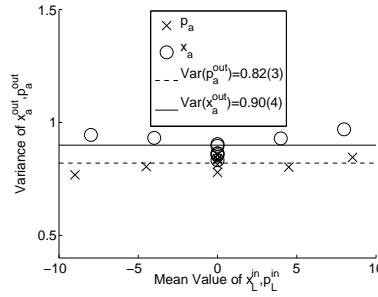


Figure 7.5: Variance of the atomic quadratures, \hat{X}_a^{out} and \hat{P}_a^{out} , as a function of the mean values of the input light variables.

the difficulties are presented in detail in chapter 9. Instead we have performed a destructive reconstruction of the mapped state. This is done by waiting for a time τ and then sending a verification light pulse through the atomic sample. Measuring the \hat{x}_L -component of the outgoing light then gives information about the light component stored in the atomic \hat{P}_a according to Eq. (2.34a). If a $\pi/2$ rotation in the atomic $\hat{X}_a\hat{P}_a$ space is performed prior to the verification pulse we obtain information about the stored atomic \hat{X}_a -component. Repeating this 10,000 times, we can reconstruct the statistics for the atomic variables after the storage procedure.

7.4.1 Mean Values

The first thing to check is that the mean value of the stored state depends linearly on the mean value of the input light state. In analogy to Eq. (7.26) the former are obtained from experimental values via the transformation:

$$\langle \hat{X}_a \hat{P}_a \text{ units} \rangle = \frac{\langle \text{meas units} \rangle}{\sqrt{2} \sqrt{\text{meas SN variance}}} \cdot \frac{1}{\kappa \sqrt{1 - \epsilon}}, \quad (7.27)$$

where the factor $\frac{1}{\kappa}$ compensates for the κ in Eq. (2.34a). κ is calculated by multiplying the Faraday angle which is measured for both pulses in each measurement cycle, with a precalibrated projection noise slope obtained as discussed in Sec. 5.6.

The reconstructed atomic mean values are shown in Fig. 7.4. First we note that the linear dependence is clear for both quadratures. This completes the proof of classical memory performance. The next thing to note is that the slope is not unity, which means that the stored state has a different mean value than the input state. The reason for this is the presence of the light induced collisions introduced in Sec. 5.4. This will be discussed further in Sec. 7.4.5. For the quadrature mapped straight from the back action of the light onto the atoms

(verification pulse without a $\pi/2$ -pulse) we have the gain of $g_{\text{BA}} = 0.836$ and for the quadrature mapped via the feedback (verification pulse with a $\pi/2$ -pulse) we have $g_{\text{F}} = 0.797$. Inserting the values on the x-axis of Fig. 7.4 into Eq. (7.5) we see that the experiment covers input modulations up to ~ 40 photons.

7.4.2 Variances

In order to verify quantum storage we also need to consider the shot-to-shot fluctuations in the stored state, which for a Gaussian state are fully characterized by the variance of the state. Just as in the entanglement experiment we find the atomic contribution to the variance of the verification pulse by subtracting the shot and electronic noise from the measured variance. Dividing the atomic contribution by $(1 - \epsilon)\kappa^2$ we obtain the atomic variance, which should ideally be given by Eq. (7.3). Again we see that knowledge about the exact size of κ is important for the reconstruction of the atomic statistics. Luckily, however, the uncertainty in the final fidelity estimate depends only weakly on κ which can be understood as follows: if κ is higher than estimated, the variance of the stored state is actually lower than estimated leading to an underestimation of the fidelity. At the same time, however, the gain factor is also lower leading to an overestimation of the fidelity. Thus, the two effects oppose each other making the fidelity estimate rather robust against variations in κ . Also note that κ refers to the interaction strength in the atomic cells. Therefore, if we calculate κ using Eq. (5.22) with the *measured* power instead the light power in the cell, we will automatically incorporate the factor $1 - \epsilon$. This is very convenient since it means that we do not need to know the precise value of ϵ to reconstruct the atomic variances reliably.

In Fig. 7.5 we show the reconstructed atomic variances corresponding to the measurements for which the mean values are plotted in Fig. 7.4. As can be seen the variance is more or less independent of the mean value of the input light quadratures. Also, the variances are lower than $3/2$ so if the gain had been unity this would have been adequate proof of a quantum storage. Since, however, the gain is not unity, we have to restrict the input range to a Gaussian subset of coherent states with a mean photon number n_o and compare the calculated fidelity with the general classical bound given in Eq. (7.15). In Fig. 7.6 we show the experimental fidelity calculated by inserting the reconstructed gains and variances into Eq. (7.11) along with the classical fidelity bound for different values of n_o . The experimental mapping fidelities are well above the classical bound for $1 \leq n_o \leq 16$. In particular we obtain e.g. $F = (66.7 \pm 1.7)\%$ for $n_o = 4$ and $F = (70.0 \pm 2.0)\%$ for $n_o = 2$, which should be compared to the classical fidelities of 55.6% and 60.0%. The uncertainties are calculated based on the uncertainties in the determination of the atomic mean values and variances and a 2.5% uncertainty in κ^2 , which for this experiment was around 1.06. The difference between our experimental fidelities and the classical bound is plotted in Fig. 7.7 illustrating that we have exceeded the classical bound by up to 11%. This verifies that the storage of the light state in fact constitutes a quantum

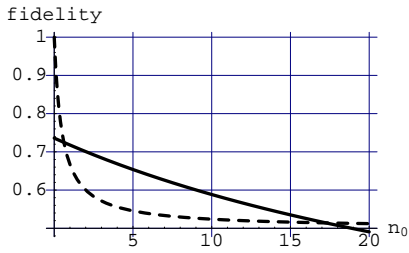


Figure 7.6: Solid: Fidelity vs. n_o based on the data from figures 7.4 and 7.5. Dashed: classical fidelity bound.

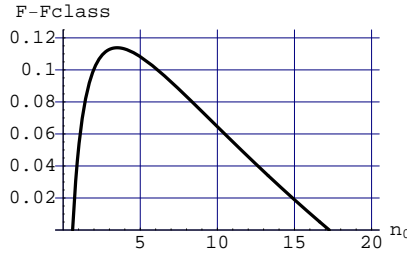


Figure 7.7: $F - F_{\text{opt}}^{\text{class}}$ (both from Fig. 7.6) vs. n_o

mapping. The results shown were obtained for a pulse duration of 1 ms.

Note that we have chosen to calculate the fidelity as the average of the squared overlap between the stored state and the ideally stored state. For non-unity gain this decreases very rapidly with coherent states having large amplitudes. However, one could argue that a storage with an arbitrary but known gain constitutes just as useful a memory as unity gain memory. If analyzed solely in terms of the added noise, our memory would perform better than the previously stated results, which can therefore be viewed as a lower bound on the memory capability.

7.4.3 Varying the Feedback Gain

In a more extensive experimental investigation we have measured the atomic variances for several different electronic feedback gains with fixed κ and thus fixed g_{BA} . The results are shown in Fig. 7.8. As expected $\text{Var}(\hat{X}_a^{\text{out}})$ is independent on g_{F} and $\text{Var}(\hat{P}_a^{\text{out}})$ depends quadratically on g_{F} exactly as predicted in Eq. (7.3). We plot this prediction with g_{BA} and the independently measured decoherence parameters of $\beta = 0.61$ and $\epsilon = 0.25$, which for such a simple theory gives quite remarkable agreement. The figure clearly shows that, because of the decoherence and light loss, if the feedback gain is increased towards unity the noise grows dramatically. We also find the best quadratic fit to the data, which is inserted into the fidelity expression Eq. (7.11) to obtain the fidelity as a function of g_{F} and n_o only. Optimizing over g_{F} we find the optimum fidelity for a given input range. This optimized fidelity is plotted in Fig. 7.9 along with the optimal g_{F} . Thus, the range of states for which we exceed the classical bound can be extended to $1 \leq n_o \leq 30$ by appropriately adjusting the feedback gain compared to the $g_{\text{F}} = 0.797$ used in Sec. 7.4.2. As can be seen the optimal gain approaches unity for high photon numbers but is significantly lower than unity for low photon numbers. The reason is that for low distribution widths a more prominent role is played by the vacuum contribution (which is perfectly transferred for zero gain and $\kappa = 0$). For e.g. $n_o = 2$ $n_o = 4$ the optimal gains are $g_{\text{F}} = 0.656$ and $g_{\text{F}} = 0.774$ respectively. Thus, the gain of Sec. 7.4.2 was more or less optimal for $n_o = 4$ (as illustrated in Fig. 7.7) whereas the fidelity for $n_o = 2$ could be

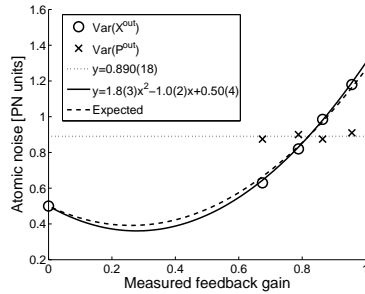


Figure 7.8: Reconstructed variances of \hat{X}_a^{out} (o's) and \hat{P}_a^{out} (x's) as a function of feedback gain. The back action gain determined by κ is kept constant.

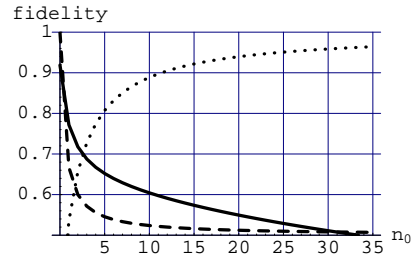


Figure 7.9: Solid: Optimal experimental fidelities based on fits from Fig. 7.8 vs. n_o . Dotted: Optimal feedback gain. Dashed: Classical boundary.

increased to $F = 0.718$.

As can be seen from the values of β and ϵ the atomic decoherence and the light loss are significant. The high light loss is due to the fact that the glass cells containing the atomic vapor were not anti-reflection coated. Therefore each glass-air interface contributes about 4% loss. Again, the main source of atomic decoherence is the light assisted collisions discussed in Sec. 5.4.

7.4.4 Memory Life Time

Next we wish to investigate the life time of the stored state in the atomic memory. To do this, we perform the entire storage procedure for a number of different storage times, τ . This was done for $\tau = 0.6, 2.6, 4.6, 9.6$ ms for fixed κ and electronic feedback strength. Both gains decay exponentially as expected with characteristic decay times 26(3)ms and 31(4)ms for g_{BA} and g_{F} respectively. According to Eq. (5.12) this corresponds to a Γ_{dark} of 12.2Hz and 10.3Hz, which agrees very well with the independently measured rates quoted in Sec. 5.4. Based on the experimental gains and variances the fidelity of storage as a function of the storage time can be calculated for different choices of input range. This is shown in Fig. 7.10 for $n_o = 2, 4, 6, 10$. As can be seen the fidelity exceeds the best classical for about 5 ms for the low input ranges at which our memory is optimal.

7.4.5 Why Not Unity Gain

In conclusion, we would like to address the question why we do not perform the experiments at unity gain and hence eliminate the need for a restricted input range. As we have seen, this is no problem for the quadrature being mapped through the electronic feedback. For the one being mapped directly through the interaction, however, it is quite different. From Eq. (7.2) we see that the effective gain for this quadrature is given by $g_{\text{BA}} = \beta\kappa$. This dependence is tested in Fig.

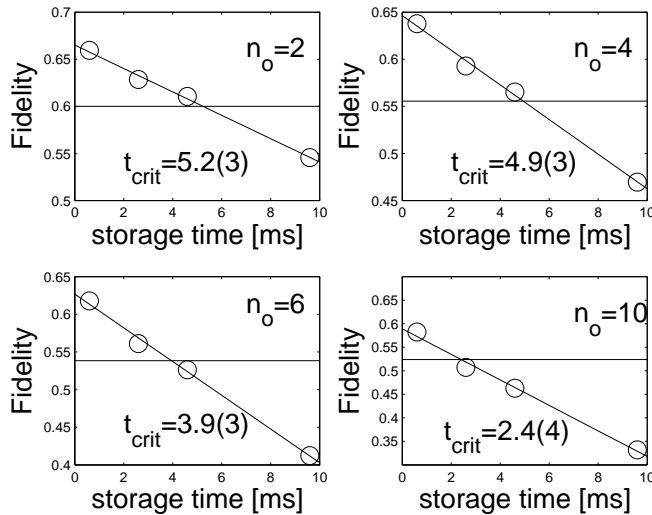


Figure 7.10: Fidelity vs. storage time for different input ranges.

7.11, where the mapping is performed for various light powers and the measured back action gain is plotted as a function of the independently determined $\kappa\beta$. The unity slope verifies our prediction for the gain.

In Sec. 5.4 the light induced collisions were characterized in detail. Here it was shown that $\beta = e^{-\Gamma t}$, where Γ depends linearly on the light power and the atomic density exactly as κ^2 does. We can therefore write the back action gain as $g_{\text{BA}} \propto \sqrt{P} \cdot \rho e^{-a \cdot P \cdot \rho}$, where P is the optical power and ρ is the atomic density. In Fig. 7.12 we fit such a dependence to the gain measured at various powers at fixed atomic density ($\theta_F = 11^\circ$). The dependence is verified and from the fit we can calculate that the back action reaches a maximum of 0.84 around 11mW after which it will decrease towards zero.

There are two potential ways of reaching higher back action gains. First one can decrease the part of the atomic decoherence coming from the atomic motion. According to Eq. (A.4) this can be done by either increasing the beam size (here $A_{\text{beam}}/A_{\text{cell}} \sim 1/3$) or the pulse duration. In fact, for the experiments discussed in the next chapter the probe duration has been increased to 2.0 ms. The second possibility is to exploit the fact that the light induced collision rates seem to fall off more rapidly with detuning than κ^2 ($\sim 1/\Delta^{3.7}$ compared to $1/\Delta^2$). This is still an ongoing experimental investigation.

7.4.6 Concluding Remarks

In this chapter the first quantum mechanical storage of a light pulse in an atomic medium was presented. For an appropriate range of input states the fidelity of

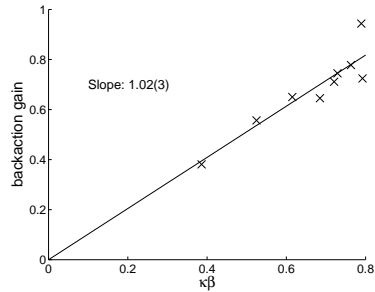


Figure 7.11: Measured g_{BA} vs. independently determined $\kappa\beta$. Linearity with unity slope is predicted in Eq. (7.2).

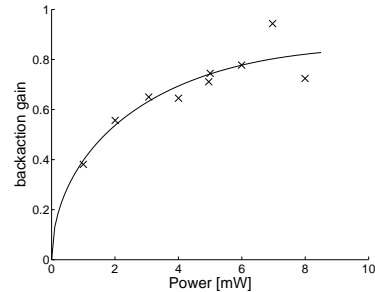


Figure 7.12: Measured g_{BA} vs. optical power. ($\theta_F = 11^\circ$)

storage exceeds the classical boundary by more than six standard deviations. The restriction of the input range is necessary because of the high decoherence rate.

One might pose the question why our quantum memory is better than just storing the light pulse in an empty cavity. The brief answer is that the latter cannot be done. To see this consider the storage of a pulse with the spectral width $\delta\nu_{store} = 1/T_{pulse}$. To represent a storage device the lifetime of the cavity $\tau = 1/\gamma$ has to be long compared with T_{pulse} . γ , however, sets the width of any spectral profile that can be coupled into the cavity. Thus, we see that only a fraction of the pulse can be coupled into the cavity and it is therefore unsuitable as a storage device.

Finally we would like to comment on the relation of our experiments to the so-called "stopped light" experiments performed using electromagnetically induced transparency (EIT). In EIT [38, 39] an otherwise opaque medium becomes effectively transparent to a weak *probe* through quantum interference with a strong *control* beam (see Fig. 7.13). The effect is illustrated in Fig. 7.14, where it can be seen that the reduction in absorption is accompanied by a dramatic increase in the slope of the index of refraction. This leads to a reduction in the group velocity and corresponding spatial compression of the pulse by several orders of magnitude [40, 106, 107]. If the compression is sufficiently large so that the entire pulse is at some point entirely contained within the sample, the control field can be turned off and the probe pulse will be "frozen" in the sample. At a later time the control field can be turned back on and the probe pulse will propagate out. In 2001 this was verified experimentally in two remarkable experiments [41, 42].

The process can be described in terms of a dressed state excitation called a *dark state polariton* [108], which does not couple to the excited level. By adjusting the intensity of the control field, excitations in the light (photons in the probe field) can coherently be transferred to atomic excitations (ground state coherences) and vice versa. Although this sounds very much like a complete

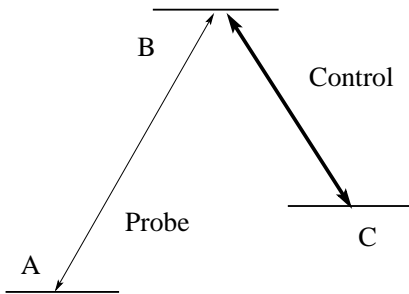


Figure 7.13: The level scheme employed in EIT.

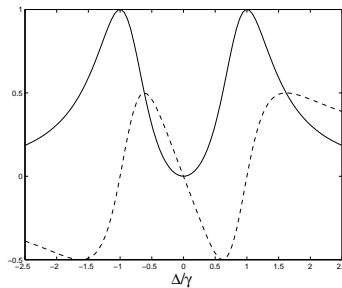


Figure 7.14: Absorption (solid) and dispersion (dashed) as a function of detuning of a weak probe field from the $A - B$ transition (Fig. 7.13) while the strong control field is resonant with the $B - C$ transition.

storage and retrieval process, two things should be noted. In the experiments only the intensity profile of the stored pulse was retrieved, so no phase coherence was verified. Second, and more importantly the retrieval efficiency was very poor $\sim 10 - 20\%$. By now we know that losses correspond to the admixture of vacuum, so clearly this is detrimental to the quantum memory fidelity.

In a seminal paper [51] the authors (DLCZ) proposed to entangle two atomic ensembles by combining a spontaneously emitted photon from each on a beam splitter and placing single photon detectors in the output ports (see Fig. 7.15). As shown in Fig. 7.15 a) all the atomic population is optically pumped into level A . A weak beam slightly detuned from the $A - B$ transition will with a certain probability drive a Raman transition and hence create a photon with a frequency determined by the $B - C$ transition accompanied by a single atom in level C . Just as in our experiments the interaction is coherently enhanced so the actual generated state will be a coherent superposition of each atom being in C and the rest in A . This is done for both samples simultaneously and after filtering out the strong component the two fields are combined on a beam splitter. If a exactly one detector clicks this will mean that exactly one atom made the transition from A to C . If the two beam paths are indistinguishable this implies that the two samples are entangled.

As a next step another set of entangled samples is created and using the EIT dynamics the atomic excitations of one sample from each pair is mapped onto single photons and again combined on a beam splitter (d) in Fig. 7.15). The outputs are again detected and a single click implies that the remaining atomic excitation is shared between the two last ensembles (2 and 4 in Fig. 7.15). In this way the entanglement distance is doubled. If in a pulse a single click is not produced, the procedure is merely repeated. The scheme has built in entanglement purification and could therefore potentially lead to quantum

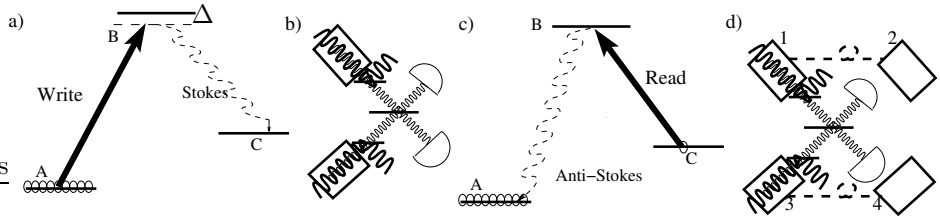


Figure 7.15: Generation of entanglement between two distant atomic ensembles following the DLCZ proposal. a) and b) entanglement of two separate samples. c) and d) Transforming entanglement of systems 1 with 2 and 3 with 4 into entanglement between 2 and 4.

networks connected by entanglement over arbitrary distances.

A lot of experimental effort has been put into the realization of the DLCZ scheme in recent years and the advances have been impressive. In 2003 the non-classical statistics between the spontaneously emitted Stokes photon and the anti-Stokes light generated when subsequently converting the atomic excitation in the same ensemble into light using EIT [44, 43]. Two years later entanglement between the photon generated as in Fig. 7.15 a) and an atomic qubit composed of two distinct mixed states of the collective ground state hyperfine coherences was demonstrated [47]. As in the ion-photon [28] and the atom-photon [29] entanglement mentioned in the introduction the entanglement was probabilistic and selected through coincidence counts. In experiments the same year [46, 49] the Stokes photon was used to herald the creation of an atomic excitation. Subsequently, this was converted converted into an anti-Stokes photon, which was stored in another atomic ensemble using EIT. After a programmable delay the excitation was mapped to light and analyzed. Non-classical correlations between the heralding photon and the retrieved light was confirmed. This sounds very much like a complete mapping and retrieval of a quantum state, which in fact it was also called in the title of [49]. One should, however, note that the storage and retrieval efficiency was never higher than 10%. This means that analyzed in terms of the fidelity of the output state compared to the ideal state the large vacuum component would probably exclude surpassing a classical limit.

Shortly after, two atomic ensembles were entangled [48, 50] via a realization of the first half of the DLCZ scheme (see Fig. 7.15 a) and b)). Thus, a single atomic excitation was shared between the two ensembles. The entanglement was analyzed by mapping the state of each ensemble into light and measuring the correlations between the two light fields. They were, in fact, shown to be entangled, so in addition to proving the entanglement between distant atomic ensembles, this also represents the first realization of transfer of an atomic entangled state onto an entangled state of light. Although the entanglement generation is probabilistic, it is unambiguously heralded and no correction for detection efficiency, propagation loss, or background subtraction has been performed. It thus truly represent a remarkable achievement in the field of quantum communication. One

should, however, be careful about assuming that this approach can easily be extended to storage and retrieval of arbitrary unknown quantum states such as e.g. qubits or coherent states, since the problem of poor retrieval efficiency has so far not been resolved.

In conclusion, the main advantage of this approach to entanglement generation compared to ours is the fact that it is inherently based on discrete variable entanglement and hence can potentially be purified and extended to arbitrary distances. This cannot be done with our continuous variable Gaussian state entanglement. In terms of the light-atom interface, however, our deterministic approach seems superior at present because the high coupling efficiency (low losses) enables higher than classical fidelity transfer of arbitrary states.

CHAPTER 8

Light Atom Teleportation

In 1993 Bennett and coworkers proposed a protocol where information about an unknown quantum state could be distributed over a quantum channel and a classical channel and reassembled at another location [17]. Through this *quantum teleportation* an unknown state could be recreated in a target system that never physically interacted with the input system.

The generic protocol of quantum teleportation is sketched in Fig. 8.1. First, a pair of entangled objects is created and shared by two parties, Alice and Bob. This step establishes a quantum link between them. Next, Alice receives an object to be teleported and performs a joint measurement on this object and her entangled object (a Bell measurement). In this way she does not obtain any information about the unknown state. Rather, this information is now distributed between the measurement result and the quantum mechanical correlations in the entangled pair. The result of the measurement is communicated via a classical communication channel to Bob, who uses it to perform local operations on his entangled object, thus completing the process of teleportation. Both the classical and the quantum channels are crucial for the protocol since at no point in the protocol information about the unknown state is entirely in one of them. The teleportation distance is set by the distance by which the entangled pair can be created. This is why the entanglement of two object in separate environments discussed in Sec. 6 represents a fundamental improvement compared to previous atomic entanglement experiments such as [26, 62]. The original proposal uses discrete qubit-type entanglement such as a spin singlet composed of two spin $1/2$ particles. In 1994 an adaptation of the scheme to continuous variables (CV) was proposed in [53].

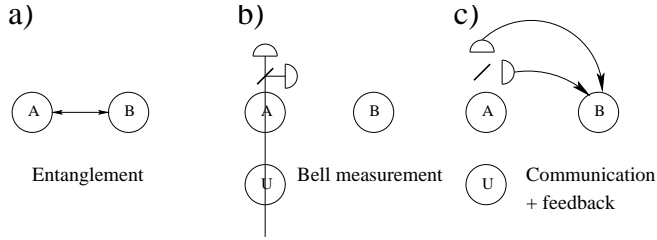


Figure 8.1: Generic teleportation scheme.

Quantum teleportation was first demonstrated using discrete states of light (single photons) [57, 109, 110] and briefly afterwards for continuous variables of light [111]. Unlike previous implementations the teleportation in this experiment worked deterministically. In the following years light teleportation was further improved with qubit teleportation over a distance of 4 km using optical relays [112], CV tripartite quantum teleportation network [113], where teleportation of an unknown quantum state can occur between any pair, but only with the assistance of the third party, and CV teleportation exceeding the $F=2/3$ no-cloning limit and entanglement swapping [58, 59]. Recently, the first demonstration of atomic teleportation was reported in [114, 115]. In both experiments a qubits state of one ion in a trap was teleported onto another ion. The teleportation distance was $\sim 5\mu\text{m}$. Apart from being the first atomic teleportation, this was also the first implementation of deterministic teleportation of a discrete variable state.

In this chapter we present the experimental results for the first demonstration of teleportation between an atomic state and a light state [103]. It is implemented through a novel protocol [65] utilizing the light-atom entanglement generated in the single cell interactions (2.42). With a teleportation distance $\sim 0.5\text{m}$ it represents an increase of a factor 10^5 compared to previous atomic teleportation experiments [114, 115].

To further illustrate the procedure we will briefly review the CV teleportation protocol using perfectly EPR entangled states originally proposed in [53]. Alice and Bob have states characterized by the canonical variables (X_A, P_A) and (X_B, P_B) respectively. They are prepared in a perfectly EPR entangled state such that $X_A - X_B = 0$ and $P_A + P_B = 0$. Thus, the uncertainty of these combinations is zero. Alice receives an unknown state characterized by (X_u, P_u) . She performs a measurement of $X_A - X_u$ and $P_A + P_u$ and transmit the results to Bob via a classical communication channel. Bob displaces each of the quadratures of his system by one of the results and ultimately obtains $X_B^{\text{out}} = X_B - (X_A - X_u) = X_u$ and $P_B^{\text{out}} = P_B + (P_A + P_u) = P_u$. So we see that with infinite EPR entanglement teleportation with unity fidelity can be achieved.

8.1 Light Atom Teleportation with the Faraday Interaction

We would like to perform teleportation of a light state onto an atomic state using the Faraday interaction. First we consider using the light-atom entanglement generated in the regular two cell QND interaction Eq. (2.34). To do this we let Alice's entangled object be a light pulse $(\tilde{X}_L, \tilde{P}_L)$ that has passed through the two samples. Bob's entangled object will consist of the two atomic samples. Next, another light pulse (X_L, P_L) is sent to Alice, who mixes the two beams on a 50:50 beam splitter. In one output port she measures \hat{S}_y and in the other \hat{S}_z . With a feedback of $\sqrt{2}g$ we obtain:

$$\begin{aligned} X_A^{out} &= X_A^{in} + \kappa \tilde{P}_L^{in} - g(\tilde{P}_L^{in} - P_L) = X_A^{in} + (\kappa - g)\tilde{P}_L^{in} + gP_L \\ P_A^{out} &= P_A^{in} - g(\tilde{X}_L^{in} + \kappa P_A^{in} + X_L) = (1 - \kappa g)P_A^{in} - g\tilde{X}_L^{in} - gX_L. \end{aligned} \quad (8.1)$$

Unity gain is achieved with $g = 1$ and in this setting $\kappa = 1$ clearly minimizes the noise, which when inserted into Eq. (7.12) gives the optimal fidelity $F = \frac{2}{3}$.

The reason for the relatively low fidelity is that the type of entanglement generated in the QND interaction is far from the optimal EPR type of entanglement. Looking at equations (2.34) we see that the different quadratures are just not mixed sufficiently together. In the single cell interaction Eq. (2.42) the degree of mixing is higher since the \hat{p}_a is no longer conserved:

$$\begin{aligned} \hat{x}_c^{out} &= \hat{x}_c^{in} + \frac{\kappa}{\sqrt{2}}\hat{p}_a^{in} + \left(\frac{\kappa}{2}\right)^2 \hat{p}_s^{in} + \frac{1}{\sqrt{3}}\left(\frac{\kappa}{2}\right)^2 \hat{p}_{s,1}^{in}, & \hat{x}_a^{out} &= \hat{x}_a^{in} + \frac{\kappa}{\sqrt{2}}\hat{p}_c^{in} \\ \hat{x}_s^{out} &= \hat{x}_s^{in} - \frac{\kappa}{\sqrt{2}}\hat{x}_a^{in} - \left(\frac{\kappa}{2}\right)^2 \hat{p}_c^{in} - \frac{1}{\sqrt{3}}\left(\frac{\kappa}{2}\right)^2 \hat{p}_{c,1}^{in}, & p_a^{out} &= p_a^{in} + \frac{\kappa}{\sqrt{2}}\hat{p}_s^{in}, \end{aligned} \quad (8.2)$$

This complex type of multi-mode entanglement turns out to be even worse than the QND type entanglement for teleportation of either a cosine or a sine mode. The maximal achievable fidelity is only $F = \sqrt{2/5} \approx 63.25\%$. To take full advantage of the single cell entanglement one should instead teleport the upper sideband given by a combination of the cosine and sine modes:

$$\hat{y} = \frac{1}{\sqrt{2}}(\hat{y}_s + \hat{q}_c), \quad \hat{q} = -\frac{1}{\sqrt{2}}(\hat{y}_c - \hat{q}_s), \quad (8.3)$$

where \hat{y}_i and \hat{q}_i ($i = c, s$) are the canonical variables corresponding to \hat{S}_y and \hat{S}_z respectively. As in chapter 7 the input states will be displaced vacuum state generated by an EOM as described in Sec. 7.3. For the sideband variables we have:

$$[\hat{y}, \hat{q}] = i, \quad \langle \hat{n} \rangle = (\langle \hat{y} \rangle^2 + \langle \hat{q} \rangle^2)/2. \quad (8.4)$$

As illustrated in Fig. 8.2 this field is mixed with the strong light pulse which carries the entanglement with the atoms on a 50:50 beam splitter. In one of the

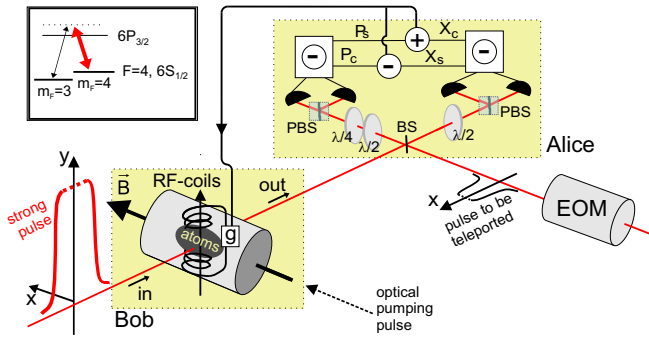


Figure 8.2: The teleportation setup used in our experiment. By sending a strong pulse of light through an atomic sample entanglement between the two systems is generated. Alice receives the entangled pulse of light, whereas Bob has the atoms. On Alice's site the entangled pulse is mixed with the pulse to be teleported on a 50:50 beam splitter (BS). A Bell measurement in the form of homodyne measurements of the optical fields in the two output ports of the BS is carried out and the results are transferred to Bob as classical photo currents. Bob performs spin rotations on the atoms to complete the teleportation protocol.

output arms we measure \hat{S}_y :

$$\hat{X}_{c,s} = \frac{1}{\sqrt{2}}[\hat{x}_{c,s}^{\text{out}} + \hat{y}_{c,s}], \quad (8.5)$$

while in the other we measure \hat{S}_z :

$$\hat{P}_{c,s} = \frac{1}{\sqrt{2}}[\hat{p}_{c,s}^{\text{out}} - \hat{q}_{c,s}]. \quad (8.6)$$

This completes the Bell measurement giving four results, $\hat{X}_{c,s}$ and $\hat{P}_{c,s}$. The light quadratures to be teleported are now contained in the combinations:

$$\hat{Q} = \hat{X}_c + \hat{P}_s = \frac{1}{\sqrt{2}}[\hat{x}_c^{\text{out}} + \hat{p}_s^{\text{out}}] - \hat{q}, \quad \hat{Y} = \hat{X}_s - \hat{P}_c = \frac{1}{\sqrt{2}}[\hat{x}_s^{\text{out}} - \hat{p}_c^{\text{out}}] + \hat{y}. \quad (8.7)$$

Feeding these combinations back onto the atoms with electronic gains $g_{x,p}$ we get:

$$\begin{aligned} \hat{x}_a^{\text{tele}} &= \hat{x}_a^{\text{out}} + g_x \hat{Y} = \hat{x}_a^{\text{out}} + \frac{g_x}{\sqrt{2}}[\hat{x}_s^{\text{out}} - \hat{p}_c^{\text{out}}] + g_x \hat{y} \\ \hat{p}_a^{\text{tele}} &= \hat{p}_a^{\text{out}} - g_p \hat{Q} = \hat{p}_a^{\text{out}} + \frac{g_p}{\sqrt{2}}[\hat{x}_c^{\text{out}} + \hat{p}_s^{\text{out}}] + g_p \hat{q}. \end{aligned} \quad (8.8)$$

This step completes the teleportation protocol. Obviously if $g_{x,p} = 1$ the mean values of the input state are transferred faithfully, thus constituting a successful *classical* mapping. In order to achieve *quantum* teleportation the variance of

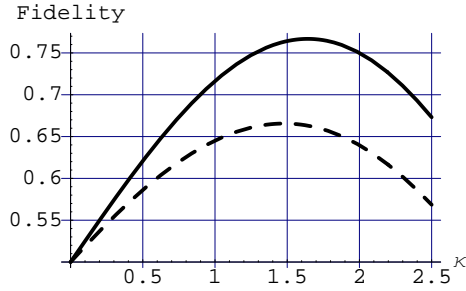


Figure 8.3: Theoretical teleportation fidelity without decoherence (solid) based on Eq. (8.9) and with realistic noise parameters (dashed), $\beta = 0.8$ and 10% light loss.

the output state has to be smaller than the classical bound Eq. (7.15). The mechanism enabling this is the interspecies entanglement between the auxiliary light pulse and the atomic sample through which the contribution from the terms \hat{x}_a^{in} , \hat{p}_a^{in} , \hat{p}_c^{in} , and \hat{p}_s^{in} can be canceled. To see this we assume unity gain and insert equations (8.2) into (8.8):

$$\begin{aligned}\hat{x}_a^{\text{tele}} &= \left(1 - \frac{\kappa}{2}\right) \hat{x}_a^{\text{in}} - \frac{1}{\sqrt{2}} \left(1 - \frac{\kappa}{2}\right)^2 \hat{p}_c^{\text{in}} + \frac{1}{\sqrt{2}} \hat{x}_s^{\text{in}} - \frac{1}{\sqrt{6}} \left(\frac{\kappa}{2}\right)^2 \hat{p}_{c,1}^{\text{in}} + \hat{y}, \\ \hat{p}_a^{\text{tele}} &= \left(1 - \frac{\kappa}{2}\right) \hat{p}_a^{\text{in}} - \frac{1}{\sqrt{2}} \left(1 - \frac{\kappa}{2}\right)^2 \hat{p}_s^{\text{in}} - \frac{1}{\sqrt{2}} \hat{x}_c^{\text{in}} - \frac{1}{\sqrt{6}} \left(\frac{\kappa}{2}\right)^2 \hat{p}_{s,1}^{\text{in}} + \hat{q}\end{aligned}\quad (8.9)$$

The atomic variance can be calculated exactly as was done for the quantum mapping. The resulting fidelity can be seen in Fig. 8.3. The optimum fidelity is $F = 0.77$ obtained at $\kappa = 1.64$. Just as in Sec. 7.1.1 atomic decoherence and light loss can be modeled by a beam splitter type admixture of vacuum. The result for $\beta = 0.8$ and 10% light loss is also shown in the figure. For these parameters the optimal fidelity is $F = 0.67$ at $\kappa = 1.48$.

8.2 Experimental Verification

In the experimental realization we split off a small fraction of the beam and send it through an EOM to create the state to be teleported. The remaining part of the light passes through a single atomic sample and is recombined with the weak beam on the beam splitter. This requires interferometric stability, which will be addressed in Sec. 8.3. The 2.0 ms probe is followed by an 0.2ms RF feedback pulse, which completes the teleportation protocol. The experiment was performed at a detuning $\Delta = 825\text{MHz}$. To prove that we have successfully performed quantum teleportation we have to determine the fidelity of the experimentally teleported state w.r.t the input state. Towards this end, exactly as in the entanglement and quantum mapping experiments, we send a second strong verifying pulse through the atoms after the teleportation is completed. Unlike

in the previous two experiments the verification is done with a 50:50 beam splitter after the atomic sample. The atomic signal is contained in $\hat{x}_{c,s}^{\text{out}}$ which is only measured in one of the outputs. This adds vacuum noise, which has to be corrected for in the reconstruction process. On the other hand information about both atomic quadratures can be retrieved in a single pulse. This simplifies the reconstruction process compared to the mapping experiment, where the reconstruction was performed in two series - one of which with a $\pi/2$ pulse in the atomic xp -space prior to the verification pulse. In the verification step we thus measure $\hat{X}_{c,s}^{\text{ver}} = \frac{1}{\sqrt{2}}[\hat{x}_{c,s}^{\text{out}} + \hat{y}_{c,s}]$, where $\hat{y}_{c,s}$ are now vacuum operators and $\hat{x}_a^{\text{in}} = \hat{x}_a^{\text{tele}}$ in Eq. (8.2).

8.2.1 Verifying the Mean Values

Calculating the mean values of the measured quadratures Eq. (8.7) of the verifying pulse we get:

$$\begin{aligned} \langle \hat{X}_c^{\text{ver}} \rangle &= \frac{\kappa}{2} \langle \hat{p}_a^{\text{tele}} \rangle = \frac{g_p \kappa}{2} \langle -\hat{Q} \rangle = \frac{g_p \kappa}{2} \langle \hat{q} \rangle, \\ \langle \hat{X}_s^{\text{ver}} \rangle &= \frac{\kappa}{2} \langle \hat{x}_a^{\text{tele}} \rangle = \frac{g_x \kappa}{2} \langle \hat{Y} \rangle = \frac{g_x \kappa}{2} \langle \hat{y} \rangle. \end{aligned} \quad (8.10)$$

Thus, we see that plotting the second pulse results vs. appropriate combinations of the first pulse results we can find the electronic feedback strength giving unity gain. The verifying pulse causes deterministic decoherence of the atomic mean values, which means that a factor $e^{-\Gamma\tau}$ has to be added to Eq. (8.10). In the experiment half the pulse duration was $\tau = 1.0\text{m sec}$, $\Gamma = 0.09(\text{m sec})^{-1}$, and $\kappa = 0.93$, which means that we expect $\langle \hat{X}_c^{\text{ver}} \rangle / \langle \hat{Q} \rangle = \langle \hat{X}_s^{\text{ver}} \rangle / \langle \hat{Y} \rangle = 0.91 \cdot 0.93/2 \approx 0.42$. In Fig. 8.4 (a) \hat{X}_c^{ver} is plotted as a function of \hat{Q} for 10,000 teleportation attempts with a slowly scanned input state phase after the electronic gain has been calibrated. This means that the mean photon number in the input pulse is constant but the modulation varies sinusoidally in time between the \hat{q} and \hat{y} . The linear fit gives a slope of 0.4248 ± 0.0010 . This along with a similar result for the other quadrature (\hat{X}_s^{ver} vs. \hat{Y}) represent the proof of the successful *classical* transfer of the mean values of the quantum mechanical operators \hat{Y} and \hat{Q} of the input light pulse onto the atomic state.

8.2.2 Reconstructing the Atomic Variances

As in the context of the quantum mapping experiment, the crucial step is to verify that the reconstructed atomic variances are lower than the classical bound. In order to derive a reconstruction procedure based on measured results we first note that in the absence of an atomic interaction we would measure $\hat{X}_{c,s}^{\text{ver}} = (\hat{x}_{c,s} + \hat{y}_{c,s})/\sqrt{2}$, which exactly add up to one unit of noise. we will call this $\text{Var}(SN)_{\text{meas}}$. Inserting (8.2) into (8.5) an expression for the reconstructed variance based on

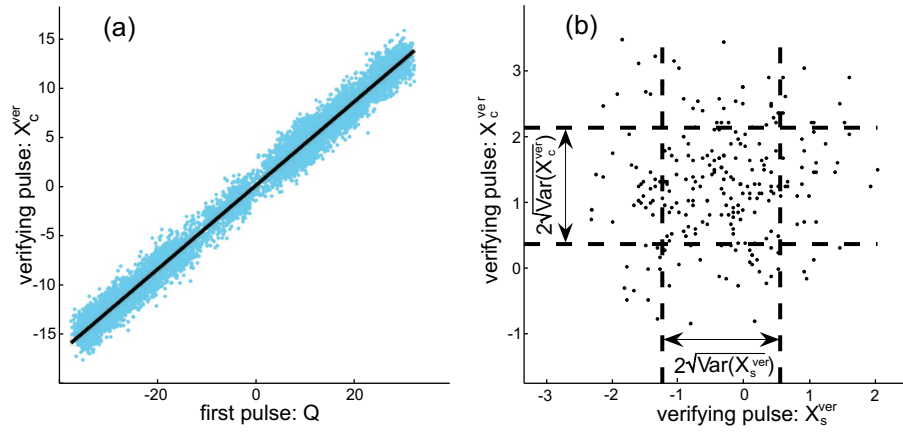


Figure 8.4: a) Calibration of the teleportation feedback gain by comparison certain combinations of the first pulse results with the verifying pulse results. The coherent input state used has a mean photon number of $\langle \hat{n} \rangle \approx 500$ and is slowly modulated in phase during the 10,000 measurement cycles presented here. b) An example of data from which the atomic variance after the teleportation is determined. Here $\langle \hat{n} \rangle \approx 5$ and the phase is fixed.

the variance of the verification pulse can be derived:

$$\text{Var}(\hat{p}_a^{\text{tele}}) = \frac{1}{2} \frac{4}{\kappa^2} \frac{\text{Var}(\hat{X}_c^{\text{ver}}) - \text{Var}(SN)_{\text{meas}}(1 + \kappa^4/24) - \text{Var}(E_{x,c})}{\text{Var}(SN)_{\text{meas}}}, \quad (8.11)$$

where $\text{Var}(E_{x,c})$ is the electronic noise corresponding to the time interval of the verifying pulse and the factor $\frac{1}{2}$ establishes the canonical variance. This equation is valid for canonical units as well as for the raw data values coming directly from the integral of the output of the lockin amplifiers over the pulse duration. Equation (8.11) thus gives the full recipe for the reconstruction of the atomic variances based on the raw data.

8.2.3 Calculating the Fidelity of Teleportation

The experiment was repeated for a number of different mean photon numbers $\langle \hat{n} \rangle = 0$ (vacuum), 5, 20, 45, 180, 500. The atomic tomographic reconstruction of each showed that the variances could be grouped into two sets, one with $\langle \hat{n} \rangle \leq 20$ and another with $\langle \hat{n} \rangle > 20$. Within each set the variance was found to be independent on the input state, but for the set containing higher photon numbers the value of the variances was slightly higher. Please remember that as discussed in Sec. 7.2 we wish to calculate the fidelity corresponding to a set of coherent input states with a mean photon number $\langle \hat{n} \rangle$ distributed according to a Gaussian with a width n_o . Thus, when estimating fidelities with $n_o \leq 20$ we use the set of measurements taken at low photon

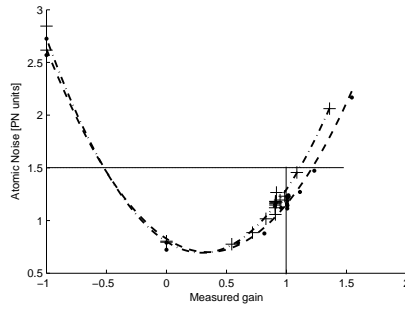


Figure 8.5: Reconstructed atomic variances vs. feedback gain $g_{x,p}$.

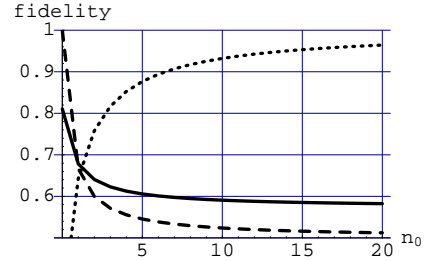


Figure 8.6: Optimal fidelity vs. the width of the input state distribution (solid) and the best classical fidelity (dashed). Dotted: the optimal feedback gain.

numbers only, whereas for $n_o \geq 20$ we include both sets. For each set we repeated the experiment for various values of the gain.

The results for $n_o \leq 20$ are shown in Fig. 8.5. First of all, it is clear that the variances of both atomic quadratures are well below $\frac{3}{2}$ at unity gain. Since, however, the data is not valid for an infinitely broad input distribution the classical boundary is different from $\frac{3}{2}$ and the optimal gain is not unity. From the quadratic fit predicted by theory we obtain $\text{Var}(\hat{x}_a^{\text{tele}})(g_x)$ and $\text{Var}(\hat{p}_a^{\text{tele}})(g_p)$ which can be inserted into the expression for the fidelity Eq. (7.11). Of course at this point our experimental observation that the variances are independent of $\langle \hat{n} \rangle$ is crucial. Just like in the case of quantum mapping the fidelity is now a function of n_o , g_x , and g_p only, which can easily be optimized with respect to g_x and g_p yielding the optimized fidelity vs. the width of the input state distribution n_o . The result of this optimization is shown in Fig. 8.6. As can be seen the experimental fidelity exceeds the best classical for $n_o \geq 2$. In particular we get $F_2 = 0.64 \pm 0.02$, $F_5 = 0.60 \pm 0.02$, $F_{10} = 0.59 \pm 0.02$, and $F_{20} = 0.58 \pm 0.02$, where the classical benchmarks are calculated from Eq. (7.15) $F_{2,5,10,20}^{\text{class}} = 0.60; 0.545; 0.52; 0.51$. The uncertainties in the results are obtained by varying each of the uncertain parameters in the reconstruction process and then adding the deviations quadratically:

$$\begin{aligned} SD(F) &= \sqrt{\delta_{\text{PN}}^2 + \delta_{\text{SN}}^2 + \delta_{\text{el}}^2 + \delta_{\text{SNR}}^2 + \delta_{\text{fit}}^2 + \delta_{\text{g}}^2} \\ &= 10^{-2} \sqrt{1.0^2 + 1.65^2 + 0.1^2 + 0.3^2 + 0.2^2 + 1.2^2 + 0.8^2} \approx 0.02, \end{aligned} \quad (8.12)$$

where δ_{PN} , δ_{SN} , and δ_{el} are the contributions to the $SD(F)$ due to fluctuations in the projection noise, shot noise, and electronics noise respectively, δ_{β} is the uncertainty due to fluctuations in the atomic decay constant, δ_{SNR} is the contribution from fluctuations in the ratio of the responses of two pairs of detectors, δ_{fit} is the deviation due to the uncertainty of the quadratic fit in Fig. 8.5, and δ_{g} is

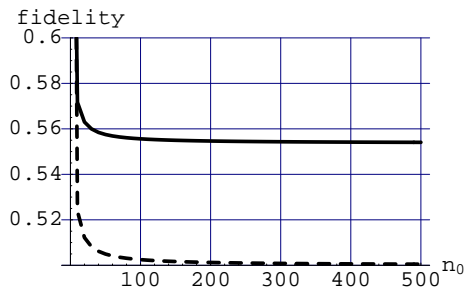


Figure 8.7: Optimal fidelity vs. the input state distribution width including the data taken at high modulations (solid). Dashed: best classical fidelity.

the contribution from gain fluctuations. The experimental violation of the classical bound is somewhat smaller than the result obtained for quantum memory in chapter 7, but it is nevertheless statistically significant.

For input states which are significantly displaced from vacuum even small fluctuations in the classical gain will lead to a detrimental displacement of the teleported state with respect to the input state thus producing a dramatically decreased fidelity. As discussed previously we do in fact observe an increase in the reconstructed variance at higher photon numbers, however since it seems to be more or less constant in the range $\langle \hat{n} \rangle = [45; 500]$ we must ascribe this to some instabilities in the teleportation setup other than the classical gain. As mentioned previously the reconstructed variances corresponding to measurements in the range $\langle \hat{n} \rangle = [20; 500]$ at various gains are a little higher than for the low modulation and the scattering is somewhat larger. Inserting the result of the quadratic fit into the expression for the fidelity and optimizing w.r.t. the gain we find the optimal fidelity vs. n_o , which is shown in Fig. 8.7. As can be seen the fidelity quickly saturates such that for $n_o > 20$ we get $F = 0.56 \pm 0.03$.

8.3 Experimental Considerations

One of the main differences between the quantum mapping and the teleportation setups is the fact that for the latter we need to combine two fields on a beam splitter. In order for the entire theoretical discussion following the introduction of the beam splitter to be valid the two fields in the input ports have to be perfectly coherent. This means that scanning the phase of one beam should (for equal powers in the two inputs) result in subsequent total destructive- and constructive interference. Of course this can only be achieved if the two fields are derived from the same laser source so a Mach-Zender type interferometer has to be assembled. Also the path length difference (here typically a few cm) should be much smaller than the coherence length of the laser, which for the TOPTICA diode laser is $\sim 70\text{m}$.

Experimentally we cannot achieve perfect overlap between the two modes so

the EOM. We just claim teleportation for the mode completely overlapping spatially and temporally with the strong local oscillator field, A . For teleportation of coherent states this is no problem since a coherent state with an arbitrary admixture of vacuum is still a coherent state. If the exact shape of the teleportation mode is unknown to Alice (which will usually be the case for $v \neq 1$) she can get exact knowledge of the state she is sending (in the mode \hat{b}_A) by using the first teleportation attempt as a calibration stage to determine the size of v . With this she can subsequently prepare an arbitrary coherent state by varying the modulation amplitude on the EOM and the phase of the interferometer. This calibration would then be valid as long as the interferometer overlap stayed stable, which in our case is typically hours. This of course only works because of the robustness of the coherent states against losses. If the input state was a single photon state in the mode \hat{b} , teleportation of the mode \hat{b}_A with $v \approx 0.5$ would not produce a single excitation in the atomic target. Thus, to enable teleportation of a non-classical light state the present setup would have to be refined.

Even though we are only interested in teleporting the mode characterized by \hat{b}_A it is important to know what the effect of the mode \tilde{b} is on the teleportation outcome. To do this we calculate the result of the \hat{S}_y measurement in one output of the beam splitter:

$$S_y = \frac{A\sqrt{q}}{2} [\hat{x}_a + \cos(\eta + \phi)\hat{x}_{\tilde{b}_A} - \sin(\eta + \phi)\hat{p}_{\tilde{b}_A}] + \frac{Ar_x\sqrt{p}(1-v)}{2} [\cos(\eta - \chi)\hat{x}_{\tilde{b}} - \sin(\eta - \chi)\hat{p}_{\tilde{b}}], \quad (8.15)$$

where $\hat{x}_k = (\hat{k} + \hat{k}^\dagger)/\sqrt{2}$, η is a phase shift introduced by the coating of the beam splitter, and χ and q , describing the strength and phase of the strong local oscillator after the beam splitter, are introduced for compactness:

$$\sqrt{q}e^{i\chi} = t_x + r_x\sqrt{pv}e^{i\phi}. \quad (8.16)$$

Remember that \hat{x}_a carries the atomic contribution and $\hat{x}_{\tilde{b}_A}$ and $\hat{p}_{\tilde{b}_A}$ carry the modulation to be teleported, so we have coherent terms (\hat{b}_A), which contribute to the teleportation, and incoherent terms (\tilde{b}), which tend to destroy the teleportation fidelity. It is now interesting to compare the size of these two which is roughly determined by:

$$\frac{\langle \text{incoh} \rangle}{\langle \text{coh} \rangle} = \frac{Ar_x\sqrt{p}(1-v)/2}{A\sqrt{q}/2} = \frac{r_x\sqrt{p}(1-v)}{\sqrt{q}}. \quad (8.17)$$

Since $q = t_x^2 + r_x^2pv + 2t_xr_x\sqrt{pv}\cos\phi$, it is clear that when varying the interferometer phase ϕ q will vary in the range $[q_{\min} = (t_x - r_x\sqrt{pv})^2 : q_{\max} = (t_x + r_x\sqrt{pv})^2]$. In Fig. 8.9 the boundaries of Eq. (8.17) are plotted as a function of the power p in the EOM arm relative to the strong field arm. As can be seen, even for $p = 0.1$ about 20% of the measured mean values arises from the incoherent terms in Eq. (8.15).

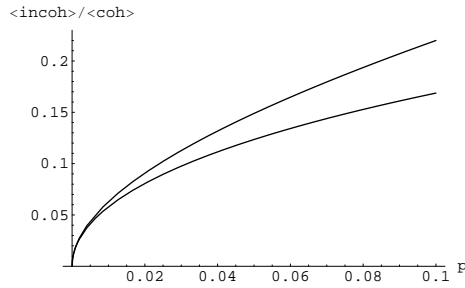


Figure 8.9: The ratio of the size of the incoherent to the coherent terms in the mean value as a function of the power in the signal arm relative to the strong field passing through the atoms. . When varying the phase of the input state the ratio will vary between the two plotted extremes. The experimental result presented in this chapter were obtained at $p \approx 0.01$

This, however, is not the only effect. More seriously, the process of reconstructing the atomic variances has to be modified because $\text{Var}(SN)_{\text{meas}}$ in Eq. (8.11) now also contains the incoherent terms from the last half of Eq. (8.15). The size of the correction is roughly the square of the incoherent to coherent ratio of Eq. (8.17). Thus, at $p = 0.1$ it would be $\sim 4\%$, which is quite an important correction.

The interferometer introduced another major experimental challenge. Every single frequency laser of course is not perfectly monochromatic but rather has a finite line width $\delta\nu$. If the difference between the optical path lengths in the two arms of the interferometer ΔL is non-zero different frequency components will interfere differently. Thus, if the spectral density at the frequency of interest (in our case 322kHz) is high a significant amount of phase noise can be converted into amplitude noise in this process. For $\Delta L = 0$ all frequency components experience the same shift (zero) and this effect disappears (white light position). In the very early phases of the teleportation experiment the Ti:Saph laser was used. It has a line width $\delta\nu < 300\text{kHz}$ so no phase to amplitude noise conversion was observed ($\Delta L \approx 10\text{cm}$). At some point the amplitude noise of this laser increased dramatically (to $\sim 20\text{dB}$ above shot noise), so it was replaced by the TOPTICA diode laser. This laser has a line width $\Delta\nu \approx 6\text{MHz}$, which of course means that the spectral density around 322kHz is much larger. Indeed, when coupling into the interferometer with the new laser we observed a large dependence of the amplitude noise after the interferometer on the ΔL .

As a solution to the described problems with the interferometer we instead decided to turn down the power in the EOM arm dramatically. At $p = 0.01$ the contribution of incoherent mean values is $\sim 4\%$ giving a contribution of $\sim 0.2\%$ to the variance estimate. Simultaneously of course the phase to amplitude noise conversion was reduced drastically since it is caused by the interference fringes of the fields at the two inputs of the beam splitter. The only negative effect is

that the interferometer can no longer be locked and hence the phase of the input state drifts at the time scale of thermal fluctuations ($\sim 1\text{min}$). As described in Sec. 8.2.1 instead of letting the phase drift it was actively scanned by slowly modulating the length of the EOM-arm with a piezo-element. From this the gain can be established from a single series of 10,000 cycles unlike in the quantum memory experiment where several series at different modulation strengths had to be taken. The atomic reconstruction process, however, is made slightly more complicated by the varying phase. In order to reduce statistical uncertainties in the reconstruction process sufficiently at least 10,000 individual teleportation runs have to be employed. For this purpose we divide the data into bins each containing such a low number of points that the input state can be considered constant. Within each bin we then find the reconstructed atomic variance and in the end we average this result over all of the bins. The results obtained in this way have been presented in the previous sections.

CHAPTER 9

Quantum Memory Retrieval

As discussed in chapter 7 storage of quantum states with a fidelity exceeding the classical boundary has been demonstrated experimentally, whereas retrieval of a stored state from a quantum memory still remains an unresolved challenge. In this chapter we will describe why retrieval is much more challenging experimentally when using the Faraday interaction and room temperature gas samples. We will then derive two protocols for retrieval which should be experimentally feasible in the current setup. We should warn the reader that the level of mathematical detail is very much increased in this chapter compared to the preceding experimental chapters. Both protocols are based on solving for the dynamics arising when a light beam is reflected back through the atomic sample after the passage (see Fig. 9.1). The complexity arises because the pulse is assumed to be so long that the different passages occur simultaneously in which case the dynamics is no longer the simple QND type. One protocol is based on two passages of the light and is essentially an extension of an existing protocol [116] and it has the same limitations on the achievable fidelity. The second protocol is based on four passages and in principle allows for complete storage and retrieval with unit fidelity - only requiring sufficient interaction strength. The fidelity will be given both for coherent input states and for qubit input states. This illustrates that although the system is based on continuous variables it can still accommodate inherently discrete states (which of course also have a continuous variable Wigner representation). In the treatment we will largely ignore the effects of decoherence although they will be discussed briefly in the context of the main four-pass protocol. Finally we would like to draw the attention to two similar results on retrieval using the Faraday interaction published almost simultaneously as the

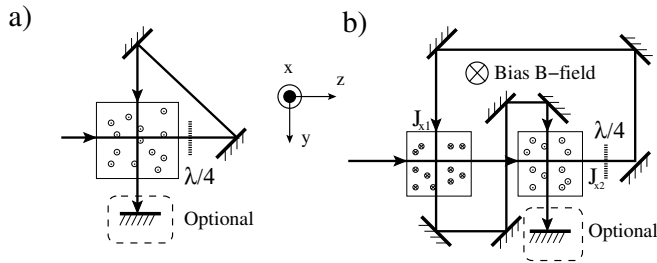


Figure 9.1: Schematic of the multi-pass protocol. a) The light is sent through the atomic sample along the z - and then along the y -direction. We reflect the light back onto the sample to improve the performance by two further passages of the light beam (optional). b) Schematic of an implementation with two atomic samples with oppositely oriented mean spin in a homogeneous magnetic field.

one discussed in this chapter.

In principle the stored state can be retrieved by inverting the roles of light and atoms in the direct mapping protocol. This would involve first an interaction between a read-out light beam with the atomic sample acting as a storage medium. According to Eq. (2.34a) this would map \hat{P}_a onto the light. Next \hat{X}_a has to be measured and feedback applied to the read-out beam according to the result of the measurement. Since, however, the atomic measurement requires a certain time during which the read-out pulse propagates at the speed of light, the feedback is only practical for pulse durations shorter than a microsecond. In the mapping experiments described in chapter 7 pulses of millisecond duration ($\sim 300\text{km}$ pulse length) are required in order to obtain a sufficiently high interaction strength, and the inverse direct mapping protocol is thus infeasible for this experimental realization.

Several years ago a quantum memory scheme, which does not involve measurements, but instead uses two orthogonal passages of the read-out pulse was proposed in Ref. [116]. The first passage is along the z -direction giving rise to the by now well known $H \propto \hat{P}_a \hat{p}_L$ interaction. After a 90° rotation in \hat{x}_L - \hat{p}_L space the light is sent through the atomic sample along the y -direction, creating a $H \propto \hat{X}_a \hat{x}_L$ interaction. This can be implemented in the two physically distinct setups illustrated in Fig. 9.1: a) with a single atomic sample and b) with two oppositely oriented samples atomic samples in a constant bias magnetic field. In the latter case, as we have seen before, the two cells combine to a single system with the same QND-type interaction as a single cell. If the two passages are separated in time (requiring a delay line at least the size of the pulse length) the dynamics is merely a sequence of QND interactions. After the second passage we obtain:

$$\begin{aligned} \hat{p}_L^{\text{out}} &= (1 - \kappa^2) \hat{p}_L^{\text{in}} - \kappa \hat{X}_a^{\text{in}} , & \hat{x}_L^{\text{out}} &= \hat{x}_L^{\text{in}} + \kappa \hat{P}_a^{\text{in}} , \\ \hat{P}_a^{\text{out}} &= (1 - \kappa^2) \hat{P}_a^{\text{in}} - \kappa \hat{x}_L^{\text{in}} , & \hat{X}_a^{\text{out}} &= \hat{X}_a^{\text{in}} + \kappa \hat{p}_L^{\text{in}} , \end{aligned} \quad (9.1)$$

where for mathematical convenience we have also applied a 90° rotation to the light after the second passage. The protocol both maps the light properties on the atoms and the atomic properties on the outgoing light. For $\kappa = 1$, mean values are faithfully stored. Calculating the output variances for coherent input states and inserting these into the fidelity expression, Eq. (7.12), uncanceled contributions from \hat{X}_a^{in} or \hat{x}_L^{in} will limit the fidelity of storage or retrieval to 82%. By initially squeezing these variables (e.g. $\hat{X}_a \rightarrow \hat{X}_a/\sqrt{\varepsilon}$, $\hat{P}_a \rightarrow \hat{P}_a\sqrt{\varepsilon}$), the fidelity may be increased towards 100%. We note that in the case of mapping this exactly reproduces the dynamics of the direct mapping protocol discussed in Sec. 7. Here the measurement of the light after a single passage and subsequent feedback onto the atoms mimics the dynamics of the second passage with respect to the atomic evolution. With respect to the dynamics of the light state the two-pass protocol is equivalent with the reverse direct mapping protocol discussed in the beginning of this chapter and it is equally inapplicable to the case of long optical pulses.

Our solution to these problems involves three novel features [117]: we allow the probe pulse to travel through the atomic sample in two orthogonal directions simultaneously, we apply a novel scheme involving four passages of the light, and we apply a time varying interaction strength. The resulting protocol can be used for storage or retrieval symmetrically. No squeezing is required and since the interaction strength in the Faraday interaction depends on the number of atoms and the number of photons there is no fundamental limit to the achievable fidelity for this protocol.

9.1 Two-pass Dynamics

We will start by treating the case of simultaneous passage for the two-pass protocol just discussed. As shown in Fig. 9.1 it can be implemented both for a single sample without a bias magnetic field and for two oppositely oriented samples with a magnetic field. We know from Sec. 2.7 that both case give rise to a QND type interaction for a single passage, so therefore we will in this chapter stick with the capitalized atomic notation. As mentioned in the introduction we will later in this chapter discuss a four-pass scheme which will be superior in terms of storage and retrieval fidelity. The reason for also presenting the two-pass protocol is threefold. First, it serves as an introduction to the mathematical methods. Second, since it is based on fewer passages the experimental implementation is simpler and the reflection losses are greatly reduced. Finally, certain dynamics arises in this protocol which has no precedent in previous protocols nor in the four-pass protocol that will enable the production of squeezed light. This will be discussed in greater detail in chapter 10.

We treat the case of simultaneous passage by taking the $\tau \rightarrow 0$ limit of a sequence of coarse grained Hamiltonian $H_\tau \propto \kappa_\tau \hat{P}_a \hat{p}_L$ and $H'_\tau \propto \kappa_\tau \hat{X}_a \hat{x}_L$. This gives the Hamiltonian

$$H(t) = \tilde{\kappa}(t) \hat{P}_a(t) \hat{p}_L(t, t) + \tilde{\kappa}(t) \hat{X}_a(t) \hat{x}_L(t - T_1, t) , \quad (9.2)$$

where T_1 is the time it takes for the light to travel between the interactions and the light operators are described by two time arguments, the first of which denotes the time at which the infinitesimal light segment arrives at the atomic sample and the second one describes the time dependence. The light operators obey the commutation relation $[\hat{x}_L(\tau, t), \hat{p}_L(\tau', t)] = i\delta(\tau - \tau')$. They have dimension $1/\sqrt{\text{time}}$ as does the time dependent interaction strength $\tilde{\kappa}(t)$ proportional to the instantaneous amplitude of the strong x-polarized driving light field, which can be varied experimentally using e.g. an electro-optic modulator (EOM). Allowing for a time dependent interaction strength will increase the fidelity and at the same time enable the storage of light pulses with arbitrary temporal profiles. It is related to the usual interaction strength by $\kappa^2 = \int dt \tilde{\kappa}(t)^2$. $\tilde{\kappa}(t)$ is assumed to be slowly varying with respect to T_1 since the time argument of κ in the second term should really be $t - T_1$. Note that the xx interaction is with the light segment which arrived at the atomic sample a time T_1 earlier than the time t , this means that Eq. (9.2) describes a light pulse which first has a pp interaction and then makes an xx interaction.

The Heisenberg equations for this system are

$$\begin{aligned}\frac{d}{dt}\hat{X}_a(t) &= \tilde{\kappa}(t)\hat{p}_L(t, t) \\ \frac{d}{dt}\hat{P}_a(t) &= -\tilde{\kappa}(t)\hat{x}_L(t - T_1, t) \\ \frac{d}{dt}\hat{x}_L(\tau, t) &= \tilde{\kappa}(t)\hat{P}_a(t)\delta(\tau - t) \\ \frac{d}{dt}\hat{p}_L(\tau, t) &= -\tilde{\kappa}(t)\hat{X}_a(t)\delta(\tau - t + T_1).\end{aligned}\tag{9.3}$$

The last two equations can be solved to give

$$\begin{aligned}\hat{x}_L(\tau, t) &= \hat{x}_L(\tau, 0) + \tilde{\kappa}(\tau)\hat{P}_a(\tau)\Theta(t - \tau) \\ \hat{p}_L(\tau, t) &= \hat{p}_L(\tau, 0) - \tilde{\kappa}(\tau)\hat{X}_a(\tau + T_1)\Theta(t - \tau - T_1),\end{aligned}\tag{9.4}$$

where the Heaviside step function ensures that dynamic only occurs when the light pulse is in contact with the atomic sample. The two solutions can be inserted into the remaining two equations in Eq. (9.3):

$$\begin{aligned}\frac{d}{dt}\hat{X}_a(t) &= \tilde{\kappa}(t)\hat{p}_L(t, 0) \\ \frac{d}{dt}\hat{P}_a(t) &= -\tilde{\kappa}(t)\hat{x}_L(t - T_1, t) - \tilde{\kappa}(t)\tilde{\kappa}(t)\hat{P}_a(t - T_1).\end{aligned}\tag{9.5}$$

With the physically reasonable assumption that the atomic variable is slowly varying on the time scale T_1 ($\hat{P}_a(t - T_1) \approx \hat{P}_a(t)$) these equations can be solved to give

$$\begin{aligned}\hat{X}_a(t) &= \hat{X}_a(0) + \int_0^t ds \tilde{\kappa}(s)\hat{p}_L(s, 0) \\ \hat{P}_a(t) &= \hat{P}_a(0)e^{-\int_0^t ds \tilde{\kappa}(s)\tilde{\kappa}(s)} - \int_0^t ds e^{-\int_s^t du \tilde{\kappa}(u)\tilde{\kappa}(u)}\hat{x}_L(s, 0).\end{aligned}\tag{9.6}$$

We note the similarity of equations (9.4) and (9.6) to the simple QND case reviewed earlier. In particular we recognize an asymmetry in which only the initial quantum fluctuations of one of the atomic quadratures are damped, which dictates the requirement of squeezed initial states for perfect quantum state transfer.

These expressions can now be inserted into Eq. (9.4) to find the output fields. Since the dual time argument on the instantaneous light operators was mostly useful in the derivation of the correct equations of motions we now introduce e.g. $\hat{x}_L^{\text{in}}(t)$ and $\hat{x}_L^{\text{out}}(t)$ instead of $\hat{x}_L(0, t)$ and $\hat{x}_L(t, t')$, where $t' > T + T_1$ denotes a time after the interaction is complete. As in previous chapters we define collective light modes with e.g. $\hat{x}_L = \int_0^T f(t)\hat{x}_L(t)dt$, where $f(t)$ specifies the mode in question. This means that a light operator without a time argument denotes a dimensionless canonical operator with $[\hat{x}_L, \hat{p}_L] = i$. For the symmetric mode with $f(t) = 1/\sqrt{T}$ we get:

$$\begin{aligned}\hat{x}_L^{\text{out}} &= \frac{1}{\sqrt{T}} \int_0^T \left(\hat{x}_L^{\text{in}}(t) + \tilde{\kappa}(t) \left(\hat{P}_a(0) e^{-\int_0^t ds \tilde{\kappa}^2} - \int_0^t ds \tilde{\kappa}(s) e^{-\int_s^t du \tilde{\kappa}^2} \hat{x}_L^{\text{in}}(s) \right) \right) dt \\ &= \frac{1}{\sqrt{T}} \int_0^T \hat{x}_L^{\text{in}}(s) \left[1 - \tilde{\kappa}(s) \int_s^T \tilde{\kappa}(t) e^{-\int_s^t du \tilde{\kappa}^2} dt \right] ds + \frac{\hat{P}_a(0)}{\sqrt{T}} \int_0^T \tilde{\kappa}(t) e^{-\int_0^t ds \tilde{\kappa}^2} dt \\ \hat{p}_L^{\text{out}} &= \frac{1}{\sqrt{T}} \int_0^T \left(\hat{p}_L^{\text{in}}(t) - \tilde{\kappa}(t) \left(\hat{X}_a(0) + \int_0^t ds \tilde{\kappa}(s) \hat{p}_L^{\text{in}}(s) \right) \right) dt \\ &= \frac{1}{\sqrt{T}} \int_0^T \hat{p}_L^{\text{in}}(s) \left[1 - \tilde{\kappa}(s) \int_s^T \tilde{\kappa}(t) dt \right] ds - \frac{\hat{X}_a(0)}{\sqrt{T}} \int_0^T \tilde{\kappa}(t) dt ,\end{aligned}\tag{9.7}$$

where we reversed the order of integration in the double integrals.

9.1.1 Constant Interaction Strength

Input output relations are easily derived for the simple case of a constant interaction strength:

$$\hat{X}_a(T) = \hat{X}_a(0) + \tilde{\kappa} \sqrt{T} p_L^{\text{in}} \tag{9.8}$$

$$\hat{P}_a(T) = \hat{P}_a(0) e^{-\tilde{\kappa}^2 T} - \tilde{\kappa} \int_0^T e^{-\tilde{\kappa}^2(T-s)} \hat{x}_L^{\text{in}}(s) ds \tag{9.9}$$

$$\hat{x}_L^{\text{out}} = \frac{1}{\sqrt{T}} \int_0^T e^{-\tilde{\kappa}^2(T-s)} \hat{x}_L^{\text{in}}(s) ds + \frac{\hat{P}_a(0)(1 - e^{-\tilde{\kappa}^2 T})}{\tilde{\kappa} \sqrt{T}} \tag{9.10}$$

$$\hat{p}_L^{\text{out}} = \frac{1}{\sqrt{T}} \int_0^T \hat{p}_L^{\text{in}}(s) [1 - \tilde{\kappa}^2(T-s)] ds - \hat{X}_a(0) \tilde{\kappa} \sqrt{T} . \tag{9.11}$$

Three things should be noted. First of all, due to the different scaling with $\tilde{\kappa}$ of the atomic terms in \hat{x}_L^{out} and \hat{p}_L^{out} it is impossible to implement retrieval with unity gain. Secondly, it is clear that light modes other than the symmetric one will

be admixed in the mapping as well as in the retrieval. Finally, the exponential damping of the input term of \hat{x}_L^{out} combined with the $1/\tilde{\kappa}\sqrt{T}$ damping of the atomic contribution seems to indicate that for high values of $\tilde{\kappa}T$ the outgoing light will have a variance below the shot noise level in that quadrature. This effect will be investigated in detail in chapter 10.

The variance of the operators can be calculated using the light correlation functions $\langle \hat{x}_L(t)\hat{x}_L(t') \rangle = \langle \hat{p}_L(t)\hat{p}_L(t') \rangle = \frac{i}{2}\delta(t-t')$. For e.g. a vacuum state we get

$$\begin{aligned} \langle \hat{x}_L^2 \rangle &= \left\langle \left(\frac{1}{\sqrt{T}} \int_0^T \hat{x}_L(t') dt' \right) \left(\frac{1}{\sqrt{T}} \int_0^T \hat{x}_L(t) dt \right) \right\rangle \\ &= \frac{1}{T} \int_0^T dt' \int_0^T \langle \hat{x}_L(t') \hat{x}_L(t) \rangle dt = \frac{1}{T} \int_0^T \frac{1}{2} = \frac{1}{2}. \end{aligned} \quad (9.12)$$

In a similar manner the output variances can be calculated

$$\begin{aligned} \text{Var}(\hat{X}_a(t)) &= \frac{1}{2} (1 + \kappa^2) \\ \text{Var}(\hat{P}_a(t)) &= \frac{1}{2} \left(\frac{1 + e^{-2\kappa^2}}{2} \right) \\ \text{Var}(\hat{x}_L^{\text{out}}) &= \frac{1}{2} \frac{3 + e^{-2\kappa^2} - 4e^{-\kappa^2}}{2\kappa^2} \\ \text{Var}(\hat{p}_L^{\text{out}}) &= \frac{1}{2} \left(1 + \frac{\kappa^4}{3} \right), \end{aligned} \quad (9.13)$$

where we introduced the total integrated interaction strength $\kappa^2 = \int_0^T \tilde{\kappa}^2(t) dt$.

Because of the unavoidable asymmetry in the two-pass retrieval protocol the optimal way to utilize this protocol is first to perform an asymmetric storage using e.g. the direct mapping protocol and then retrieve using the two-pass interaction such that the overall protocol implements storage and retrieval at unity gain. For this purpose we use equations (7.1) as input states for the atomic system in equations (9.10) and (9.11):

$$\begin{aligned} \tilde{x}_L^{\text{out}} &= c_x \tilde{x}_L^{\text{in}} + \frac{1 - e^{-\kappa^2}}{\kappa^2} \left[\hat{X}_a^{\text{in}} + \kappa_{\text{map}} \hat{p}_L^{\text{in}} \right] \\ \tilde{p}_L^{\text{out}} &= c_p \hat{p}_L^{\text{in}} - \kappa \left[(1 - \kappa_{\text{map}} g_{\text{map}}) \hat{P}_a^{\text{in}} - g_{\text{map}} \hat{x}_L^{\text{in}} \right], \end{aligned} \quad (9.14)$$

where κ_{map} and g_{map} are the interaction strength and gain in the direct mapping. For compactness we introduce \tilde{x} and \hat{p} denoting vacuum modes with spectral profiles determined by the time-dependent function in the integrals of equations (9.10) and (9.11) respectively and $c_x^2 = \frac{1 - e^{-2\kappa^2}}{2\kappa^2}$ and $c_p^2 = 1 + \kappa^4/3 + \kappa^2$. Note that we have performed a 90° rotation of the atoms prior to the retrieval because

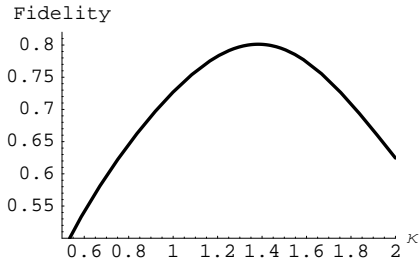


Figure 9.2: The coherent state fidelity of a combined direct mapping and two-pass storage subject to the unity gain conditions, Eq. (9.15), vs. the total interaction strength in the retrieval with constant $\tilde{\kappa}(t)$.

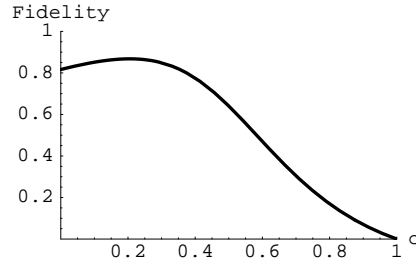


Figure 9.3: The coherent state fidelity of a combined direct mapping and two-pass storage subject to the unity gain conditions, Eq. (9.23), vs. the c -parameter specifying the time dependent interaction strength in the retrieval ($\tilde{\kappa}(t) = 1/\sqrt{2(T-t)/c}$).

this turns out to be optimal. For the complete memory protocol we will require unity gain:

$$\kappa g_{\text{map}} = 1 \quad \text{and} \quad \frac{1 - e^{-\kappa^2}}{\kappa} \kappa_{\text{map}} = 1. \quad (9.15)$$

Inserting these conditions into Eq. (9.14) we can easily calculate the variances of the output state and insert these into Eq. (7.12) giving the fidelity for coherent states. The result is shown in Fig. 9.2. The optimal fidelity is $F^{\text{opt}} = 0.801$ for $\kappa = 1.38$, $\kappa_{\text{map}} = 1.62$, and $g_{\text{map}} = 0.723$. Squeezing the initial atomic state and the retrieval pulse will only increase the fidelity by a couple of percent because both conjugate quadratures of each are present in the output. Had we not performed the atomic rotation prior to the retrieval the optimal fidelity would instead be $F^{\text{opt}} = 0.685$ for $\kappa = 1.06$, $\kappa_{\text{map}} = 0.948$, and $g_{\text{map}} = 1.57$.

9.1.2 Time-dependent Interaction Strength

We can try to remedy the admixture of other light modes in Eq. (9.7) with a non-uniform interaction strength. To do this we want to choose a profile so that the terms in the square brackets of Eq. (9.7) are constant:

$$\tilde{\kappa}(s) \int_s^T \tilde{\kappa}(t) dt = c, \quad \tilde{\kappa}(s) \int_s^T \tilde{\kappa}(t) e^{-\int_s^t du \tilde{\kappa}(u)^2} dt = c' \quad (9.16)$$

Differentiating the former with respect to s we get:

$$\frac{d\tilde{\kappa}}{ds} \int_s^T \tilde{\kappa}(t) dt - \tilde{\kappa}^2(s) = 0 \quad \Rightarrow \quad \frac{d\tilde{\kappa}}{ds} = \frac{\tilde{\kappa}^2(s)}{\int_s^T \tilde{\kappa}(t) dt} = \frac{\tilde{\kappa}(s)^3}{c}, \quad (9.17)$$

where in the last step we used the definition of c . This differential equation can easily be solved:

$$\tilde{\kappa}(t) = \frac{1}{\sqrt{\frac{2}{c}(T-t)}} . \quad (9.18)$$

In a similar manner the equation for the other light quadrature can be shown to give:

$$\tilde{\kappa}(t) = \frac{1}{\sqrt{\frac{2(1+c')}{c'}(T-t)}} . \quad (9.19)$$

We thus see that utilizing a shape as in Eq. (9.18) we solve both equation simultaneously, albeit with different constants, $c' = c/(1-c)$. We can now express the retrieval in terms of the symmetric light variables entirely:

$$\hat{p}_L^{\text{out}} = (1-c)\hat{p}_L^{\text{in}} - \hat{X}_a(0)\sqrt{2c} \quad (9.20)$$

$$\hat{x}_L^{\text{out}} = \left(1 - \frac{c}{1-c}\right)\hat{x}_L^{\text{in}} + \hat{P}_a(0)\frac{\sqrt{2c}}{1-c} = \hat{x}_L^{\text{in}}\frac{1-2c}{1-c} + \hat{P}_a(0)\frac{\sqrt{2c}}{1-c} . \quad (9.21)$$

Again we see that unity gain retrieval cannot be achieved but the noise trade-off is made very explicit as compared to the case of constant $\tilde{\kappa}$. Looking at the mapping equations (9.6) it is evident that a similar trick cannot be applied to the mapping interaction since only a symmetric interaction constant will ensure the storage of only \hat{p}_L^{in} , whereas this clearly will cause the admixture of additional vacuum modes in the other quadrature.

As in Sec. 9.1.1 we can create a complete storage and retrieval protocol this time by inserting Eq. (7.1) into into equations (9.20) and (9.21). This time it turns out to be optimal not to rotate the atomic state after the storage:

$$\begin{aligned} \tilde{x}_L^{\text{out}} &= \frac{1-2c}{1-c}\tilde{x}_L^{\text{out}} + \frac{\sqrt{2c}}{1-c} \left[(1-\kappa_{\text{map}}g_{\text{map}})\hat{P}_a^{\text{in}} + g_{\text{map}}\hat{x}_L^{\text{in}} \right] \\ \tilde{p}_L^{\text{out}} &= (1-c)\tilde{p}_L^{\text{out}} - \sqrt{2c} \left[\hat{X}_a^{\text{in}} + \kappa_{\text{map}}\hat{p}_L^{\text{in}} \right] , \end{aligned} \quad (9.22)$$

where as before κ_{map} and g_{map} are the interaction strength and gain in the direct mapping. This time the unity gain conditions are:

$$\kappa_{\text{map}} = 1/\sqrt{2c} \quad \text{and} \quad g_{\text{map}} = \frac{1-c}{\sqrt{2c}} . \quad (9.23)$$

The fidelity corresponding to these conditions is plotted in Fig. 9.3. The optimal fidelity is $F^{\text{opt}} = 0.868$ for $c = 0.205$, $\kappa_{\text{map}} = 1.56$, and $g_{\text{map}} = 0.509$. We note that because of the asymmetric mapping total fidelities above the 82% fidelity bound on the direct mapping can be achieved. With an atomic rotation prior to the retrieval the optimal fidelity would instead be $F^{\text{opt}} = 0.828$ for $c = 0.0822$, $\kappa_{\text{map}} = 0.372$, and $g_{\text{map}} = 2.47$. With initial state squeezing the fidelity for both the protocol with the atomic rotation and the one without can be increased to $F = 0.90$ with 5.2 dB and 9.4 dB of atomic squeezing respectively. In both cases 1.0 dB of squeezing of the retrieval pulse is optimal.

9.2 Four-pass Protocol

The necessity of squeezed input states in the two-pass protocol is caused by the asymmetry in Eq. (9.6) between the atomic variables: $\hat{P}_a(0)$ is exponentially damped, whereas $\hat{X}_a(0)$ remains undamped, hence requiring initial atomic state squeezing. The symmetry can be restored by reflecting the light back through the atomic medium, see Fig. 9.1. In the resulting four-pass protocol the light will experience an interaction sequence $\hat{P}_a\hat{p}_L$, $\hat{X}_a\hat{x}_L$, $\hat{X}_a\hat{x}_L$, and $\hat{P}_a\hat{p}_L$. Experimentally the output beam will then have to be separated from the input beam following the fourth passage. The Hamiltonian for this interaction is:

$$H(t) = \tilde{\kappa}(t)\hat{P}_a(t)p(t, t) + \tilde{\kappa}(t)\hat{X}_a(t)\hat{x}_L(t - T_1, t) \\ + \tilde{\kappa}(t)\hat{X}_a(t)\hat{x}_L(t - T_1 - T_2, t) + \tilde{\kappa}(t)\hat{P}_a(t)\hat{p}_L(t - 2T_1 - T_2, t), \quad (9.24)$$

where T_2 is the time it takes between the two $\hat{X}_a\hat{x}_L$ interactions. Completely analogously to Sec. 9.1 a differential equation for the time evolution of the atomic and light variables can be formulated and solved to obtain:

$$\hat{X}_a(t) = \hat{X}_a(0)e^{-2\int_0^t du\tilde{\kappa}(u)^2} + 2\int_0^t dt'\tilde{\kappa}e^{-2\int_{t'}^t du\tilde{\kappa}(u)^2}\hat{p}_L^{\text{in}}(t') \\ \hat{P}_a(t) = \hat{P}_a(0)e^{-2\int_0^t du\tilde{\kappa}(u)^2} - 2\int_0^t dt'\tilde{\kappa}e^{-2\int_{t'}^t du\tilde{\kappa}(u)^2}\hat{x}_L^{\text{in}}(t') \quad (9.25) \\ \hat{x}_L^{\text{out}}(t) = \hat{x}_L^{\text{in}}(t) + 2\tilde{\kappa}(t)\hat{P}_a(t) \\ \hat{p}_L^{\text{out}}(t) = \hat{p}_L^{\text{in}}(t) - 2\tilde{\kappa}(t)\hat{X}_a(t).$$

Note, that this protocol involves a significant amount of passages so for an atomic system consisting of two atomic samples each contained within glass cells as in our experiments the total light reflection loss would be eight times the single cell loss. Since this was $\sim 10\%$ in our previous experiments this would be quite a detrimental effect. This can, however, to a large extent be remedied by adding anti-reflection coating to the glass cells, something that has been done to the new generation of glass cells giving a total reflection loss of $\sim 1\%$. In a single cell implementation consisting e.g. of a dense cold sample within a vacuum chamber the reflection losses can be also be minimized by anti-reflection coating the optical access windows or by having the additional mirrors within the vacuum chamber.

9.2.1 Four-pass Mapping

By introducing the annihilation operators $\hat{a}_a = (\hat{X}_a + i\hat{P}_a)/\sqrt{2}$ and $\hat{a}_L = (\hat{x}_L + i\hat{p}_L)/\sqrt{2}$ the entire interaction can be written as a beam splitter relation:

$$\hat{a}_a(t) = \hat{a}_a(0)e^{-2\int_0^t du\tilde{\kappa}(u)^2} - 2i\int_0^t dt'\tilde{\kappa}e^{-2\int_{t'}^t du\tilde{\kappa}(u)^2}\hat{a}_L^{\text{in}}(t'). \quad (9.26)$$

To store a light pulse described by $\hat{a}_L^{\text{in}} = \int_0^T dt f(t) \hat{a}_L^{\text{in}}(t)$, $f(t)$ being the arbitrary temporal mode function, we want $\hat{a}_a(T) = \hat{a}_L^{\text{in}}$ which is equivalent to

$$\frac{1}{\tilde{\kappa}} \frac{d\tilde{\kappa}}{dt} + 2\tilde{\kappa}^2 = \frac{1}{f} \frac{df}{dt}. \quad (9.27)$$

Given a (real) $f(t)$ this differential equation can be solved to obtain the appropriate shape of the interaction strength $\tilde{\kappa}$. Note, that the shape of $\tilde{\kappa}$ for storage and retrieval may be different so that the retrieved pulse may be transformed into any desirable shape. As a specific example let us consider a constant field mode of duration T with $f(t) = 1/\sqrt{T}$. In the process of mapping, the initial atomic state is damped exponentially but so is the contribution from the early part of the input light pulse. This can be counteracted by an increased interaction strength for the front part of the pulse giving $\tilde{\kappa}(t) = \frac{1}{2\sqrt{t}}$ for the optimal mapping interaction. Hence by suitable tailoring of $\tilde{\kappa}$ the protocol allows for ideal storage of an incoming light state without any initial squeezing!

9.2.2 Four-pass Retrieval

Noting the similarity between the four-pass solutions in Eq. (9.25) and the two-pass equations for \hat{P}_a and \hat{x}_L in equations (9.4) and (9.6) the result of inserting the atomic variables into the light ones can easily be derived in analogue to Eq. (9.7):

$$\begin{aligned} \hat{a}_L^{\text{out}} = & \frac{1}{\sqrt{T}} \int_0^T \hat{a}_L(s) \left[1 - 4\tilde{\kappa}(s) \int_s^T \tilde{\kappa}(t) e^{-2 \int_s^t du \tilde{\kappa}^2} dt \right] ds \\ & - \frac{i2\hat{a}_a}{\sqrt{T}} \int_0^T \tilde{\kappa}(t) e^{-2 \int_0^t ds \tilde{\kappa}^2} dt. \end{aligned} \quad (9.28)$$

As in Sec. 9.1 an interaction strength of the form $\tilde{\kappa}(t) = c/\sqrt{(T-t)}$ will make the terms in the square brackets of Eq. (9.28) constant

$$\hat{a}_L^{\text{out}} = \frac{1}{\sqrt{T}} \frac{1-4c^2}{1+4c^2} \int_0^T \hat{a}_L(s) ds - i\hat{a}_a \frac{4c}{1+4c^2}. \quad (9.29)$$

Thus, for $c = 1/2$ the initial light contribution vanishes and the atomic contribution will be mapped with perfect fidelity. When retrieving a stored state the rear end of the light pulse reads out a damped atomic state and the divergence needs to be placed at this end of the pulse.

9.2.3 Avoiding the Divergence with a Cut-off

Unfortunately all of the tailored shapes for the interaction strength contain a divergence at one of the ends of the pulse. In addition, the integrated interaction strength $\kappa^2 = \int \tilde{\kappa}^2 dt$ also diverges, so the interaction requires infinitely many

photons. In the following we will discuss a number of different ways of creating a physically realizable protocol. First, we truncate the interaction strength by setting it equal to a constant, ϕ , in a region around the divergence. In particular, for the mapping we let $\tilde{\kappa}(t) = \frac{1}{2\sqrt{t}}$ for $t > \tau$ and $\tilde{\kappa}(t) = \frac{1}{2\sqrt{\tau}}$ for $0 \leq t \leq \tau$. We wish to calculate fidelity of the transfer for coherent states. For this we merely need to know the variance of the output state and the gain in the mapping, i.e. the coefficient in front of \hat{a}_L^{in} in Eq. (9.26). To calculate the latter we write the right hand side of Eq. (9.26) as a sum of three different orthogonal modes, $\hat{a}_a(0)$, \hat{a}_L and $\hat{\hat{a}}_L$

$$\hat{a}_a(t) = c_a \hat{a}_a(0) + g_{\text{map}} \hat{a}_L + c_2 \hat{\hat{a}}_L . \quad (9.30)$$

Taking the commutator of $\hat{a}_a(T)$ with \hat{a}_L^\dagger will pick out the required coefficient:

$$\begin{aligned} g_{\text{map}} &= [\hat{a}_a(T), \hat{a}_L^\dagger] = \left[-2i \int_0^t dt' \tilde{\kappa} e^{-2 \int_{t'}^t du \tilde{\kappa}(u)^2} \hat{a}_L^{\text{in}}(t'), \frac{1}{\sqrt{T}} \int_0^T dt \hat{a}_L^\dagger(t) \right] \\ &= \frac{-2i}{\sqrt{T}} \int_0^t dt' \tilde{\kappa} e^{-2 \int_{t'}^t du \tilde{\kappa}(u)^2} \int_0^T dt [\hat{a}_L^{\text{in}}(t'), \hat{a}_L^\dagger(t)] \\ &= \frac{2}{\sqrt{T}} \int_0^T dt \tilde{\kappa} e^{-2 \int_t^T du \tilde{\kappa}^2} = 1 - e^{-4\kappa^2} (2\sqrt{e} - e) , \end{aligned} \quad (9.31)$$

where we ignored the additional phase due to the factor i and used $[\hat{a}_L^{\text{in}}(t'), \hat{a}_L^\dagger(t)] = \delta(t - t')$ and the relation $\frac{\tau}{T} = e^{1-4\kappa^2}$ obtained from the total integrated interaction strength $\kappa^2 = \int_0^T \tilde{\kappa}(t)^2 dt = \frac{1}{4}(1 - \ln \frac{\tau}{T})$. For $\phi = 0$ we instead get, $g_{\text{map}} = 1 - e^{-4\kappa^2}$. For the retrieval we calculate the coefficient in front of the atomic term in Eq. (9.28) with $\tilde{\kappa} = \frac{1}{2\sqrt{T-t}}$ for $t < \tau'$ and ϕ' for $\tau' \leq t \leq T$. Choosing $\phi' = \frac{1}{2\sqrt{T-\tau'}}$ and $\phi' = 0$ turns out to give exactly the same gains as in the mapping, thus reflecting the high degree of symmetry in the protocol. The variances of the output states of the four-pass protocol are always 1/2 because of the coherent beam splitter nature of the interaction. This can also be checked by a straight forward calculation of the variance of equations by transforming equations (9.26) and (9.28) into xp variables and using the associated two-time correlation functions as in Sec. 9.1.1.

A very illustrative result can be obtained by instead letting $\tilde{\kappa}(t) = \frac{1}{2\sqrt{t+\tau}}$ in the mapping. In this case Eq. (9.26) transforms into:

$$\hat{a}_a(T) = \hat{a}_a(0) \sqrt{e^{-4\kappa^2}} - i \sqrt{1 - e^{-4\kappa^2}} \hat{a}_L^{\text{in}} , \quad (9.32)$$

where we used $\frac{\tau}{T+\tau} = e^{-4\kappa^2}$ obtained from a calculation of the total integrated interaction strength. Here we clearly see that the output state has variance 1/2.

Equation (9.32) represents a beam splitter with arbitrary splitting ratio involving only two modes. For $\tau = 0$ we regain the perfect mapping and for e.g. $\tau = T$ we get a 50:50 beam splitter. This adds to the growing toolbox of interesting interactions between atomic ensembles and light pulses, which pave

the way for a number of hybrid light-atom protocols, e.g., for teleportation and entanglement swapping.

Finally we can examine the performance of the four-pass mapping and retrieval with a constant interaction strength. To calculate the gain of mapping one has to calculate the commutator of the output state of atoms with \hat{a}_L^\dagger of the input light state exactly as was done in Eq. (9.31). The integral is easily performed giving a gain of $g_{\text{map}} = \frac{1-e^{-2\kappa^2}}{\kappa}$, which is fundamentally different from the gains with tailored $\tilde{\kappa}$ because it does not converge towards unity. In fact it does not take the value unity for any choice of κ . The closest is $g_{\text{map}} = 0.90$ for $\kappa = 0.79$. Thus, it will be unsuitable for any storage requiring close to unity gain. Calculating the retrieval gain as the factor in front of the atomic operator in Eq. (9.28) it is again found to be identical to the mapping gain. Also, as in all the other 4-pass protocols the output state has variance 1/2 both in mapping and in retrieval.

9.3 Qubit Fidelities

As in the experimental chapters we quantify the quantum memory performance via the fidelity $F = \langle \Psi_{\text{ideal}} | \rho | \Psi_{\text{ideal}} \rangle$, where Ψ_{ideal} is the ideal state and ρ is the retrieved density matrix. Previously we have calculated the gains and variances for various choices of the interaction strength in both the two- and the four-pass protocols. These enabled us to calculate the fidelity for coherent Gaussian states. Now we wish to assess the quality of the protocols for a non-classical state, in particular an unknown qubit stored in the zero and one photon subspace of the light field. In the four-pass protocol, this can be calculated directly from equations (9.26) and (9.28), by noting that imperfect operation results in the admixture of vacuum noise into the mode we are interested in, and the effect (or an actual source of loss or decoherence) is therefore fairly easily determined, e.g., by noting that within the 0 and 1 photon subspace (9.26) corresponds to the relation for a decaying two-level system (see Sec. 9.3.1). Calculating the qubit fidelity for a general protocol is a much more complicated task. For this purpose we have developed a theory capable of calculating the fidelity with respect to an arbitrary superposition of Fock states for any protocol. This will be discussed in Sec. 9.3.2.

The present protocols can also be extended to employ two atomic memory units (ensembles) A and B to store or retrieve a qubit originally represented by a single photon in two modes L and M , $|\psi\rangle_{LM} = \alpha|10\rangle_{LM} + \beta|01\rangle_{LM}$. This is important since this encoding is used in a vast majority of current experiments on optical quantum information processing with discrete variables. The fidelity of storage and/or retrieval can be calculated using similar techniques as those presented here for the single-mode qubit.

	$\tilde{\kappa}$ shape	g_x	g_p	Var_x	Var_p
4pass	$\phi = 0$	$1 - e^{-4\kappa^2}$	-	$\frac{1}{2}$	-
	$\phi = \tilde{\kappa}(\tau)$	$1 - e^{-4\kappa^2}(2\sqrt{e} - e)$	-	$\frac{1}{2}$	-
	$\tilde{\kappa} = \frac{1}{2\sqrt{t+\tau}}$ (BS)	$\sqrt{1 - e^{-4\kappa^2}}$	-	$\frac{1}{2}$	-
	flat	$\frac{1 - e^{-2\kappa^2}}{\kappa}$	-	$\frac{1}{2}$	-
2pass	flat	$\frac{1 - e^{-\kappa^2}}{\kappa}$	κ	$\frac{3 + e^{-2\kappa^2} - 4e^{-\kappa^2}}{4\kappa^2}$	$\frac{1}{2} + \frac{\kappa^4}{6}$

Table 9.1: Gains and variances for various realistic (finite κ^2) quantum memory protocols

9.3.1 Simple "Decay" Model for the 4pass Fidelity

As illustrated by Eq. (9.32) the four-pass protocol is effectively an atom-light beam splitter. In e.g. the mapping the effect of the non-unity gain and the residual atomic contribution can be modeled simply by a decohering two level system. A two-level density matrix experiencing spontaneous decay will transform as:

$$\rho(t) = \begin{bmatrix} \rho_{11}(0) + (1 - e^{-\Gamma t})\rho_{22}(0) & \rho_{12}(0)e^{-\Gamma t/2} \\ \rho_{21}(0)e^{-\Gamma t/2} & \rho_{22}(0)e^{-\Gamma t} \end{bmatrix} \quad (9.33)$$

If the light is initially in a qubit state $|\psi\rangle = \cos(\theta/2)|0\rangle + \sin(\theta/2)e^{i\phi}|1\rangle$ the initial density matrix will be:

$$\rho^{\text{in}} = \begin{bmatrix} \cos^2(\theta/2) & \cos(\theta/2)\sin(\theta/2)e^{i\phi} \\ \cos(\theta/2)\sin(\theta/2)e^{-i\phi} & \sin^2(\theta/2) \end{bmatrix} \quad (9.34)$$

Noting that ρ^{in} corresponds to a pure state we calculate the fidelity as $F = \text{Tr}(\rho^{\text{in}}\rho^{\text{out}})$ and averaging over the Bloch sphere we get:

$$F_{\text{aver}} = \frac{1}{4\pi} \int_0^\pi d\theta \sin(\theta) \int_0^{2\pi} d\phi F = \frac{1}{6}(3 + 2\sqrt{e^{-\Gamma t}} + e^{-\Gamma t}) \quad (9.35)$$

To calculate the fidelity for each choice the shape of the interaction strength in the four-pass protocol we merely make the substitution $e^{-\Gamma t} \rightarrow g^2$, where the gains can be found in table 9.3.1. In the limit of $\kappa^2 \gg 1$ we get for the e.g. the three different realistic choices for the mapping:

$$F_{\text{aver}} \rightarrow \begin{cases} 1 - \frac{2}{3}e^{-4\kappa^2}, & \phi = 0 \\ 1 - \frac{2}{3}e^{-4\kappa^2}(2\sqrt{e} - e), & \phi = 1/(2\sqrt{\tau}) \\ 1 - \frac{1}{3}e^{-4\kappa^2}, & \tilde{\kappa} = \frac{1}{2\sqrt{t+\tau}} \text{ (BS)} \end{cases} \quad (9.36)$$

The full results are plotted in Fig. 9.4. The asymptotic exponential behavior is clearly visible. As can be seen in the figure, the two-mode beam splitter interaction is slightly more efficient than the continuous cut off shape. A combined storage and retrieval fidelity is easily calculated by multiplying the gains of each

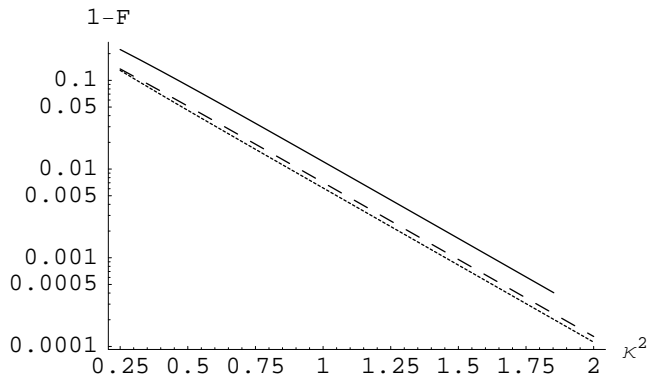


Figure 9.4: 1-fidelity (qubit) vs. κ^2 for different realistic (finite κ^2) four-pass protocols. Full-drawn: $\phi = 0$, dashed: $\phi = \tilde{\kappa}(\tau)$, dotted: $\tilde{\kappa} = 1/(2\sqrt{t + \tau}$ (two-mode beam splitter, mapping only).

and inserting the result into Eq. (9.35). For e.g. the continuous cut off shape, we get $F \rightarrow 1 - \frac{4}{3}(2\sqrt{e} - e)e^{-4\kappa^2}$ for $\kappa^2 \gg 1$. This treatment clearly illustrates that inclusion of spontaneous emission is trivial since it merely causes a lower gain. When doing so one should remember that the κ^2 calculated here is the single pass integrated interaction strength. The spontaneous emission is of course proportional to the number of photons interacting with the atoms in each passage. Thus, when calculating the effect of spontaneous emission in e.g. a four-pass protocol one should use $\eta_T = \kappa_{\text{tot}}^2/\alpha$, where $\kappa_{\text{tot}}^2 = 4\kappa^2$ and α is the optical depth on resonance. Spontaneous emission will reduce the fidelity of the protocol by an amount proportional to η_T , so that in combination with Eq. (9.36) the total error ($1 - F$) is of the order of $\sim \exp(-\alpha\eta_T) + \eta_T$. Optimizing this expression with respect to η_T we find that $\eta_{\text{opt}} \sim \frac{\log \alpha}{\alpha}$. Inserting this into the expression for the error we note that it scales as $\log(\alpha)/\alpha$. It is thus advantageous to make α large as possible.

9.3.2 General Fidelity Calculation

The method for calculation of the qubit fidelity used in the previous section only applies to a very small range of symmetric protocols. We are also interested in the fidelity for e.g. the two-pass protocol. To do this, we write the effect of an arbitrary interaction as $\mathbf{Y}^{\text{out}} = U^\dagger \mathbf{Y}^{\text{in}} U$, where \mathbf{Y} is a vector containing x 's and p 's for orthogonal modes defined from the incoming light mode, the atomic mode, and the temporal field modes populated in the interaction. Treating e.g. the case of mapping, the reduced density matrix for the atomic system is given by:

$$\rho = \text{Tr}_L(U O_L |v\rangle\langle v| O_L^\dagger U^\dagger) \equiv \mathcal{E}(|\psi\rangle\langle\psi|), \quad (9.37)$$

where O_L creates the incoming light state $|\psi\rangle$ from the vacuum $|v\rangle = |0\rangle_L|0\rangle_A$. The overlap between the created state and the ideal state is then given by:

$$OL = \langle \Psi_{\text{ideal}} | \mathcal{E}(|\psi\rangle\langle\psi|) | \Psi_{\text{ideal}} \rangle, \quad (9.38)$$

where $|\Psi_{\text{ideal}}\rangle$ is the ideally transferred state. In order to describe any superposition of Fock states, we form the generating function:

$$G(\mathbf{v}) = \text{Tr}_L(A \langle 0 | e^{\beta^* \hat{a}_A} U e^{\alpha \hat{a}_L^\dagger} |v\rangle \langle v| e^{\alpha^* \hat{a}_L} U^\dagger e^{\beta \hat{a}_A^\dagger} |0\rangle_A), \quad (9.39)$$

where $\mathbf{v} = (\alpha, \alpha^*, \beta, \beta^*)$ should be treated as four independent variables. Using the fact that $|\beta\rangle = D(\beta)|v\rangle = e^{-|\beta|^2/2} e^{\beta \hat{a}^\dagger} |v\rangle$ it can be seen that the Q-function [39, 100] of ρ for an incoming coherent light state, $Q(\beta|\alpha) \equiv \frac{1}{\pi} \langle \beta | \mathcal{E}(|\alpha\rangle\langle\alpha|) | \beta \rangle$ is proportional to the generating function, $G = \pi Q(\beta|\alpha) e^{|\alpha|^2 + |\beta|^2}$. It follows from the linearity of equations (9.6,9.25) that the Q-function of $\mathcal{E}(|\alpha\rangle\langle\alpha|)$ is Gaussian. In other words, starting with a Gaussian coherent state $|\alpha\rangle$ the interaction produces a Gaussian state. The Q-function defined as the overlap of the resulting state with an arbitrary coherent state $|\beta\rangle$ is again a Gaussian function. Thus, the resulting state $\mathcal{E}(|\alpha\rangle\langle\alpha|)$ is completely characterized by the transfer gains g_x and g_p of the mean values of the two quadratures and the output variances of these, V_x and V_p . From Eq. (7.6) we know the overlap of two Gaussian states:

$$Q(\beta|\alpha) = \frac{1}{\pi \sqrt{\tilde{V}_x \tilde{V}_p}} \exp \left[-\frac{(\beta + \beta^* - g_x(\alpha + \alpha^*))^2}{4\tilde{V}_x} + \frac{(\beta - \beta^* - g_p(\alpha - \alpha^*))^2}{4\tilde{V}_p} \right], \quad (9.40)$$

where $\tilde{V}_x = V_x + \frac{1}{2}$, $\tilde{V}_p = V_p + \frac{1}{2}$, and we used e.g. $\alpha = \frac{\hat{x} + i\hat{p}}{\sqrt{2}}$. By differentiating G an appropriate number of times with respect to α and α^* and subsequently putting $\alpha = \alpha^* = 0$ an arbitrary number of \hat{a}^\dagger and \hat{a} can be pulled down and acting on the vacuum state from the left and the right respectively will generate any Fock state of light as input. Similarly differentiations with respect to β and β^* extract the overlap with the ideally stored state. To calculate the fidelity for e.g. a qubit state $|\psi\rangle = a|0\rangle + b|1\rangle$ the fidelity is given by:

$$\begin{aligned} F_q &= \langle \psi | U | \psi \rangle \langle \psi | U^\dagger | \psi \rangle \\ &= \left[a^* + b^* \frac{\partial}{\partial \beta^*} \langle 0 | e^{\beta^* \hat{a}} \right] U \left[a + b \frac{\partial}{\partial \alpha} e^{\alpha \hat{a}^\dagger} | 0 \rangle \right] \\ &\quad \left[a^* + b^* \frac{\partial}{\partial \alpha^*} \langle 0 | e^{\alpha^* \hat{a}} \right] U^\dagger \left[a + b \frac{\partial}{\partial \beta} e^{\beta \hat{a}^\dagger} | 0 \rangle \right] \\ &= \left(a^* + b^* \frac{\partial}{\partial \beta^*} \right) \left(a + b \frac{\partial}{\partial \alpha} \right) \left(a^* + b^* \frac{\partial}{\partial \alpha^*} \right) \left(a + b \frac{\partial}{\partial \beta} \right) G|_{\alpha=\alpha^*=\beta=\beta^*=0}. \end{aligned} \quad (9.41)$$

Since the generating function does not depend on the qubit coefficients the averaging over the qubit Bloch sphere can be performed without specifying

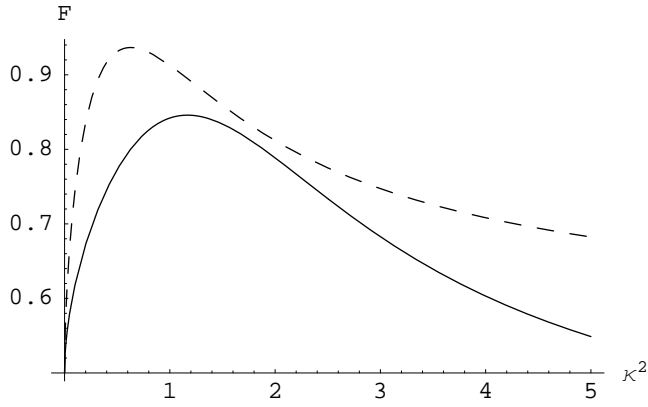


Figure 9.5: Qubit fidelity of retrieval using the two-pass protocol (solid) and the fidelity of mapping or retrieval using the four-pass protocol (dashed) both with constant interaction strength.

which protocol (and thereby which G) is involved. Writing the qubit as $|\psi\rangle = \cos(\theta/2)|0\rangle + \sin(\theta/2)e^{i\phi}|1\rangle$ the Bloch sphere averaging can be performed as:

$$\begin{aligned}
 F_{q,\text{aver}} &= \frac{1}{4\pi} \int_0^\pi d\theta \sin(\theta) \int_0^{2\pi} d\phi F_q \\
 &= \frac{1}{6} \left(2 + \frac{\partial}{\partial \alpha^*} \frac{\partial}{\partial \beta} + \frac{\partial}{\partial \beta} \frac{\partial}{\partial \beta^*} \right. \\
 &\quad \left. + \frac{\partial}{\partial \alpha} \left(\frac{\partial}{\partial \alpha^*} (1 + 2 \frac{\partial}{\partial \beta} \frac{\partial}{\partial \beta^*}) + \frac{\partial}{\partial \beta^*} \right) \right) G|_{\alpha=\alpha^*=\beta=\beta^*=0} .
 \end{aligned} \tag{9.42}$$

Performing the differentiation we get a fairly complicated expression:

$$F = \frac{V_p V_x (g_x^2 + g_p^2) + 8V_x^2 V_p^2 + 4(V_x V_p)^{5/2} + \sum V_i^2 V_j (2g_j - 3g_j^2 - 3) + 3V_i^2 g_j^2}{12(V_x V_p)^{5/2}} , \tag{9.43}$$

where the sum is over $(i, j) = \{(x, p), (p, x)\}$. Thus the only non-trivial task that remains for each protocol is to calculate the action of each on arbitrary coherent states, i.e. calculate the gains and output variances. For a symmetric protocol ($g_x = g_p \equiv g$ and $V_x = V_p \equiv V$) this expression simplifies greatly:

$$F = \frac{g^2(4 - 3V) - 3V + 2gV + V^2 + 2V^3}{6V^3} \rightarrow \frac{3 + g^2 + g}{6} , \quad (V = 1) . \tag{9.44}$$

Thus, for unity variance in the output state of a symmetric protocol we retrieve exactly the expression for the fidelity derived in Sec. 9.3.1. Taking the appropriate gains and variances taken from table 9.3.1 the fidelity for a constant interaction strength can be calculated and plotted in Fig. 9.5 both for the two- and the four-pass protocol. The fidelity for these reach a maximum of $F = 0.934$

at $\kappa^2 = 0.628$ and $F = 0.846$ at $\kappa^2 = 1.17$ respectively. Asymptotically they decrease towards final fidelities of $F = 1/2$ and $F = 1/3$.

CHAPTER 10

Polarization Squeezing by Faraday Rotation

Highly squeezed states of light are valuable for numerous quantum information protocols and high precision metrology. Several techniques exist for the generation of squeezed states. In [118] the non-linear phase evolution due to the Kerr effect in an optical fiber was used to produce 5.1 dB of polarization squeezing. Cold atomic samples in high-finesse cavities cause similar Kerr-like effects, and 1.5 dB of quadrature squeezing [119] and ~ 0.5 dB of polarization squeezing [120] has been observed. The most well established technique to date, however, is to use non-linear crystals in very good cavities (e.g. ~ 7 dB in [121]). Here we show, however, that by reflecting a light beam so that it interacts twice through the off-resonant Faraday-type interaction with an atomic sample, a simple, robust, and efficient source of strongly squeezed light is obtained, which may well outperform the above mentioned schemes.

Our proposed physical set-up is identical to the two-pass retrieval discussed in Sec. 9.1 and is illustrated in Fig. 9.1 (without the optional mirror after the second passage). As the retrieval, it can be implemented either using a single atomic sample (part a) of Fig. 9.1 or using two oppositely oriented samples as shown in part b) of Fig. 9.1. As mentioned in the discussion following equations (9.8-9.11) the input light and atomic terms of \hat{x}_L^{out} are damped and in the case of constant interaction strength Eq. (9.12) shows that $\text{Var}(\hat{x}_L^{\text{out}})$ goes to zero as $\kappa^2 \rightarrow \infty$. This suggests that the interaction could in principle create arbitrary degrees of squeezing merely by increasing the number of photons and/or the atomic density sufficiently.

This effect is inherently connected to the simultaneous passage dynamics. This can be seen by noting that in the case of complete passage in one direction before the second passage is begun it is the initial unsqueezed \hat{P}_a which maps onto the field variable in the first interaction, and x_{out} will thus be even more noisy than in the input state. This fact can easily be seen in Eq. (9.1). To check the robustness of our protocol we will in this chapter rederive the equations of motion in the presence of light losses, $\epsilon \equiv 1 - \tau^2$, between the two passages of the light through the atomic sample and continuous atomic damping due to decoherence. (For compactness we will in the following use τ to quantify light loss rather than ϵ as in previous chapters.) This modifies Eq. (9.4) to:

$$\hat{x}_L^{\text{out}}(t) = \tau(\hat{x}_L^{\text{in}}(t) + \tilde{\kappa}\hat{P}_a(t)) + \sqrt{1 - \tau^2}F_x(t), \quad (10.1a)$$

$$\hat{p}_L^{\text{out}}(t) = \tau\hat{p}_L^{\text{in}}(t) - \tau\tilde{\kappa}\hat{X}_a(t) + \sqrt{1 - \tau^2}F_p(t), \quad (10.1b)$$

where $F_{x(p)}(t)$ are Langevin noise terms obeying $[F_x(t), F_p(t')] = i\delta(t - t')$ and $[F_x(t), F_x(t')] = [F_p(t), F_p(t')] = 0$. The extra factor τ in front of the atomic and light terms in Eq. (10.1b) accounts for the reduced interaction strength in the second light-atom interaction because of the reduced photon flux ($\Phi \rightarrow \tau^2\Phi$) between the passages. As discussed in chapter 9 $\tilde{\kappa}$ has the dimension $1/\sqrt{\text{time}}$, and $\tilde{\kappa}^2$ will be the natural scale for the frequency dependence of our results.

The atomic dissipation can both be caused by the weak excitation by the optical fields, which causes a small spontaneous emission rate γ , and by the fact that we may implement optical pumping with a rate γ_p to retain the atomic macroscopic polarization along the x-axis. The mean spin will thus obey $\frac{dJ_x}{dt} = -\gamma J_x + \gamma_p(N/2 - J_x)$ with a macroscopic steady state value $J_x = \frac{\gamma_p}{\gamma + \gamma_p}N/2$. Here we specialized to a spin 1/2 system but the extension to a higher spin system is straight forward. The atomic variables \hat{X}_a and \hat{P}_a decay with the rate $\gamma_1 = \gamma + \gamma_p$. The decay is accompanied by noise terms $\sqrt{2\gamma_2}G_{x(p)}(t)$, where $G_{x(p)}(t)$ have the same commutator properties as the $F_{x(p)}(t)$ operators introduced for the field losses. Due to the division by $\sqrt{J_x}$ in the Holstein-Primakoff approximation, we obtain the value $\gamma_2 = \gamma_1/(\frac{\gamma_p}{\gamma + \gamma_p}) = (\gamma + \gamma_p)^2/\gamma_p$ for the strength of the noise term. If there are other decoherence mechanisms present, γ_1 and γ_2 of course have to be modified correspondingly. Altogether Eq. (9.5) is modified to:

$$\frac{d}{dt}\hat{X}_a(t) = \tilde{\kappa}p_{in}(t) - \gamma_1\hat{X}_a(t) + \sqrt{2\gamma_2}G_x(t), \quad (10.2a)$$

$$\frac{d}{dt}\hat{P}_a(t) = -\tilde{\kappa}\tau x'_i(t) - \gamma_1\hat{P}_a(t) + \sqrt{2\gamma_2}G_p(t), \quad (10.2b)$$

Again we see the effect of the reduced interaction strength in the second interaction by the extra factor τ on the light part of Eq. (10.2b).

10.1 CW Squeezing

To solve the equations under continuous wave (CW) operation, we change to the frequency domain, given that $h(t) = \frac{1}{\sqrt{2\pi}} \int e^{i\omega t} h(\omega) d\omega$ for all atomic and light

operators. This approach assumes steady state operation so optical pumping is essential. Otherwise the steady state would be a completely depolarized sample producing no squeezing ($\gamma_2 \rightarrow \infty$). The Fourier transformation changes the argument from time to frequency in the field equations (10.1), and it changes the differential equations (10.2) into the algebraic equations

$$\begin{aligned} i\omega \hat{X}_a(\omega) &= \tilde{\kappa} p_{in}(\omega) - \gamma_1 \hat{X}_a(\omega) + \sqrt{2\gamma_2} G_x(\omega) \\ i\omega \hat{P}_a(\omega) &= -\tilde{\kappa} \tau x'_i(\omega) - \gamma_1 \hat{P}_a(\omega) + \sqrt{2\gamma_2} G_p(\omega). \end{aligned} \quad (10.3)$$

We can now systematically express both the atomic variables and the output field variables in terms of the input field and noise operators, and we find by elementary operations,

$$x_{out}(\omega) = \frac{(\gamma_1 + i\omega)(\tau x_{in} + \rho F_x(\omega)) + \tau \sqrt{2\gamma_2} \tilde{\kappa} G_p(\omega)}{\gamma_1 + i\omega + \tau^2 \tilde{\kappa}^2}. \quad (10.4)$$

If we assume the vacuum values for the noise power spectrum of the incident classical field and the noise variables $\langle h(t)h(t') \rangle = \frac{1}{2} \delta(t-t') \Rightarrow \langle h(\omega)h(\omega') \rangle = \frac{1}{2} \delta(\omega+\omega')$, the noise spectrum of squeezing of the field is given by the expectation value $\langle x_{out}(\omega)x_{out}(\omega') \rangle = V_x(\omega)\delta(\omega+\omega')$, and we obtain directly from (10.4),

$$V_x(\omega) = \frac{1}{2} \left(1 - \frac{2(\gamma_1 - \gamma_2)\tilde{\kappa}^2\tau^2 + \tilde{\kappa}^4\tau^4}{(\gamma_1 + \tilde{\kappa}^2\tau^2)^2 + \omega^2} \right). \quad (10.5)$$

The squeezing spectrum is a Lorentzian, with a width given by the atomic decoherence rate, the coupling strength to the atoms and the transmission efficiency of light between the two passages of the gas. Interestingly, the effect of losses between the two light passages of the gas is merely to modify the value of the interaction strength, $\tilde{\kappa}' = \tilde{\kappa}\tau$. This effect was also observed in the much simpler case of a single interaction in Sec. 3.4.

Assuming that the dominant atomic decoherence mechanism is light absorption, and writing $\tilde{\kappa}^2 = \gamma\alpha$ and parameterizing $\gamma_p = \beta\gamma$, the maximum squeezing (at $\omega = 0$) is:

$$V_x(0) = \frac{1}{2} \frac{(1+\beta)^2(\beta + 2\alpha\tau^2)}{\beta(1+\beta + \alpha\tau^2)^2}, \quad (10.6)$$

Optimizing Eq. (10.6), we get

$$V_{opt} = \frac{1}{2} \frac{(2\alpha\tau^2 - 1)^3}{(\alpha\tau^2 - 1)(1 + \alpha\tau^2)^3} \rightarrow \frac{4}{\alpha\tau^2} \quad \alpha\tau^2 \gg 1 \quad (10.7)$$

for $\beta = \frac{1+\alpha\tau^2}{\alpha\tau^2-2}$. In Fig. 10.1 we plot Eq. (10.7) along with the optimal value for β . As can be seen, degrees of squeezing of the order of 10 dB should realistically be achieved for optical depths $\alpha \approx 100$ which is routinely attained in cold atomic samples as in [122]. In a BEC optical densities of up to 10^3 can be achieved potentially paving the way for unprecedented degrees of squeezing. The high degrees of squeezing are attained while the mean spin $J_x = \beta/(1+\beta) \cdot N/2$ is

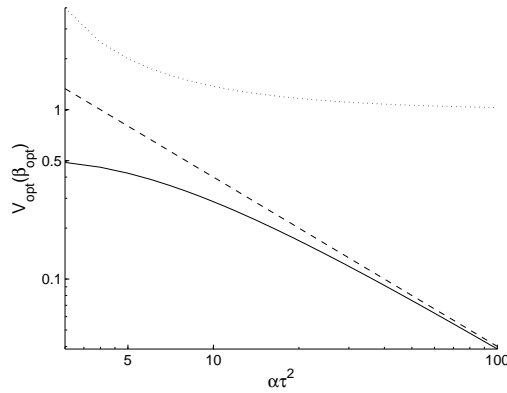


Figure 10.1: The optimal degree of squeezing V_{opt} , Eq. (10.7) (solid line) approached asymptotically by the expression $4/(\alpha\tau^2)$ (dashed line) as functions of $\alpha\tau^2$. Both curves assume the optimal strength of the optical pumping, $\beta = \gamma_p/\gamma$, which is shown as the upper dotted line.

reduced by a factor on order unity compared to its maximal value (strong optical pumping). For $\alpha\tau^2 \gg \beta \gg 1$ the mean spin is only reduced slightly and the non-optimal degree of squeezing approaches $\beta/(\alpha\tau^2)$, which can still be significant.

Optical transmission losses after the last atomic interaction can readily be modeled with a transmission coefficient and a noise term as in equations (10.1), and the relevant single mode or continuous wave variances V are modified according to, $V \rightarrow \tilde{\tau}^2 V + \tilde{\rho}^2 \frac{1}{2}$.

10.2 Pulsed Squeezing

The atoms can also be optically pumped into the macroscopically polarized state and interact only with a finite duration pulse of light, so that the reduction in the mean spin, with rate γ , is small. The equations (10.1) and (10.2), with $\gamma_1 = \gamma_2 = \gamma$ can be solved directly in the time domain, expressing the time dependent output fields as integrals over the incident field and noise operators. At this point, there are rich possibilities to vary the incident field envelope and the mode function identified with the output field with the purpose to optimize the squeezing. For simplicity, we shall here assume an incident square pulse, and we shall consider the amount of squeezing in a mode defined by the same pulse envelope, i.e., we consider the single mode field operators $\hat{q}_T = \frac{1}{\sqrt{T}} \int_0^T \hat{q}_{\text{out}}(t) dt$, where $\hat{q} = \hat{x}$ or \hat{p} , and where T is the duration of the light pulse. From our full time dependent solution we obtain the output variances:

$$\text{Var}(q_T) = \frac{1}{2} \left(1 \mp \frac{\tilde{\kappa}^4 \tau_q^2}{2\gamma_q^3 T} (2\gamma_q T + 1 - (2 - e^{-\gamma_q T})^2) \right), \quad (10.8)$$

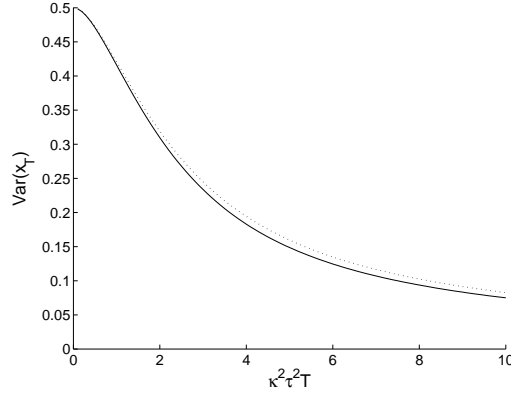


Figure 10.2: The variance $\text{Var}(x_T)$ after passage of a square pulse through the single cell set-up (see Fig. 9.1 a)) The variance is shown as a function of $\tilde{\kappa}^2 \tau^2 T$ with finite damping $\gamma T = 0.1$ (dotted line) and with no damping (solid line).

where $\hat{q} = \hat{x}, \hat{p}$, $\tau_x = \tau^2$, $\tau_p = \tau$, $\gamma_x = \gamma + \tilde{\kappa}^2 \tau^2$, $\gamma_p = \gamma$, and where the $-(+)$ sign apply to the $\hat{x}_T(\hat{p}_T)$ component. In Fig. 10.2 we plot the attainable degree of squeezing as a function of the dimensionless quantity $\tilde{\kappa}^2 \tau^2 T$. The assumption of this calculation is that the mean spin is preserved, and we show in the figure the results for finite damping $\gamma T = 0.1$ and for no damping $\gamma T = 0$, which provide quite equivalent results. The attainable degree of squeezing is clearly sizable. In the limit of no damping, Eq.(10.8) turns into the simple expressions derived in Eq. (9.12)

$$\text{Var}(\hat{x}_T) = \frac{3 + e^{-2\kappa^2} - 4e^{-\kappa^2}}{4\kappa^2}, \quad \text{Var}(\hat{p}_T) = \frac{1}{2} + \frac{\kappa^4}{6}, \quad (10.9)$$

where $\kappa^2 = \tilde{\kappa}^2 T$. We note that the product of the two variance is $1/4$ for $T = 0$ but while the \hat{x} component is gets squeezed the uncertainty product grows as $\kappa^2/8$ for $\kappa^2 \gg 1$.

Our proposal can also be implemented with two oppositely oriented atomic samples and a homogeneous magnetic field as illustrated in Fig. 9.1 b). To model this we introduce atomic variables $\hat{p}_{ai} = \hat{J}_{z,i}/\sqrt{J_x}$, and $\hat{x}_{ai} = \pm \hat{J}_{y,i}/\sqrt{J_x}$, where $i = 1, 2$ denotes the cell number. This gives equations of motion very similar to equations (10.1) and (10.2) and the Larmor precession caused by the constant magnetic field is modeled by adding terms $\pm \Omega \hat{x}_{ai}$ and $\mp \Omega \hat{p}_{ai}$ to the differential equations for \hat{p}_{ai} and \hat{x}_{ai} respectively. Note that as discussed in Sec. 2.8 the rotation is effectively in opposite directions for canonical description of the two atomic samples. Solving the coupled equations we get

$$V_x(\omega) = \frac{1}{2} \left(1 - \frac{4\tilde{\kappa}^4(\gamma_1^2 + \omega^2) + 4\tilde{\kappa}^2(\gamma_1 - \gamma_2)(\gamma_1^2 + \omega^2 + \Omega^2)}{\gamma_1^2 A^2 + 2A\gamma_1(\omega^2 + \Omega^2) + (\omega^2 - \Omega^2)^2 + 4\tilde{\kappa}^4 \omega^2} \right), \quad (10.10)$$

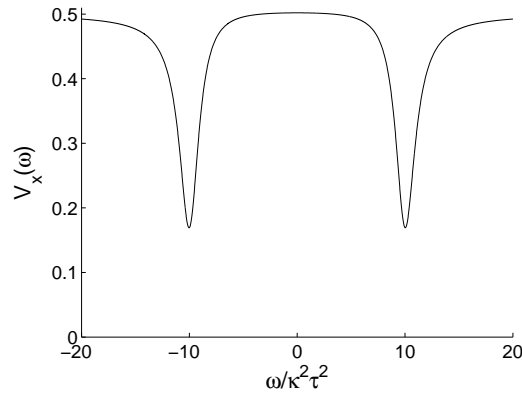


Figure 10.3: Squeezing spectrum for continuous wave field transmitted twice through two atomic ensembles which are Larmor precessing at frequency Ω . The parameters in the figure are $\Omega = 10\tilde{\kappa}^2$, $\gamma_1 = 0.1\tilde{\kappa}^2$, and $\gamma_2 = 0.2\tilde{\kappa}^2$ (corresponding to $\gamma = \gamma_p$).

where $\tilde{\kappa}' = \tilde{\kappa}\tau$ and $A = \gamma_1 + 2\tilde{\kappa}^2$. Again losses between the two passages merely modify the interaction strength by a factor as was also the case in the single cell implementation (Eq. (10.5)). In the limit of fast rotations ($\Omega \gg \gamma, \tilde{\kappa}^2$) we get two well separated peaks in the squeezing spectrum centered around $\omega = \pm\Omega$ as shown in Fig. 10.3. In the experiments described in the previous chapters we had $\tilde{\kappa}^2 \sim 1(\text{ms})^{-1}$ and $\Omega \sim 300\text{kHz}$ so the approximation of fast rotations is extremely good and under these conditions we would get a squeezing bandwidth of the order of kHz. Introducing $\omega = \pm\Omega + \delta$ and letting $|\Omega| \gg \delta, \gamma_1$, Eq. (10.10) reduces to a Lorentzian dependence on the frequency off-set with respect to $\pm\Omega$ with the same parameters as Eq. (10.5) for a single sample without rotations. Previously in this thesis it has been shown that the Faraday-QND interaction of a single sample without a constant bias magnetic field is regained for two oppositely oriented samples in the presence of a bias field. Our result shows that this correspondence extends to this manifestly non-QND situation, where in principle dynamics faster than the magnetic precession frequency is included.

In summary, we have shown that both light pulses and cw light fields passing twice through an atomic gas or through two atomic samples become significantly squeezed. The width of the squeezing spectrum is governed by the coupling strength κ^2 , and the optimum of squeezing is controlled by the resonant optical depth. Realistic estimates for these parameters in a number of current experiments suggest that the attainable squeezing competes well with the achievements of other schemes.

CHAPTER 11

Summary and Outlook

11.1 Summary

In this thesis we have presented three fundamental experimental advances towards the realization of a distributed quantum network. First of all, we have demonstrated the first realization of entanglement between two atomic objects in separate environments. This was two macroscopic atomic gas samples situated 0.5m apart. We have demonstrated $\sim 40\%$ noise reduction compared to the boundary for separable states.

Moreover, applying feedback to the atomic state based on a measurement of the light carrying information about the atomic state we have realized an unconditionally entangled state, i.e. a state that is entangled without requiring knowledge of previous measurement results. It is important to distinguish between unconditional and deterministic. Our entire light-atom interface is inherently deterministic in the sense that the interaction can be turned on at a user specified time and it succeeds in every realization. This is in sharp contrast to many other approaches to the light-atom interface and is definitely one of the main strengths of the approach.

The basis of all of this is a precise knowledge about characteristics of the coherent spin state, which forms the boundary between purely classical and quantum mechanical correlations. We can reliably create this state and have theoretical predictions for the noise level which match the observed to within 10%. Based on the simplicity of the model including atomic motion this agreement is actually quite good.

Using essentially the same experimental setup as in the unconditional entan-

gument experiment we have demonstrated the first mapping of an arbitrary light state - in this case weak coherent states - onto an atomic memory state with a fidelity exceeding the classical bound. Achieving a reliable transfer between light - representing a communication medium - and an atomic system for long time storage is one of the main challenges in the field of quantum communication.

We have also implemented quantum mechanical storage using light-atom teleportation, in which coherent states of light were transferred non-locally - i.e. without ever having interacted physically with the target atomic state. Such transfer paves the way for the realization of long distance quantum communication in distributed quantum networks.

Two factors should be pointed out as essential for the high fidelity transfer. First of all the transfer has to work deterministically, since otherwise a large vacuum component is introduced into the target state. Secondly, the atom-light interface has to be implemented with high efficiency. Unlike e.g. approaches based on EIT our coupling efficiency can approach unity - limited primarily by reflection losses of light and light induced decoherence.

Theoretically, we now understand the fundamental process of entanglement generation in great detail including the effect of decoherence. We have also solved the challenge of developing an experimentally feasible protocol for the retrieval of states stored in a quantum memory. Also, the protocol for the generation of squeezed light hints at potential applications of the approach outside the field of quantum information.

Finally, we would like to comment on the question of discrete versus continuous states. Although our quantum memory is inherently based on continuous variables it can also facilitate the storage of discrete variable states such as qubits. This was illustrated by explicit calculations in the context of the proposed retrieval protocol. One should however remember that for such states losses of light will play a much more dominant role than for coherent states of light.

11.2 Outlook

11.2.1 Atom-atom Teleportation

Although teleportation of the state of one atomic system onto another atomic system has recently been achieved between two trapped ions [115, 114] it still has not been implemented for an atomic continuous variable system. More importantly however, atomic teleportation still has not been achieved between two atomic systems in separate environments. This would constitute a major step forward in the field of quantum information and therefore an extension of our light-atom teleportation to two atomic systems would be highly desirable.

In this section we will illustrate how the canonical formalism for the Faraday interaction makes it significantly easier to generate new variants of well known quantum information protocols by combining the single cell interaction equations (2.39) in various ways. Performing similar calculations based on equations (2.26)

and (2.27) quickly becomes intractable.

Three Cell Implementation

The most conventional way of performing atom-atom teleportation utilizing the Faraday interaction with light is to implement a scheme as sketched in Fig. 8.1, where each system consists of a single atomic ensemble. The samples containing the initial (U) and final (B) states should have the same orientation of the mean spin, whereas the remaining sample (A) should be oriented in the opposite direction. For this setup, sending a light pulse through samples A and B and subsequently measuring \hat{x}_s and \hat{x}_c will entangle the two as described theoretically and experimentally in chapters 3, 4, and 6. Next a new light pulse is sent through samples A and U and \hat{x}_s and \hat{x}_c are measured. The teleportation is then completed by feeding back the four measurement results to the target sample (B) with appropriate gains. The effect of the interactions is easily determined using the single cell interactions Eq. (2.42). Doing this, it can be seen that the gains for the second pulse are fixed to $g(\hat{x}_{c(s)}) = \pm \frac{\sqrt{2}}{\kappa}$ if unity gain is to be achieved. After the application of this feedback the target state is:

$$\begin{aligned}\hat{x}_{aB} &\rightarrow \hat{x}_{aU} + \left(1 - g \frac{\kappa}{\sqrt{2}}\right) (\hat{x}_{aB} - \hat{x}_{aA}) + \hat{p}_c \left(\frac{\kappa}{\sqrt{2}} - \frac{\kappa}{\sqrt{2}}\right) + g\hat{x}_s - \frac{\kappa}{\sqrt{2}}\tilde{\hat{x}}_s \\ \hat{p}_{aB} &\rightarrow \hat{p}_{aU} + \left(1 - g \frac{\kappa}{\sqrt{2}}\right) (\hat{p}_{aB} + \hat{p}_{aA}) + \hat{p}_s \left(\frac{\kappa}{\sqrt{2}} - \frac{\kappa}{\sqrt{2}}\right) - g\hat{x}_c + \frac{\kappa}{\sqrt{2}}\tilde{\hat{x}}_c,\end{aligned}\tag{11.1}$$

where $g = g(\hat{x}_s) = -g(\hat{x}_c)$. As can be seen all the contributions from the light p are canceled exactly in both quadratures. This is very important because it means that the fidelity of the protocol can be improved by squeezing the light x quadratures of both pulses. From Eq. (11.1) the variance of the output state can be calculated and the gain that minimizes it found. It turns out to be $g_{\text{opt}} = \frac{\sqrt{2}\kappa}{1+\kappa^2}$, which gives the atomic variances:

$$\text{Var}(\hat{x}_{aB}) = \text{Var}(\hat{p}_{aB}) = \frac{1}{2} \left(1 + \frac{2}{1+\kappa^2} + \frac{2}{\kappa^2}\right).\tag{11.2}$$

With the substitution $\kappa^2 \rightarrow 2\kappa^2$ this expression is equivalent to the one derived in [36] for three sample teleportation without rotations. Since the variances asymptotically tend towards 1/2 in the $\kappa^2 \rightarrow \infty$ limit we get unity fidelity in this limit. Squeezing the variance of the x quadratures of both of the light beams by a factor χ Eq. (11.2) still holds but with the substitution $\kappa^2 \rightarrow \chi\kappa^2$ so the speed of convergence towards unity fidelity is merely increased. In the actual experiment we have substantial decoherence, which can in a simple fashion be added to the theory as outlined in Sec. 3.4. In Fig. 11.1 the resulting fidelities with atomic decoherence $\beta = 0.8$ and light loss $\epsilon = 0.1$ can be compared to the fidelities calculated from Eq. (11.2) with and without 6dB of light squeezing. As can

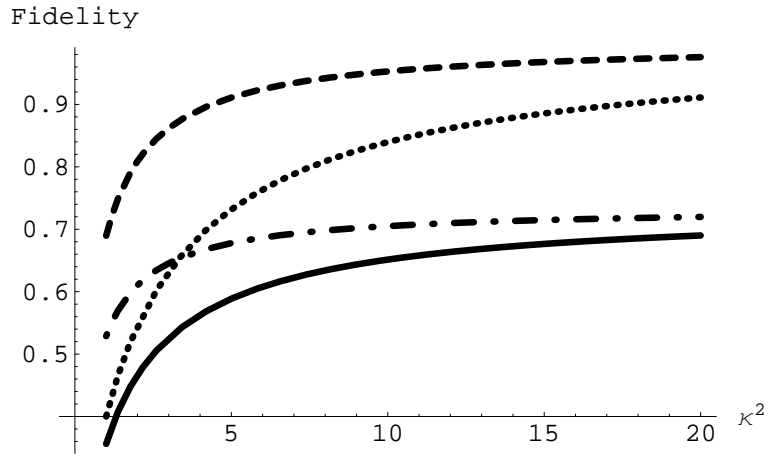


Figure 11.1: Atom-atom teleportation in the conventional three cell setup. Dotted: no decoherence, no input light squeezing. Solid: $\epsilon = 0.1$, $\beta = 0.8$, no squeezing. Dashed: no decoherence, 6dB sq. Dash-dotted: $\epsilon = 0.1$, $\beta = 0.8$, 6dB squeezing

be seen, without decoherence fidelities substantially above the classical boundary can be achieved with realistic values of the interaction strength ($\kappa^2 \sim 2$), whereas somewhat higher values are needed when decoherence is included. With decoherence the achievable fidelity can be shown to be fundamentally limited to $F = 1/(2 - \beta^2)$.

Two Cell Implementation

We now want to investigate whether atom-atom teleportation can be achieved using light as the auxiliary system (A). In other words, can teleportation between two atomic systems be achieved by merely using a shifted state of one of the samples as the teleportation object (U), sending light through both samples sequentially, measuring the light, and feeding back the result to the other sample (B). If the two atomic samples are oppositely oriented, this procedure is simply the procedure used in the generation of unconditional entanglement as discussed in Sec. 6.2. After the feedback, the state of the second sample is described by:

$$\begin{aligned}\hat{x}_{aB} &\rightarrow \hat{x}_{aU} - \frac{\sqrt{2}}{\kappa} \hat{x}_s + \frac{\kappa}{\sqrt{2}} \hat{p}_c \\ \hat{p}_{aB} &\rightarrow -\hat{p}_{aU} + \frac{\sqrt{2}}{\kappa} \hat{x}_c + \frac{\kappa}{\sqrt{2}} \hat{p}_s,\end{aligned}\tag{11.3}$$

so the transfer can be done. Unfortunately, analyzing the fidelity yields $F_{\text{opt}} = 0.5$ at $\kappa = \sqrt{2}$ so atom-atom teleportation exceeding the classical limit is impossible in the anti-parallel setting. Also, it can easily be seen that squeezing the incoming

light beam will not help since all four light variables are present in the atomic final state with equal weight.

The main reason for the failure is the fact that the light p quadrature remains uncanceled after the feedback. For this purpose the mapping of the light p quadratures onto itself during the single cell interaction would be a desirable effect. Therefore we try the same calculation with two parallel spin samples, in which this back action noise is not canceled. Indeed, we get:

$$\begin{aligned}\hat{x}_{aB} &\rightarrow -\hat{x}_{aU} - \frac{\sqrt{2}}{\kappa}\hat{x}_s + \frac{\kappa}{\sqrt{6}}\hat{p}_{c,1} \\ \hat{p}_{aB} &\rightarrow -\hat{p}_{aU} - \frac{\sqrt{2}}{\kappa}\hat{x}_c + \frac{\kappa}{\sqrt{6}}\hat{p}_{s,1},\end{aligned}\tag{11.4}$$

which gives an optimum fidelity of $F_{\text{opt}} = 0.63$ at $\kappa^2 = 3.5$. Again each atomic quadrature contains an x and a p quadrature from the light and at the optimal interaction strength they both contribute equally. As in the case of atomic teleportation using three samples squeezing the input light effectively redefines the interaction strength. Given a κ^2 a squeezing of $\chi = \frac{2\sqrt{3}}{\kappa^2}$ will give the optimum fidelity. Thus to achieve the optimal fidelity for $\kappa^2 = 1$ requires approximately 5dB of light squeezing. This discussion was based on the assumption of a broadband squeezed source such that both the symmetric and the anti-symmetric (Eq. (2.41)) are squeezed simultaneously. If we had a source of squeezing with a squeezing bandwidth comparable to the reciprocal of the pulse duration one could envisage squeezing the symmetric mode without simultaneously anti-squeezing the anti-symmetric one. Then fidelities approaching 0.92 could theoretically be achieved. Note, that chapter 10 exactly describes the generation of such squeezed states with squeezing in a narrow band around a selected RF-frequency. Although this protocol may not quite be promising enough to warrant experimental implementation at present I think that it serves to illustrate the point that armed with the single cell interaction equations, a napkin, and e.g. a boring lecture or dinner party novel protocols can fairly easily be derived.

11.2.2 Interfacing with Non-classical Light States

Another high priority goal would be to demonstrate experimental mapping or teleportation of a non-classical state. First, one might consider transferring a squeezed state of light into a squeezed atomic state. Looking at Eq. (7.1) describing the mapping protocol we see that this cannot be done for squeezing in the \hat{p} quadrature because of the uncanceled \hat{X}_a . Transferring squeezing into \hat{P}_a , however, can be done. In fact, we know from Sec. 6.2 that a Faraday interaction with coherent light followed by feedback of the detected light creates an unconditionally entangled state, corresponding to the squeezing of certain non-local atomic variables. Of course, if the input light is squeezed the subsequent atomic squeezing can be increased correspondingly. Calculating the variance of \hat{P}_a after

the storage with a squeezed input $\text{Var}(\hat{x}_L) = \frac{1}{2\varepsilon}$ ($\varepsilon > 1$) we get:

$$\text{Var}(\hat{P}_a^{\text{out}}) = \frac{1}{2} ((1 - \kappa g)^2 + g^2/\varepsilon) \rightarrow \frac{1}{2} \frac{1}{1 + \varepsilon \kappa^2}. \quad (11.5)$$

Here the variance obtained by applying the optimum gain of $g_{\text{opt}} = \varepsilon \kappa / (1 + \varepsilon \kappa^2)$ is also given. As can be seen the attainable degree of atomic squeezing can be greatly increased using squeezed light as an input.

It would also be very interesting to store one of two entangled beams and subsequently verifying entanglement between the atomic system and the remaining light beam. Imagine that we have two light beams described by $(\hat{x}_{L1}, \hat{p}_{L1})$ and $(\hat{x}_{L2}, \hat{p}_{L2})$ with an EPR variance of $\text{Var}(\hat{x}_{L1} - \hat{x}_{L2}) = \text{Var}(\hat{p}_{L1} + \hat{p}_{L2}) = 1/\varepsilon$ ($\varepsilon > 1$). the entanglement condition is $\text{Var}(\hat{p}_{L1} + \hat{p}_{L2}) + \text{Var}(\hat{x}_{L1} - \hat{x}_{L2}) < 2$. With e.g. 6dB of entanglement ($\varepsilon = 4$) we see that we can tolerate up to three units of vacuum noise combined in the two atomic quadratures. In the experimental realization described in Sec. 7 the added noise in each quadrature was slightly below one unit so this may indeed be feasible.

So far all of the states that we have discussed are Gaussian states. The demonstration that Gaussian states cannot be distilled [79, 85] has spurred an intense interest in leaving the Gaussian regime. In our group [123] and elsewhere [124] a non-classical light state very reminiscent of the superposition of two weak coherent states (Schrödinger Kitten) has been created via subtraction of a photon from a squeezed vacuum beam. Storage of such states or single photon states in an atomic memory would constitute a major step towards the implementation of linear optics quantum computing [125, 52]. Such states have been generated to be compatible with an atomic quantum memory [123] by having a high purity of the spatial and temporal modes of the field. However, in order to be applicable for our room temperature based quantum memory the temporal profile of the light states have to be matched to our probe durations, which in order to achieve sufficient coupling strength have to be $\sim 1\text{ms}$. This is several orders of magnitude from the width of e.g. $\sim 100\text{ns}$ demonstrated in [123]. Thus, it would be extremely interesting to implement the Faraday based quantum memory in cold dense atomic sample, where the increased optical depth allow for much shorter pulse durations. This is currently being pursued in our group.

APPENDIX A

Effect of Atomic Motion

Since in our experiments the atoms are at room temperature and, for experimental reasons, the light beam does not cover the entire cross section of the atomic sample, the atoms move across the beam several times (~ 10) during the time of a pulse. This averaging effect insures that all atoms spend roughly the same amount of time inside the beam but, as we shall see, it still has important implications for the noise properties. In brief, the atomic motion modifies the projection noise level and acts as an additional source of decoherence since two subsequent probe pulses interact with the individual atoms with different weights. The results are related to the work of [126].

A.1 Modeling Atomic Motion

To be more quantitative, we introduce new pseudo-angular momentum operators $J_q \rightarrow \sum_j p_j F_q^{(j)}$, where p_j is the fraction of time the j 'th atom spends interacting with the laser beam and $q = x, y, z$. These have the commutator:

$$\left[\sum_{j=1}^{N_{\text{at}}} p_j F_y^{(j)}, \sum_{j=1}^{N_{\text{at}}} p_j F_z^{(j)} \right] = \sum_{j=1}^{N_{\text{at}}} p_j^2 [F_y^{(j)}, F_z^{(j)}] = i \sum_{j=1}^{N_{\text{at}}} p_j^2 F_x^{(j)}. \quad (\text{A.1})$$

This leads to the Heisenberg uncertainty relation (for a highly polarized sample with $F_x \approx F$)

$$\text{Var} \left(\sum_{j=1}^{N_{\text{at}}} p_j F_y^{(j)} \right) \text{Var} \left(\sum_{j=1}^{N_{\text{at}}} p_j F_z^{(j)} \right) \geq \left(\frac{J}{2} p^2 (1 + \sigma^2) \right)^2 \quad (\text{A.2})$$

where we have introduced the mean $p = \langle p_j \rangle$ and variance $\text{Var}(p_i) = \sigma^2 \cdot p^2$ of p_j . With this definition, σ is the relative standard deviation of p . Since, for the coherent spin state,

$$\text{Var} \left(\sum_{j=1}^{N_{\text{at}}} p_j F_z^{(j)} \right) = \frac{J}{2} p^2 (1 + \sigma^2) = \text{Var}(\text{CSS}), \quad (\text{A.3})$$

this highly polarized state corresponds to a minimum uncertainty state. The measured noise is then limited by the Heisenberg uncertainty principle and we confidently call this projection noise. To maintain the correct commutation relation $[X, P] = i$ we experimentally normalize the atomic operators to the *measured* projection noise, i.e. instead of defining $X = J_y/\sqrt{J}$ we effectively have $X = \sum_j p_j F_y^{(j)} / \sqrt{J p^2 (1 + \sigma^2)}$.

The average fraction of time p each atom spends inside the beam is clearly $p = A_{\text{beam}}/A_{\text{cell}}$. Let us now discuss the scaling of σ^2 with simple physical parameters. The fact that the variance may be non-zero arises from the finite time available for the averaging process carried out by the atomic motion. A typical traversing time across the vapor cell is $\tau = L/v_0$ where L is the cell dimension and v_0 is e.g. the one-dimensional rms speed of the atoms. We may think of this atomic motion as n independent journeys across the vapor cell volume, where $n \approx T/\tau = T v_0/L$. We then model the motion through the beam with mean occupancy p by assuming in each walk across the cell volume that either (1) the atom spends all the time τ inside the beam, which should happen with probability p , or (2) the atom spends all the time τ outside the beam which should happen with probability $1 - p$.

We then count the number of times n_{inside} that an atom was inside the beam out of the possible n journeys. In this simple model n_{inside} is a stochastic variable which is binomially distributed with mean np and variance $np(1 - p)$. We are interested in the fraction of time ($\approx n_{\text{inside}}/n$) spent inside the beam. It follows $\langle n_{\text{inside}}/n \rangle = p$ and $\sigma^2 = \text{Var}([n_{\text{inside}}/n]/p) = (1 - p)/np$. Hence the simple model leads to

$$p = \frac{A_{\text{beam}}}{A_{\text{cell}}} \quad \text{and} \quad \sigma^2 = \frac{(A_{\text{cell}} - A_{\text{beam}})L}{A_{\text{beam}}T v_0} \chi, \quad (\text{A.4})$$

where we have inserted a factor χ to take into account deviations from the very simple estimate. Numerical simulations performed for a cubic cell have shown that the relative variance σ^2 is roughly four times smaller than the estimate above. Note the characteristic scaling with T^{-1} and with the area $(A_{\text{cell}} - A_{\text{beam}})$

not covered by the light beam (when A_{beam} is close to its maximum value A_{cell}). We also expect a slightly increased σ^2 due to the difference in effective detuning from atom to atom caused by Doppler broadening.

A.2 Atomic Motion as a Source of Decoherence

To see how atomic motion acts as an effective source of decoherence, imagine that we perform some manipulations of atoms using one laser pulse and subsequently probe these manipulations with another laser pulse. Since atoms move during interactions the probed quantum operator changes in time. Comparing the operator at the 1st and 2nd times we get

$$\begin{aligned} \text{Var} \left(\sum_{i=1}^{N_{\text{at}}} p_{i,2\text{nd}} F_{z,2\text{nd}}^{(i)} - \sum_{i=1}^{N_{\text{at}}} p_{i,1\text{st}} F_{z,1\text{st}}^{(i)} \right) &= \sum_{i=1}^{N_{\text{at}}} \text{Var}(F_{z,1\text{st}}^{(i)}) \langle (p_{i,2\text{nd}} - p_{i,1\text{st}})^2 \rangle \\ &= \frac{J}{2} \cdot 2p^2 \sigma^2 = 2\text{Var}(\text{CSS})(1 - \beta) \quad \text{with} \quad \beta = \frac{1}{1 + \sigma^2}. \end{aligned} \tag{A.5}$$

We assumed $p_{i,1\text{st}}$ and $p_{i,2\text{nd}}$ to be uncorrelated, which is reasonable since a collision with the cell wall randomizes the velocity of the atoms. Also, we took $F_{z,1\text{st}}^{(i)} = F_{z,2\text{nd}}^{(i)}$. This corresponds to having no decoherence at all apart from the effect of atomic motion which is the only effect studied in this calculation. To interpret the above calculations we consider a standard decoherence calculation. Consider a true spin operator J_z subject to decoherence parametrized by the number β such that

$$J_{z,1\text{st}} \rightarrow J_{z,2\text{nd}} = \beta J_{z,1\text{st}} + \sqrt{1 - \beta^2} J_{\text{vac}} \quad \text{with} \quad \text{Var}(J_{\text{vac}}) = \frac{J}{2} = \text{Var}(\text{CSS}). \tag{A.6}$$

Then the operator changes by an amount characterized by the variance

$$\begin{aligned} \text{Var}(J_z^{2\text{nd}} - J_z^{1\text{st}}) &= \text{Var} \left(J_z^{1\text{st}}(1 - \beta) - \sqrt{1 - \beta^2} J_{\text{vac}} \right) \\ &= J(1 - \beta) = 2\text{Var}(\text{CSS})(1 - \beta) \end{aligned} \tag{A.7}$$

which is exactly the same as in (A.5). We are led to the conclusion that atomic motion inevitably gives rise to an effective decoherence. We thus see that, whereas the increased coherent spin state noise with increased σ^2 might seem to suggest that non-classical states are more easily created (by producing states with noise lower than the CSS), this is compensated for by an increased decoherence of the state. Therefore, higher σ^2 does not lead to higher fidelity protocols.

APPENDIX B

Covariance Matrix Update with Decoherence

We now derive an expression for the time evolution of the covariance matrix due to photon loss and atomic decay. For a coherent state this is trivial - it merely transforms into another coherent state with a reduced displacement. Highly correlated states such as squeezed or entangled states, however, are much more sensitive to losses and decoherence. To quantify this, we write the collective spin operator for N spin- J particles as $J_\alpha = \sum_{i=1}^N j_{i\alpha}$, where $\alpha = x, y, z$. The mean values and correlations of this collective operator can be written as:

$$\begin{aligned} \langle J_\alpha \rangle &= \sum_{i=1}^N \langle j_{i\alpha} \rangle = JN \langle j_{i\alpha} \rangle , \\ \langle J_\alpha^2 \rangle &= \sum_{i,k}^N \langle j_{i\alpha} j_{k\alpha} \rangle = \frac{JN}{2} + N(N-1) \langle j_{i\alpha} j_{k\alpha} \rangle , \end{aligned} \tag{B.1}$$

where we used the symmetry of the state under exchange of particles and the first term in the last expression represents the coherent state variance. In terms of mean values we will primarily be interested in the direction of the mean spin, $\alpha = x$, and in terms of correlations the transverse components $\alpha = y, z$ will be interesting. From Eq. B.1 we get an expression for the two-particle correlations as a function of the second moment of the collective spin operator:

$$\langle j_{i\alpha} j_{k\alpha} \rangle = \frac{\langle J_\alpha^2 \rangle - JN/2}{N(N-1)} . \tag{B.2}$$

We will now assume that $N - N'$ of the atoms are excited, undergo spontaneous emission, and end up in an uncorrelated thermal state:

$$\langle (J'_\alpha)^2 \rangle = \langle J_\alpha^2 \rangle \frac{N'(N' - 1)}{N(N - 1)} + \frac{N'(N - N')}{N - 1} \frac{J}{2} + (N - N') V_{\text{therm}} , \quad (\text{B.3})$$

where as discussed in Sec. 5.6.4 $V_{\text{therm}} = \frac{J(J+1)}{3} \chi$. Here χ allows for a fraction of the atoms going into non-interacting states. Note that for a spin $\frac{1}{2}$ system V_{therm} coincides with the coherent state variance $V_{\text{CSS}} = J/2$. For probing the $F = 4$ hyperfine level of cesium and complete rethermalization after spontaneous emission $\chi = \frac{2 \cdot 4 + 1}{(2 \cdot 4 + 1) + (2 \cdot 3 + 1)} = \frac{9}{16}$ because of the presence of the $F = 3$ hyperfine level.

Defining the fraction $\eta_\tau = (N - N')/N$ of the atoms which decay into a random mixture of the ground states during a time interval τ and taking $N \gg 1$ we get:

$$\begin{aligned} \langle J_\alpha'^2 \rangle &= (1 - \eta_\tau)^2 \langle J_\alpha^2 \rangle + \eta_\tau (1 - \eta_\tau) \frac{JN}{2} + \eta_\tau \frac{JN(J+1)}{3} \chi \\ &\approx (1 - \eta_\tau)^2 \langle J_\alpha^2 \rangle + \eta_\tau \frac{JN}{2} + \eta_\tau \frac{JN(J+1)}{3} \chi . \end{aligned} \quad (\text{B.4})$$

The atomic decay leads to a corresponding reduction of the mean spin $J'_x = (1 - \eta_\tau) J_x$. Taking into account that the covariance matrix is two times the covariance of the transverse spin components scaled by the macroscopic longitudinal mean spin, we obtain for the corresponding diagonal covariance matrix element:

$$\gamma_{a,ii}^{\text{out}} = (1 - \eta_\tau) \gamma_{a,ii}^{\text{in}} + \eta_\tau \left[1 + \chi \frac{2(J+1)}{3} \right] \frac{JN}{J_x} \equiv (1 - \eta_\tau) \gamma_{a,ii}^{\text{in}} + \eta_\tau \xi . \quad (\text{B.5})$$

For $J = 1/2$ and $\chi = 1$ and a continuous interaction ($J_x(t) = J_x(0)e^{-\eta t}$) we obtain $\xi(t) = 2e^{\eta t}$. For off-diagonal elements only the first term of Eq. (B.5) is present.

If instead of decaying towards a thermal state the atoms are driven towards the CSS by the decoherence mechanism, the mean spin will be unaffected, whereas the mean value of the transverse spin components are reduced by a factor $1 - \eta_\tau$. In this case Eq. (B.5) translates into:

$$\gamma_{a,ii}^{\text{out}} = (1 - \eta_\tau)^2 \gamma_{a,ii}^{\text{in}} + \eta_\tau (2 - \eta_\tau) \approx (1 - 2\eta_\tau) \gamma_{a,ii}^{\text{in}} + 2\eta_\tau . \quad (\text{B.6})$$

We see that, unlike in Eq. (B.5), if $\gamma_{a,ii}^{\text{in}} = 1$ this will also be the case after the decoherence, thus showing that the CSS is a stationary state with respect to this type of decoherence. This type is important since such a process is our dominant experimental decoherence mechanism as discussed in Sec. 5.4.

Getting back to the case of spontaneous emission, the gas now contains two components: the atoms which have not decayed, described by the first two terms in Eq. (B.4) and the ones which have decayed, described by the last term. The question now arises, what is the atomic state after a number of such interactions.

Physically, if nothing else happens to the atoms, subsequent interaction with the light can have no further effect on the random component, but a new fraction of atoms will be randomized. Thus, in each iteration only the terms coming from the coherent component of atoms should be damped by $(1 - \eta_\tau)^2$:

$$\begin{aligned}
\langle J_{\alpha,1}^2 \rangle &= (1 - \eta_\tau)^2 \langle J_{\alpha,0}^2 \rangle + \eta_\tau \frac{JN}{2} + \eta_\tau \zeta JN \\
\langle J_{\alpha,2}^2 \rangle &= (1 - \eta_\tau)^2 [(1 - \eta_\tau)^2 \langle J_{\alpha,0}^2 \rangle + \eta_\tau \frac{JN}{2}] \\
&\quad + \eta_\tau \frac{JN(1 - \eta_\tau)}{2} + \eta_\tau [1 + (1 - \eta_\tau)] \zeta JN \\
&\quad \dots = \dots \\
\langle J_{\alpha,n}^2 \rangle &= (1 - \eta_\tau)^{2n} \langle J_{\alpha,0}^2 \rangle \\
&\quad + \eta_\tau \left[(1 - \eta_\tau)^{n-1} + \sum_{j=n}^{2(n-1)} (1 - \eta_\tau)^j \right] \frac{JN}{2} \\
&\quad + \eta_\tau \sum_{j=0}^{n-1} (1 - \eta_\tau)^j \zeta JN, \tag{B.7}
\end{aligned}$$

where for convenience $\zeta = (J + 1)\chi/3$. In the limit $n \rightarrow \infty$ only the last term, representing the fully random component of the gas, will contribute. The geometrical series gives $1/\eta_\tau$, so we see that the initial squeezing will decay exponentially as expected and we will end up with N unpolarized atoms each contributing $V_{\text{therm}} = \zeta J$ to the variance as expected.

Remembering that the mean spin after n iterations is $J_{x,n} = (1 - \eta_\tau)^n J_{x,0} = (1 - \eta_\tau)^n JN$, Eq. (B.7) can be transformed into an expression for the diagonal entries in the covariance matrix:

$$\gamma_{a,ii}^n = (1 - \eta_\tau)^n \gamma_{a,ii}^0 + \eta_\tau \left[\frac{1}{1 - \eta_\tau} + \sum_{j=0}^{n-2} (1 - \eta_\tau)^j + 2\zeta \sum_{j=-n}^{-1} (1 - \eta_\tau)^j \right]. \tag{B.8}$$

This analysis treats the atoms that have decayed and the ones that have not decayed on unequal footing, and it hence breaks with the Gaussian state Ansatz, which assumes that all information is in the collective variance and mean values for the entire atomic ensemble. The analysis does not make it easy to treat the coherent part of the interactions and the measurement back action, that we are interested in, and we hence wish to investigate, whether restoration to the Gaussian state Ansatz will yield a large discrepancy with the exact results. To this end, we go back to the update formula, Eq. (B.4), and insist that the variance obtained here should be treated as the variance describing a Gaussian state ensemble, i.e., we do not discriminate between the two kinds of atoms. In subsequent time steps, we thus simply iterate Eq. (B.5), as if all atoms contribute

evenly to the joint variance. The result of this iteration is readily obtained:

$$\gamma_{a,ii}^n = (1 - \eta_\tau)^n \gamma_{a,ii}^0 + \eta_\tau \xi \sum_{j=1}^n (1 - \eta_\tau)^{n-2j}. \quad (\text{B.9})$$

Note that every other term is missing as compared to Eq. (B.8). Calculating the difference between Eq. (B.8) Eq. (B.9) we obtain the error in using the latter:

$$\begin{aligned} \text{error} &= \eta_\tau \left(\xi \sum_{j=1}^n (1 - \eta_\tau)^{n-2j} - \sum_{j=0}^{n-2} (1 - \eta_\tau)^j - 2\zeta \sum_{j=-n}^{-1} (1 - \eta_\tau)^j \right) \\ &= \eta_\tau \left(\frac{2\zeta - 1}{2} \sum_{j=0}^n (1 - \eta_\tau)^j + \frac{1 - 2\zeta}{2} \sum_{j=-n}^{-1} (1 - \eta_\tau)^j \right) \\ &= \eta_\tau \left(\frac{2\zeta - 1}{2} \left[\frac{1 - (1 - \eta_\tau)^{n+1}}{1 - (1 - \eta_\tau)} \right] + \frac{1 - 2\zeta}{2} \left[\frac{1 - (1 - \eta_\tau)^{-n+1}}{1 - 1/(1 - \eta_\tau)} - 1 \right] \right) \\ &\rightarrow \left(\frac{2\zeta - 1}{2} [1 - e^{-\eta t}] + \frac{1 - 2\zeta}{2} [1 - e^{\eta t}] \right), \end{aligned} \quad (\text{B.10})$$

where in the end the continuous limit $t = n\tau$ with $\eta\tau \rightarrow 0$ and $n \rightarrow \infty$ was taken and terms obviously disappearing in this limit were ignored in the entire calculation. Remembering that $\zeta = (J + 1)\chi/3$ we see that the error vanishes for a spin 1/2 system, thus offering ample support for the use of the update formula, Eq. (B.5), with the underlying assumption of a Gaussian state, together with the evolution of γ due to interaction and measurements. This is certainly not the case for other spin systems where one should apply the update equation with caution - expecting errors of the order of $1 - e^{\eta t}$. Note that the error only arises when Eq. (B.5) is used iteratively. It can be applied once to any spin system with equal validity. Please note that the validity is primarily limited by the requirement that the accumulated decoherence during the entire interaction time should be sufficiently small. This requirement arises because the physical decoherence occurs as a random process continuously in time. This gives an exponential decay of mean values, whereas Eq. (B.5) represents a linear approximation to this.

The derivation of the update equation for the light part of the covariance matrix follows the same logic as in the atomic case except that it is much simpler since no thermal component is added. In this case we get:

$$\gamma_L(t + \tau) = (1 - \epsilon)\gamma_L(t) + \epsilon \mathbf{I}, \quad (\text{B.11})$$

where ϵ is the fraction of the light lost and \mathbf{I} is an identity matrix ensuring that the last term is only added to the diagonal elements.

APPENDIX C

High Order Stark Shift

Let us calculate the Stark effect from the probe laser on the magnetic sub levels $|F, m\rangle$. We let the light be strong and linearly polarized along the vector

$$\mathbf{e}_1 = \mathbf{e}_x \cos \alpha + \mathbf{e}_y \sin \alpha, \quad (\text{C.1})$$

i.e. α is the angle between the macroscopic spin direction (the x -axis) and the probe polarization direction. Light is propagating in the z -direction. The Stark effect on magnetic sublevels is much weaker than the splitting caused by the constant bias magnetic field and can be calculated in non-degenerate perturbation theory from the interaction Hamiltonian (2.20). The a_0 term is common to all levels, the a_1 term is zero on average since $\langle \hat{S}_z \rangle = 0$, and we are left with the higher order components proportional to a_2 .

With \hat{a}_1 the creation operator along the strong direction we have $\hat{a}_x = \hat{a}_1 \cos \alpha$ and $\hat{a}_y = \hat{a}_1 \sin \alpha$ (neglecting the direction orthogonal to \hat{a}_1 which is in the vacuum state for linear polarization). With $\hat{S}_\pm = \hat{S}_x \pm i\hat{S}_y$ we derive from (2.5) that

$$\langle \hat{S}_+(t) \rangle = \frac{\phi(t)}{2} e^{2i\alpha} \quad \text{and} \quad \langle \hat{S}_-(t) \rangle = \frac{\phi(t)}{2} e^{-2i\alpha}, \quad (\text{C.2})$$

where $\phi(t)$ is the photon flux and Stokes operators are normalized to photons per second. In order to calculate the higher order terms of the interaction Hamiltonian for a single atom we leave out the integral $\int \dots \rho A dz$ in (2.20) and renormalize light operators (by absorbing the speed of light c) to photons per second

and find

$$\hat{H}_{\text{int}}^{\text{eff}} = -\frac{\hbar\gamma}{8A\Delta} \frac{\lambda^2}{2\pi} a_2 \cdot \phi(t) \cdot (j_z^2 - [j_x^2 - j_y^2] \cos(2\alpha) - [\hat{j}_x \hat{j}_y + \hat{j}_y \hat{j}_x] \sin(2\alpha)). \quad (\text{C.3})$$

We also replaced \hat{j}_{\pm} by $\hat{j}_x \pm i\hat{j}_y$. We need to calculate the expectation value of this Hamiltonian for the different energy eigenstates $|m\rangle$ quantized along the x -direction. We have

$$\begin{aligned} \langle m | \hat{j}_x^2 | m \rangle &= m^2, \\ \langle m | \hat{j}_y^2 | m \rangle &= \frac{F(F+1) - m^2}{2}, \\ \langle m | \hat{j}_z^2 | m \rangle &= \frac{F(F+1) - m^2}{2}, \\ \langle m | \hat{j}_x \hat{j}_y + \hat{j}_y \hat{j}_x | m \rangle &= 0. \end{aligned} \quad (\text{C.4})$$

The first of these is obvious since $|m\rangle$ is quantized along the x -axis. We have $\langle \hat{j}_y^2 \rangle = \langle \hat{j}_z^2 \rangle$ by symmetry and the value is found from the fact that $\hat{j}_x^2 + \hat{j}_y^2 + \hat{j}_z^2 = F(F+1)$. Also, by symmetry we have in an eigenstate of \hat{j}_x that $\langle m | \hat{j}_y \hat{j}_x | m \rangle = m \cdot \langle m | \hat{j}_y | m \rangle = 0$ which leads to the final line. Calculating the expectation value of (C.3) we get

$$E_m^{\text{Stark}} = \frac{\hbar\gamma}{8A\Delta} \frac{\lambda^2}{2\pi} a_2 \cdot \phi(t) \cdot \left[\frac{1 + 3 \cos(2\alpha)}{2} \cdot m^2 - \frac{1 + \cos(2\alpha)}{2} F(F+1) \right]. \quad (\text{C.5})$$

What is important for us is the shift $\delta\nu_{m+1,m} = (E_{m+1}^{\text{Stark}} - E_m^{\text{Stark}})/h$ of a magnetic resonance line which then becomes

$$\delta\nu_{m+1,m}^{\text{Stark}} [\text{Hz}] = \frac{\gamma\lambda^2 a_2}{64\pi^2 A\Delta} \cdot \phi(t) \cdot [1 + 3 \cos(2\alpha)] \cdot [2m + 1]. \quad (\text{C.6})$$

This Stark shift is problematic for several protocols, especially the setup with two oppositely oriented samples. Note, that for atoms polarized in the $m_F = 4$ state the relevant transition $m_F = 4 \leftrightarrow m_F = 3$ has a Stark shift proportional to $2 \cdot 3 + 1 = 7$. An oppositely oriented sample with $m_F = -4$ has for the transition $m_F = -3 \leftrightarrow m_F = -4$ a Stark shift proportional to $2 \cdot (-4) + 1 = -7$. Hence, these two transition frequencies cannot be overlapped both in the presence and absence of light (see Fig. C.1 for an illustration).

One remedy for this is to choose the light to be linearly polarized at an angle $\alpha = 54.7^\circ$ corresponding to $3 \cos(2\alpha) = -1$, and the Stark term disappears. For this polarization, however, amplitude noise of the laser contributes to the noise of \hat{S}_y . This noise can be significant and through Eq. (C.3) couple into the atomic \hat{j}_z (see [1] for a detailed treatment of this effect). For this reason we minimize this effect by choosing a light polarization along or perpendicular to the mean spin.

Another remedy is to add an extra bias magnetic field along the x -direction when the laser light is on. In this way the frequency of the desired transitions can

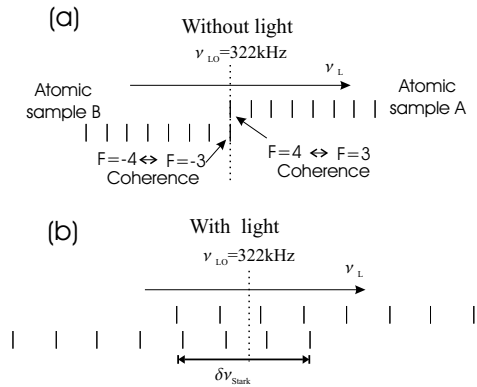


Figure C.1: An illustration of the problem with the light induced Stark shift of the Zeeman sub levels. Without applying additional fields the two important Zeeman resonances cannot be overlapped both without light (a) and with light (b).

be kept stable. This is the approach we have taken and it works well. One should note though, that with our laser pulse timing in the vicinity of one millisecond, it is not completely trivial to make a magnetic pulse following the laser intensity since eddy currents in metallic parts and induced electric fields in other current loops for magnetic fields should be taken into account. A convenient diagnostic method is to apply a classical shift to the spin states along the lines of Eq. (5.6) prior to the application of two laser pulses. An \hat{S}_y detection of the light will show in real time the mean value of the spin state components \hat{J}'_y and \hat{J}'_z . These should be constant through each laser pulse and conserved in the dark time in between (apart from a possible decay) if all frequencies are well adjusted. In Fig. 5.12 the phase between \hat{J}'_y and \hat{J}'_z with and without the Stark shift compensation is shown.

APPENDIX D

Important Abbreviations

AOM In an *acusto-optic modulator* a crystal acts as an effective diffraction grating for light via a spatial modulation of the refractive index created by a piezoelectric transducer oscillating at a frequency of 125MHz. A diffracted beam emerges at angles given by $\sin(\theta) = m\lambda/(2\Lambda)$, where Λ is the wavelength of the sound wave and m is the diffraction order. Alternatively, the process can be thought of as absorption of a phonon, which shifts the frequency of the light in e.g. the first order beam by 125MHz. We use AOM's to shape the intensity profile of the probe beams.

CSS The *coherent spin state* is a Gaussian state, which fulfills the Heisenberg uncertainty relation with symmetric uncertainties in \hat{J}_y and \hat{J}_z . It consists of the collective state of N independent atoms all in the outermost magnetic sublevel (in our case $m_F = \pm 4$).

EOM In an *electro-optic modulator* the difference between the indices of refraction along the optical axes depends linearly on a high-voltage applied transversely to the direction of light propagation through the crystal. As described in Sec. 5.2.2 we use the EOM to shape the temporal intensity profile of the probe pulses. In addition, as described in Sec. 7.3 the EOM is used to generate weak displaced vacuum states, which act as input states in the quantum mapping and teleportation experiments of this thesis.

MORS The *magneto-optical resonance signal* is the signal obtained when scanning an RF-magnetic field transverse to the mean spin across the Zeeman resonances in a particular ground state hyperfine multiplet. The spin state

is monitored continuously via the Faraday interaction and a subsequent \hat{S}_y measurement (see Sec. 5.3.1). We use the signal to obtain information about the degree of optical pumping and to investigate the effect of different decoherence mechanisms (see Sec. 5.4)

PN *Projection noise* refers to the contribution of the light noise coming from an atomic sample in the CSS. The determination of this noise level is crucial to our experiments. The experimental investigation of PN is described in Sec. 5.6.

SN *Shot noise* of light is the minimum noise a classical light source can exhibit. It arises due to the Poissonian photon statistics. In this thesis we will always mean the variance of \hat{S}_y or \hat{S}_z for light in a coherent state when referring to SN. As can be seen from Eq. (2.9) this noise depends linearly on the number of photons - a property that was verified experimentally in Fig. 5.7.

Bibliography

- [1] B. Julsgaard, Ph.D. thesis, Dep. of Physics and Astronomy, University of Aarhus, Denmark, 2003, available at <http://www.phys.au.dk/main/publications/PhD/>.
- [2] A. Einstein, B. Podolsky, and N. Rosen, *Phys. Rev.* **47**, 777 (1935).
- [3] E. Schrödinger, *Die Naturwissenschaften* **23**, 807 (1935).
- [4] J. S. Bell, *Physics* **1**, 195 (1964).
- [5] S. J. Freedman and J. F. Clauser, *Phys. Rev. Lett.* **28**, 938 (1972).
- [6] M. Laméhi-Rachti and W. Mittig, *Phys. Rev. D* **14**, 2543 (1976).
- [7] A. Aspect, J. Dalibard, and G. Roger, *Phys. Rev. Lett.* **49**, 1804 (1982).
- [8] Z. Y. Ou and L. Mandel, *Phys. Rev. Lett.* **61**, 50 (1988).
- [9] R. Garcia-Patron *et al.*, *Phys. Rev. Lett.* **93**, 130409 (2004).
- [10] C. H. Bennett and G. Brassard, in *Proceedings of IEEE International Conference on Computers, Systems, and Signal Processing* (IEEE, New York, 1984), p. 175.
- [11] W. Wootters and W. Zurek, *Nature* **299**, 802 (1982).
- [12] M. Curty, M. Lewenstein, and N. Lütkenhaus, *Phys. Rev. Lett.* **92**, 217903 (2004).
- [13] A. K. Ekert, *Phys. Rev. Lett.* **67**, 661 (1991).
- [14] R. L. Rivest, A. Shamir, and L. M. Adleman, *Communication of the ACM* **21**, 120 (1978).
- [15] C. H. Bennett and S. J. Wiesner, *Phys. Rev. Lett.* **69**, 2881 (1992).
- [16] S. L. Braunstein and H. J. Kimble, *Phys. Rev. Lett.* **61**, 042302 (2000).

- [17] C. H. Bennett *et al.*, Phys. Rev. Lett. **70**, 1895 (1993).
- [18] P. W. Shor, in *Proceedings of the 35th Annual Symposium on the Foundations of the Computer Science* (IEEE Computer Society Press, Los Alamitos, California, 1994), p. 124.
- [19] C. K. Hong and L. Mandel, Phys. Rev. Lett. **59**, 2044 (1987).
- [20] P. G. Kwiat *et al.*, Phys. Rev. Lett. **75**, 4337 (1995).
- [21] D. Bouwmeester *et al.*, Phys. Rev. Lett. **82**, 1345 (1999).
- [22] J. W. Pan *et al.*, Phys. Rev. Lett. **86**, 4435 (2001).
- [23] Z. Zhao *et al.*, Nature **430**, 54 (2004).
- [24] Z. Y. Ou, S. F. Pereira, H. J. Kimble, and K. C. Peng, Phys. Rev. Lett. **68**, 3663 (1992).
- [25] Q. A. Turchette *et al.*, Phys. Rev. Lett. **81**, 3631 (1998).
- [26] C. A. Sackett *et al.*, Nature **404**, 256 (2000).
- [27] E. Hagley *et al.*, Phys. Rev. Lett. **79**, 1 (1997).
- [28] B. B. Blinov, D. L. Moehring, L. M. Duan, and C. Monroe, Nature **428**, 153 (2004).
- [29] J. Volz *et al.*, Phys. Rev. Lett. **96**, 030404 (2006).
- [30] A. Kuhn, M. Hennrich, and G. Rempe, Phys. Rev. Lett. **89**, 067901 (2002).
- [31] J. McKeever *et al.*, Science **303**, 1992 (2004).
- [32] J. I. Cirac, P. Zoller, H. J. Kimble, and H. Mabuchi, Phys. Rev. Lett. **78**, 3221 (1997).
- [33] A. Kuzmich, K. Mølmer, and E. S. Polzik, Phys. Rev. Lett. **79**, 4782 (1997).
- [34] J. Hald, J. L. Sørensen, C. Schori, and E. S. Polzik, Phys. Rev. Lett. **83**, 1319 (2005).
- [35] A. Kuzmich, N. P. Bigelow, and L. Mandel, Europhys. Lett. **42**, 481 (1998).
- [36] L. M. Duan, J. I. Cirac, P. Zoller, and E. S. Polzik, Phys. Rev. Lett. **85**, 5643 (2000).
- [37] A. Kuzmich, L. Mandel, and N. P. Bigelow, Phys. Rev. Lett. **85**, 1594 (2000).
- [38] S. E. Harris, Phys. Today **50**, 36 (1997).

- [39] M. O. Scully and M. S. Zubairy, in *Quantum Optics* (Univ. Press, Cambridge, 1997).
- [40] L. V. Hau, S. E. Harris, Z. Dutton, and C. H. Beohoozi, *Nature* **397**, 594 (1999).
- [41] C. Liu, Z. Dutton, C. H. Behroozi, and L. V. Hau, *Nature* **409**, 490 (2001).
- [42] D. F. Phillips *et al.*, *Phys. Rev. Lett.* **86**, 783 (2001).
- [43] A. Kuzmich *et al.*, *Nature* **423**, 731 (2003).
- [44] C. H. van der Wal *et al.*, *Science* **301**, 196 (2003).
- [45] C. W. Chou, S. V. Polyakov, A. Kuzmich, and H. J. Kimble, *Phys. Rev. Lett.* **92**, 213601 (2004).
- [46] M. D. Eisaman *et al.*, *Nature* **438**, 837 (2005).
- [47] D. N. Matsukevich *et al.*, *Phys. Rev. Lett.* **95**, 040405 (2005).
- [48] C. W. Chou *et al.*, *Nature* **438**, 828 (2005).
- [49] T. Chaneliere *et al.*, *Nature* **438**, 833 (2005).
- [50] D. N. Matsukevich *et al.*, *Phys. Rev. Lett.* **96**, 030405 (2006).
- [51] L.-M. Duan, M. D. Lukin, J. I. Cirac, and P. Zoller, *Nature* **414**, 413 (2001).
- [52] E. Knill, R. Laflamme, and G. J. Milburn, *Nature* **409**, 46 (2001).
- [53] L. Vaidman, *Phys. Rev. A* **49**, 1473 (1994).
- [54] H. J. Briegel, W. D. Abd J. I. Cirac, and P. Zoller, *Phys. Rev. Lett.* **81**, 5932 (1998).
- [55] L. Childress, J. M. Taylor, A. S. Sørensen, and M. D. Lukin, *Phys. Rev. Lett.* **96**, 070504 (2006).
- [56] P. van Loock *et al.*, *Phys. Rev. Lett.* **96**, 240501 (2006).
- [57] H. W. Jian-Wei Pan, Dik Bouwmeester and A. Zeilinger, *Phys. Rev. Lett.* **80**, 3891 (1998).
- [58] X. Jia *et al.*, *Phys. Rev. Lett.* **93**, 250503 (2004).
- [59] N. Takei, H. Yonezawa, T. Aoki, and A. Furusawa, *Phys. Rev. Lett.* **94**, 220502 (2005).
- [60] C. H. Bennett *et al.*, *Phys. Rev. Lett.* **76**, 722 (1996).
- [61] D. Deutsch *et al.*, *Phys. Rev. Lett.* **77**, 2818 (1996).

- [62] B. Julsgaard, A. Kozhokin, and E. S. Polzik, *Nature* **413**, 400 (2001).
- [63] W. Happer and B. S. Mathur, *Phys. Rev. Lett.* **18**, 577 (1967).
- [64] D. Kupriyanov *et al.*, *Phys. Rev. A* **71**, 032348 (2005).
- [65] K. Hammerer, E. S. Polzik, and J. I. Cirac, *Phys. Rev. A* **72**, 052313 (2005).
- [66] P. Milonni and J. Eberly, *Lasers* (John Wiley & sons, New York, 1988).
- [67] J. H. Müller *et al.*, *Phys. Rev. A* **71**, 033803 (2005).
- [68] M. W. Sørensen, Master's thesis, Niels Bohr Institute, Copenhagen University, Denmark, 2005.
- [69] Y. Takahashi *et al.*, *Phys. Rev. A* **60**, 4974 (1999).
- [70] T. Holstein and H. Primakoff, *Phys. Review* **58**, 1098 (1940).
- [71] C. H. Bennett, D. P. DiVincenzo, J. A. Smolin, and W. K. Wootters, *Phys. Rev. A* **54**, 3824 (1996).
- [72] J. Eisert and M. B. Plenio, *Int. J. Qunt. Inf.* **1**, 479 (2003).
- [73] W. K. Wootters, *Phys. Rev. Lett* **80**, 2245 (1998).
- [74] K. Zyczkowski, P. Horodecki, A. Sanpera, and M. Lewenstein, *Phys. Rev. A* **58**, 883 (1998).
- [75] J. Eisert and M. B. Plenio, *J. Mod. Opt* **46**, 145 (1999).
- [76] M. Horodecki, P. Horodecki, and R. Horodecki, *Phys. Lett. A* **223**, 1 (1996).
- [77] R. Simon, *Phys. Rev. Lett.* **84**, 2726 (2000).
- [78] L. M. Duan, G. Giedke, J. I. Cirac, and P. Zoller, *Phys. Rev. Lett.* **84**, 2722 (2000).
- [79] G. Giedke and J. I. Cirac, *Phys. Rev. A* **66**, 032316 (2002).
- [80] A. DiLisi and K. Mølmer, *Phys. Rev. A* **66**, 052303 (2002).
- [81] A. DiLisi, S. DeSiena, and F. Illuminati, *Phys. Rev. A* **70**, 012301 (2004).
- [82] A. Serafini, F. Illuminati, and S. DeSiena, *J. Phys. B* **37**, 21 (2004).
- [83] S. L. Braunstein and P. van Loock, *Rev. Mod. Phys.* **77**, 513 (2005).
- [84] G. Giedke, Ph.D. thesis, Leopold-Franze-Universität Innsbruck, 2001.
- [85] J. Eisert, S. Scheel, and M. B. Plenio, *Phys. Rev. Lett.* **89**, 137903 (2002).
- [86] J. Sherson and K. Mølmer, *Phys. Rev. A* **71**, 033813 (2005).

- [87] L. B. Madsen and K. Mølmer, Phys. Rev. A **70**, 052324 (2004).
- [88] K. Mølmer and L. B. Madsen, Phys. Rev. A **70**, 052102 (2004).
- [89] V. Petersen, L. B. Madsen, and K. Mølmer, Phys. Rev. A **71**, 012312 (2005).
- [90] J. K. Stockton, J. M. Geremia, A. C. Doherty., and H. Mabuchi, Phys. Rev. A **69**, 032109 (2004).
- [91] G. Giedke *et al.*, Phys. Rev. Lett. **91**, 107901 (2003).
- [92] M. A. Bouchiat and J. Brossel, Phys. Rev. **147**, 41 (1966).
- [93] E. B. Alexandrov *et al.*, Laser Phys. **6**, 244 (1996).
- [94] E. B. Alexandrov *et al.*, Phys. Rev. A **66**, 042903 (2002).
- [95] S. Haroche and F. Hartmann, Phys. Rev. A **6**, 1280 (1972).
- [96] J. Shirley, Phys. Rev. A **8**, 347 (1973).
- [97] O. Schmidt, K.-M. Knaak, R. Wynands, and D. Meschede, Appl. Phys. B **59**, 167 (1994).
- [98] R. W. P. Drever *et al.*, Appl. Phys. B **31**, 97 (1983).
- [99] G. C. Bjorklund, M. D. Levenson, W. Lenth, and C. Ortiz, Appl. Phys. B **32**, 145 (1983).
- [100] H.-A. Bachor, *A guide to experiments in quantum optics* (Wiley-VCH, Weinheim, 1998).
- [101] B. Julsgaard, J. Sherson, J. L. Sørensen, and E. S. Polzik, J. Opt. B: Quantum Semiclass. Opt. **6**, 5 (2004).
- [102] J. Geremia, J. K. Stockton, and H. Mabuchi, Science **304**, 270 (2004).
- [103] J. F. Sherson *et al.*, quant-ph/0605095 (2006), accepted for Nature (unpublished).
- [104] B. Julsgaard *et al.*, Nature **432**, 482 (2004).
- [105] K. Hammerer, M. M. Wolf, E. S. Polzik, and J. I. Cirac, Phys. Rev. Lett. **94**, 150503 (2005).
- [106] M. M. Kash *et al.*, Phys. Rev. Lett. **82**, 5229 (1999).
- [107] D. Budker, D. F. Kimball, S. M. Rochester, and V. V. Yashchuk, Phys. Rev. Lett. **83**, 1767 (1999).
- [108] M. Fleischhauer and M. D. Lukin, Phys. Rev. Lett. **84**, 5094 (2000).

- [109] D. Bouwmeester *et al.*, Nature **390**, 575 (1997).
- [110] D. Boschi *et al.*, Phys. Rev. Lett. **80**, 1121 (1998).
- [111] A. Furusawa *et al.*, Science **282**, 706 (1998).
- [112] H. de Riedmatten *et al.*, Phys. Rev. Lett. **92**, 047904 (2004).
- [113] H. Yonezawa, T. Aoki, and A. Furusawa, Nature **431**, 430 (2004).
- [114] M. Riebe *et al.*, Nature **429**, 734 (2004).
- [115] M. D. Barrett *et al.*, Nature **429**, 737 (2004).
- [116] A. Kuzmich and E. S. Polzik, in *Quantum Information with Continuous Variables*, edited by S. L. Braunstein and A. K. Pati (Kluwer, Dordrecht, 2003), pp. 231–265, eds. S. L. Braunstein and A. K. Pati.
- [117] J. Sherson *et al.*, quant-ph/0505170 (unpublished).
- [118] J. Heersink, V. Josse, G. Leuchs, and U. L. Andersen, Optics Letters **30**, 1192 (2005).
- [119] A. Lambrecht, T. Coudreau, A. M. Steinberg, and E. Giacobino, Europhys. Lett. **36**, 93 (1996).
- [120] V. Josse *et al.*, Phys Rev. Lett. **91**, 103601 (2003).
- [121] S. Suzuki *et al.*, quant-ph/0602036 (unpublished).
- [122] J. Geremia, J. Stockton, and H. Mabuchi, Science **304**, 270 (2004).
- [123] J. S. Neergaard-Nielsen *et al.*, quant-ph/0602198 (unpublished).
- [124] A. Ourjoumtsev, R. Tualle-Brouri, J. Laurat, and P. Grangier, Science **312**, 83 (2006).
- [125] T. C. Ralph, A. Gilchrist, and G. J. Milburn, Phys. Rev. A **68**, 042319 ((2003)).
- [126] A. Kuzmich and T. A. B. Kennedy, Phys. Rev. Lett. **92**, 030407 (2004).